Experimental and Numerical Investigations of Flames Stabilized by Swirl Flow and Bluff-body:Flame Structures and Flame Instabilities

Tong, Yiheng

2017

Document Version:
Publisher's PDF, also known as Version of record

Experimental and Numerical Investigations of Flames Stabilized by Swirl Flow and Bluff-body:

Flame Structures and Flame Instabilities

Yiheng Tong

LUND
UNIVERSITY

DOCTORAL DISSERTATION
by due permission of the Faculty of Engineering at Lund University, will be publicly defenced on Wednesday 14th November 2017, at 10:15 a.m. in Lecture Hall E in the M-building, Ole Römers väg 1, Lund, Sweden.

Faculty opponent
Professor Ashwani K. Gupta, Department of Mechanical Engineering, University of Maryland, College Park, U.S.A.

Organization	Document name
LUND UNIVERSITY	DOCTORAL DISSERTATION
Department of Energy Sciences PO Box 118, 22100, Lund, Sweden	Date of issue 2017-10-16
Author(s) Yiheng Tong	Sponsoring organization China Scholarship Council (CSC)

Title and subtitle

Experimental and Numerical Investigations of Flames Stabilized by Swirl Flow and Bluff-body: Flame Structures and Flame Instabilities

Abstract

Combustion and its control are essential to our existence on this planet since we knew it. Nowadays, the largest share of the world's electricity and most of our transportation systems are powered by combustion. In addition, industrial processes also rely heavily upon combustion. In most industrial combustion systems, combustion occurs under turbulent flow conditions that can produce combustion instabilities. These are problematical since they can result in oscillations in thrust, low- or high-cycle fatigue of system components, flame blowoff or flashback, and oscillations in combustion efficiency together with high emission levels or even damage to the combustion systems. Thus, flame stabilization is of fundamental importance in the design, the efficient performance and the reliable operation of the combustion systems.

Experimental and numerical investigations of swirl and bluff-body stabilized flames are presented in the thesis. Both premixed and diffusion flames are investigated in detail. Different parameters including the operating conditions, the burner geometries, fuel injection strategies are examined. High-speed PIV, high-speed PLIF and intensified CH* chemiluminescence, together with thermography and corresponding image analysis methods are adopted in the experimental work. In addition, DES and LES turbulence models on the basis of ANSYS Fluent and OpenFOAM, respectively, are employed in the numerical studies. The doctoral work is concerned above all with flame structures and flame instabilities.

For swirl stabilized lean premixed flames, the operating conditions, including the total mass flow rate and the equivalence ratio of the reactants all play an important role in determining flame structures and lean blowout limits of swirl stabilized lean premixed flames. The geometries of the confinement, including the cross-sectional shape and the cylindrical confinement diameter, strongly affect the swirl stabilized flame structures and flame dynamics. Proposals are made regarding the mechanisms behind the forming of swirl stabilized lifted M-shape flames and corresponding flame dynamics. Fuel injection strategy employed also affects the characteristics of low-swirl stabilized flames, such as the time-averaged flame structures and the flame oscillations that occur. An axial fuel injection strategy leads to a more compact flame and a leaner blowout limit than a tangential fuel injection method does. The flame oscillation frequency near lean blowout is affected when fuel injection strategy is altered. When the global equivalence ratio decreases, flame dynamics frequency is reduced until the occurrence of flame lean blowout.

A central fuel or air jet through the bluff-body axis makes the bluff-body stabilized premixed flame less stable. When a central fuel injection takes place, the flame is found to be lifted off from the bluff-body, with a circular motion of the flame tip along the outer edge of the bluff-body. The injection of a central fuel or air jet results in a higher lean blowout limit. At the same time, the temperature on the upper surface of the bluff-body becomes lower.

Different patterns of bluff-body stabilized diffusion flames are presented: the recirculation zone flame, the stable jet diffusion flame, the lifted flame, the split-flashing flame being included here. The position of a bluff-body in relation to the annular channel exit affects the instabilities of the diffusion flame, particularly when the annular air flow velocity is high. Mounting the bluff-body downstream of the annular channel exit makes it able to better stabilize the flame. The flame stabilization is achieved by the recirculation bubble that was adjacent to the outer wall of the bluff-body.

A diffusion flame stabilized by a combination of swirl and bluff-body is studied both experimentally and numerically. The effects both of a bluff-body on a swirl-stabilized diffusion flame and of swirl on a bluff-body stabilized diffusion flame are investigated. Diffusion flame 'flashback' is studied, the mechanisms behind it being proposed. When a larger bluff-body is employed, air driven recirculation zone is found to be located further upstream near the burner exit. The flame is found to be better stabilized by use of a larger bluff-body and/or a stronger swirling flow.

Key words: flame structures, flame instabilities, blowout limits, flashback, swirl-stabilized flame, bluff-body, PIV, CH* chemiluminescence

Classification system and/or index terms (if any)

Supplementary bibliographical information		Language: English
ISSN 0282-1990		ISBN: 978-91-7753-409-9 (print) 978-91-7753-410-5 (pdf)
Recipient's notes	Number of pages: 88	Price
	Security classification	

Experimental and Numerical Investigations of Flames Stabilized by Swirl Flow and Bluff-body:

Flame Structures and Flame Instabilities

Yiheng Tong

LUND
UNIVERSITY

Thesis for the degree of Doctor of Philosophy in Engineering.

Division of Thermal Power Engineering
Department of Energy Sciences
Faculty of Engineering (LTH)
Lund University
Box 118
SE-221 00 LUND
SWEDEN

ISBN 978-91-7753-409-9 (print)
ISBN 978-91-7753-410-5 (pdf)

ISSN 0282-1990

Printed in Sweden by Media-Tryck, Lund University.
Lund 2017

Abstract

Combustion and its control are essential to our existence on this planet since we knew it. Nowadays, the largest share of the world's electricity and most of our transportation systems are powered by combustion. In addition, industrial processes also rely heavily upon combustion. In most industrial combustion systems, combustion occurs under turbulent flow conditions that can produce combustion instabilities. These are problematical since they can result in oscillations in thrust, low- or high-cycle fatigue of system components, flame blowoff or flashback, and oscillations in combustion efficiency together with high emission levels or even damage to the combustion systems. Thus, flame stabilization is of fundamental importance in the design, the efficient performance and the reliable operation of the combustion systems.

Experimental and numerical investigations of swirl and bluff-body stabilized flames are presented in the thesis. Both premixed and diffusion flames are investigated in detail. Different parameters including the operating conditions, the burner geometries, fuel injection strategies are examined. High-speed PIV, high-speed PLIF and intensified CH* chemiluminescence, together with thermography and corresponding image analysis methods are adopted in the experimental work. In addition, DES and LES turbulence models on the basis of ANSYS Fluent and OpenFOAM, respectively, are employed in the numerical studies. The doctoral work is concerned above all with flame structures and flame instabilities.

For swirl stabilized lean premixed flames, the operating conditions, including the total mass flow rate and the equivalence ratio of the reactants all play an important role in determining flame structures and lean blowout limits of swirl stabilized lean premixed flames. The geometries of the confinement, including the cross-sectional shape and the cylindrical confinement diameter, strongly affect the swirl stabilized flame structures and flame dynamics. Proposals are made regarding the mechanisms behind the forming of swirl stabilized lifted M-shape flames and corresponding flame dynamics. Fuel injection strategy employed also affects the characteristics of low-swirl stabilized flames,

such as the time-averaged flame structures and the flame oscillations that occur. An axial fuel injection strategy leads to a more compact flame and a leaner blowout limit than a tangential fuel injection method does. The flame oscillation frequency near lean blowout is affected when fuel injection strategy is altered. When the global equivalence ratio decreases, flame dynamics frequency is reduced until the occurrence of flame lean blowout.

A central fuel or air jet through the bluff-body axis makes the bluff-body stabilized premixed flame less stable. When a central fuel injection takes place, the flame is found to be lifted off from the bluff-body, with a circular motion of the flame tip along the outer edge of the bluff-body. The injection of a central fuel or air jet results in a higher lean blowout limit. At the same time, the temperature on the upper surface of the bluff-body becomes lower.

Different patterns of bluff-body stabilized diffusion flames are presented: the recirculation zone flame, the stable jet diffusion flame, the lifted flame, the split-flashing flame being included here. The position of a bluff-body in relation to the annular channel exit affects the instabilities of the diffusion flame, particularly when the annular air flow velocity is high. Mounting the bluff-body downstream of the annular channel exit makes it able to better stabilize the flame. The flame stabilization is achieved by the recirculation bubble that was adjacent to the outer wall of the bluff-body.

A diffusion flame stabilized by a combination of swirl and bluff-body is studied both experimentally and numerically. The effects both of a bluff-body on a swirl-stabilized diffusion flame and of swirl on a bluff-body stabilized diffusion flame are investigated. Diffusion flame 'flashback' is studied, the mechanisms behind it being proposed. When a larger bluff-body is employed, air driven recirculation zone is found to be located further upstream near the burner exit. The flame is found to be better stabilized by use of a larger bluff-body and/or a stronger swirling flow.

Popular Science Summary

Combustion and its control play an important role in everyday life. Combustion has been the cornerstone of industrial development for nearly two centuries. The burning of fuel to produce heat and power is an integral part of industrial processes generally. Combustion of fossil fuel produces the largest share of the world's electrical power. In addition, most transportation systems rely on combustion. The drawbacks of combustion in daily life are the formations of environmental pollutions, causing fires threatening people's lives, etc. Although considerable progress has been made over the years in achieving a basic scientific understanding of combustion, these drawbacks still remain. The strong regulatory and competitive forces at work aimed at developing combustion equipment with greater flexibility, improved performance and less environmental impact, all at a reasonable cost are needed. Being able to achieve these goals is a basic objective in efforts to obtain a better understanding of combustion and its control.

In most industrial combustion systems, combustion occurs in process involving highly turbulent flow, a matter that strongly increases the complexity. In addition, the turbulent flow can result in instabilities in combustion in the form of oscillations of large-amplitude and marked changes in flame structures inside the combustor. The occurrence of such instabilities is generally problematic since it can produce oscillations in pressure and velocity of large-amplitude, which in turn can lead to oscillations in thrust, to severe vibrations that can interfere with the operation of the control-system, to enhanced heat transfer and thermal stresses to combustor walls, to oscillatory mechanical loads that result in the low- or high-cycle fatigue of system components, to flame blowoff (the flame extinction) or flashback (the flame propagating into the upstream region), and to oscillations in combustion efficiency along with high emission levels. These phenomena may result in premature component wear that can lead to costly shutdown or to failure with missions that are undertaken. Thus, flame stabilization is of fundamental importance in the design, efficient performance and reliable operation of combustion systems.

In addition, flame instability can create unstable flame structures and marked variations in the heat that released from combustion. The interaction of flame structures and flow

fields determines the flame instabilities and its performance in terms of emissions as well. The geometries of the combustor/confinement and the burner as well as the operating conditions that are present (such as the flow swirl strength) affect the flow fields and the flame behaviors considerably. It is thus highly important to investigate the mechanisms involved in flame stabilization.

Flame stabilization is usually accomplished through the recirculation of combustion products with high temperature so as to continually ignite the reactants. The hot recirculating gases transfer heat to the cold reactants to ignite them and thus to maintain the spread of flame. The burnt gases transfer heat to the recirculation zone, this serving to balance the heat lost in igniting the combustible gases. Two common methods of generating recirculating flows to stabilize the flames are the use of swirl flow and of a bluff-body. Swirl flow is the flow with strong tangential component of the velocity, while a bluff-body can be defined as a solid body inside the flow field that creates a recirculation downstream of it.

In the thesis, experimental and numerical investigations of flames stabilized by swirl flow and a disk-shape bluff-body are presented. The experimental work was carried out on a model gas turbine swirl burner under atmospheric conditions and on an adjustable bluff-body burner both with and without swirl flow. Advanced laser-based non-intrusive diagnostics techniques and flame visualization methods were employed in the experimental study. In addition, numerical simulation work was carried out to complement the experimental work in efforts to better understand the flame behaviors involved.

Acknowledgments

This work has been carried out at the Division of Thermal Power Engineering, Department of Energy Sciences at Lund University, Lund, Sweden.

First of all, I would like to thank my main supervisor, Professor Jens Klingmann, and my co-supervisor, Associate Professor Marcus Thern, for providing me the opportunity to carry out my Ph.D. study at the Department of Energy Sciences at Lund University. Their academic guidance, encouragement and all the support I have received from them have helped me enormously during the past four years. It is my honor to be supervised by them.

I would like to thank senior lecturer Zhongshan Li at the Division of Combustion Physics for the help he provided me in connection with experimental investigations of the adjustable bluff-body burner. I would like thank Shuang Chen, Wubin Weng and Zhenkan Wang at the Division of Combustion Physics, without whose kind help, my experiments would never have been successfully carried out. I would like to thank Professor Qinglian Li at the National University of Defense Technology in China for his encouraging me to study and live abroad. I would like to thank Professor Bengt Sundén who introduced me to my main supervisor. Without his recommendation I would not have the chance to carry out my Ph.D. study in Lund University.

In addition, many thanks to all my colleagues, the administrators and the technicians at the Department of Energy Sciences for providing me a harmonious study environment. I would like to thank Parisa Sayad for guiding me very much in the lab, and Srikanth Deshpande, who was my officemate for two years and shared with me his experience about how to be a Ph.D. student. Many thanks to Cheng Gong, Xiao Liu, Senbin Yu and Jiatang Wang for your help in my numerical studies; thanks to Georgios Paterakis, Alessandro Schönborn, Mao Li and Lei Wang for your help in my experimental work. I would like to thank all my friends in Lund for adding color to my life abroad.

I would like to give special thanks to my beloved family members and friends in China for your sincere love and support all these years.

My living costs for the past four years were supported financially by the China Scholarship Council (CSC) which I gratefully acknowledge. The Department of Energy Sciences, LTH, Lund University as well as National University of Defense Technology in China gave me the opportunity to join summer schools, which I would like to gratefully acknowledge. I would like to acknowledge ÅForsk for giving me the opportunity to attend the ASME conference in U.S.A. by founding me with the travel grants. The simulation work in the thesis was carried out using the computer facilities provided by the Lund University Center for Scientific and Technical Computing (LUNARC).

List of Publications

Publications included in the thesis:

I **Tong Yiheng**, Mao Li, and Jens Klingmann. Influence of Combustor Geometry on Swirl Stabilized Premixed Methane-Air Flame. ASME Turbo Expo 2016: Turbomachinery Technical Conference and Exposition. American Society of Mechanical Engineers, 2016.

II **Tong Y**, Li M, Thern M, Klingmann J. An Experimental Study of Effects of Confinement Ratio on Swirl Stabilized Flame Macrostructures. In ASME 2017 Power Conference Joint with ICOPE-17 collocated with the ASME 2017 11th International Conference on Energy Sustainability, the ASME 2017 15th International Conference on Fuel Cell Science, Engineering and Technology, and the ASME 2017 Nuclear Forum 2017 Jun 26 (pp. V001T04A007-V001T04A007). American Society of Mechanical Engineers.

III **Yiheng Tong**, Senbin Yu, Xiao Liu and Jens Klingmann. Experimental study on dynamics of a confined low swirl partially premixed methane-hydrogen-air flame. *Accepted by International Journal of Hydrogen Energy.*

IV **Yiheng Tong**, Shuang Chen, Mao Li, Zhongshan Li and Jens Klingmann. Experimental study on bluff-body stabilized premixed flame with a central air/fuel jet. *Submitted to Energies.*

V **Yiheng Tong**, Xiao Liu, Shuang Chen, Zhongshan Li, Jens Klingmann. Experimental and Numerical Study about Effects of Bluff-body Position on Diffusion Flame Instabilities. *Submitted to Applied Thermal Engineering.*

VI **Yiheng Tong**, Xiao Liu, Zhenkan Wang, Jens Klingmann. Experimental and Numerical Study of Bluff-body and Swirl Stabilized Diffusion Flames. *Submitted to Fuel.*

Publications not included in the thesis:

VII **Yiheng Tong**, Senbin Yu, Xiao Liu, Mao Li and Jens Klingmann. Experimental study of confined partially premixed flame in low swirl flow. 10th Mediterranean Combustion Symposium. Naples, Italy, September 17-21, 2017.

VIII **Tong, Y.**, Li, M., Thern, M., Klingmann, J., Weng, W., Chen, S., & Li, Z. (2017). Experimental Investigation on Effects of Central Air Jet on the Bluff-body Stabilized Premixed Methane-air Flame. Energy Procedia, 107, 23-32.

IX **Tong Y**, Li M, Klingmann J, Chen S, Li Z. Experimental Investigation on the Influences of Bluff-Body's Position on Diffusion Flame Structures. In ASME 2017 Power Conference Joint with ICOPE-17 collocated with the ASME 2017 11th International Conference on Energy Sustainability, the ASME 2017 15th International Conference on Fuel Cell Science, Engineering and Technology, and the ASME 2017 Nuclear Forum 2017 Jun 26 (pp. V001T04A009-V001T04A009). American Society of Mechanical Engineers.

X Li, M., **Tong, Y.**, Thern, M., & Klingmann, J. (2017). Influence of the Steam Addition on Premixed Methane Air Combustion at Atmospheric Pressure. Energies, 10(7), 1070.

XI Li, M., **Tong, Y.**, Thern, M., & Klingmann, J. (2017). Investigation of Methane Oxy-Fuel Combustion in a Swirl-Stabilized Gas Turbine Model Combustor. Energies, 10(5), 648.

XII Li, M., **Tong, Y.**, Klingmann, J., & Thern, M. (2017). Impact of Vitiation on a Swirl-stabilized and Premixed Methane Flame. *Accepted by Energies.*

XIII Li, M., **Tong, Y.**, Klingmann, J., & Thern, M. Experimental Study of Hydrogen Addition Effects on a Swirl-stabilized Methane-Air Flame. *Submitted to Energies*

Nomenclature

Latin Characters

b	blockage ratio [-]
c	confinement ratio [-]
c	reaction progress variable [-]
d_a	diameter of the annular channel [mm]
d_b	diameter of the bluff-body [mm]
d_c	diameter of the confinement [mm]
d_j	diameter of the central jet [mm]
fl	focal length [mm]
f	dominant frequency of flame oscillation [Hz]
f	mixture fraction [-]
h	axial position [mm]
h_b	height of the bluff-body [mm]
h_q	height of the quartz tube [mm]
H_{COHR}	position of flame's corner of heat release [mm]
h_q	length of the quartz tube [mm]
h_t	height of the tangential inlet [mm]
L_F	representative flame length [mm]
m	total mass flow rate of reactants [ln/min] or [SLPM]
m_a	mass flow rate of the axial air [ln/min] or [SLPM]
m_{air}	total mass flow rate of air [ln/min] or [SLPM]

m_{CH4}	mass flow rate of methane [ln/min] or [SLPM]
m_f	mass flow rate of fuel [ln/min] or [SLPM]
m_{H2}	mass flow rate of hydrogen [ln/min] or [SLPM]
m_t	mass flow rate of the tangential air [ln/min] or [SLPM]
r	radial position [mm]
S	the swirl number [-]
S_g	geometrical swirl number [-]
T_0	representative bluff-body upper surface temperature in the base case [K]
T_{edge}	temperature at the inner edge of the bluff-body [K]
T_{in}	inlet temperature of the reactants [K]
U_a	velocity of the annular flow [m/s]
$U_{c\text{-}a}$	velocity of the central air jet [m/s]
$U_{c\text{-}f}$	velocity of the central fuel jet [m/s]
U_j	velocity of the central jet [m/s]
w	tangential inlet width [mm]
w_f	flame width [mm]

Greek symnols

α	flame open angle [°]
ΔH	Distance from bluff-body upper surface to annular channel exit [mm]
Δm_{air}	step of the change in the mass flow rate of air [SLPM]
Δt	time delay between two laser pulses [μs]
Φ	equivalence ratio [-]
Φ_g	global equivalence ratio [-]
Φ_{LBO}	lean blowout equivalence ratio [-]

Abbreviations

CFD	computational fluid dynamics
CFL	Courant–Friedrichs–Lewy
CIVB	combustion induced vortex breakdown
COHR	corner of heat release
DES	Detached Eddy Simulation
DLE	dry low emission
FFT	Fast Fourier Transform
fps	frame per second
FWHM	full width at half maximum
IDDES	improved delayed Deached Eddy Simulation
IEA	International Energy Agency
IRZ	inner recirculation zone
ISL	inner sheary layer
LBO	lean blowout
LDA	Laser Doppler Anemometry
LDV	Laser Doppler Velocimetry
LES	Large Eddy Simulation
LIP	Laser Induced Phosphor
ORZ	outer recirculation zone
OSL	outer shear layer
PDF	probability density function
PISO	pressure implicit with splitting of operator
PIV	Particle Image Velocimetry
PLIF	Planar Laser Induced Fluorescence
PVC	Precessing Vortex Core
RANS	Reynolds-Averaged Navier–Stokes
RMS	root mean square

SGS	subgrid-scale
SLPM	standard liter per minute
SST	shear stress transport
URANS	unsteady RANS

Chemical components

CH^*	electronically excided methylidyne radical
CH_2O	formaldehyde
CH_4	methane
CO	carbon monoxide
CO_2	carbon dioxide
H_2	hydrogen
H_2O	water
N_2	nitrogen
NOx	nitrogen oxides
O_2	oxygen
OH^*	electronically excided hydroxide radical
TiO_2	titanium dioxide

Contents

1.Introduction

1.1 Motivation

Combustion and its control are essential to our existence on this planet since we knew it. According to the International Energy Agency (IEA), the largest share of the world's electricity is produced by combustion of fossil fuel [1]. Most of our transportation systems, i.e. the vehicles, aircrafts and most trains as well as ships, rely heavily on combustion. Industrial process, including those in furnaces, boilers, refineries, glass melters, solid dryers and the curing of surface coatings, to name a few examples, also rely heavily on combustion [2]. At the same time, among the drawbacks of combustion in daily life are that it produces environmental pollutions, causes system damages and also causes fires that threaten people's lives. In view of the importance of combustion in society generally, as thorough an understanding of combustion and its control as possible is needed.

In most industrial combustion systems, combustion occurs under turbulent flow conditions, which strongly increases the complexities. In addition, the turbulent flow may result in instabilities in combustion. Such instabilities are characterized by large amplitude oscillations and changes in flame structures inside a combustor. The occurrence of instabilities is generally problematic since they produce large amplitude oscillations in pressure and velocity that can lead to oscillations in thrust, severe vibrations that can seriously interfere with control-system operations, enhanced heat transfer and thermal stresses to combustor walls, oscillatory mechanical loads that can result in either low- or high-cycle fatigue of system components, flame blowoff or flashback, and oscillations in combustion efficiency with high emission levels. Such phenomena can result in premature component wear that can lead to costly shutdown or catastrophic failure of various components or of the mission that was undertaken, as shown in Figure 1.1 [3]. Thus, flame stabilization is of utmost importance in the design, the efficient performance and the reliable operation of combustion systems.

Flame stabilization is usually accomplished by causing some of the combustion products to recirculate and hence to continually ignite the reactants. The hot recirculating gases transfer heat to the colder reactants to ignite them and thus initiate flame spread. The burnt gases transfer heat to the recirculation zone to balance out the heat lost in igniting the combustible gases. Sufficient energy must be fed to the stabilization region to continuously ignite the coming gas flow. Two common methods of generating recirculating flows to stabilized the flames are studied: stabilizing flames by means of swirl flow and by use of a bluff-body.

Figure 1.1 New burner assembly (left) and damaged by combustion instability (right) [3].

In addition, flame stabilization process is always accompanied by significant changes in flame structures. The interaction of flame structures and flow fields determines to a considerable extent the flame instabilities that appear and the emission performance achieved. The geometry of the combustor and of the burner as well as the operating conditions (the flow swirl strength in particularly) strongly affect the flow fields and thus determine the flame behavior to a considerable extent. It is thus important to investigate the effects of swirl flow and of a bluff-body on flame structures and flame instabilities.

In addition, the concept of lean premixed combustion in gas turbines has been widely accepted in recent years as an effective method to the stringent standards of emissions. Having flames burnt under lean conditions can reduce the emission of NOx considerably due to the low flame temperatures involved. At the same time, under fuel lean conditions, flame instabilities can more readily to occur. In order to achieve flame stability, the flames in some industrial gas turbines are stabilized aerodynamically by inducing swirl flow of the reactants or utilizing a bluff-body. The underlying mechanisms that bring about flame instability involve complex interactions between flame structures, flow fields, heat and mass transfer, chemical reactions, and burner

geometries. Thus, it is important to obtain a deeper understanding of flow fields, flame structures and flame instabilities in swirl and bluff-body stabilized flames.

1.2 Objectives

The major aim of thesis is to investigate the effects of the operating conditions, the burner and combustor geometries and fuel injection strategies on the flow fields, flame structures and the flame instability characteristics. The combined experimental and numerical investigations here were conducted on a variable-swirl burner and an adjustable bluff-body burner with and without swirl. Premixed, non-premixed (diffusion) and partially premixed flames were investigated. The detailed objectives of the thesis are:

1. For swirl stabilized flames:

- To study the effects of the operating conditions and the confinement geometries on lean premixed flame instabilities and flame structures. The operating conditions include the mass flow rates and the equivalence ratio of the reactants. The geometrical parameters of the confinement include its cross-sectional shape and its diameter.

- To study dynamics of low-swirl stabilized partially premixed flames with use of different fuel injection strategies, with the aim of better understanding the mechanisms controlling flame structures and flame dynamics under fuel lean conditions.

2. For bluff-body stabilized flames:

- To investigate the effects of a central fuel and air injection on bluff-body stabilized premixed flames. Of particular interests are flame dynamics, flame structures, the flame blowout limits and the temperature on the upper surface of the bluff-body.

- To investigate the effects of the burner geometries on bluff-body stabilized diffusion flame structures and its instabilities; the effects of the position of the disk-shape bluff-body on the flow fields and their interactions with flame stabilizations.

3. For the combined swirl and bluff-body stabilized flames:

- To investigate the effect of bluff-body size and the swirl strength on non-premixed flame stabilization and flame structures.

The framework of the doctoral thesis is formed based on the research objectives mentioned above and the output three peer-reviewed articles that were published or accepted as well as three manuscripts that are now under review.

1.3 Approaches and methodologies

Investigations of swirl stabilized flames were carried out on a confined variable-swirl burner. Flame dynamics, flame structures and the lean blowout features were made visible by use of an optical quartz tube. Different operating conditions including the inlet temperature, the mass flow rates, the swirl strength and the equivalence ratio of the reactants could be adopted and controlled. The variables concerned with the confinement geometries included the cross-sectional shape and the diameter of the confinement.

Research on bluff-body stabilized flame behaviors was carried out on an adjustable bluff-body burner without swirl. The velocities of air and fuel flow could be validated by a separately controlled air and fuel supply system. The position of the as well as the shape of the bluff-body were adjustable as well.

Studies of the combined bluff-body and swirl stabilized diffusion flames were conducted on a modified version of the adjustable bluff-body burner with swirl. The bluff-body was removable and the swirl strength could be adjusted by changing the mass flow rates of the tangential and the axial flow.

In order to be able to better visualize the flow fields, flame structures and flame dynamics, following measurement techniques and image analysis methods were adopted in the experimental work:

- High spatial resolution, long exposure time CH* chemiluminescence photography as well as the use of corresponding inverse Abel image reconstruction methods, were utilized for visualizing the time-averaged flame structures.

- High-speed intensified CH* chemiluminescence photography and corresponding image analysis methods, together with Fast Fourier Transform (FFT) methods, were utilized in studying flame dynamics.

- High-speed Particle Image Velocimetry (PIV) measurement was utilized to capture the flow fields both in the iso-thermal and combusting cases.

- High-speed Planar Laser Induced Fluoresce (PLIF) measurement was adopted for obtaining the distribution of CH_2O in the combined swirl and bluff-body stabilized flames.

- A thermographic camera was utilized for visualizing the temperature distribution on the upper surface of the bluff-body in the adjustable bluff-body burner.

In addition, numerical simulations were performed as well. 3D unsteady numerical simulations of bluff-body stabilized non-premixed flames were conducted based on ANSYS Fluent and OpenFOAM. Large Eddy Simulation (LES) and Detached Eddy Simulation (DES) were adopted in the simulation of flame structures in the adjustable bluff-body burner with and without swirl respectively.

1.4 Thesis outline

The thesis is composed of seven chapters in which tow published, one accepted and three submitted papers are summarized. The papers, which are attached at the end of thesis, contain the major results of the doctoral work.

Chapter 1: The aims and objectives of the research reported on in the thesis are introduced. The various approaches and an overview of thesis as a whole are also included.

Chapter 2: A survey of literatures on flames that are stabilized by swirl flow and a bluff-body is presented. Comparisons of swirl and bluff-body stabilized flames are also provided. In addition, matters of flow structures, flame patterns, flame instabilities and their interactions are highlighted.

Chapter 3: The experimental setup and the various approaches, including a variable-swirl burner, an adjustable bluff-body burner with and without swirl, are described in detail.

Chapter 4: The measurement techniques adopted are described, details of corresponding image analysis methods employed being provided as well.

Chapter 5: The numerical assumptions and models utilized in the simulations are presented, details of the mesh and of the numerical setups also being described.

Chapter 6: The major results of the work carried out are presented and discussed, summaries of the papers also being provided.

Chapter 7: The main conclusions of thesis are highlighted and suggestions for further investigation are proposed.

2.Flames Stabilized by Swirl Flow and Bluff-body

This chapter reviews recent research on swirl and bluff-body stabilized flames. Particular emphasis is placed on flame structures, flame instabilities and their interactions with flow fields. Both premixed and diffusion flame behavior based on the results of both experimental and numerical studies are reviewed in the chapter.

2.1 Swirl flow

2.1.1 Swirl strength

As mentioned in Chapter 1, swirl flow is widely adopted in stabilizing lean premixed flames, especially in gas turbine combustors. Swirl flow is commonly generated by use of two different swirlers: the guiding vane swirler and the tangential flow entry swirler. Compared with a guiding vane swirler, the tangential entry system has better performance in the vorticity contribution to the core from the endwall boundary. However, the major drawbacks of tangential entry swirl generator are the higher degree of asymmetry and the effects brought about by the Taylor-Gortler vortices that are formed on the tube wall [4].

Flow having a tangential momentum generates the centrifugal force directed at the confinement wall. A pressure gradient in the radial-direction is then formed in order to sustain equilibrium with the centrifugal force, this being termed as simple radial equilibrium flow [5]. The equation concerning the momentum in radial direction of the pressure gradient can be calculated as

$$\frac{\partial v_r}{\partial t} + (V \cdot \nabla) v_r - \frac{1}{r} v_\theta^2 = -\frac{1}{\rho} \frac{\partial p}{\partial r} + g_r + \nu \left(\nabla^2 v_r - \frac{v_r}{r^2} - \frac{2}{r^2} \frac{\partial v_\theta}{\partial \theta} \right) \tag{2.1}$$

It is assumed here that under steady state conditions the axial and the radial velocities are functions of radius, axial symmetry and radial direction velocity. Then the momentum equation in radial direction can be simplified to

$$\frac{\partial p}{\partial r} = \rho \frac{1}{r} v_\theta^2 \tag{2.2}$$

It was found that when the flow expands and the azimuthal velocity decays with an increase in the axial distance, the pressure in the downstream region recovers. A positive pressure gradient is generated along the axis, which consequently leads to the formation of a recirculation zone, providing the swirl strength is high enough. In some gas turbine combustors, the sudden expansion of the cross-sectional area from the burner to the combustor can enhance the formation of vortex breakdown in terms of pressure gradient: the vortex core grows rapidly and generates an adverse pressure gradient, which is further enhanced by the pressure recovery due to the general decrease in axial velocity [6]. Several types of vortex breakdown were observed and described in both laminar and turbulent flows [7-11]. The method by which the swirling flow is generated (i.e. use of guiding vane or of tangential flow entry) as well as the geometries of the burner and confinement have strong effects on the vortex breakdown and thus on the flow fields [6, 12].

Several non-dimensional parameters have been proposed in characterizing turbulent swirling flow. These include Reynolds number, the swirl ratio, the circulation number, Rossby number, Strouhal number, the geometrical swirl number and the swirl number [4]. In the thesis, the swirl number, *S*, was selected to evaluate the swirl strength in the investigations of flames in the variable-swirl burner. It is defined as the ratio of the axial flux of the tangential momentum to the axial flux of the axial momentum times a characteristic length, i.e. the radius of the burner exit, *R*:

$$S = \frac{M_t}{R M_a} \tag{2.3}$$

where M_t is the axial flux of the tangential momentum, and M_a is the axial flux of the axial momentum. M_t and M_a can be calculated with use of equations (2.4) and (2.5), respectively:

$$M_t = 2\pi \int_0^R \rho w u r^2 dr \tag{2.4}$$

$$M_a = 2\pi \int_0^R \rho u^2 r dr + \int_0^R p r dr \tag{2.5}$$

where ρ is the density of the incoming flow, u is the axial velocity, w is the tangential velocity, r is the radius and p is the static pressure at the combustor inlet. In some calculations of S, such as in the one used in the thesis, the pressure term in equation (2.5) is often neglected.

In addition, in investigating flame behavior in the adjustable bluff-body burner with swirl flow, the geometrical swirl number, S_g, was utilized. The same as in the literatures [13, 14], S_g is defined as

$$S_g = \frac{\pi r_{ch} d_b}{2A_t} \left(\frac{m_t}{m_t + m_a} \right)^2 \tag{2.6}$$

where A_t is the total area of the eight tangential air inlets, d_b is the diameter of the central body, r_{ch} is the radius of the annular channel $r_{ch} = d_a - d_t$, d_a is the outer diameter of the annular pipe, m_t is the tangential mass flow rate and m_a is the mass flow rate of the axial flow. The geometrical swirl number is determined by the mass flow ratio of the tangential to the axial flow, together with the burner geometries.

2.1.2 Swirl flow structures

As shown in Figure 2.1.1 and described in [5], when the swirling effects are sufficiently strong, the central vortex breakdown and thus an inner recirculation zone (IRZ, sometimes referred to as the central recirculation zone) are formed. The vortex breakdown is characterized by the existence of internal stagnation points and reversing flows which enhances flame stabilization. An outer recirculation zone (ORZ, sometimes referred to as the corner recirculation zone) is generated as well due to effects produced by the confinement wall. In the swirling flow field, vortex breakdown is often associated with a negative axial velocity field, although different breakdown structures may also appear [4]. The vortex breakdown is formed due to the adverse pressure gradient that develops along the combustor axis under conditions with high swirl

strength [6]. There is an inner shear layer (ISL) located between the main flow and the inner recirculation zone, the outer shear layer (OSL) being located between the main flow and the outer recirculation zone.

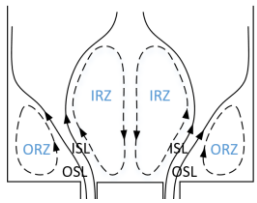

Figure 2.1 The typical swirl flow structures inside a confinement.

Furthermore, the most common type of coherent vortex structure in swirl flow is the so-called precessing vortex core (PVC) [15-20]. A three-dimensional PVC and other vortex structures are shown in Figure 2.2. It was found that the PVC develops when a central vortex core starts to precess around the axis of symmetry at a well-defined frequency. This phenomenon is usually associated with vortex breakdown and the corresponding recirculation zone in flows with high Reynolds number [21].

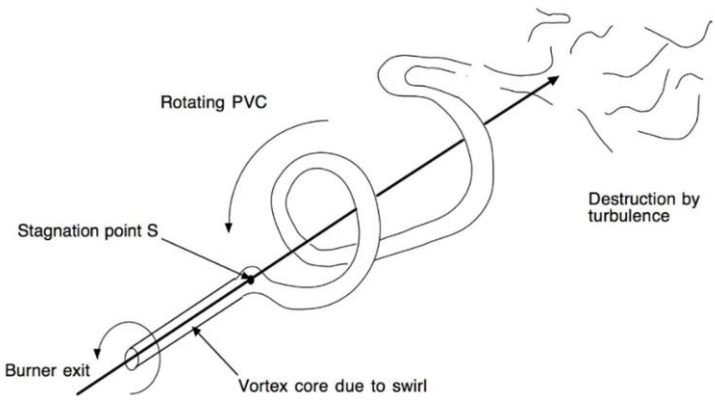

Figure 2.2 Three-dimensional reconstruction of vortex structures in swirl flow [22].

2.2 Flames stabilized by swirl flow

As mentioned above, the development of dry low emission (DLE) burner concept in industrial context lead to the use of lean premixed gas turbine systems as well as high performance flame stabilization techniques. In lean premixed gas turbine combustors,

swirl flows are commonly employed. The primary role of swirl is to create a low velocity region where the flame can be anchored [23]. Moreover, the inner recirculation zone of the swirl flow acts as an aerodynamic blockage in stabilizing the flame. The combustion products recirculate in the inner recirculation zone and thus continually ignite fuel mixture. The hot burnt gases transfer heat to the recirculation zone to balance out the heat lost in igniting the combustible mixtures.

2.2.1 Flame structures within swirl flow

Flame shapes (or referred to as flame topologies or flame macrostructures) in a swirl-stabilized lean premixed gas turbine combustor have been studied extensively in recent years. The flame shape is strongly affected by the operating conditions, the heat transfer to the confinement wall together with the geometries of the burner and the confinement [21, 24-28]. Guiberti et al. [28] stated that there are primarily two types of flame shape: the M-shape flame and the V-shape flame, as shown in Figure 2.3(b) and in Figure 2.3(c). The V-shape flame is stabilized in the inner shear layer; whereas the M-shape flame is formed with the reaction zones both in the inner shear layer (ISL) and the outer shear layer (OSL). Flashback of the trailing edge of the V-shape flame along the confinement wall was suggested as being the trigger for the sudden transition from the V-shape flame to the M-shape flame [25, 28]. This was supported by numerical computations indicating that heat losses to the burner walls favored the occurrence of the V-shape flame [29]. Guiberti, T. F. et al. [30] concluded that for a fixed swirl strength and a small confinement ratio, a critical Karlovitz number could predict the flame transition phenomenon rather well.

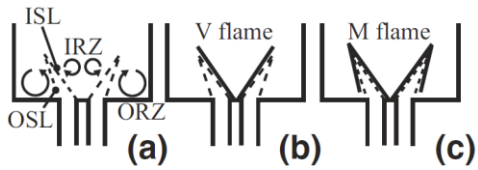

Figure 2.3 (a) A schematic of flow fields in a swirlling jet flow with a central bluff-body; (b) the typical V-shape flame and (c) the typical M-shape flame [28].

Further types of swirl stabilized flame structures were observed as well. S. J. Shanbhogue et al. [27] designated in their study a time-averaged flame shape as being a flame 'macrostructure'. As shown in Figure 2.4, they observed four different flame macrostructures appearing as the equivalence ratio was changed during their experiments. In addition to the typical V-shape and M-shape flames (or referred to as IRZ and ORZ flames respectively in their study), they observed both a columnar flame that was detached from the center body and a 'bubble' flame. Chterev et al. [24] observed four different flame shapes in their experimental and numerical work. They named the different flame shapes with use of Roman numbers, such as flame I (the

columnar flame), II (the inner shear layer stabilized bubble flame), III (the inner shear layer stabilized V-shape flame) and IV (both inner and outer shear layers stabilized M-shape flame), in a swirl-stabilized combustor in which a center body was mounted at the burner exit. Alekseenko et al. [31] studied unconfined premixed propane-air flames with different flow swirl numbers. They observed three flame types: attached flames, quasi-tubular flames and lifted flames. Malanoski et al. [32] separated swirl flame structures into two groups, based on the flow structures (whether the vortex breakdown bubble was attached to the center body). They found the recirculation zones that were formed downstream of the center body had a marked effect on the flame macrostructures.

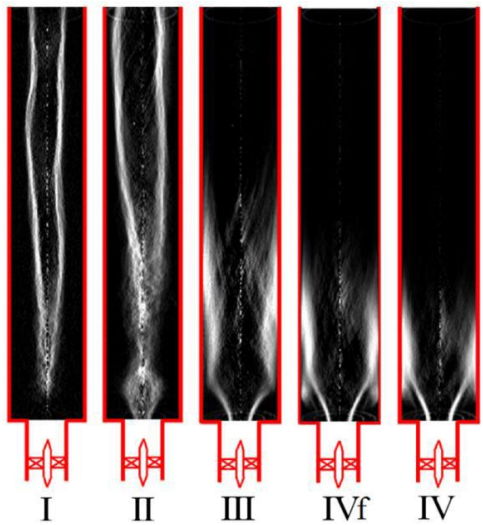

Figure 2.4 (a) An inverse Abel reconstructed chemiluminescence of (I) the columnar shape flame, (II) the bubble shape flame, (III) the V-shape flame and (IVf and IV) the M-shape flame [27].

2.2.2 Flame instabilities within swirl flow

Flame instability refers to damaging oscillations in pressure associated with oscillations in the heat release rate from combustion [33]. Several mechanisms capable of bringing about combustion instabilities in swirl flow in gas turbine combustors have been identified, as shown in Figure 2.5. The mechanisms are summarized to be: (1) fuel feed line-acoustic coupling; (2) equivalence ratio oscillations; (3) oscillatory atomization, vaporization, and mixing; (4) oscillatory flame area variation and (5) vortex shedding [3]. The alternations of flame and flow structures were commonly observed during the flame oscillation process.

Soufien T. et al. [34, 35] reported that a circular motion in the outer recirculation zone around the confinement centerline was the reason for low frequency flame oscillation.

They found that the flame instability was strongly correlated with the flame macrostructures. Soufien T. et al. [36] also found that the sudden and intermittent ignition of reactants recirculating in the outer recirculation zone led to flame fluctuations and thus to the transition of flame macrostructures.

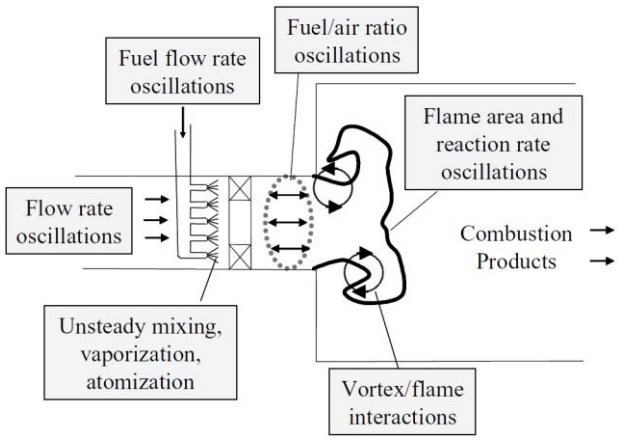

Figure 2.5 Diagram of the mechanisms responsible for swirl stabilized flame instabilities in gas turbine combustors [3].

Other flame instability related events include flame flashback, lean blowout and autoignition. Flame flashback commonly occurs in premixed flame when the flame propagates upstream into the premixing zone or along the boundary into the upstream region [37-42]. Sayad, P. et al. [37, 42] summarized four different mechanisms that can lead to flashback in a swirl stabilized flame: flashback in the boundary, flashback due to combustion induced vortex breakdown (CIVB), autoignition in the premixing zone upstream and flame propagation in high velocity core flow. In addition, Sommerer et al. [40] pointed out the flame instabilities as being a fifth factor that could lead to flame flashback. Lean blowout describes the process of flame extinction under fuel lean conditions. For premixed combustion, two theoretical mechanisms can be utilized for explaining the lean blowout phenomenon: (1) as defined by Kanury [43], the blow out phenomenon arises when the time allowed by the flow is not long enough for the reactions to proceed to ignition or deflagration; (2) as suggested in the literatures [33, 42, 44-46], flame blow out occurs under conditions of an imbalance between the entrance rate of reactants into the recirculation zone and the burning rate of fuel-oxidizer mixtures involved. This can be reduced to a Damköhler number blow-off criterion, making use of a chemical time derived from the well stirred reactor [46]. Autoignition can occur in the premixed cases when the residence time of the reactants exceeds the ignition delay (which is determined by the local temperature, pressure and equivalence ratio). It can be defined as the spontaneous ignition of a fuel/oxidizer mixture in the absence of any concentrated ignition source (such as a flame or a spark)

[47]. Autoignition in the premixing zone could readily result in flame dynamics that increase the emissions or possibly cause structural damage to the combustor.

2.2.3 Interactions between flames and swirl flow fields

The flow fields in a swirl-stabilized combustor can change with the heat released from combustion, especially near the axis of the combustor [3]. In addition, the mass flow rate and fuel to air ratio for the swirl generator affects the position of the stagnation point as well as the flow structures [24, 48]. At the same time, the flame stability characteristics can affect the size of the inner recirculation zone [5]. Stöhr et al. [49] stated that PVC affected the flame in two aspects. Firstly, the chemical reaction rates near the stagnation point and the inner shear layer were accelerated by PVC. Secondly, PVC enhanced the mixing of burned gas with the unburned fuel-air mixture. It can also change the flame behavior through inducing an enlargement of the flame surface or bringing about a strain-induced local flame extinction. However, it can in some cases lead to low-frequency acoustic oscillations in gas turbine combustors. The flame eccentricity caused by PVC is suggested to be detrimental to the upstream flame propagation and effective in inhibiting flame flashback in a swirl stabilized gas turbine model combustor [19]. In addition, the behavior of PVC is significantly altered by the heat released from combustion and by other operating parameters [50].

2.3 Flow fields downstream of a bluff-body

A bluff-body can be utilized to stabilize both premixed and diffusion flames. The typical flow fields downstream of an unconfined bluff-body in the case of premixed flame stabilization are shown in Figure 2.6 [51]. Three regions can be identified: the boundary layer along the bluff-body, the separated free shear layer and the wake region. A pair of recirculation zones is generated with a relatively low pressure region downstream of the bluff-body.

In addition, in the case of bluff-body stabilized diffusion flames, a central fuel jet is commonly found, this making the flow fields more complicated. The typical flow fields downstream of the bluff-body with a central jet are shown in Figure 2.7 [52]. Two recirculation zones, namely the inner and the outer recirculation zone, can be observed. The outer recirculation zone is driven by the annular flow whereas the inner recirculation zone is driven by the central jet. These two recirculation zones interact with one another and play an important role in diffusion flame structures and thus

determine the occurrence of flame stabilization. Dally et al. [53] identified three mixing layers in the recirculation zone: (a). an external mixing layer located between the annular air flow and the outer recirculation zone (shown as the annular flow shear layer in Figure 2.7); (b). an intermediate layer between the inner and the outer recirculation zones (shown as the mixing shear layer in Figure 2.7); (c). an internal layer between the inter vortex and the central fuel jet (shown as the jet shear layer in Figure 2.7).

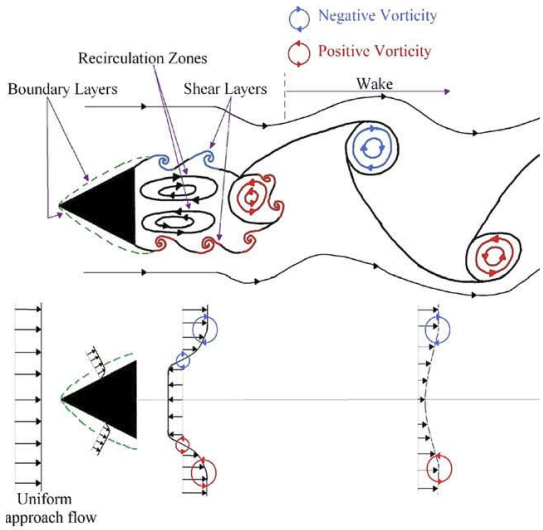

Figure 2.6 A schematic of typical flow fields of a bluff-body stabilized premixed flame[51].

The flow structures downstream of a bluff-body with a central jet are strongly dependent upon the velocity ratio [52] or the momentum ratio [53] of the central jet to the annular flow. For an axisymmetric bluff-body burner, Roquemore et al. [52] divided the flow topologies into three modes (as shown in Figure 2.7), based on fuel to air velocity ratio in the iso-thermal flow. With an increase in the velocity ratio of the central jet to the annular air flow, the flow structures were found to change from the annular jet dominating, to a transitional pattern, and finally to the central jet dominating. Esquiva-Dano et al. [54] distinguished three flow patterns based on the number of the stagnation points in the central axis of the flow. When the annular air dominated the flow structures downstream of the bluff-body, two stagnation points could be observed along the centerline. These two stagnation points were related to the central jet penetration and the length of the recirculation zone, respectively. When the central fuel jet dominated the flow structures, there was no stagnation point located along the centerline. The occurrence of the transition mode was when neither the central fuel jet nor the annular air jet dominated the flow fields. The transition mode

was an intermediate state in which only one stagnation point could be observed. Ma and Harn [55] numerically studied the effects of the blockage ratio, the cone angle and fuel-air velocity ratio on the flow fields downstream of the bluff-body. It was found that when the blockage ratio was high, a larger recirculation zone would be formed. However, a less degree of variation in the velocity gradient in the major mixing zone could be observed in the case with a high blockage ratio. It was predicted that in cases of a higher blockage ratio, the mixing of the central fuel jet with the annular air flows would proceed less effectively.

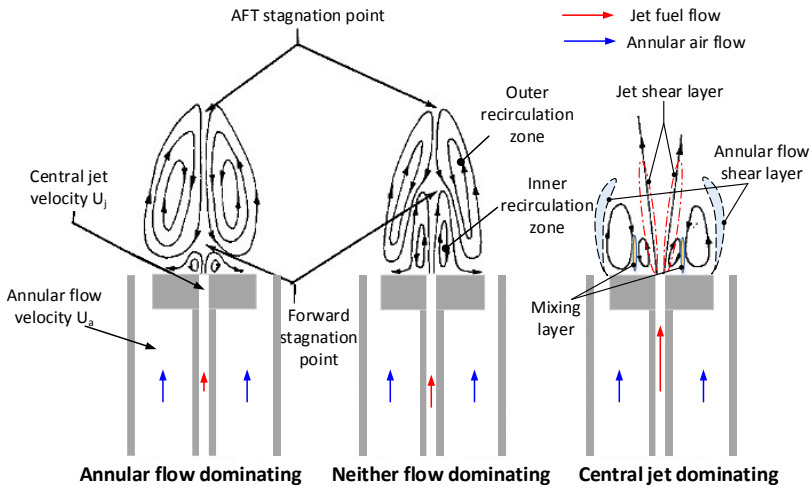

Figure 2.7 A schematic of the typical flow fields downstream of a bluff-body with a central jet (reproduced from [52]).

2.4 Flames stabilized by a bluff-body

As mentioned above, a bluff-body could be utilized to stabilize both premixed and diffusion flames. The use of a bluff-body flame holder is commonly employed in flame stabilization due to the enhanced mixing characteristics and the ease of combustion control it provides. The recirculation of hot gas behind the bluff-body can help to reignite gas mixtures, and thus to stabilize the flame [56]. In addition, the longer residence time downstream of the flame holder may also enhance flame stabilization. A bluff-body has been utilized as well to increase the heat conduction that takes place and to shorten the flame length both in steam boiler and in gas turbine combustors [57].

2.4.1 Flame structures within a bluff-body burner

Bluff-body stabilized diffusion flame structures are of considerable interest to researchers since they can be strongly related to the flame stabilization characteristics involved. Chen et al. [58] proposed a regime diagram of bluff-body stabilized flame patterns applying to (a) a recirculation zone flame, (b) a central jet dominated flame, (c) a jet-like flame, (d) a partially quenched flame and (e) a lifted flame. Tang et al. [56] referred to flame structures considering stable flames, transitional-state flames, unstable flames and flame blowout. They also observed split-flashing flames, split flames and lift-off flames appearing under certain operating conditions. San et al. [57] studied rifled bluff-body frustums and they divided the flame patterns into the categories of jet flames, flickering flames, bubble flames, lifted flames and turbulent flames. Yang et al. [59] classified diffusion flames behind the disc stabilizer into five different modes: (1) recirculation zone flames, (2) central jet dominated flames, (3) jet like flames, (4) partially quenched flames and (5) lift-off flames. Masri and Bilger [60] also reported there to be three types of bluff-body stabilized turbulent natural gas and liquefied petrol gas flames: (A) short, recirculation controlled flames, (B) transitional flames, and (C) long, fuel jet dominated flames. Subsequently, Huang and Lin [61] divided the commercial propane diffusion flames into the following seven types: (I) the recirculated region flame, (II) the transition flame, (III) the unsteady detached flame, (IV) the laminar ring flame, (V) the developing ring flame, (VI) the split flashing flame and (VII) the lifted flame. Esquiva-Dano et al. [54] investigated the effects of the shape of the bluff-body on the behavior of diffusion flames. With respect to decreasing in the velocity ratio of the jet to the annular air flow, they classified flames into five different regimes: (1) laminar flame regime, (2) transition I flame regime, (3) laminar ring flame regime, (4) transition II flame regime and (5) recirculating flame regime, these being followed by flame extinction. In the transition I flame regime, bulge flame, detached flame and reattached flame were observed. They also reported that the tulip-shape bluff-body promoted the flame stabilization. Whereas the disk-shape bluff-body, which created a larger recirculation zone, performed worse in stabilizing the flame. Fuel penetration and fuel-air mixing process were concluded as the dominant factors in determining the flame patterns and the flame stabilization. However, Longwell et al.[44] reported that a larger recirculation zone downstream of the bluff-body could better stabilize a premixed flame. They emphasized the fact that in a larger recirculation zone, the reactants involved can have longer residence time and thus better promote flame stabilization. It was noted by Shanbhogue et al. [51] that the flame patterns were strongly associated with flame dynamics that were present. They reported that flame blowoff occurred as a sequence of events: first extinction along the flame sheet, then

large scale wake disruption and finally flame blowoff. These flame behaviors were claimed to depend upon wake cooling and shrinking. In addition, significant differences between the iso-thermal and the reacting flow structures were reported.

2.4.2 Flame instabilities within a bluff-body burner

As described in the literature [2], when a bluff-body stabilized diffusion flame is stable, the flame root is commonly found to be attached to the bluff-body. As fuel flowrate changes, holes begin to form in the flame sheet until no continuous flame is attached to the bluff-body, this finally leading to a blowout. Accordingly, there are two critical conditions related to flame stability: liftoff and blowout. Various other researchers have also defined the appearance of holes in flame sheets as representing a third state of the diffusion flame instability [56] [58]. In addition, bluff-body stabilized flame dynamics as well as flame-area variations, which may be originated from oscillations in the shear layer and from vortex merging, can also be regarded as diffusion flame instabilities within the bluff-body burner [3].

Tang et al. [56] found that unstable diffusion flames were triggered by local extinctions at the neck region, when Reynolds number of fuel approached the unstable limit, in a bluff-body burner. The unstable limit of a flame was determined to a significant extent by Reynolds number of the annular air. Unstable flames corresponded to the occurrence of flame splitting or local flame quenching which was caused by the local strain rate exceeding a critical value [62]. Chen et al. [58] reported there to be two different flame stability limits: local flame extinction dominating the lifting of jet-like flames and the partial quenching of blue-neck flame in jet-dominated flames. Stability of jet-like flames is governed by local flame extinction at the position where the outer mixing layer of air vortex meets the central jet flame fronts. Schefer et al. [63] concluded that fuel concentration in the recirculation zone played an important role in determining the flame stabilization. They also claimed that when the confinement ratio was lower than 0.25, the confinement would not have significant effects on diffusion flame stabilization or flame structures. The flame blowoff of bluff-body stabilized flames was reviewed by Shanbhogue et al. [51], who described the growth of flame holes in the flame sheet: once a flame hole was initiated, its size might either stay constant, grow, or shrink (through 'flame healing'). It was associated with whether the edge flame remained stationary, retreats (a 'failure wave'), or advances (an 'ignition front') into the hole. They also proposed that the classical Damköhler number correlations did not describe the ultimate blowoff condition itself, but rather described instead the conditions under which flame extinction began to occur.

2.4.3 Interactions between flames and flow fields within a bluff-body burner

Schefer et al. [63] reported that the velocity ratio of the central jet to the annular flow determined the number of stagnation points together with the size and the strength of the recirculation zones. They were applicable to both reactive and non-reactive cases within different confinements. Whereas, Yang et al.[64] studied the reacting flow structures and distinguished them in terms of four different modes. It was also concluded that the flow patterns were strongly determined by the interaction between flow and combustion. Schefer et al. [65] compared the iso-thermal case with the combusting case regarding the velocity fields downstream of the bluff-body, when holding the velocity ratio of the central jet to the annular flow constant at U_j / U_a = 0.84. It was concluded that the velocity in the centerline region was altered between one case and the other; whereas the velocity distributions in the remainder of the flows were quantitatively similar to one another. They also reported that combustion would result in an increase in the central jet penetration. However, Huang and Lin[66] reported that the lifted flames did not significantly affect the flow structures near the bluff-body. In the lifted flames, combustion in the recirculation bubble led to a lower pressure locally and thus enhanced the reinforcement of the development of the central jet. It was found that the flow patterns and the turbulent intensities could affect combustion by ways of fuel entrainment, diffusion and mixing capabilities. They classified the flow structures into pre-penetration, penetration and large shear flows according to the velocity ratios of the central jet to the annular flow.

2.5 Temperature on the surface of a bluff-body

Considerable research has been carried out on the premixed flames that were stabilized by a simple bluff-body without a central jet [44, 51, 67-75]. However, there has been only a limited amount of research concerning with the heat load to the bluff-body. Nishimura et al. [76] utilized a fine wire thermocouple in studying the temperature fluctuations of the diffusion flame in a bluff-body burner. The temperature distribution along the axial line of the burner, including temperature on the surface of the bluff-body was presented. Euler et al. [77, 78] measured the temperature on the surface of the bluff-body of Cambridge/Sandia Stratified Swirl Burner using Laser Induced Phosphor (LIP) thermometry. Different premixed and stratification cases with and without swirl were tested. They concluded that the overall operation of the burner was adiabatic since the radiative and convective heat transfer by the bluff-body amounted to less than 0.5% of thermal input of combustion. They also noted that there were few

measurements of the temperature distribution of the flame holder, whereas that temperature clearly had a strong effect on the flame stabilization. In fact, in practical applications in gas turbine combustors, the major challenge involved in use of a bluff-body appears to be the severe heat load and the extremely high temperature on the surface of the bluff-body. The heat load to the bluff-body could be expected to strongly affect the stability limits of the premixed flame [79]. In addition, the temperature distribution on the surface of the bluff-body is important in regard to the lifetime of the combustion system [80]. There is a need of practical methodologies that are able to reduce the heat load on the surface of the bluff-body.

2.6 Geometries of bluff-body burners

Bluff-body stabilized diffusion flames are found in a variety of applications, such as gas turbine combustors, afterburners, heat recovery steam generators, and industrial furnaces [58]. In order to stabilize a diffusion flame, the bluff-body is commonly designed to be located along the axis of an annular channel in such a way that fuel jet passes through the center of the bluff-body.

In addition, in bluff-body stabilized diffusion flames, the geometries of the burner can be altered by changing the shape and the position of the bluff-body as well as the blockage ratio and the confinement ratio of the burner. Different geometries of the burner with different bluff-body flame holders are summarized and listed in Table 2.1. Researchers often prefer to place the bluff-body at the level of the annular channel exit, as can be noted in the literatures [54-56] [58] [61] and [64]. The bluff-body shapes most commonly employed are disk-shape or conical shape. Various other bluff-body burner geometries have also drawn the attention of investigators, such as placing the bluff-body downstream [57] [68] [81, 82] or upstream [83] of the annular channel exit, or using a rifled bluff-body [57].

In addition, Yang et al. [59] studied the effects of the blockage ratio on flame stabilization and flame patterns. They concluded that when the blockage ratio increased, the main reaction zone regularly moved upstream to the inner side of the recirculation zone. It was similar with the phenomenon when fuel-to-air velocity ratio was increased. Esquiva at al. [54], in turn, investigated the effects of the shape of a bluff-body on the flame regime that appeared. A tulip-shape bluff-body was found to perform better in stabilizing the flame than a disk-shape flame holder did. Kumar and Mishra [84, 85] studied the effects of the size of a disk-shape bluff-body on a liquefied petroleum gas

Table 2.1 Different bluff-body burners investigated in the literatures and in the present study

References	d_j[mm]	d_b [mm]	U_j [m/s]	d_a [mm]	U_a [m/s]	ΔH [mm]	Shape	Cone angle
Guo et al. [81, 82, 88]	4	40	2.5-50	60	3.72-12.5	20	Disk/Conical	180/60
Yang et al.[58, 59, 64, 87]	3.5	30-45	0-50	55.1	0-20	0	Disk	180
Esquiva-Dano et al.[54]	5	40	0-14	200	3.65	0	Disk/Tulip	180
Huang and Lin[61, 66]	3.4	20	12.5-103	30	3.56-4.52	0	Disk	180
Tang et al.[56]	2.2	27.3	0-219	42	0-10.4	0	Conical	45
San et al.[57]	5	30	0-10	30	0-2.5	30	Conical	36.87
Caetano and Silva [83]	7.1	60	4.2-17.9	200	4/8	-	-	180
Ma and Harn [55]	8.05	25.2/38.8/43.2	10/14/25	50.25	14/17.9/25	0	Disk/Conical	15/30/45/180
Kumar and Mishra [84, 85]	5	6.5/12.8/18.1	0.816	57	0.016/0.033	0	Disk	180
Chaudhuri and Cetegen [68-70]	-	10	-	20/40	5-16	90	Disk	180
Roy and Sreedhara [86]	3.6	50	80/134	-	40	0	Disk	180
Present thesis	4	15	0-30	30	0-8	0/10	Disk	180

(LPG)–H_2 jet diffusion flame. It was found that as the diameter of the bluff-body was increased, the flame length became shorter. The recirculation zone downstream of the bluff-body performed better in mixing the reactants, then the reaction zone was likely to propagate toward the bluff body. As a consequence, this led to a reduction in the length of the flame. However, research concerned with the effects of the position of the bluff-body (specially whether it is at the level to the annular air channel exit or higher than it) on the recirculation zones and flame structures is rare. At the same time, as indicated above, researchers have already utilized burners with different positions of the bluff-body in their research. Whether and to what extent the position of the bluff-body can affect the flame patterns is still a topic in need of study. In the burner design process, more information concerning with the effects of the position of the bluff-body on the flame behaviors is clearly required.

2.7 Comparison of flames stabilized by swirl flow and bluff-body

Chen et al. [89] compared swirl and bluff-body stabilized diffusion flames, concluding that: if a bluff-body flame and a swirl flame were operated under conditions such that they had the same non-dimensional vortex strength (of air driven vortex) and the same non-dimensional fuel jet momentum, the two flames would display similar flame properties and trends. They also reported that bluff-body flows had the same vortex velocity as swirl flows did, with the swirl number being approximately 0.5 (with an accuracy of plus or minus 0.1 in swirl number). They observed two types of flame structures (Type 1, a fuel-jet dominated flame and Type 2, a recirculating flame) both in the bluff-body and swirl stabilized flames. They also concluded that flame behavior was strongly determined by the flow fields downstream of the bluff-body or the swirler. In addition, for large powers and high inlet flow speeds, creating a recirculation zone behind a bluff-body may not be sufficient to ensure that flame stabilization was maintained while pressure losses were minimized [22]. In such cases, swirl flow could be utilized in industrial burners to stabilize the diffusion flame [90]. A. Mestre and A. Benoit [91]also pointed out the advantage of the use swirl flow in flame stabilization is that the absence of a solid flame holder in the combustor avoids flame impingement on the surface of the flame holder, thus ensuring minimum maintenance and extended life for the combustion system.

There are also some research dealing with the combination of bluff-body and swirl stabilized flames, especially diffusion flames. Masri and his colleagues [92-99] utilized

modern laser-based diagnostic methods to study the combination of a bluff-body and swirl flow in stabilizing the diffusion flames. Their experimental results could serve as detailed data validations of the numerical research that has been conducted by other researchers.

B. Ge and S.-S. Zang [100] examined experimentally the effects of adding a bluff-body to swirl stabilized flames, as well as the effects of adding swirl to bluff-body stabilized flames. Kashir et al. [101] studied combustion characteristics of a blended methane-hydrogen diffusion flame stabilized by a combination of a bluff-body and swirl flow. They tested their numerical model with experimental data from Masri et al. [95]. They also compared the typical flow fields downstream of the bluff-body with and without a swirling flow, as shown in Figure 2.8. The inner recirculation zone was driven by the central fuel jet, whereas the outer recirculation zone was created by the bluff-body and was driven by the annular air flow. With an increase in the swirl number of the annular flow, an additional swirling flow driven 'secondary vortex' was formed further downstream of the bluff-body. The flow fields appeared in an hourglass shape. K.R. Dinesh et al. [102] studied numerically the flow structures of a turbulent jet, a bluff-body stabilized turbulent jet and a bluff-body stabilized swirling turbulent jet in a co-flow environment. They concluded that the combination of bluff body and swirl could significantly increase the mixing of the central jet with the annular flow in the radial direction and thus could reduce the axial extent of the high concentration zone.

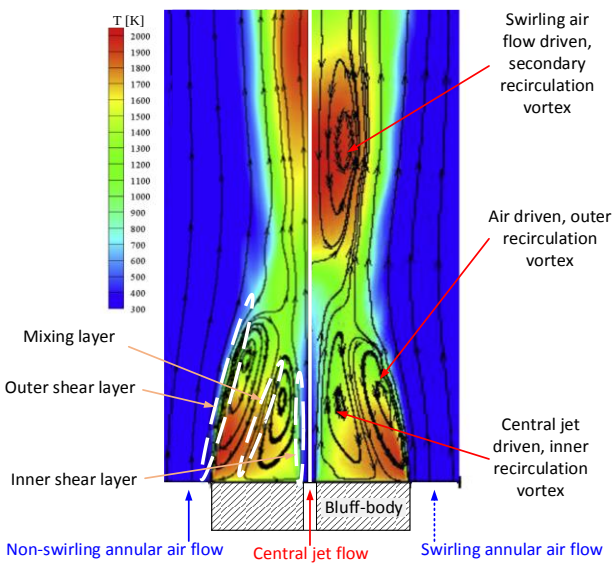

Figure 2.8 The typical time-averaged flow and flame structures downstream of a bluff-body with (right) and without (left) swirling annular flow (reproduced from [101]).

3.Experimental Setups

Two experimental facilities were utilized in the research: (1) a confined variable-swirl combustor designed and built at the Division of Thermal Power Engineering, LTH, Lund University for studying the swirl stabilized flame behaviors in a gas turbine model combustor; (2) an adjustable bluff-body burner designed and manufactured on a cooperative basis by the Division of Thermal Power Engineering and the Division of Combustion Physics, LTH, Lund University for studying both the bluff-body stabilized and combined swirl and bluff-body stabilized flame structures and corresponding flame dynamics. These two experimental facilities will be described in detail in the present chapter.

3.1 The variable-swirl burner

The experimental setup for the confined variable-swirl burner, together with a high-speed PIV system, a high-speed intensified CH* photography system and a high spatial resolution CH* photography system are shown in Figure 3.1. Further details concerning with the confined variable-swirl burner and its dimensions are shown in Figure 3.2 and Figure 3.3.

As shown in Figure 3.1 and in Figure 3.2, tangential and axial flows enter the combustor through the variable swirler. The swirler was used to generate variable strength swirl flows through combining axial and tangential flows. The swirler had four tangential flow inlet channels in width of 3mm and height of 10mm, as shown in Figure 3.3; while the axial inlet diameter was 15mm. The burner had the potential of varying the swirl strength by changing the proportions of the mass flow rates of the axial and the tangential flows. In addition, two feedback-controlled air heaters (Sylvania Sureheat Jet) were used to heat up the tangential and axial air flows individually with the maximum input thermal power of 8 kW. Fuel was injected into and premixed with the

axial/tangential flow downstream of the heater and at least 200 mm upstream of the swirler. This enabled fuel and air to be mixed perfectly in air/tangential flow prior to their entering the swirler. The swirler was located directly upstream of a short mixing tube with length of 30 mm. The mass flow rates of the axial/tangential air flows and fuel flow were metered individually, using the laminar-flow differential-pressure mass flow meters (Alicat MCR series). Airflow temperature at the exit of the mixing tube was measured as the inlet flow temperature, T_{in}, by a K-type thermocouple. The perfectly premixed fuel-air reactants in the one flow direction (axial or tangential direction) then further mixed with flow from the other direction in the mixing tube. The premixing tube led into a stepped expansion, referred to hereafter as the 'dump plane'. At the dump plane, a small injection hole for the premixed pilot mixture was located. The pilot flame was only used in the ignition process until a stable main flame had been obtained. The optical confinement, which had access for the flame visualization and the flow field measurements, was located downstream of the mixing tube. The confinement was held in place by pneumatic pressure provided by four pneumatic actuators that acted upon it. The pneumatic system allowed swift sealing and removal of the confinement. A spark plug, which was utilized to ignite the premixed torch flame, was mounted at the exit of the confinement. In addition, an exhaust gas sampling probe was placed at the exit of the optical quartz tube, as shown in Figure 3.3.

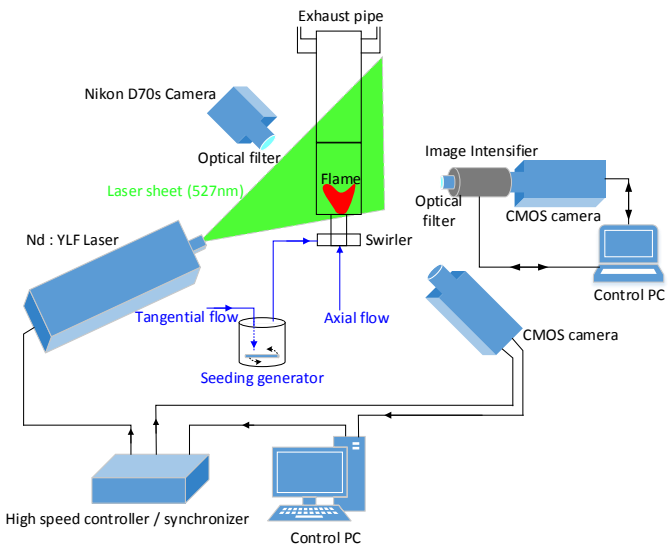

Figure 3.1 A schematic of the experimental setup for the variable-swirl burner.

The large cylindrical confinement shown in Figure 3.2 and Figure 3.3 is a quartz tube having an inner diameter of 63 mm and a length of 120 mm. The dimensions of all three confinements employed in the doctoral work are listed and compared with one another in Table 3.1. Two cylindrical confinements and one confinement with a rectangular cross-section were involved. The rectangular confinement was enclosed by four optical quartz windows held in place by a metal frame. Since the cross-sectional area of the small cylindrical confinement and that of the rectangular confinement were approximately the same, the bulk velocities inside these two confinements were comparable under the same operating conditions. These two confinements were employed to study the effects of the cross-section geometry on flame structures and the flame instabilities.

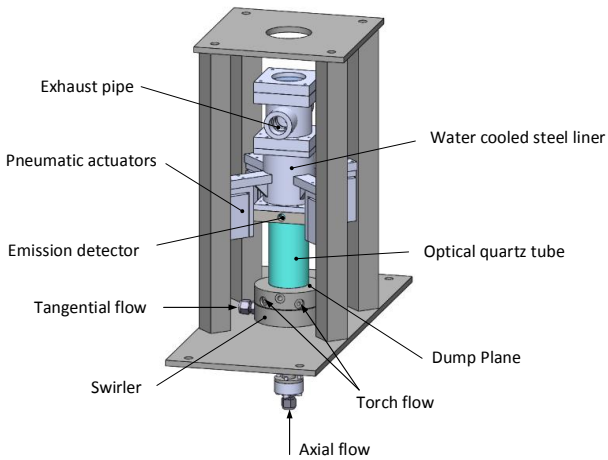

Figure 3.2 A schematic of the confined variable-swirl burner with the large cylindrical confinement.

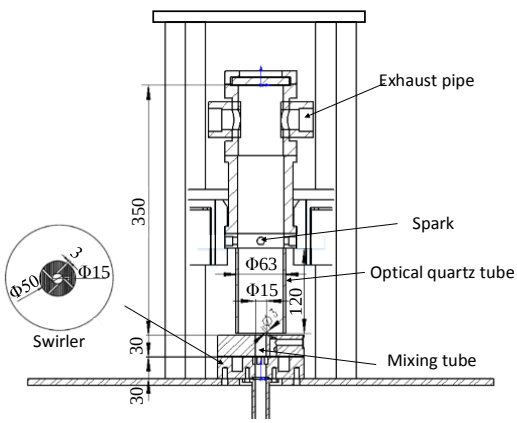

Figure 3.3 Cross-section of the confined variable-swirl burner with the large cylindrical confinement.

Table 3.1 Dimensions of three different confinements investigaed in the thesis.

Confinement	Large cylindrical	Small cylindrical	Rectangular
Cross-section shape	Circular	Circular	Rectangular
Inner diameter [mm]	63	39	-
Outer diameter [mm]	66	42	-
Long window width [mm]	-	-	40
Short window width [mm]	-	-	30
Cross-section area [mm^2]	3117.25	1194.59	1200
Length [mm]	120	120	120

3.2 The adjustable bluff-body burner

The adjustable bluff-body burner was employed to study both the premixed and the diffusion flame structures and the flame instabilities. Two versions of the burner were utilized throughout the doctoral work. Version 1 was used to study the effects of a central jet on the behaviors the premixed flame and on the heat load on the surface of the bluff-body (**Paper IV**). In addition, the effects of the position of a bluff-body on the diffusion flame patterns that appeared were investigated for the first version of the burner as well (**Paper V**). For the modified version of the adjustable bluff-body burner (Version 2), swirl flow was induced in order to study the flames stabilized by a combination of swirl flow and a bluff-body (**Paper VI**).

3.2.1 Adjustable bluff-body burner: Version 1

The adjustable bluff-body burner (Version 1) and the experimental setup are shown schematically in Figure 3.4. The annular channel of the burner had an inner diameter of 30 mm. The removable stainless steel bluff-body was mounted in the center of the annular channel, which had an inner diameter of 4 mm for the central jet and an outer diameter of 14 mm. The blockage ratio of the burner, as shown in Figure 3.4, was then $b = (d_b / d_a)^2 = 0.218$. Two bluff-body geometries were studied in the thesis work, the one involving a simple disk-shape bluff-body and the other one having a 45° conical shape. Since the position of the central pipe could be adjusted, the distance from the upper surface of the bluff-body to the annular channel exit (ΔH, as shown in Figure 3.6) was variable. The central pipe had an inner diameter of 4 mm and the thickness of the central pipe wall was 2 mm. The disk-shape bluff-body had a thickness of 5 mm, as shown in Figure 3.6. A ceramic honeycomb was mounted in the annular channel to provide a uniform annular flow and to avoid flame flashback into the further upstream region in the annular channel. As shown in Figure 3.4 and in Figure 3.6, there was no

swirl induced upstream of the bluff-body. The flame was only stabilized by the bluff-body, which was different from the modified burner (Version 2).

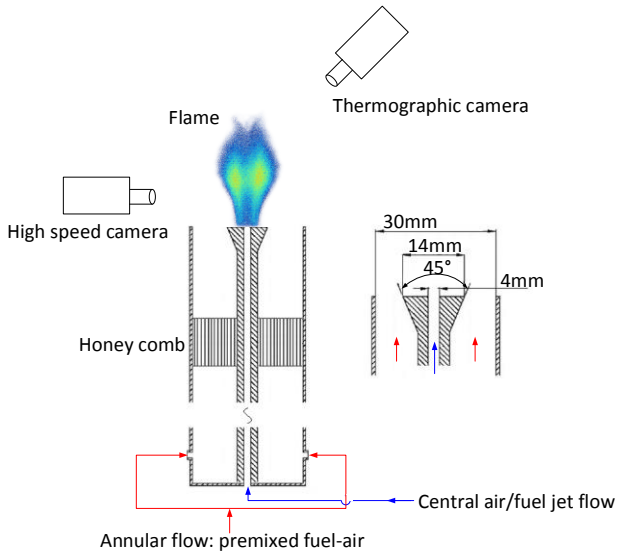

Figure 3.4 A schematic of the experimental setup of the adjustable bluff-body burner (Version 1).

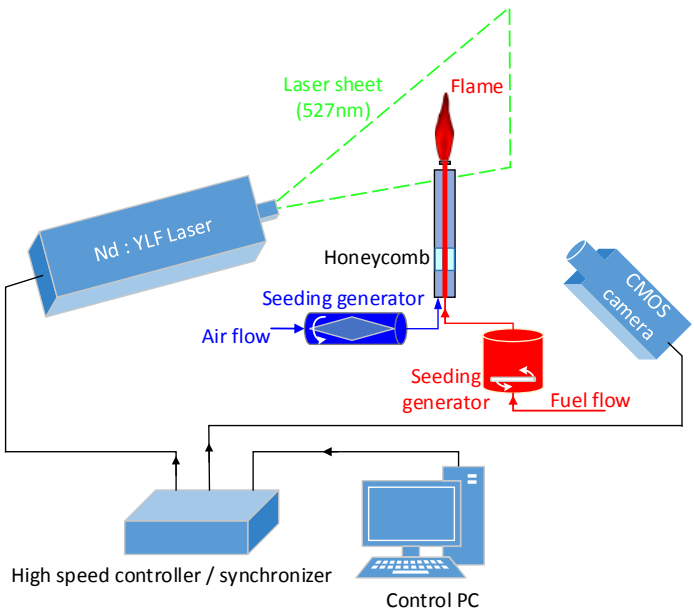

Figure 3.5 A schematic of the experimental setup and the high-speed PIV system associated with the adjustable bluff-body burner (Version 1).

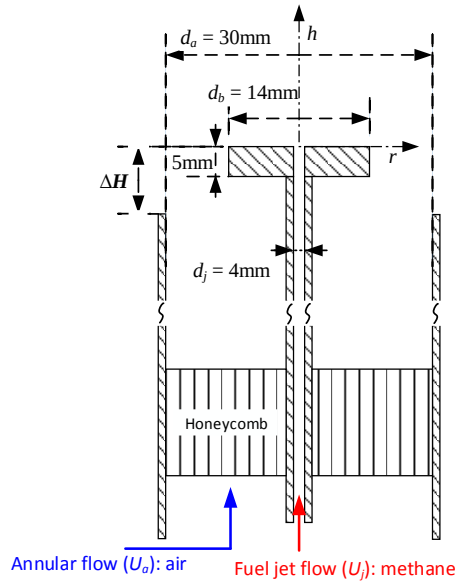

Figure 3.6 A schematic of the adjustable bluff-body burner (Version 1).

Different fuel and air injection strategies for the adjustable bluff-body burner could be adopted. To be more specifically, in investigating the effects of a central jet on bluff-body stabilized premixed flames, as shown in Figure 3.4, the annular flow was fed by premixed fuel and air, whereas the central jet was either pure air or pure fuel. When studying the effects of the positions of the bluff-body on the instabilities of the diffusion flames, as shown in Figure 3.6, the central jet was fed with pure fuel while the annular channel was fed with pure air.

3.2.2 Adjustable bluff-body burner: Version 2

The purpose of modifying the original adjustable bluff-body burner (Version 1) was to investigate the effects of a bluff-body on swirl stabilized diffusion flames, as well as the effects of adding swirl flow on bluff-body stabilized flames. The experimental setup is shown schematically in Figure 3.7 and the modified adjustable bluff-body burner is shown in Figure 3.8. The removable bluff-body was mounted at the exit of fuel pipe. Two sizes of the disk-shape bluff-bodies (d_b = 14 mm and 20 mm) were adopted in the experiments in investigating the effects of a bluff-body on the flow fields and flame structures. Since the annular flow channel of the burner had a diameter of d_a = 32 mm, the blockage ratios were $b = (d_b / d_a)^2$ = 0.191 and 0.391, respectively. The height of the two bluff-bodies were the same at h_b = 5 mm. An optical quartz tube (h_q = 50 mm),

through which the flame propagating upstream of the bluff-body could be observed, was placed upstream of the burner exit. As shown in Figure 3.8, the swirl flow was generated by eight tangential flow inlets, each having a height of 10 mm and a width of 3 mm.

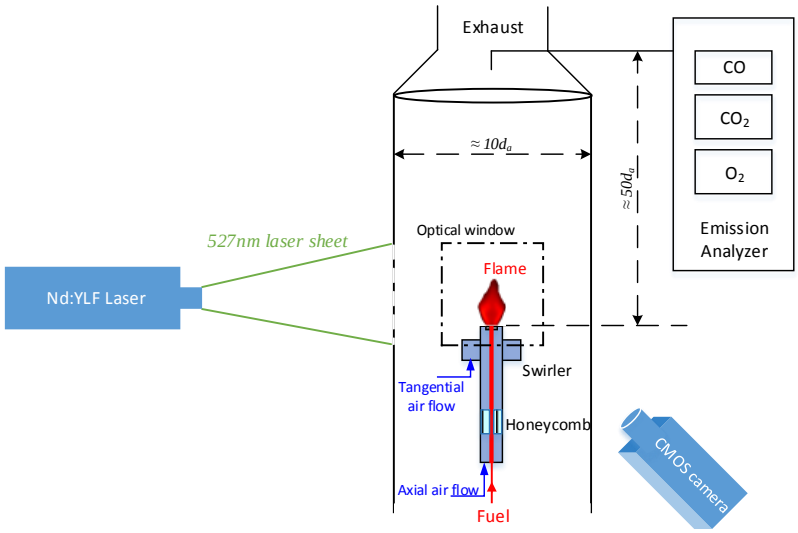

Figure 3.7 A schematic of the experimental setup and the high-speed PIV system associate with the adjustable bluff-body burner (Version 2).

In order to obtain the global emissions from the combustion, a burner confinement was adopted. The confinement for the setup had a diameter of approximately $d_c = 10d_a$. Thus, the confinement ratio was $c = (d_a / d_c)^2 = 0.01$. It has been reported that when the confinement ratio is lower than $c = 0.25$, the effects of the confinement on the bluff-body stabilized flame structures can be ignored [63]. Optical windows of the confinement allowed visualization of the flame and the adoption of PIV measurements. It is worth noting that the PLIF measurements were carried out without the confinement in order to have a stronger fluorescence signal. As shown in Figure 3.8, fuel was supplied through the central jet pipe ($d_j = 4$ mm), while the swirling air flow being fed through the annular channel. Methane was selected as fuel for the central jet, since it was the main component of natural gas. In addition, the established detailed chemical reaction mechanisms of methane were available for the numerical simulations.

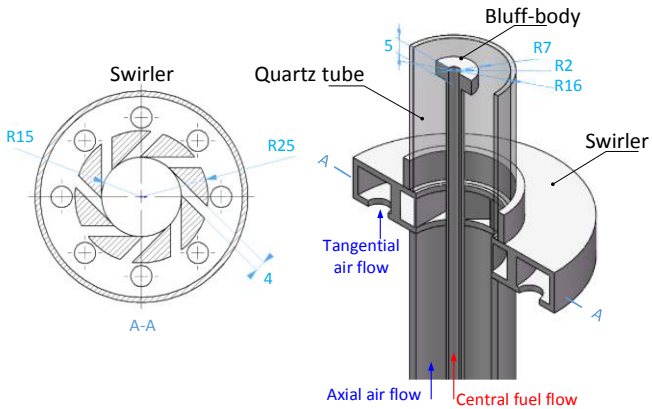

Figure 3.8 A schematic of the adjutable bluff-body burner (Version 2).

4.Experimental Techniques and Image Analysis Methods

In order to quantify and control the experimental conditions, several basic mass flow, temperature and pressure measurements were used in the doctoral work. In addition, certain more advanced velocity measurements were adopted, and a variety of flame visualization methods together with corresponding image analysis methods were employed. The flow fields in the iso-thermal and combusting cases were registered by means of a high-speed PIV system, while flame structures being visualized by means of the broad-band or filtered CH* chemiluminescence and a high-speed PLIF system, together with corresponding image analysis methods. In addition, the temperature on the surface of the bluff-body was obtained through use of the infrared thermography measurement. In this chapter, a brief account at theoretical background of these measurements will be presented.

4.1 High-speed PIV system

Particle Image Velocimetry (PIV) is a non-intrusive laser-based diagnostic technique providing instantaneous velocity vectors measurements in a cross-section of the flow field. It involves the use of modern laser techniques and digital cameras, together with dedicated computing hardware, measuring the real-time velocities of micron-sized particles following the flow. With sequences of velocity vector maps, one can obtain the statistics, the spatial correlations and other relevant data in the flow field. A presentation of the working principles upon which the PIV system is based is provided in Figure 4.1. Digital camera lens images the particle-seeded flow (which is being illuminated in the target area by a laser sheet) onto the sensor array of a digital camera. The camera captures and records each laser pulse in a sequence of two pulses in separate image frames. The sequenced frame 1 and frame 2 are then divided into small

interrogation windows. The interrogation areas are cross-correlated with each other. Through the peak search of the cross-correlation, the common particle displacement in the frames that are sequenced could be obtained. The velocity associated with the interrogation window could be obtained on the basis of the time delay of the two laser pulses. A velocity vector map over the entire target area was obtained by repeating the cross-correlation for each interrogation window over the two image frames captured by the camera. Further details concerning the cross-correlation and data analysis algorithms can be found in the product manual of DaVis 8.1 [103].

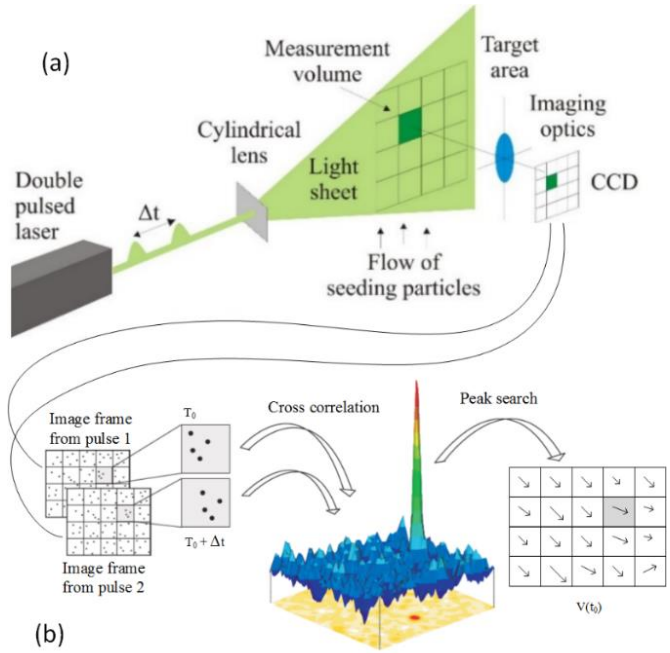

Figure 4.1 (a) A schematic of PIV system and (b) cross correlation used in evaluating PIV results (reproduced from [104]).

In the thesis, a high-speed PIV system (Lavision Flowmaster) was utilized to capture the flow fields in both the iso-thermal and the combusting cases. A diode-pumped, dual-cavity Nd:YLF laser (Litron LDY) was utilized to illuminate the central plane of the burner having a laser sheet thickness of approximately 1 mm, using a diverging laser sheet generated by an optical lens. The high-speed laser had a wavelength of 527nm and a frequency of 2 kHz. The time delay between the two laser pulses was set to Δt = 50 µs. The laser light scattered off the TiO_2 seed particles and was recorded at a repetition rate of 2kHz with the high-speed CMOS camera (Vision Research Phantom V 611). The TiO_2 particles were seeded into the flow field using LaVision solid particle

seeder (LaVision Particle blaster 100) and/or a rotating drum particle seeder (Scitek PS-10). A multi-pass cross-correlation algorithm, which was available in the DaVis (v.8.1.4) computer software, was utilized to evaluate the velocity fields. The cross-correlation was carried out on interrogation areas of 64×64 pixels and subsequently 32×32 pixels with a window overlap of 50%.

4.2 Flame chemiluminescence

Optical emissions from the flames were captured to investigate the unsteady and time-averaged flame structures, as well as the flame instabilities in different experimental cases. The methane-air flame can emit radiation under the following conditions [105]: (1) black body radiation from soot or high carbon content particles, which is mainly found in diffusion flames; (2) radiative heat transfers due to H_2O and CO_2 radiation at high temperature from rotation-emission bands; (3) radiation emitted from atoms, molecules, or radicals, returning from an electronically excited state to the ground state, which is generally known as chemiluminescence. Figure 4.2 shows a typical chemiluminescence spectrum of an atmospheric turbulent methane-air flame. The dashed line in Figure 4.2 is an approximation for the broad-band emission from CO_2. The highlighted areas represent signals of interest from OH* and CH*. In addition, the transmission curves of the band-pass filters are shown. In the thesis, CH* chemiluminescence was selected for marking the distribution of heat release from the flame.

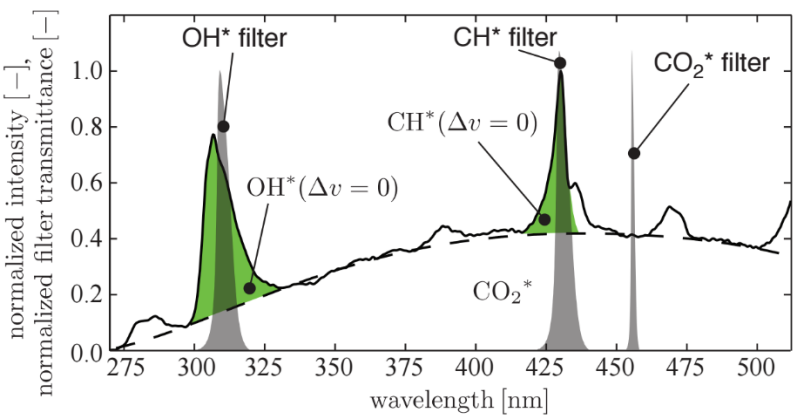

Figure 4.2 The typical chemiluminescence spectrum of the turbulent methane-air flame under atmospheric conditions [106].

A high spatial resolution Nikon D70s camera together with a 430 ± 10 nm band-pass filter were adopted to capture the CH* chemiluminescence from the flame. The resolution of the image was 3008×2000 pixels. The long exposure time (compared with any turbulent fluctuations) and averaging of the raw images had the effect of averaging out the instantaneous winkles of the flame front, thus yielding the equivalent of time-averaged flame structures. Since CH* chemiluminescence intensity peaks at a light wavelength of 431 nm in the blue range, only the blue layer in the raw RGB format images was used in the image analysis process (as is the case in [28]). In addition, in order to obtain the representative flame length (L_F), CH* chemiluminescence intensity within the time-averaged image was first summed in the lateral direction, as shown in Figure 4.3(b). Since the CH* intensity has a linear relationship with the heat release rate [107], the integrated CH* intensity indicates the distribution of the heat release along the axial direction. The position of flame's center of heat release (H_{COHR}), as shown in Figure 4.3(b), is the axial location with maximum CH* chemiluminescence intensity [108]. The full width at half maximum (FWHM) of the heat release distribution profile is also shown in Figure 4.3(b). This value was calculated by finding the width in the axial profile at an intensity value of half of the peak value [108]. The FWHM characterizes the axial distribution of the flame's heat release [109]; thus, it could be regarded as the representative flame length (L_F).

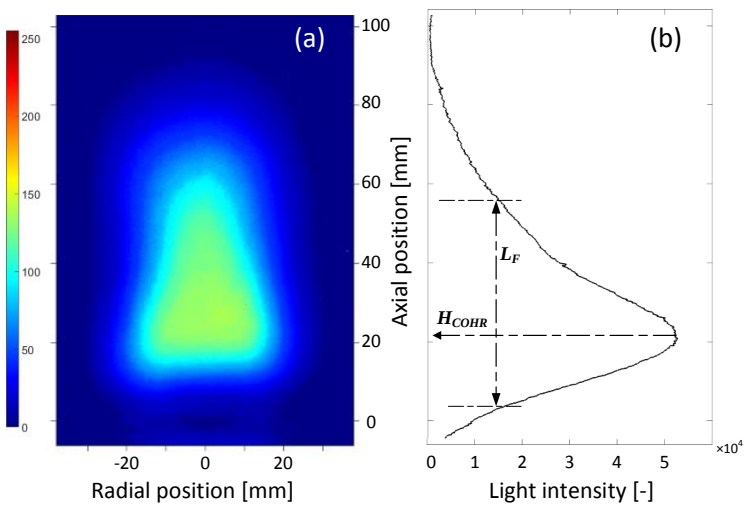

Figure 4.3 (a)The typical time-averaged CH* flame structures and (b) the height of the flame's center of heat release (H_{COHR}), together with flame length (L_F) of full width at half maximum (FWHM) measurement overlaid.

In addition, the raw image of CH* chemiluminescence was obtained by use of a line-of-sight method. It can be deconvolved using the inverse Abel image reconstruction method, based on the assumption of an axisymmetric flame. The inverse Abel reconstruction or the Abel inversion of the projection is the reconstruction of a circularly symmetric two-dimensional function from its projection onto an axis [110]. As will be shown later in **Chapter 6**, the inverse Abel reconstructed image better marks the location of the time-averaged flame brush in the central plane of the confinement. The major drawback of the inverse Abel reconstruction method is the strong noise along the centerline of the reconstructed image.

In order to obtain flame dynamics, as shown in Figure 3.1, a high-speed CMOS camera (Vision Research Phantom V7.1) coupled with an image intensifier (Hamamatsu C4598), a 430 ± 5 nm band-pass filter and a phosphate glass lens (UV-Nikkor 105mm, f/4.5) was used to record CH* chemiluminescence from the flame. The camera had a spatial resolution of 600×800 pixels and a depth of 24 bit. A time series of 1450 images was obtained at a recording rate of 4000 frames per second (*fps*). In order to resolve the time-varying flame structures, the exposure time of the camera was set to 20 μs. An example of the CH* chemiluminescence from the flame is shown in Figure 4.4(a), with the white line denoting the quartz tube wall. The oscillation of the flame can be obtained by Fast Fourier Transform (FFT) of the time series of the total intensities of each transient images [5]. An example of flame oscillation having a dominant frequency of f = 172 Hz is shown in Figure 4.4(b).

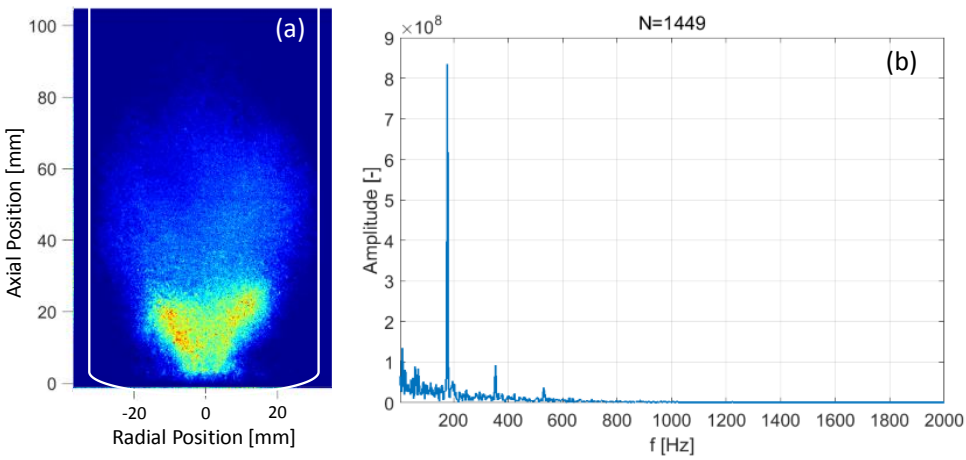

Figure 4.4 (a) An example of CH* chemiluminescence from the flame obtained by the intensified high-speed photography and (b) flame oscillation obtained on the basis of the image intensity.

4.3 High-speed PLIF

Planar Laser Induced Fluorescence (PLIF) is a modern laser-based combustion diagnostic technique for measuring emissions of excited molecules or atoms, when they are released from a higher energy band. The working principle involved is shown in Figure 4.5. There, v denotes vibrational quantum numbers, VET and RET standing for vibrational energy transfer and rotational energy transfer, respectively. The target specie is excited by a laser with a special wavelength that matches its transition energy. The fluorescence light is then emitted on the basis of the de-excitation process. The fluorescence may emits the same or slightly different (usually longer) wavelength than those of the excitation source, as shown in Figure 4.5. Thus, optical filters can be used to suppress the irradiating laser light. The absorbed and the emitted energies are unique to the target species that can be chosen selectively. Information concerning both temperature and concentration could then be extracted from them [111].

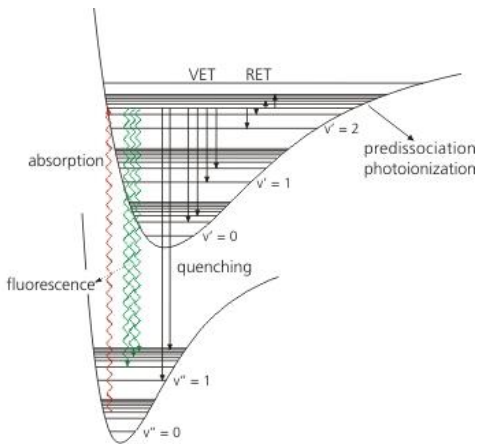

Figure 4.5 A schematic diagram of the energy transfer processes in a typical radical [111].

Formaldehyde (CH_2O) is an important combustion intermediate found within the 'cool flame' region prior to the primary reaction zone within hydrocarbon-fueled flames. It plays a critical role in fuel oxidation, auto-ignition, lifted flame stabilization and engine knock. Figure 4.6 shows the experimental setup of CH_2O PLIF for the adjustable bluff-body burner (Version 2). A burst-mode laser (QuasiModo by Spectral Energies, LLC) was used to excite CH_2O molecules at 355 nm. Further detailed information concerning CH_2O PLIF can be found in [112]. A cylindrical lens (f = -40 mm) and a spherical lens (f = +500 mm) were used to form the laser sheet, 70 mm in height and less than 0.5 mm in thickness, passing through the center of the burner.

A high-speed COMS camera (Photron Fastcam SA-Z) was placed perpendicular to the laser sheet plane. The exposure time was set to 250 ns in order to reduce the influence of chemiluminescence and Planck radiation from the diffusion flame. A long pass filter (GG385) was used to prevent the scattering of laser light from entering the camera. A camera lens (f_l= 50 mm, F#=1.2), together with a 12 mm extension ring were mounted in front of the camera to create a field of view by 74 × 65 mm^2.

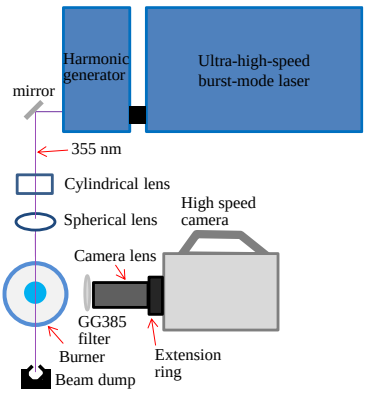

Figure 4.6 A schematic of experimental setup for the high-speed CH_2O PLIF.

The pulse width of the laser was 10 ns. Thus, the motion of the diffusion flame was 'frozen' in each image. The camera and the laser were synchronized by a digital delay and a pulse generator (DG535) at 22.5 kHz. The camera with a resolution of 1024 x 896 pixels started before the start of the burst-mode laser. Thus, the high-speed camera recorded the natural luminosity image of the diffusion flame without the laser, which was then used as a background image. By subtracting the background image, the noise of chemiluminescence and Planck radiation from soot in the diffusion flame could be suppressed. Figure 4.7 shows the raw images of CH_2O PLIF first with a sooty background and then the result after background subtraction.

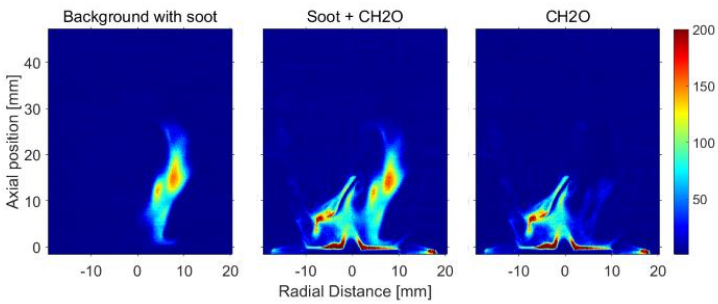

Figure 4.7 An example of CH_2O PLIF in a sooty flame.

4.4 Infrared thermography

Infrared thermography is equipment or method that detects infrared energy emitted from an object, converts it to temperature, and displays an image of the temperature distribution. Most popular infrared cameras capture radiometric thermal images that contain apparent temperature measurements for each pixel within the image. It is an instrument technique for measuring the temperature on the surfaces of objects.

An infrared thermographic camera (Testo 881-3) was used to record the temperature distribution on the upper surface of the bluff-body. The adjustable bluff-body burner (Version 1) was unconfined, which made measuring of that temperature practical and reliable. The thermographic camera, with a spatial resolution of 160×120 pixels, was placed above the burner, as shown in Figure 3.4. The camera could measure the temperature in the range of 253 K to 823 K, the reading error of the measured temperature within the span of 273 K to 623 K being less than 2%. As shown in Figure 4.8 and the same as presented in the literature [77], the temperature distribution peaked in the center on the upper surface of the bluff-body. In the present study, however, the high temperature distribution at -2 mm < r < 2 mm was probably caused by the reflection of infrared light from the curved inner wall of the injection hole. So temperature data in the center injection hole was treated as noise and thus deleted in the analysis process. The temperature at the inner edge of the central injection hole is selected and analyzed as the representative temperature T_{edge}. In the base case (which will be described in detail in **Chapter 6**), the temperature T_{edge} was referred to as T_0. The emissivity (ε) of stainless steel type 301 is within the range of 0.54 to 0.63. The error caused by selecting the emissivity from 0.54 to 0.63 was within 2%. In the thesis, the emissivity was selected at a value of 0.58.

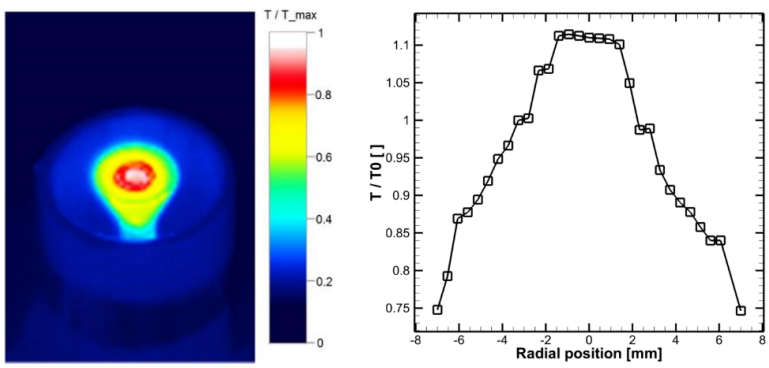

Figure 4.8 The typical infrared image of the bluff-body (left) and the temperature distribution along the radial direction (right).

In order to obtain the representative temperature on the upper surface of the bluff-body, the unstable change of T_{edge} during the flame shutdown process was recorded, as shown in Figure 4.9. With the shutdown of fuel supply, the temperature dropped, the gradient being sharp initially because of the weak flame that remained being attached to the bluff-body. When the flame had vanished completely, the surface temperature changed slowly over time due to the heat convection from the bluff-body to the environment. T_{edge} then decreased at a rate of less than 4 K/s. Thus, the representative temperature was taken within 1s after the flame was completely quenched. The corresponding error for that was within 2%.

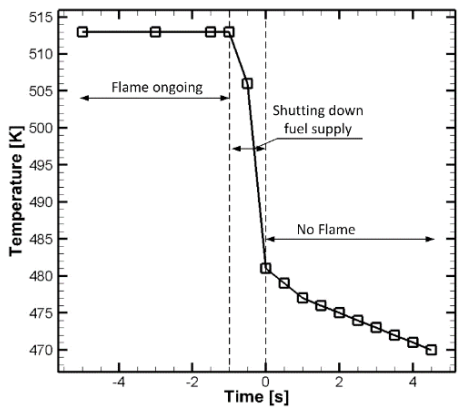

Figure 4.9 The typical changes of T_{edge} during shutting down of fuel supply.

5.Numerical Methods

An advantage of the experimental investigations is that the results can be expected to be rather reliable. However, its cost is usually considerably and the results may well be limited to the measurement techniques. The use of computational fluid dynamics (CFD) can thus be seen as highly advantageous due to the fact that it is easier to carry out and its lower cost. CFD has by now reached a stage at which flow fields in practical situation can be predicted sufficiently well to aid appreciably in the design of some equipment as well as in investigating the fundamental flow physics. It can thus be utilized to better understand and to resolve many fundamental issues within fluid mechanics. Its use has been extended to flows with combustion through the solving of additional conservation equations for individual species. Also, CFD can be used to gather more data than those obtained through the experimental investigations, so as to obtain greater insight into experimental results. However, the verification of data obtained from CFD, through comparing it with corresponding results of experimental investigations, is also needed. The use of a combination of experimental and numerical techniques, so as to complement the drawbacks of using techniques of the one type but not the other, has been aimed at in the thesis.

5.1 Turbulence modelling

Turbulent flows are characterized by eddies with a wide range of length and time scales. The largest eddies are typically comparable in size to the characteristic length of the mean flow (for example, the thickness of the shear layer). The smallest scales are responsible for the dissipation of turbulent kinetic energy. There are three main approaches that can be taken for unsteady turbulent flow simulations: Unsteady Reynolds-averaged Navier-Stokes (URANS), Large Eddy Simulation (LES) and Direct Numerical Simulation (DNS). In URANS simulation, all turbulence scales are modeled, which reduces simulation costs. However, URANS has lower levels of

accuracy. In addition, the simulation costs for DNS, which resolves the whole spectrum of turbulent scales without scaling, is extremely high. Thus, it is difficult to make use of it in simulations of 3D turbulent flow together with detailed combustion mechanisms. In LES, large eddies are resolved directly, whereas small eddies are modeled. It therefore falls between DNS and RANS in terms of the scales that resolved. LES has been proved to be a powerful tool for the prediction of transient turbulent reacting flows and flame structures with a high degree of resolution and with sufficient accuracy. Unsteady three dimensional effects and transient detailed flow fields have been reported to be predicted better by LES than by URANS [113].

5.1.1 LES model

There are four conceptual steps in LES [114]: (1) a filtering operation is defined, aiming at decomposing the velocity fields into a filtered component (large eddies) and a residual (or subgrid-scale, SGS) component; (2) the evaluation of large eddies is derived through use of Navier-Stokes equations, whereas the SGS stress tensor is derived from the residual motions; (3) modelling of the SGS stress tensors mostly by use of an eddy-viscosity model; (4) the model filtered equations being solved numerically, this providing the large scale motions of the turbulent flow. By employing the Favre filter, the governing equations for the incompressible LES model can be expressed as

$$\frac{\partial \tilde{u}_i}{\partial x_i} = 0 \tag{5.1}$$

$$\frac{\partial \bar{u}_i}{\partial t} + \frac{\partial \left(\overline{u_i u_j} \right)}{\partial x_j} = -\frac{1}{\rho} \frac{\partial \bar{p}}{\partial x_i} + \nu \frac{\partial}{\partial x_j} \left(\frac{\partial \bar{u}_i}{\partial x_j} + \frac{\partial \bar{u}_j}{\partial x_i} \right) \tag{5.2}$$

LES filter can be applied to a spatial and temporal field to perform a spatial and/or a temporal filtering operation. The subgrid-scale stresses stemming from the filtering operation in LES models are unknown, and require modeling. Most of the SGS models are based on Boussinesq hypothesis and some models are now available in ANSYS Fluent [115].

5.1.2 DES model

The use of LES models is only recommended, however, for flows in which wall boundary layers (where the local Reynolds number is usually high) are not relevant and

need not be resolved. Accordingly, the detached eddy simulation (DES) model, which is a hybrid LES-URANS model combining use of URANS in the wall boundary layer with use of LES in the separation zones, was adopted in the present study. In addition, the improved delayed detached eddy simulation (IDDES) model, which is based on the shear stress transport (SST) *k-ω* model, shows better performance than DES does. IDDES model appears to present a more flexible and convenient scale-resolving simulation (SRS) model for flows having a high Reynolds number [115]. The transport equation for the turbulent kinetic energy (*k*) and the specific dissipation rate (*ω*) in the SST-IDDES model can be given as follows:

$$\frac{\partial \rho k}{\partial t} + \nabla \cdot \left(\bar{\rho} \tilde{U} k \right) = \nabla \cdot \left[\left(\mu + \frac{\mu_T}{\sigma_k} \right) \nabla k \right] + P_k - \rho \beta^* k w F_{IDDES} \tag{5.3}$$

$$\begin{aligned} &\frac{\partial \rho \omega}{\partial t} + \nabla \cdot \left(\bar{\rho} \tilde{U} \omega \right) \\ &= \nabla \cdot \left[\left(\mu + \frac{\mu_T}{\sigma_\omega} \right) \nabla \omega \right] + \left(1 - F_1 \right) \frac{2 \rho \nabla k \cdot \nabla \omega}{\omega \sigma_\omega^*} - \rho \beta^* k w F_{IDDES} + \frac{\alpha P_k \omega}{k} - \beta \rho \omega^2 \end{aligned} \tag{5.4}$$

$$F_{IDDES} = \frac{l_{RANS}}{l_{IDDES}} = \frac{\sqrt{k} \Big/ \left(\beta^* \omega \right)}{l_{IDDES}} \tag{5.5}$$

It is shown above that F_{IDDES} is related to the RANS turbulent length scale and the LES length scale. For further information concerning the formulations of the IDDES model and different length scales, the readers could refer to ANSYS theory guide [115] and the literature [116]. In the present study, the IDDES model was utilized to simulate different diffusion flame behaviors in the adjustable bluff-body burner (Version 1) in cases with different positions of a bluff-body.

5.2 Combustion models

5.2.1 The partially premixed combustion model

In use of ANSYS Fluent, the partially premixed combustion model was adopted for studying the effects of the position of a bluff-body on flame structures in the adjustable bluff-body burner (Version 1). The transport PDF model [117], the EDC model concerned with detailed mechanisms [118] and the flamelet-based combustion model

[119] are commonly used in the simulation of non-premixed combustion. It was shown that the different models just referred to all provide results conforming fairly well with the experimental data. The partially premixed non-adiabatic flamelet combustion model was adopted for use in the thesis work in view of its computational accuracy and the short computational CPU time it involves. This model solves a transport equation for the reaction progress variable (c) as well as the mean mixture fraction (f). Thus it can simulate non-premixed flames (based on use of f), premixed flames (based on use of c) and partially premixed flames (based on use of both f and c). The mixture fraction (f) quantifies the extent of mixing with each other of fuel and oxidizer streams in non-premixed combustion. It can be expressed by the atomic mass fraction as

$$f = \frac{Z_i - Z_{i,o}}{Z_{i,f} - Z_{i,o}} \tag{5.6}$$

where z_i is the elemental mass fraction for species i, the subscript o stands for the value at the oxidizer flow side, and the subscript f denoting the value at fuel side. In the diffusion flamelet model, f is assumed to follow the β-function probability density function (PDF), the scalar dissipation fluctuations being ignored. The chemistry of combustion is then reduced and described completely by the transport equations of c and f, this enabling the flamelet calculations to be preprocessed and to be stored in the look-up tables. It reduces the computational costs considerably. The transport equation for f, under the assumption of equal diffusivities, is then

$$\frac{\partial\left(\rho\overline{f}\right)}{\partial t} + \nabla\cdot\left(\rho\vec{v}\overline{f}\right) = \nabla\cdot\left(\frac{\mu_l + \mu_\tau}{\sigma_\tau}\nabla\overline{f}\right) + S_m \tag{5.7}$$

where μ_l is the laminar viscosity and μ_t is the turbulent viscosity. S_m is the source term, concerning the mass transfer from a liquid or a solid phase into a gas phase during the chemical reaction. For the diffusion flamelet model adopted for LES region within the IDDES model, the variance of mixture fraction, f'', is modeled as

$$\overline{f''^2} = C_{\mathrm{var}} L_S^2 \left|\nabla\overline{f}\right|^2 \tag{5.8}$$

where C_{var} is a constant having a value of C_{var} = 0.5 and L_s is the subgrid length scale. In addition, the progress variable c is a parameter that characterizes the evolution of the global chemical status from being purely mixed and unburnt (c = 0) to being fully burnt (c = 1). The flame front propagation is modeled by solving a transport equation for the density-weighted mean reaction progress variable, denoted by $\overline{c}$:

$$\frac{\partial(\rho\bar{c})}{\partial t}+\nabla\cdot(\rho\bar{v}\bar{c})=\nabla\cdot\left(\frac{\mu_\tau\nabla\bar{c}}{Sc_\tau}\right)+\rho S_c \tag{5.9}$$

where Sc_t is the turbulent Schmidt number and S_c is the reaction progress source term. Density weighted mean scalars (such as species fractions and temperature) are calculated from the probability density function (PDF) of *f* and *c*. More detailed descriptions in connection with the turbulent models and the partially premixed steady flamelet model are available in ANSYS Fluent Theory Guide [115]. The reduced version of GRI-MECH 1.2 [120] concerning 19 species and 84 reactions of methane and air, involving reasonable computation costs, was selected here. The Peters turbulent flame speed model [121] was selected in the partially premixed flame model simulation.

5.2.2 Composition PDF model

The composition PDF model was utilized for studying flames stabilized by a combination of swirl flow and a bluff-body in the adjustable bluff-body burner (Version 2). The PDF model has emerged as one of the most promising approaches for evaluating the effects of turbulent fluctuations on the modeling of turbulent combustion [122]. Although the use of PDF transport simulation is computationally more expensive than the use of partially premixed flamelet model [115], the strength of the PDF method is that the chemical source term in that model appears in closed form. Hence the composition PDF model eliminates the need for direct modeling of the mean chemical source terms [123]. As compared with the other transported PDF models, including the composition-velocity PDF model and the composition-velocity-frequency PDF model, the composition PDF model is more tractable and computationally efficient [124]. There are two different discretizations of the composition PDF transport equation, namely Lagrangian method and Eulerian method. The Lagrangian method is clearly more accurate than the Eulerian method, but requires a significantly longer run time to converge [115]. In the thesis, therefore, the Eulerian composition PDF on the basis of OpenFOAM was adopted for studying flames stabilized by a combination of swirl flow and a bluff-body.

For the one-point, one-time joint PDF $\tilde{P}_{sgs}(\psi;\mathrm{x},\mathrm{t})$ of the composition vector $\psi=[Y_1,Y_2,\cdots,Y_{Ns},h]$, the modeled transport equation is given by

$$\bar{\rho}\frac{\partial \tilde{P}(\psi)}{\partial t}+\bar{\rho}\tilde{u}_j\frac{\partial \tilde{P}(\psi)}{\partial x_j}+\frac{\partial}{\partial \psi_\alpha}\left[\bar{\rho}\dot{\omega}_\alpha(\psi)\tilde{P}(\psi)\right]$$
$$=-\frac{\partial}{\partial x_i}\left[\left\langle u_i''|\psi\right\rangle\bar{\rho}\tilde{P}(\psi)\right]+\frac{\partial}{\partial \psi_\alpha}\left[\left\langle\frac{\partial J_i^\alpha}{\partial x_i}|\psi\right\rangle\tilde{P}(\psi)\right] \quad (5.10)$$

where the sub-grid eddy-viscosity and the interaction-by-exchange-with-mean (IEM) are used to model the sub-grid transport and the micro-mixing terms, respectively. The Eulerian Stochastic Fields (ESF) method [122, 124, 125] is employed to solve the composition PDF equations. The governing equation for the *n*th stochastic field can be expressed as

$$\bar{\rho}d\xi_\alpha^n=-\bar{\rho}\tilde{u}_i\frac{\partial \xi_\alpha^n}{\partial x_i}dt+\bar{\rho}S_\alpha^r(\psi^n)dt+\frac{\partial}{\partial x_i}(\Gamma_t\frac{\partial \xi_\alpha^n}{\partial x_i})dt$$
$$-\frac{1}{2}\bar{\rho}C_\phi\omega_T(\xi_\alpha^n-\tilde{\phi}_\alpha)dt+\bar{\rho}\sqrt{2\frac{\Gamma_t}{\bar{\rho}}}\frac{\partial \xi_\alpha^n}{\partial x_i}dW_i^n \quad (5.11)$$

where dW^n represents a vector Wiener process that is spatially uniform but different for each field. The chemical kinetic mechanism of Smooke and Giovangigli [126], which is made up of 16 species and 35 reactions, was utilized in the thesis work. It gives a laminar flame speed similar to that of the more comprehensive mechanisms for methane/air combustion, such as GRI3.0 [127], under atmospheric pressure and room temperature conditions. Due to its relatively low computational costs, use of the mechanism of Smooke and Giovangigli [126] is preferred since the composition PDF model is time demanding.

5.3 Numerical setups

5.3.1 Mesh and boundary conditions for the adjustable bluff-body burner (Version 1)

In the numerical study of effects of the position of a bluff-body on diffusion flame structures in the adjustable bluff-body (Version 1), the incompressible governing equations for mass, momentum and mixture fractions were solved with use of a structured 3D grid, as shown in Figure 5.1. The resolution effects that were investigated

used up to 2.19 million nodes. As can be observed in Figure 5.1, the computational domain covered 290 mm in the streamwise direction with h = 200 mm downstream of the bluff-body. The downstream outlet was 160 mm in the radial direction. The hybrid grids were refined in a cylindrical domain at 0 mm < r < 15 mm and -10 mm < h < 50 mm. The boundary refinement was also adopted for the upper and side walls of the bluff-body. Strong shear stresses, the boundary layer flow, strong fuel-air mixing and most of the chemical reactions were found in this cylindrical region. The walls fo the annular channel and the bluff-body were set to adiabatic, as suggested by Euler et al. [77, 78] on the basis of their experimental investigations. When simulating the isothermal flow structures without the presence of a central jet, the central jet boundary was switched from velocity inlet to adiabatic wall conditions.

A second-order upwind scheme was used for spatial discretization, whereas a bounded second order implicit scheme was selected for the transient formulation. A coupled pressure-velocity coupling algorithm was used to solve the discretized equations. The CFL number in the present work was set to 0.7. Since the boundary flow near the outer surface of the bluff-body was important in determining the flame behavior, use of IDDES turbulence model was adopted in the numerical simulations.

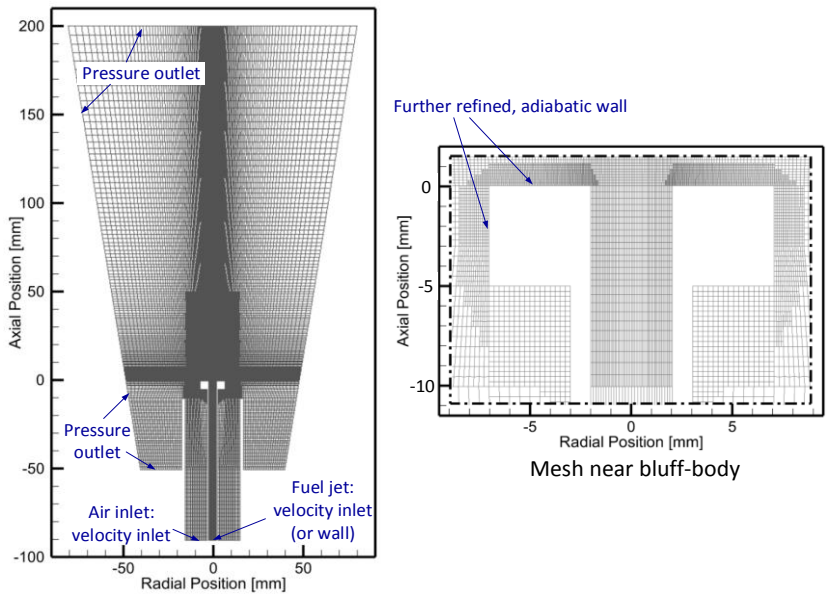

Figure 5.1 Computational domain and boundary conditions for the adjustable bluff-body burner (Version 1).

5.3.2 Mesh and boundary conditions for the adjustable bluff-body burner (Version 2)

The computational domain and the boundary conditions in the numerical study of the combined bluff-body and swirl flame on the adjustable bluff-body burner (Version 2) are shown in Figure 5.2. Just as in the experiments, fuel was supplied at a constant jet bulk velocity through the central tube, as indicated in Figure 5.2. The velocities of the tangential and the axial flow were set so as to agree with those of the experimental cases. Downstream of the swirler, a conical domain was considered in the simulation. A conical domain extending $75d_j$ in the downstream direction was adopted for the simulation, with $r = 15d_j$ in the radial direction at the swirler exit plane and $r = 45d_j$ at the outlet plane. The minimum length scale of the grid was 0.2 mm inside the quartz tube and the reaction zone. The total grid number was approximately 3 million.

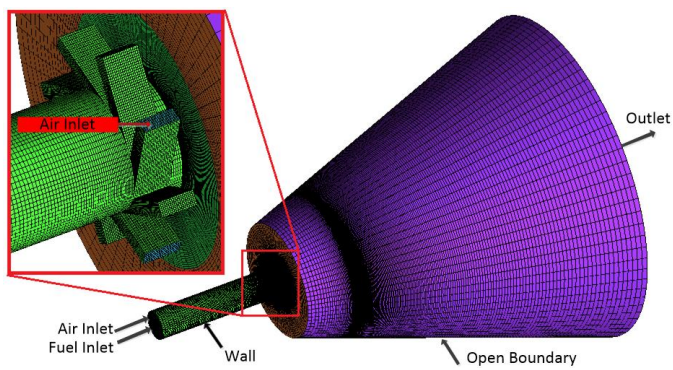

Figure 5.2 The computational domain and the boundary conditions for the adjustable bluff-body burner (Version 2).

The open source CFD library, OpenFOAM [128], was adopted for numerical integration of the governing equations. The second-order filtered linear implicit scheme was used for the spatial discretization and the second-order backward Euler scheme was used for the temporal integration. The pressure implicit with splitting of the operator (PISO) algorithm was employed for the pressure-velocity coupling. At the wall boundaries, non-slip boundary conditions were applied. A velocity mapping method involving use of a prescribed mass flow rate of fuel was employed at fuel inlet. At the open boundaries, pressure conditions were employed that allowed the ambient air to be entrained into the domain and the fluid to flow outside the domain. The experiments were conducted at atmospheric conditions, both air and fuel inlet temperatures being 294 K. These conditions were also adopted as the initial and boundary conditions in the numerical investigations.

6.Results and Summary of Publications

This chapter concerns the results of the experimental and the numerical studies and how they can be interpreted. This is taken up in three sections: (1) flames stabilized by swirl flow, (2) flames stabilized by a bluff-body and (3) flames stabilized by a combination of swirl flow and a bluff-body. In the investigation of swirl stabilized flames, the effects of operating conditions, confinement geometries and fuel injection strategies were studied. The results in this section are also reported in **Paper I**, **II** and **III**. The second section concerns the effects of a central jet and the position of a bluff-body on bluff-body stabilized flames. The results have been reported in **Paper IV** and **V**. The third part concerns the flames stabilized by a combination of swirl flow and a bluff-body. The results obtained are reported in **Paper VI**. All three sections were concerned with flame structures and flame instabilities, together with their interaction with the flow fields involved. Following discussions of these matters, short summaries of the papers and an overview of the contribution of each of the papers are presented. Further details of the results and the discussions can be found in the papers that are appended to the thesis.

6.1 Flames stabilized by swirl flow

The studies of swirl stabilized flames reported in this section were carried out on the confined variable-swirl burner (shown in Figure 3.2 and Figure 3.3). In investigating the effects of a particular unique operating condition on the behavior of the flame, the other operating conditions were kept constant. For example, in investigating the effects of the mass flow rate of the reactants on flame structures, the inlet temperature, the swirl number and the equivalence ratio of the reactants were held constant within a particular confinement.

As mentioned in **Chapter 3**, the swirl number at the burner exit was varied by a change in the momentum ratio of the tangential to the axial flows through the swirler. In the thesis work, S was calculated on the basis of an empirical relationship map obtained using Laser Doppler Anemometry (LDA) measurements 1 mm above the dump plane, on the same test facility in the literature [129] as that in the thesis work.

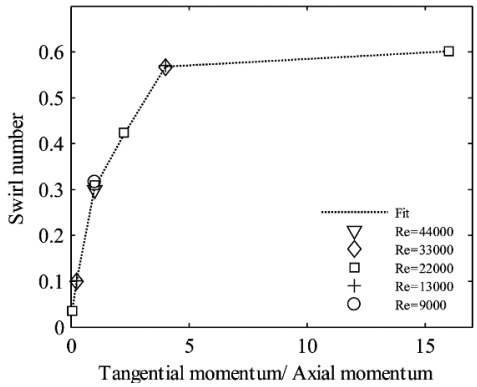

Figure 6.1 The swirl number versus the momentum ratio of the tangential to the axial flow [129].

6.1.1 Effects of the operating conditions (Paper I and II)

6.1.1.1 The total mass flow rate of the reactants

When holding the equivalence ratio constant, m changes linearly with m_{air}. With an increase in m_{air}, L_F became lengthened, whereas H_{COHR} remained approximately constant. At the same time, the flame area was enlarged as the flame detached from the dump plane. It was also observed that the flame became unstable as m_{air} was increased.

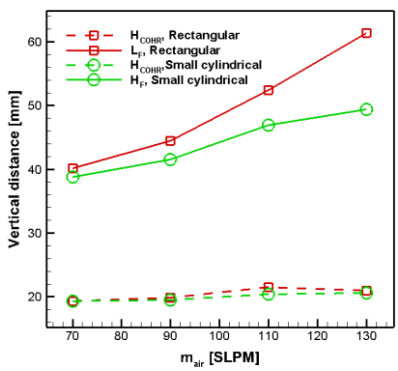

Figure 6.2 Effects of m_{air} on L_F and on H_{COHR} at Φ = 0.7, S = 0.6 and T_{in} = 397K.

As shown in Figure 6.3, when S = 0.66, the opening angle of the flame and its impingement location to the confinement wall did not change appreciably with alternation of the mass flow rate of air. In addition, it is found that Φ_{LBO} first increases along with the increase in m_{air} to a critical value and then decreases with the further increase in m_{air}, in all the three confinements investigated in the present thesis.

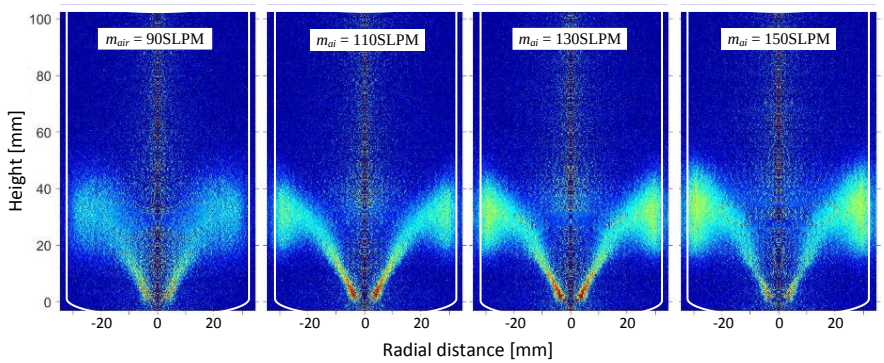

Figure 6.3 The effects of m_{air} on inverse Abel reconstructed time-averaged flame structures (CH* chemiluminescence), when Φ = 0.7, S = 0.66 and T_{in} = 297K in the large cylindrical confinement.

6.1.1.2 The equivalence ratio

A decrease in the equivalence ratio led to the time-averaged flame shape changing from an M-shape to a V-shape. In addition, two types of M-shape flames: the flame root propagating either inside or outside the premixing tube, could be observed within the large cylindrical confinement, as shown schematically in Figure 6.4.

The mechanisms that led to the forming of different M-shape and V-shape flames, together with corresponding flame dynamics, are shown in Figure 6.4 and Figure 6.5, respectively. The comparisons of the mechanisms in the present study and these taken from the literature [28] are also given in Figure 6.4 and Figure 6.5. In the present study, the outer recirculation zone was filled with fresh fuel-air reactants, whereas in the literature [28] the outer recirculation zone was filled with combustion products, as shown in Figure 6.4. In the thesis work, the flashback of the flame trailing edge along the boundary layer near the combustor wall into the outer recirculation zone led to the formation of an M-shape flame. Moreover, combustion occurred mainly in the inner shear layer, as shown in Figure 6.4(b). The M-shape flame in the burner with a central rod was found to be formed by the reaction in both the inner and the outer shear layers, as shown in Figure 6.4(c) [24, 25, 28, 35, 36].

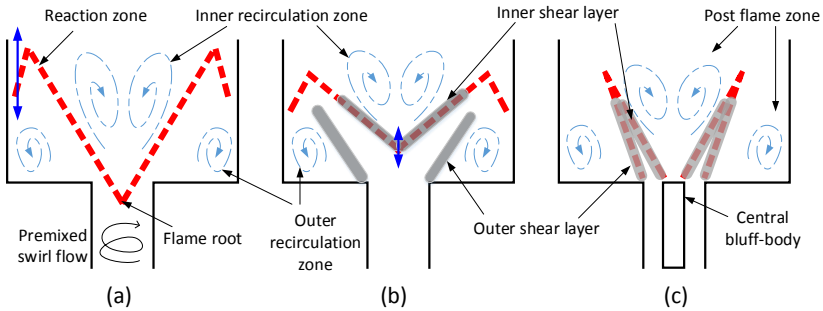

Figure 6.4 Examples of different M-shape flames and flame dynamics in the cylindrical confinement. (a) An M-shape flame with flame root inside the premixing tube. (b) A lifted M-shape flame with flame root out of the premixing tube. (c) An attached M-shape flame for the burner with a central bluff-body (reproduced from [28]).

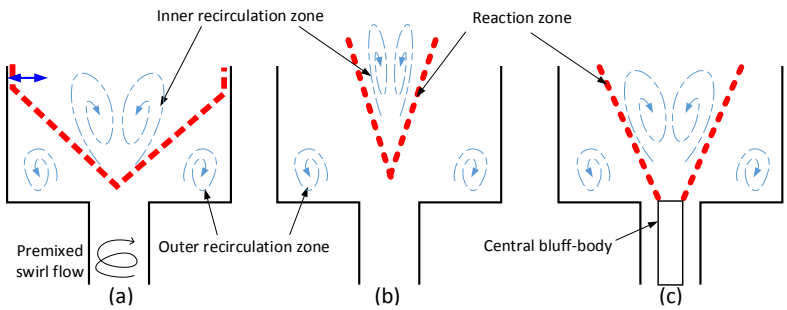

Figure 6.5 Examples of different V-shape flames and flame dynamics in the cylindrical confinement. (a) A lifted V-shape flame with the trailing edge of the flame attached to the confinement wall. (b) A lifted V-shape flame with the trailing edge of the flame detached from the confinement wall. (c) An attached V-shape flame for the burner with a central bluff-body (reproduced from [28]).

Different flame oscillations, including: (1) the flame root propagating in an unstable manner inwards and outwards of the premixing tube, (2) the flame trailing edge flashing back into the outer recirculation zone or propagating along the confinement wall downstream to the exit, (3) the shift of the flame shapes from wall-attached to wall-detached V-shape flames, were observed during the alternation of flame structures, as shown with the blue double-arrow lines in Figure 6.4 and Figure 6.5.

6.1.2 Effects of confinement geometries (Paper I and II)

6.1.2.1 The cross-sectional shape

As can be seen in Figure 6.2, under the same operating conditions, flame in the rectangular confinement has a longer L_F than that in the small cylindrical confinement. Whereas H_{COHR} is less affected by the cross-sectional geometry of the confinement. One

can note in Figure 6.6 that flames in the small cylindrical confinement have leaner blowout limits, indicating the cylindrical confinement to perform better in stabilizing the lean premixed flames.

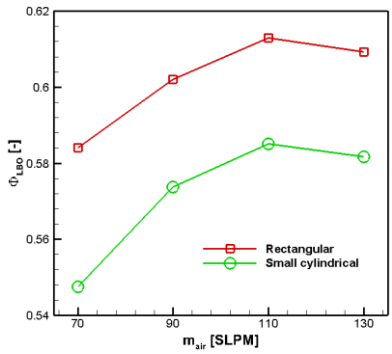

Figure 6.6 Effects of the cross-sectional geometry on the lean blowout limits at S = 0.6, T_{in} = 397 K.

6.1.2.2 The diameter of the cylindrical confinement

Flame macrostructures differed from one another in the changing of the confinement diameters. Two blowout phenomena, including the blowout due to oscillation and the peaceful lean blowout, were observed within the large cylindrical confinement. However, no oscillation flame blowout was observed within the small cylindrical confinement. Thus, the blowout limits caused by peaceful lean blowout within the two confinements are reported and compared with one another in Figure 6.7. It can be noted that the flame within the large cylindrical confinement had lower lean blowout limits, indicating a better performance in stabilizing the flame. In addition, in all these two confinements, prior to flame blowout, the flame showed a weak long V-shape.

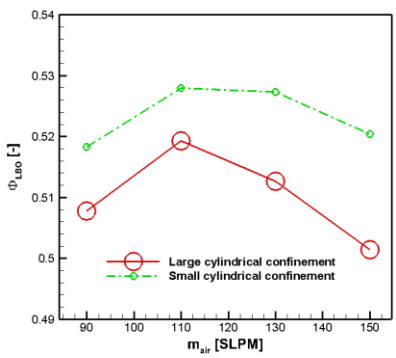

Figure 6.7 Effects of the diameter of the confinement and the mass flow rate of air on the lean blowout limits, when S = 0.66 and T_{in} = 297K.

6.1.3 Effects of fuel injection strategy (Paper III)

Two fuel injection methods were investigated in the thesis: fuel being injected through the axial flow and through the tangential flow, as listed in Table 6.1. All of the experiments were conducted at atmospheric pressure and room temperature on the variable-swirl burner with the large cylindrical confinement. Fuel (a mixture of methane and hydrogen) was injected and premixed with either the tangential or the axial air flow at least 200 mm upstream of the swirler. The presumably perfectly mixed fuel-air mixtures was then further mixed with air flow (from the other flow inlet) inside the mixing tube. The variation of global equivalence ratio, Φ_g, was achieved through alternation of the mass flow rate of methane.

Table 6.1 Test conditions of swirl stabilized partially premixed flames with use of different fuel injection strategies.

Case name	Axial flow rate [SLPM]			Tangential flow rate [SLPM]			Swirl number
	CH_4	H_2	Air	CH_4	H_2	Air	
A-S28	12.6~LBO	3	75	0	0	75	0.284±0.002
T-S33	0	0	75	12.6~LBO	3	75	0.337±0.002
A-S33	10~LBO	3	70	0	0	80	0.332±0.002
T-S28	0	0	80	10~LBO	3	70	0.289±0.002
A-S31	10~LBO	3	72.5	0	0	77.5	0.310±0.002
T-S31	0	0	77.5	10~LBO	3	72.5	0.311±0.002

6.1.3.1 Flame behaviors under conditions far from blowout

As shown in Figure 6.8, when Φ_g = 0.85, the time-averaged flame structures appeared a bell shape in case with a tangential fuel injection strategy, whereas the axial fuel injection resulted in a more compact flame. The same as utilized in the literatures [56, 130, 131], the paths of CH* chemiluminescence produced by the flame at the central line in cases A-S28 and T-S33 are shown in Figure 6.9. It stitches the central line of each raw image in the time consequence order. To be more specifically, for example, the first column pixels of the image in Figure 6.9 was from the central line of the first raw image in a time series images for case A-S28. The white lines there show schematically the direction of the flame propagating along the central axis in one oscillation cycle. As can be clearly seen that flames in both these two cases had strong oscillations. These two cases were similar in the flame oscillation frequencies produced, these being at $f \approx$ 170 Hz. The flame lifted higher when an axial fuel injection strategy was employed. In the case A-S28, the flame became weaker when it was propagating upstream. In the other case, strong heat release was found both in the upstream and in the downstream flame propagation process.

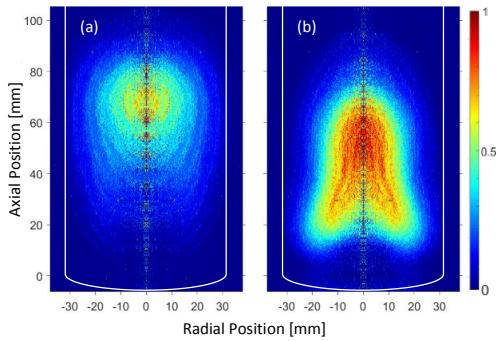

Figure 6.8 Inverse Abel reconstructed time-averaged flame structures (CH* chemiluminescence) in (a) case A-S28 and (b) case T-S33, when holding Φg = 0.85.

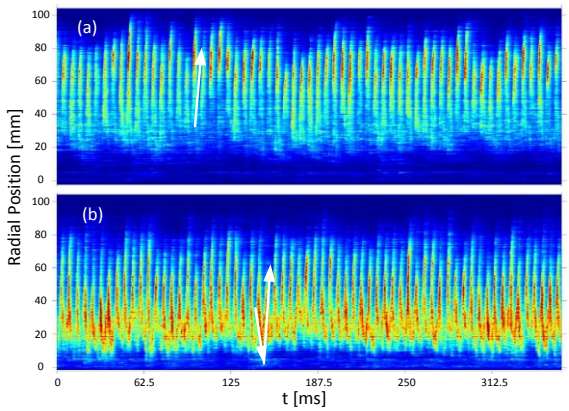

Figure 6.9 Flame segment paths (CH* chemiluminescence) along the centre line for (a) case A-S28 and (b) case A-S31, when holding Φ_g = 0.85.

6.1.3.2 Flame behaviors near lean blowout

As shown in Figure 6.10, when holding Φ_g = 0.62 near lean blowout limit of the flame, the time-averaged flame structures took on a heart shape in the case with tangential fuel injection; whereas otherwise the flame showed an arrow-shape detached from the dump plane. The heart shape flame propagated unsteadily into the premixing tube and outwardly from it. Strong flame oscillations could be observed simultaneously.

When holding Φ_g = 0.62, flame segment paths in the central line for cases with different fuel injection strategies and different swirl numbers are shown in Figure 6.11. Significant oscillations near lean blowout can be observed. Flames in cases with the same fuel injection strategy were found to be similar in terms of the dominant oscillation frequency. The flames flashback into the premixing tube was only observed in cases with a tangential fuel injection method. The flame motion in these two cases

near lean blowout were found to differ from that occurred under comparatively rich conditions (Φ_g = 0.85) shown in Figure 6.9.

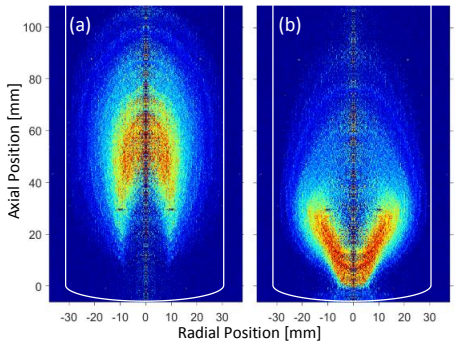

Figure 6.10 Inverse Abel reconstructed flame structures (CH* chemiluminescence) when holding Φ_g = 0.62 near lean blowout: (a)case A-S28 and (b)case T-S33.

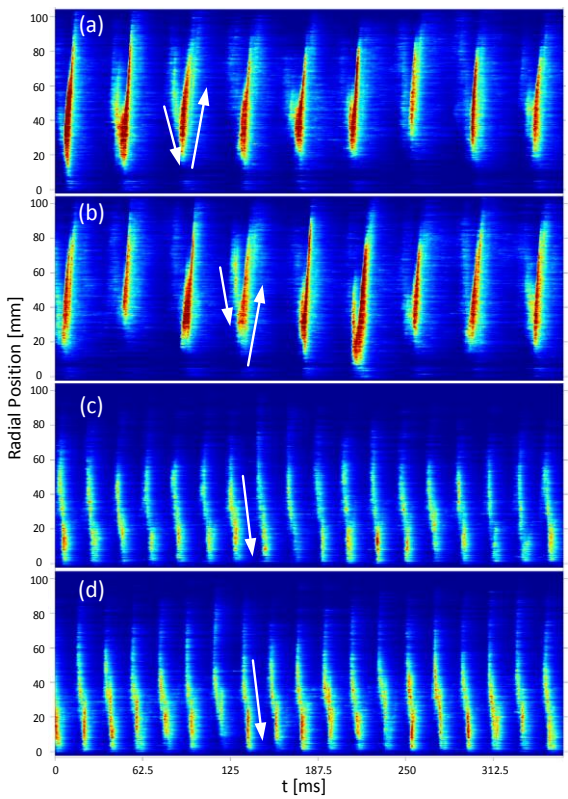

Figure 6.11 Paths of the flame segment (CH* chemiluminescence) in the centre line for (a) case A-S28, (b) case A-S31, (c) case T-S33 and (d) case T-S31, near lean blowout at Φ_g = 0.62.

The axial velocity segment paths in the central axis for the reacting case T-S33 near lean blowout are shown in Figure 6.12. The axial velocity there also shows clear oscillations indicating there to be strong interactions between the flame and the flow fields. Higher axial velocities were found in the region near the burner exit, while strong reversing flow locating further downstream. This indicates the formation as well as the location of the vortex breakdown. When the location of vortex breakdown advanced upstream close to or even inside the premixing tube, a sudden increase in axial velocity was found to occur after that. Meanwhile, the recirculation vortex was pushed downstream and then finally disappeared.

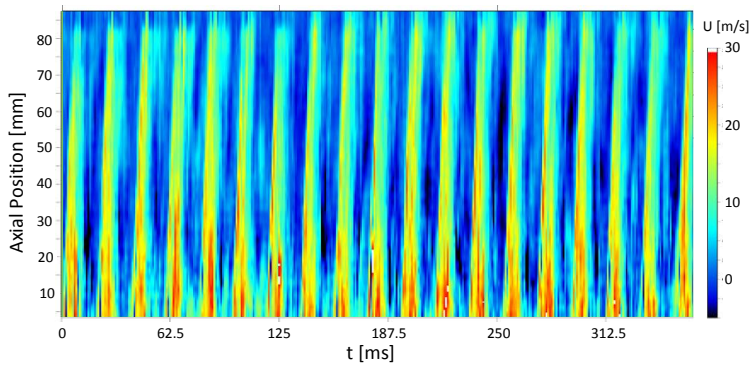

Figure 6.12 Axial velocity segment paths in the center line for case T-S33 at Φ_g = 0.62.

6.1.3.3 Flame dynamics and lean blowout limits

As shown in Figure 6.13, when the global equivalence ratio is high (Φ_g > 0.72), all of the flames tend to show a high frequency oscillation at $f \approx$ 170 Hz. Whereas, when the value of Φ_g is reduced, strong flame oscillations with a lower oscillation frequency were noted. Near flame blowout, cases in which the axial fuel injection methods were carried out tend to show a flame oscillation at $f \approx$ 20 Hz, whereas in other cases the dominant flame oscillation frequency was higher, at a level of $f \approx$ 50 Hz. A slight change of the swirl strength (from S = 0.28 to S = 0.31) did not tend to have a significant effect on flame dynamics in the present investigation.

As shown in Figure 6.14, the tangential fuel injection method resulted in a higher Φ_{LBO}, which indicated a worse performance in flame stabilization. In addition, a stronger effect of the swirl number on Φ_{LBO} could be noted in cases in which a tangential fuel injection strategy was employed than that in other cases.

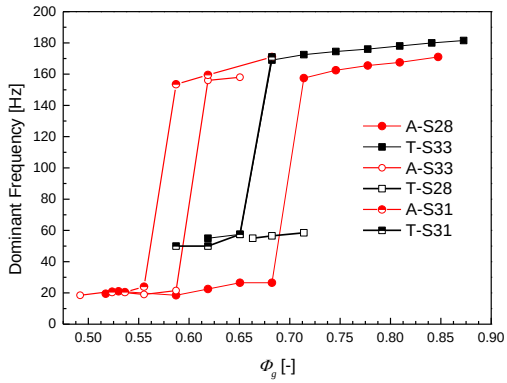

Figure 6.13 The dominant frequency versus the global equivalence ratio (Φ_g).

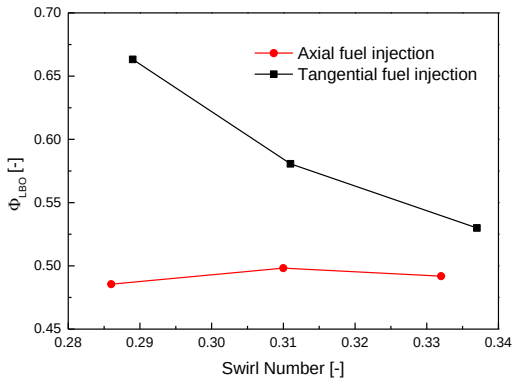

Figure 6.14 The lean blowout limits versus the swirl number for different fuel injection methods.

6.2 Flames stabilized by a bluff-body

6.2.1 Effects of a central jet on premixed flames (Paper IV)

The effects of a central jet on bluff-body stabilized premixed flames were investigated based on the adjustable bluff-body burner, as shown in Figure 3.4. The experiments were carried out without confinement under the atmospheric conditions. In the base case without any central jet while holding the annular flow at Φ = 0.64 and U_a = 2.77 m/s, the temperature T_{edge} at the inner edge of the bluff-body was referred to as T_0 in the thesis. The effects of a central jet on T_{edge} are evaluated by comparisons of T_{edge} in different cases with T_0 in the base case.

6.2.1.1 Effects of a central air jet

It can be observed in Figure 6.15 that without injection of a central air jet, the heat release peaked on the central axis. However, with the injection of a central air jet, the main heat release zone occurred elsewhere than on the burner axis. With a small amount of central air ($U_{c\text{-}a}$ / U_a = 0.79), the flame width (w_f, as shown in Figure 6.15) was larger than that in the base case. The small amount of the central air jet might form an inner vortex (generating the locally extremely lean condition), as shown schematically using the white triangle in Figure 6.15, preventing the flame being attached to the bluff-body as well as the heat convection of the combusted products to the surface of the bluff-body. An increase in the velocity of the central air jet led to the flame becoming shorter, at the same time the flame width becoming smaller. Meanwhile, the flame turned to be weaker as the heat release zone shrank. An instability of the premixed flame (the split-flashing flame) might appear when more central air was injected into the flow fields, as shown in Figure 6.15.

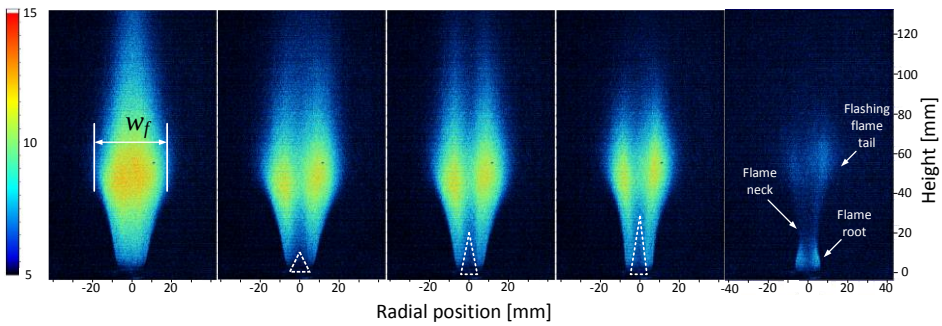

Figure 6.15 Time-averaged bluff-body stabilized premixed flame structures (broad-band chemiluminescence) associated with a central air jet (from left to right: $U_{c\text{-}a}$ / U_a = 0, 0.79, 3.94, 7.87 and 13.22).

As shown in Figure 6.16, with an increase in the velocity of the central air jet, the flame blowoff limits as a whole increased. When $U_{c\text{-}a}$ / U_a was low, the flame was extremely unstable with an easily occurrence of flame blowout. A further increase in $U_{c\text{-}a}$ led to a decrease in the flame blowoff limit. Increasing $U_{c\text{-}a}$ further resulted in a further increase in the flame blowout limits. Two different blowout phenomena were observed: with and without the appearance of a split-flashing flame mode, and they are strongly determined by $U_{c\text{-}a}$.

When $U_{c\text{-}a}$ / $U_a \approx 1$, the temperature of the bluff-body surface could easily drop to less than 80% of T_0, as shown in Figure 6.16. Afterwards, an increase in $U_{c\text{-}a}$ would lead to

the temperature ratio returning to a value of approximately 87%. The injection of a central air jet, as a whole, reduce the heat load to the upper surface of the bluff-body.

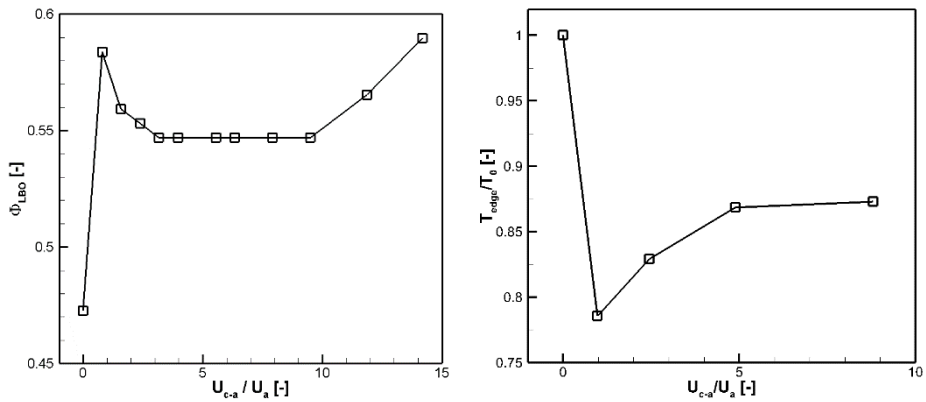

Figure 6.16 Effects of a central air jet on the flame blowoff limits (left) and the temperature on the upper surface of the bluff-body (right).

6.2.1.1 Effects of a central fuel jet

As shown in Figure 6.17, with injection of the central fuel jet, the flame became detached from the bluff-body. The height of the flame liftoff increased with an increase in $U_{c\text{-}f}$. With a large amount of central fuel jet, the yellowish flame behaved more like a diffusion jet flame, the annular flow serving as the oxidant and the central fuel jet serving as the main fuel source.

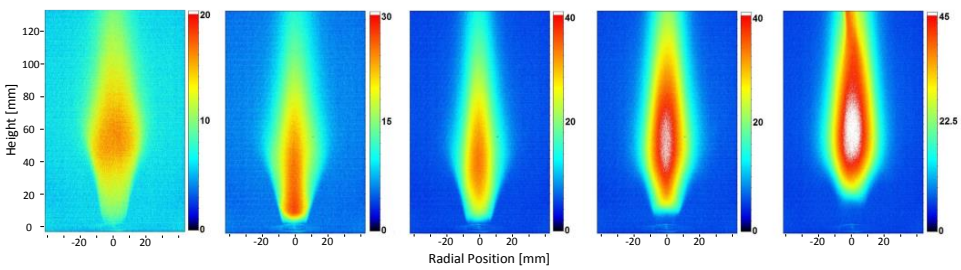

Figure 6.17 Time-averaged flame structures (broad-band chemiluminescence) with a central fuel injection (from left to right: $U_{c\text{-}f}$ / U_a = 0, 0.045, 0.089, 0.22 and 0.36).

With the injection of a central fuel jet, the flame became unstable with the flame tip being attached to the outer edge of the bluff-body. The attached point of the flame tip was unstable, moving circularly with a dominant oscillation frequency along the outer edge of the bluff-body, as shown in Figure 6.18. That dominant frequency decreased with the increase in $U_{c\text{-}f}$.

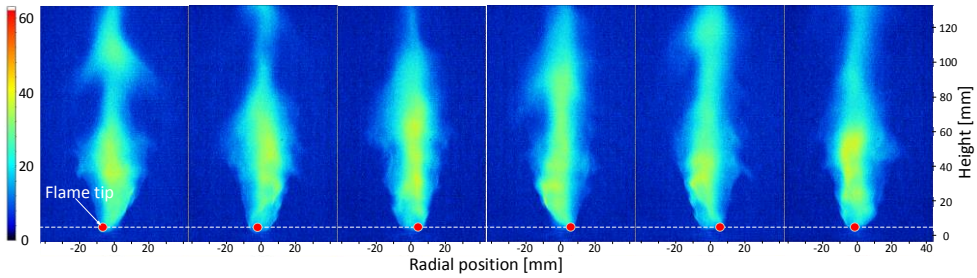

Figure 6.18 Typical flame instability behavior caused by the injection of a central fuel jet (the flame tip moving circularly around the outer edge of the bluff-body).

In addition, as shown in Figure 6.19, following injection of the central fuel jet, T_{edge} decreased significantly, possibly to even less than 75% of T_0. The liftoff of the flame led to the reduction of heat load to the surface of the bluff-body.

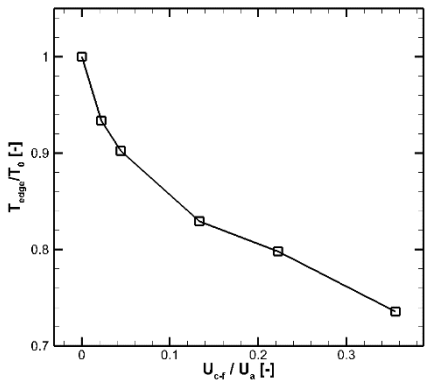

Figure 6.19 Effects of a central fuel jet on the temperature on the surface of a bluff-body.

6.2.2 Effects of the position of a bluff-body on diffusion flames (Paper V)

With the positions of a bluff-body being ΔH = 0 mm and ΔH = 10 mm, different flame patterns: the recirculation zone flame, the stable jet diffusion flame, the lifted flame and the split-flashing flame, were observed in the adjustable bluff-body burner (Version 1), as shown in Figure 6.20. An alternation of fuel and air flow velocities led to the variances of flame patterns within these two burner geometries. The flame pattern regimes versus different velocities of air and fuel in different burner geometries with ΔH = 0 mm and ΔH = 10 mm are shown in Figure 6.21.

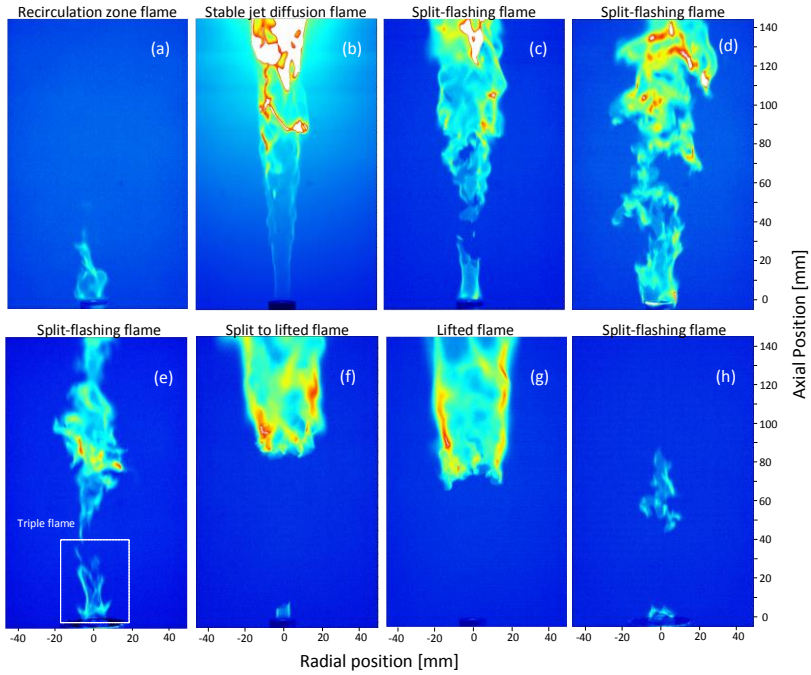

Figure 6.20 Typical flame patterns (broad-band chemiluminescence): (a)the recirculation zone flame, (b)the stable jet diffusion flame, (c,d,e): the split flame, (f) the transition from the split flame to the lifted flame, (g) the lifted flame and (h) the split-flashing flame.

As can be seen in Figure 6.21, when $U_a < 2$ m/s, two flame patterns could be observed for these two burner geometries. Whereas for moderate values of U_a, there were three flame patterns altogether under different operating conditions. The flame transition points for these two burner geometries were similar to one another when $U_a < 6.8$ m/s. However, when $U_a > 6.8$ m/s, these two burner geometries differed from one another in terms of flame instabilities. The flame could not be stabilized in the upper left region in Figure 6.21(a); whereas in Figure 6.21(b) in the same region, the flame could be stabilized with a recirculation zone flame pattern in the burner with $\Delta H = 10$ mm. Two flame extinction phenomena were observed in the experiments. The first type of flame extinction was due to a decisive *increase* in the velocity of the central fuel jet when $U_j >$ 10 m/s, which was referred to as *flame blowoff* shown in the middle right region in Figure 6.21(a) and (b). The split flame occurred prior to flame blowoff from a stable diffusion flame pattern. Another type of flame extinction, shown in the upper left in Figure 6.21(a), was that caused by a decisive *decrease* in the velocity of the central fuel flow referred to here as *flame blowout*.

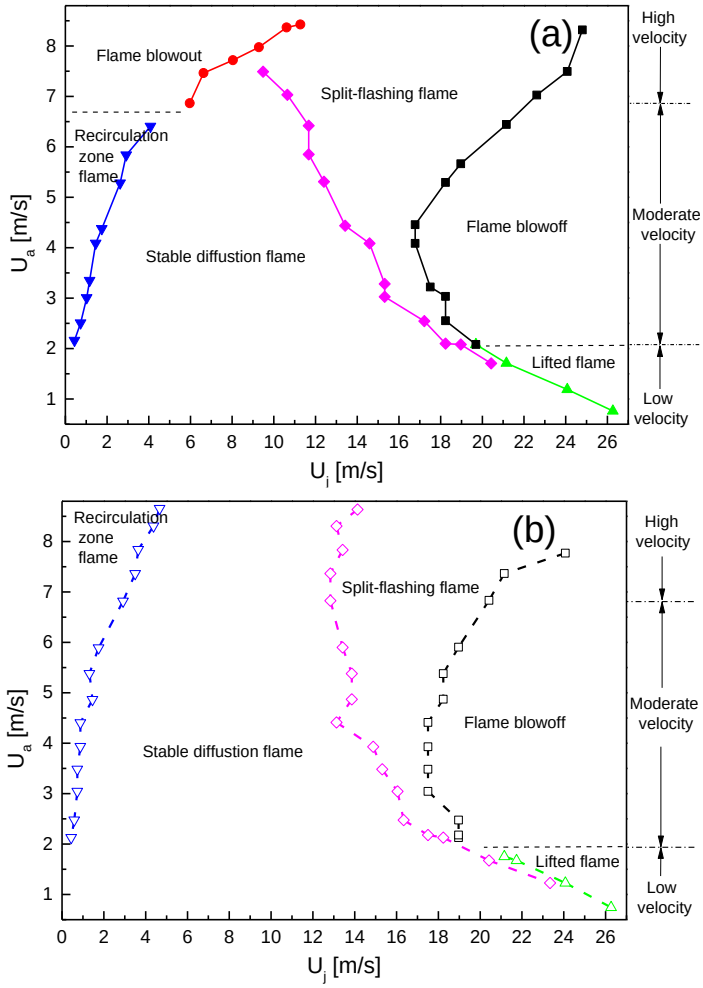

Figure 6.21 Flame pattern regimes concerned with different air and fuel velocities in burners with (a) ΔH = 0 mm and (b) ΔH = 10 mm.

Placing the bluff-body 10 mm above the annular channel exit enhanced flame stabilization, especially when U_a was high. In that burner, the flame tip propagated further upstream, even into the region where h = -5 mm. As can be seen in Figure 6.22, a recirculation bubble adjacent to the outer wall of the bluff-body could be noted. The pathway for the convection of the central fuel into that recirculation zone is shown schematically by the red dashed lines. The mixing of central fuel jet with the annular air could be expressed as follows: (a) that fuel first mixes with air in the shear layer located between the fuel driven inner recirculation zone and the air driven outer recirculation zone; (b) that fuel rich mixture then becomes further convected to the recirculation bubble adjacent to the outer wall of the bluff-body and (c) that a further

mixing of fuel with air takes place inside the wall-adjacent recirculation zone. Since the local mixture of reactants might well be within the flammability limits or preferably the local equivalence ratio is Φ = 1, the flame can be originated from and thus stabilized in the wall-adjacent recirculation zone with a sufficiently low scalar dissipation rate. As a consequence, flame stabilization is enhanced for the burner with ΔH = 10 mm.

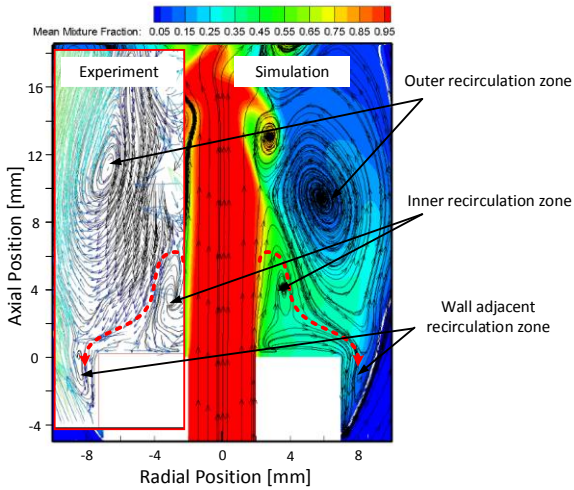

Figure 6.22 A comparison of simulation results with experimental data in regard to flow structures near the bluff-body (the red dashed line showing the pathway that fuel convection takes).

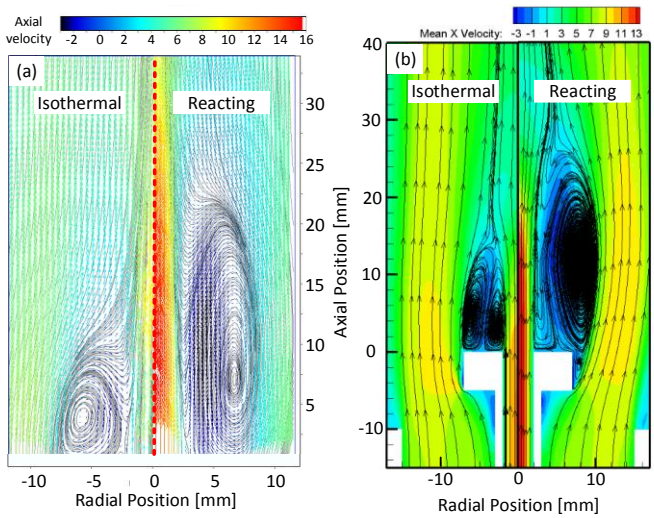

Figure 6.23 Effects of combustion on the flow fields: (a) experimental results and (b)simulation results.

In addition, as shown in Figure 6.23, combustion changed the flow fields downstream of the bluff-body considerably. The location of the outer recirculation zone core moved further downstream in the reacting case. At the same time, the velocity of the central jet also accelerated by combustion. Moreover, the wall-adjacent recirculation zone could only be observed in the reacting cases due to the flow expansion in the inner and outer recirculation bubbles. The interaction between flow fields and the combustion that occurs determines different flame structures and flame stability characteristics.

6.3 Flames stabilized by a combination of swirl flow and a bluff-body

Flames stabilized by a combination of swirl flow and different bluff-bodies were studied under atmospheric conditions, in the adjustable bluff-body burner (Version 2). The experimental conditions are listed in Table 6.2.

Table 6.2 Experimental conditions of flames stabilized by a combination of swirl flow and/or different bluff-bodies.

Case Name	d_b [mm]	m_t [ln/min]	m_a [ln/min]	m_f [ln/min]	m_a/m [-]	S_g [-]
T200-A0-d0	-	200	0	3	1	4.08
T150-A50-d0	-	150	50	3	0.75	2.30
T200-A0-d14	14	200	0	3	1	2.83
T150-A50-d14	14	150	50	3	0.75	1.59
T100-A100-d14	14	100	100	3	0.5	0.71
T50-A150-d14	14	50	150	3	0.25	0.18
T0-A200-d14	14	0	200	3	0	0
T200-A0-d20	20	200	0	3	1	1.88
T150-A50-d20	20	150	50	3	0.75	1.06
T100-A100-d20	20	100	100	3	0.5	0.47
T50-A150-d20	20	50	150	3	0.25	0.11
T0-A200-d20	20	0	200	3	0	0

6.3.1 Effects of the size of a bluff-body (Paper VI)

Holding m_t, m_a and m_f constant, the effects of the size of a bluff-body on flame structures could be obtained, as shown in Figure 6.24. The flame expansion downstream near the burner exit with a flame open angle, α, was marked by the dashed-dotted line in the third row in Figure 6.24. It decreased when the size of the bluff-body was getting smaller. Further downstream of the flame expansion region, in all three cases shown in Figure 6.24, a flame tail was generated. The flame tail in case T150-

A50-d0 was longer than that in the other cases. One can also note that in case T150-A50-d0, the flame tip 'flashback' upstream into the quartz tube, which was different from the flame behaviors in other cases. The flame was shorter and more compact in case T150-A50-d20 than that in the other cases. The bluish flame zone, which was located upstream of the flame tail region, was found closer to the bluff-body in case T150-A50-d20 than that in the other two cases.

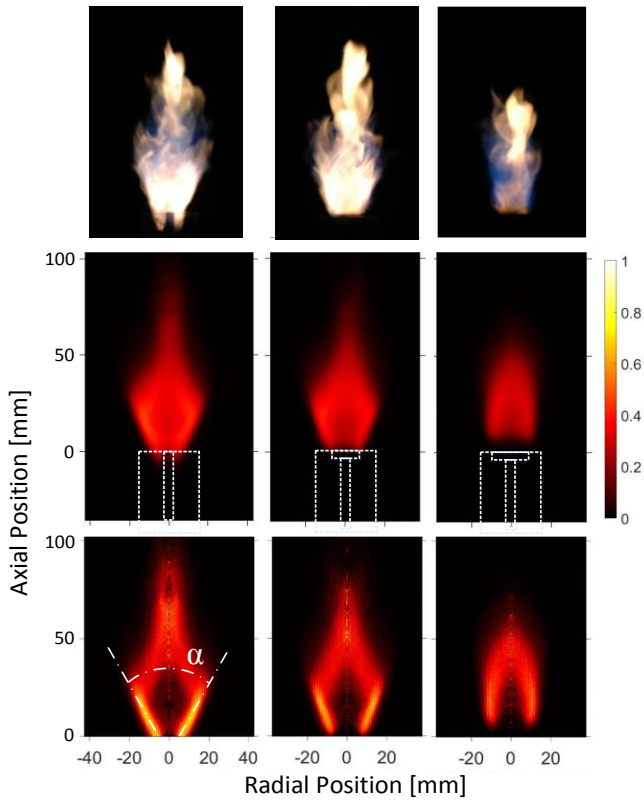

Figure 6.24 Flame structures in different cases. Left column: T150-A50-d0; center column: T150-A50-d14; right column: T150-A50-d20; upper row: broad-band chemiluminescence; middle row: time-averaged CH* chemiluminescence; lower row: inverse Abel reconstructed CH* chemiluminescence downstream of the bluff-body.

The typical CH_2O PLIF results for cases with different bluff-body sizes are shown and compared with each other in Figure 6.25. The same as described in Figure 6.24, the spatial distribution of CH_2O in the case T150-A50-d20 is more compact than it is in the other two cases. The simulation results show fairly good agreement with the experimental data, especially in describing the expanded CH_2O brush. In the lower row in Figure 6.25, one can note that in case T150-A50-d0, due to the strong swirling flow,

a recirculation bubble was formed at h = 35 mm downstream of the jet exit. The reverse flow motion in the air driven recirculation vortex forced the central fuel jet to propagate upstream and hence pushed fuel jet expansion radially. In addition, a small recirculation bubbler was being generated beside the central pipe close to the jet exit. That recirculation vortex enhanced fuel-air mixing and brought fuel into the upstream region of h < 0 mm by convection in the mixing layer between fuel driven and air driven vortexes. It was thus the flame in case T150-A50-d0 could be observed propagating upstream into the region of h < 0 mm, as shown in Figure 6.25. In addition, a part of the central fuel jet penetrated the annular air driven recirculation zone. As a consequence, a flame tail could be generated in all three cases shown in Figure 6.25. In comparing the flow fields in the three different cases shown in Figure 6.25, it could be noted that with an increase in the size of the bluff-body, air driven recirculation vortex was located increasingly close to the jet exit. In case T150-A50-d20, a large recirculation bubble was found to be attached to the upper surface of the bluff-body. The air driven recirculation vortex was generated by the bluff-body other than the swirling flow. Its presence was due to the fact that even when the flow swirl number was S_g = 0, the similar recirculation bubble could still be generated.

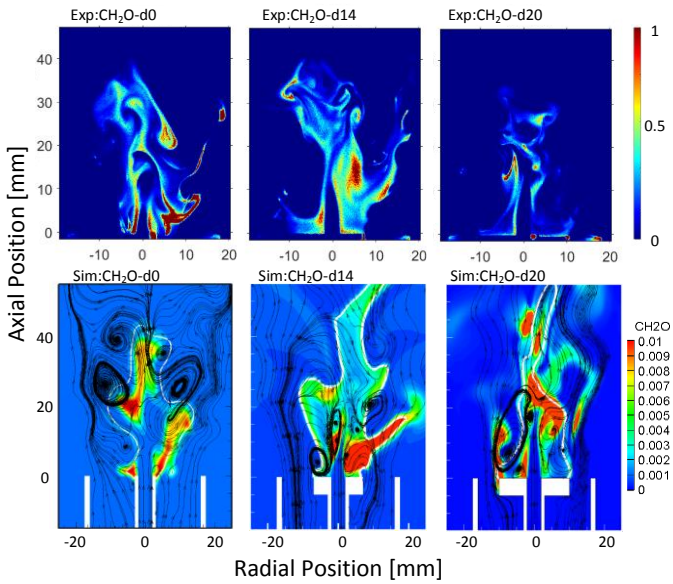

Figure 6.25 Comparison of the experimental results and the numerical data for different cases: Left column: T150-A50-d0; center column: T150-A50-d14; right column: T150-A50-d20. Upper row: experimental data concerning CH_2O distribution; lower row: numerical data concerning CH_2O distribution and the flow fields, the white lines denoting the iso-contour of the stoichiometric mixture.

The interesting phenomenon with flame 'flashback' into a region further upstream is more clearly seen in cases with m_t = 200 ln/min, as shown in Figure 6.26. From the broad-band chemiluminescence of flame structures it can be seen that more soot was produced in case T200-A0-d0 than that in the other two cases. The flame in case T200-A0-d20 had the most bluish color, indicating it to have the best mixing of fuel and air. The blue line in the simulation results in the lower row in Figure 6.26 denotes the region of stoichiometric mixture that marks the spatial distribution of fuel. In cases T200-A0-d0 and T200-A0-d14, the strong reverse flow in air driven vortex pushed a part of the central fuel jet in air-fuel mixing layer upstream into the quartz tube. In case T200-A0-d20, however, the flame could not be pushed upstream into the quartz tube, due to blockage of the large bluff-body there. It was also found that the time-averaged fuel-driven inner vortex was smaller in the case for which d_b = 20 mm than in the other cases, due to the stronger reverse flow momentum it possessed. Without a bluff-body, the central fuel jet could penetrate higher.

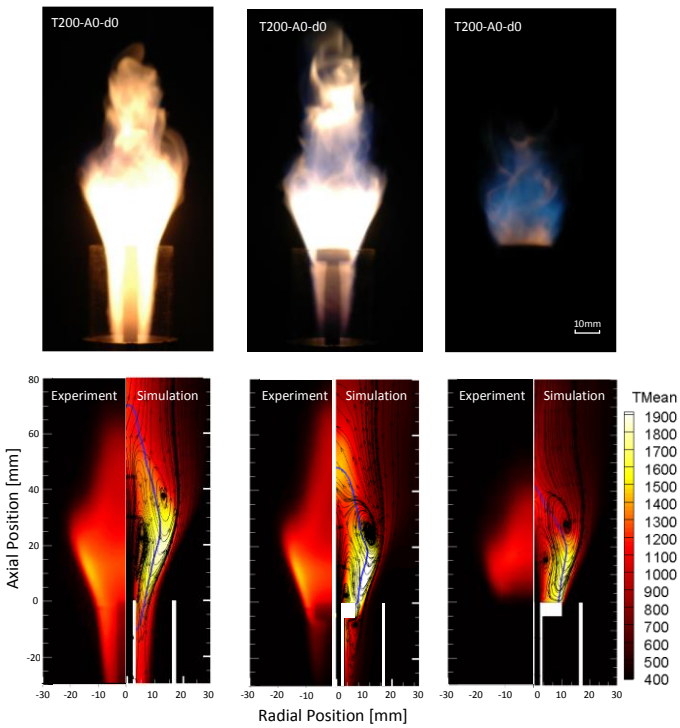

Figure 6.26 Different flame structures in three different cases: T200-A0-d0 (left column), T200-A0-d14(middle column) and T200-A0-d20 (right column). Upper row: broad-band chemiluminescence; lower column: comparisons of the time-averaged CH* chemiluminescence obtained in the experiments (left) with the temperature distributions and the flow fields obtained in the simulations (right).

6.3.2 Effects of the swirl strength (Paper VI)

Figure 6.27 shows the effects of a bluff-body and the swirl strength on L_F and H_{COHR}. One could note that flame in case with d_b = 14 mm had the longer L_F and the higher H_{COHR} than that in case with a larger bluff-body. In case with d_b = 14 mm, an increase in the mass flow rate of the tangential air led to the formation of a shorter and more compact flame. However, in the case with d_b = 20 mm, L_F and H_{COHR} did not change significantly with the alternation of the swirl strength. Flame could not be stabilized in the burner without a bluff-body when m_t <120 ln/min. The bluff-body enhanced the diffusion flame stabilization especially for cases in which the flow swirl number was low.

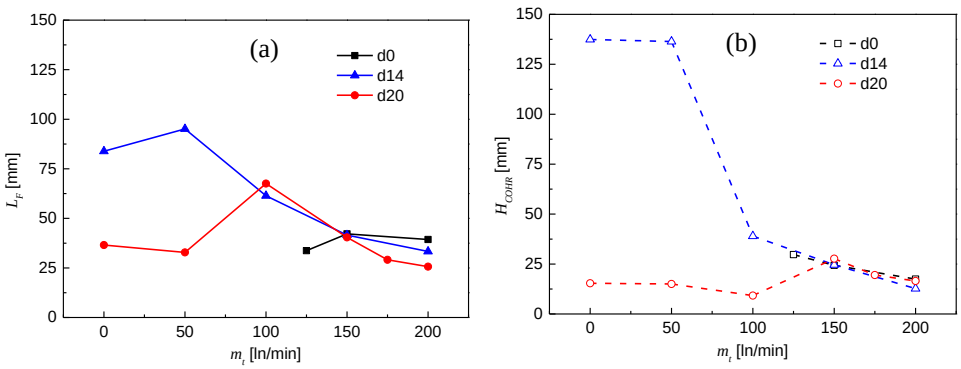

Figure 6.27 L_F (a) and H_{COHR} (b) versus mass flow rate of the tangential air flow.

Comparing flame structures shown in Figure 6.24 and Figure 6.26, for the burner in which d_b = 20 mm, a slight decrease in flame length and a widening of the flame open angle along with an increase in the swirl number could be observed. An increase in the swirl number enhanced the outer recirculation zone and thus the momentum of the reverse flow. It resisted the central jet penetration, hence forming a shorter flame. Meanwhile, the flame became bluish with a stronger swirl strength in the burner in which d_b = 20 mm indicating a much better mixing of central fuel and annular air.

6.4 Summary of publications

I. **Tong Yiheng**, Mao Li, and Jens Klingmann. Influence of Combustor Geometry on Swirl Stabilized Premixed Methane-Air Flame. ASME Turbo Expo 2016: Turbomachinery Technical Conference and Exposition. American Society of Mechanical Engineers, 2016.

In this paper, the effects of the confinement geometries on the swirl stabilized flame structures and the lean blowout limits were investigated. Two confinement geometries, a rectangular one and a cylindrical one, both having the same cross-sectional area, were used in the experimental study. The effects of the mass flow rates on the lean blowout limits, the effects of the equivalence ratio on flame dynamics were studied as well. Flame structures and flame dynamics followed with the help an intensified high-speed filtered CH* camera. CO emissions were registered as well.

My contributions: As both the corresponding and the first author of this paper, I conducted the literature review and carried out the experiments together with Mao Li, under the supervision of Jens Klingmann. I analyzed the experimental data and wrote the draft of the paper. Jens Klingmann revised the paper.

II. **Tong Y**, Li M, Thern M, Klingmann J. An Experimental Study of Effects of Confinement Ratio on Swirl Stabilized Flame Macrostructures. In ASME 2017 Power Conference Joint with ICOPE-17 collocated with the ASME 2017 11th International Conference on Energy Sustainability, the ASME 2017 15th International Conference on Fuel Cell Science, Engineering and Technology, and the ASME 2017 Nuclear Forum 2017 Jun 26 (pp. V001T04A007-V001T04A007). American Society of Mechanical Engineers.

In this paper, the effects of the diameter of a cylindrical confinement on swirl stabilized flame structures and flame instabilities were investigated. The time-averaged CH* chemiluminescence flame structures obtained were analyzed with use of the inverse Abel image reconstruction methods. Mechanisms forming different M-shape flames and the interactions of flame structures and flame instabilities were proposed.
My contributions: As the lead author of this paper, I designed and conducted the experiments with the help of Mao Li. I analyzed and discussed the experimental data under the supervision of Jens Klingmann and Marcus Thern. I wrote the paper and Jens Klingmann revised it. I presented the paper during the conference.

III. **Yiheng Tong**, Senbin Yu, Xiao Liu and Jens Klingmann. Experimental study on dynamics of a confined low swirl partially premixed methane-hydrogen-air flame. *Accepted by International Journal of Hydrogen Energy.*

The effects of two different fuel injection methods on swirl stabilized flame dynamics and flame structures were investigated experimentally in this paper. The total mass flow rate of air and the mass flow rate of hydrogen were kept constant, whereas the mass flow rate of methane being varied. Flame dynamics far from and near lean blowout limits were studied. Intensified high-speed CH* chemiluminescence and high-speed

PIV were employed for visualizing flame dynamics and the flow fields, respectively. The effects of slight changes in swirl strength on the flame behavior and lean blowout limits were discussed as well.
My contributions: As the first author of the paper, I designed and conducted the experiments with the help of Senbin Yu and Xiao Liu. I analyzed and discussed the experimental data under the supervision of Jens Klingmann. The outcomes of the work were discussed together with the co-authors. I wrote the paper and revised it on the basis of comments from Jens Klingmann.

IV. **Yiheng Tong**, Shuang Chen, Mao Li, Zhongshan Li and Jens Klingmann. Experimental study on bluff-body stabilized premixed flame with a central air/fuel jet. *Submitted to Energies.*

The premixed flame structures stabilized by a bluff-body together with the lean blowout limits of that flame, under conditions with a central air or fuel jet, were investigated in the paper. The temperature on the surface of the bluff-body in different cases having different central jet velocities were studied as well. The dynamics of the flame tip and the unstable structures of the flame were visualized using the high-speed CMOS camera. The lean blowout limits of the flame provided with additional central air injection were studied as well.
My contributions: As the first author of the paper, I designed the burner with the help from Shuang Chen and Zhongshan Li. I conducted the experiments and carried out the data analysis with Mao Li, under the supervision of Jen Klingmann. The results obtained were discussed together with the co-authors. I wrote the paper and revised it based on comments from Zhongshan Li and Jens Klingmann.

V. **Yiheng Tong**, Xiao Liu, Shuang Chen, Zhongshan Li, Jens Klingmann. Experimental and Numerical Study about Effects of Bluff-body Position on Diffusion Flame Instabilities. *Submitted to Applied Thermal Engineering.*

The paper concerns the effects of the position of a disk-shape bluff-body on diffusion flame patterns and flame instabilities. Both experimental and numerical work was carried out to obtain as thorough an understanding as possible of interactions between the flow fields and the flame behaviors. Two bluff-body positions, ΔH = 0 mm and ΔH = 10 mm, were investigated. The simulation results matched rather well with the experimental data. Mounting the bluff-body outside the exit of the annular channel was found to enhance the flame stabilization through a small recirculation bubble adjacent to the outer wall of the bluff-body. Combustion was found to change the flow fields appreciably, compared with the iso-thermal conditions.
My contributions: As the lead author of this paper, I designed the burner with the help

from Shuang Chen and Zhongshan Li. I performed the experimental and numerical work with the assistance of Xiao Liu, under the supervision of Jens Klingmann; Xiao Liu helped me with the data analysis. The outcomes of the work were discussed together with the co-authors. I wrote the draft of the paper and revised it in line with comments from Jens Klingmann.

VI. **Yiheng Tong**, Xiao Liu, Zhenkan Wang, Jens Klingmann. Experimental and Numerical Study of Bluff-body and Swirl Stabilized Diffusion Flames. *Submitted to Fuel.*

A combined experimental and numerical investigation of bluff-body and swirl stabilized diffusion flames was carried out in the paper. The effects of bluff-body size on swirl stabilized flame structures and the emissions, together with effects of swirl on bluff-body stabilized flame behavior were studied. High-speed PIV and high resolution LES methods were employed to obtain as thorough an understanding as possible of the interaction between the flow fields and flame structures. Both the total mass flow rate of air and the mass flow rate of fuel were held constant, thus the global equivalence ratio and thermal power being kept constant. The diffusion flame 'flashback' was observed, the factors behind it being analyzed in detail.
My contributions: As the lead author of this paper, I designed the experiments with the help of Xiao Liu. I conducted the experimental work, Zhenkan Wang conducted the PLIF measurements; I performed the numerical work and the data analysis together with Xiao Liu. The results of the work were discussed together with all the co-authors. I wrote the paper and revised it on the basis of comments from Jens Klingmann.

7.Conclusions and Suggestions for Future Work

7.1 Conclusions

Experimental and numerical investigations of flames stabilized by swirl flow and a bluff-body were conducted in the thesis. The experimental research included measurements of high-speed PIV, high-speed PLIF, thermography, intensified high-speed CH* chemiluminescence, while the numerical investigations were based on LES and DES in ANSYS Fluent and OpenFOAM. The experiments were conducted on the variable-swirl burner, the adjustable bluff-body burner both Version 1 and the modified Version 2 of it. Fuel used in the present investigation was mainly methane, while the effects of fuel injection strategies on flame dynamics were being studied with hydrogen mixed into the reactants. The investigation as a whole concerned flame structures and flame instabilities, as well as their interactions with flow fields. The main conclusions of thesis that could be drown were as follows:

- The operating conditions, including the total mass flow rate and the equivalence ratio of the reactants play an important role in determining the structures and the dynamics of swirl stabilized lean premixed flames.

- The geometries of the confinement, including its cross-sectional shape and the diameter of a cylindrical confinement, strongly affect the swirl stabilized flame structures and flame dynamics. Proposals are made concerning the mechanisms behind the swirl stabilized lifted M-shape flames that were studied and the corresponding flame dynamics.

- Fuel injection strategy employed affects the characteristics of low swirl stabilized flame: i.e. the time-averaged flame structures and the flame oscillations. An axial

fuel injection strategy leads to a more compact flame and to leaner blowout limits, than a tangential fuel injection strategy does. The flame oscillation frequencies, which are found when occurrence of a lean blowout is approached, depend on fuel injection strategy.

- A central air or fuel injection makes bluff-body stabilized premixed flame more unstable. At the same time, as with use of a central air or fuel jet, the temperature on the upper surface of the bluff-body becomes lower.

- The position of a bluff-body in relation to the exit of the annular channel affects the diffusion flame patterns. Mounting the bluff-body 10 mm downstream of the annular channel exit serves to better stabilize the flame. The recirculation bubble adjacent to the outer wall of the bluff-body enhances the stabilization of the flame.

- The combinations of a bluff-body and swirl flow in stabilizing the diffusion flame were studied both experimentally and numerically. Diffusion flame 'flashback' was observed and the mechanisms behind it were proposed. With use of a larger bluff-body, air-driven recirculation zone was found to be located further upstream close to the burner exit. Flames were found to be better stabilized with use of a larger bluff-body and/or a stronger swirling flow.

7.2 Suggestions for future work

Based on the findings of the present doctoral thesis, various directions for future work are recommended:

- Simultaneous high-speed PIV and multi-species PLIF, together with highly accurate LES or DES simulations, would be useful for gaining a better understanding of the interactions between flow fields and flame structures and thus the flame dynamics involved.

- The effects of a central bluff-body on the confined swirl stabilized premixed flame structures and instabilities should be studied further.

- Further detailed numerical simulations and investigations of flame dynamics within different geometries of confinements, especially within the rectangular and the cylindrical confinements, are suggested.

- Simulations of the lean premixed flame dynamics under low-swirl conditions with use of different fuel injection strategies are suggested.

- Further investigation of the emissions occurring under different operating conditions and burner geometries would appear to be very promising.

References

[1] I.E. Agency, World Energy Outlook 2016, in, International Energy Agency, 2016.

[2] S.R. Turns, An introduction to combustion, McGraw-hill New York, 1996.

[3] T.C. Lieuwen, V. Yang, Combustion instabilities in gas turbine engines(operational experience, fundamental mechanisms and modeling), Progress in astronautics and aeronautics, (2005).

[4] Y. Wu, Large Eddy Simulation of Turbulent Swirling Flows in Combustor Related Geometries, 2013.

[5] M.-K. Kim, J. Yoon, S. Park, M.-C. Lee, Y. Yoon, Effects of unstable flame structure and recirculation zones in a swirl-stabilized dump combustor, Applied Thermal Engineering, 58 (2013) 125-135.

[6] O. Lucca-Negro, T. O'doherty, Vortex breakdown: a review, Progress in Energy and Combustion Science, 27 (2001) 431-481.

[7] T. Sarpkaya, On stationary and travelling vortex breakdowns, Journal of Fluid Mechanics, 45 (1971) 545-559.

[8] T. Sarpkaya, Vortex breakdown in swirling conical flows, AIAA J, 9 (1971) 1792-1799.

[9] J.H. Faler, S. Leibovich, An experimental map of the internal structure of a vortex breakdown, Journal of Fluid Mechanics, 86 (1978) 313-335.

[10] J.H. Faler, S. Leibovich, Disrupted states of vortex flow and vortex breakdown, The Physics of Fluids, 20 (1977) 1385-1400.

[11] R.E. Spall, Transition from spiral - to bubble - type vortex breakdown, Physics of Fluids, 8 (1996) 1330-1332.

[12] Y. Fu, J. Cai, S.-M. Jeng, H. Mongia, Confinement effects on the swirling flow of a counter-rotating swirl cup, in: ASME Turbo Expo 2005: Power for Land, Sea, and Air, American Society of Mechanical Engineers, 2005, pp. 469-478.

[13] A.M. Elbaz, W.L. Roberts, Investigation of the effects of quarl and initial conditions on swirling non-premixed methane flames: Flow field, temperature, and species distributions, Fuel, 169 (2016) 120-134.

[14] T. Claypole, N. Syred, The effect of swirl burner aerodynamics on NOx formation, in: Symposium (International) on Combustion, Vol. 18, Elsevier, 1981, pp. 81-89.

[15] P. Anacleto, E. Fernandes, M. Heitor, S. Shtork, Swirl flow structure and flame characteristics in a model lean premixed combustor, Combustion science and technology, 175 (2003) 1369-1388.

[16] S. Wang, V. Yang, G. Hsiao, S.-Y. Hsieh, H.C. Mongia, Large-eddy simulations of gas-turbine swirl injector flow dynamics, Journal of Fluid Mechanics, 583 (2007) 99-122.

[17] S. Roux, G. Lartigue, T. Poinsot, U. Meier, C. Bérat, Studies of mean and unsteady flow in a swirled combustor using experiments, acoustic analysis, and large eddy simulations, Combustion and flame, 141 (2005) 40-54.

[18] P. Wang, X.-S. Bai, M. Wessman, J. Klingmann, Large eddy simulation and experimental studies of a confined turbulent swirling flow, Physics of Fluids, 16 (2004) 3306-3324.

[19] A. Schönborn, P. Sayad, J. Klingmann, Influence of precessing vortex core on flame flashback in swirling hydrogen flames, International Journal of Hydrogen Energy, 39 (2014) 20233-20241.

[20] K. Oberleithner, M. Stöhr, S.H. Im, C.M. Arndt, A.M. Steinberg, Formation and flame-induced suppression of the precessing vortex core in a swirl combustor: experiments and linear stability analysis, Combustion and flame, 162 (2015) 3100-3114.

[21] Y. Huang, V. Yang, Dynamics and stability of lean-premixed swirl-stabilized combustion, Progress in Energy and Combustion Science, 35 (2009) 293-364.

[22] T. Poinsot, D. Veynante, Theoretical and numerical combustion, RT Edwards, Inc., 2005.

[23] J. Driscoll, J. Temme, Role of swirl in flame stabilization, (2011).

[24] I. Chterev, C. Foley, D. Foti, S. Kostka, A. Caswell, N. Jiang, A. Lynch, D. Noble, S. Menon, J. Seitzman, Flame and flow topologies in an annular swirling flow, Combustion science and technology, 186 (2014) 1041-1074.

[25] T. Guiberti, D. Durox, P. Scouflaire, T. Schuller, Impact of heat loss and hydrogen enrichment on the shape of confined swirling flames, Proceedings of the Combustion Institute, 35 (2015) 1385-1392.

[26] D. Wicksall, A. Agrawal, R. Schefer, J. Keller, The interaction of flame and flow field in a lean premixed swirl-stabilized combustor operated on H 2/CH 4/air, Proceedings of the Combustion Institute, 30 (2005) 2875-2883.

[27] S. Shanbhogue, Y. Sanusi, S. Taamallah, M. Habib, E. Mokheimer, A. Ghoniem, Flame macrostructures, combustion instability and extinction strain scaling in swirl-stabilized premixed CH 4/H 2 combustion, Combustion and flame, 163 (2016) 494-507.

[28] T.F. Guiberti, D. Durox, L. Zimmer, T. Schuller, Analysis of topology transitions of swirl flames interacting with the combustor side wall, Combustion and flame, 162 (2015) 4342-4357.

[29] L.T.W. Chong, T. Komarek, M. Zellhuber, J. Lenz, C. Hirsch, W. Polifke, Influence of strain and heat loss on flame stabilization in a non-adiabatic combustor, in: Proc. Of European Comb. Meeting, 2009.

[30] T. Guiberti, L. Zimmer, D. Durox, T. Schuller, Experimental analysis of V-to M-shape transition of premixed CH4/H2/air swirling flames, in: ASME Turbo Expo 2013: Turbine Technical Conference and Exposition, American Society of Mechanical Engineers, 2013, pp. V01AT04A063-V001AT004A063.

[31] S.V. Alekseenko, V.M. Dulin, Y.S. Kozorezov, D.M. Markovich, S.I. Shtork, M.P. Tokarev, Flow structure of swirling turbulent propane flames, Flow, turbulence and combustion, 87 (2011) 569-595.

[32] M. Malanoski, M. Aguilar, D.-H. Shin, T. Lieuwen, Flame leading edge and flow dynamics in a swirling, lifted flame, Combustion science and technology, 186 (2014) 1816-1843.

[33] T. Lieuwen, V. McDonell, E. Petersen, D. Santavicca, Fuel flexibility influences on premixed combustor blowout, flashback, autoignition, and stability, Journal of Engineering for Gas Turbines and Power, 130 (2008) 011506.

[34] S. Taamallah, Z.A. LaBry, S.J. Shanbhogue, A.F. Ghoniem, Thermo-acoustic instabilities in lean premixed swirl-stabilized combustion and their link to acoustically coupled and decoupled flame macrostructures, Proceedings of the Combustion Institute, 35 (2015) 3273-3282.

[35] S. Taamallah, Z.A. LaBry, S.J. Shanbhogue, M.A. Habib, A.F. Ghoniem, Correspondence Between “Stable” Flame Macrostructure and Thermo-acoustic Instability in Premixed Swirl-Stabilized Turbulent Combustion, Journal of Engineering for Gas Turbines and Power, 137 (2015) 071505.

[36] S. Taamallah, S.J. Shanbhogue, A.F. Ghoniem, Turbulent flame stabilization modes in premixed swirl combustion: Physical mechanism and Karlovitz number-based criterion, Combustion and flame, 166 (2016) 19-33.

[37] P. Sayad, A. Schönborn, M. Li, J. Klingmann, Visualization of different flashback mechanisms for H2/CH4 mixtures in a variable-swirl burner, Journal of Engineering for Gas Turbines and Power, 137 (2015) 031507.

[38] N. Syred, M. Abdulsada, A. Griffiths, T. O’Doherty, P. Bowen, The effect of hydrogen containing fuel blends upon flashback in swirl burners, Applied Energy, 89 (2012) 106-110.

[39] M. Konle, T. Sattelmayer, Interaction of heat release and vortex breakdown during flame flashback driven by combustion induced vortex breakdown, Experiments in fluids, 47 (2009) 627.

[40] Y. Sommerer, D. Galley, T. Poinsot, S. Ducruix, F. Lacas, D. Veynante, Large eddy simulation and experimental study of flashback and blow-off in a lean partially premixed swirled burner, Journal of Turbulence, 5 (2004) 1-3.

[41] P. Sayad, A. Schönborn, J. Klingmann, Experimental investigation of the stability limits of premixed syngas-air flames at two moderate swirl numbers, Combustion and flame, 164 (2016) 270-282.

[42] P. Sayad, operational stability of lean premixed combustion in gas turbines: an experimental study on gaseous alternative fuels, (2016).

[43] K.A. Murty, Introduction to combustion phenomena, CRC Press, 1975.

[44] J.P. Longwell, E.E. Frost, M.A. Weiss, Flame stability in bluff body recirculation zones, Industrial & Engineering Chemistry, 45 (1953) 1629-1633.

[45] D.R. Noble, Q. Zhang, A. Shareef, J. Tootle, A. Meyers, T. Lieuwen, Syngas mixture composition effects upon flashback and blowout, ASME Paper No. GT2006-90470, (2006).

[46] D.E. Cavaliere, J. Kariuki, E. Mastorakos, A Comparison of the Blow-Off Behaviour of Swirl-Stabilized Premixed, Non-Premixed and Spray Flames, Flow Turbulence And Combustion, 91 (2013) 347-372.

[47] A.H. Lefebvre, D.R. Ballal, Gas turbine combustion, CRC Press, 2010.

[48] R.C. Chanaud, Observations of oscillatory motion in certain swirling flows, Journal of Fluid Mechanics, 21 (1965) 111-127.

[49] M. Stöhr, R. Sadanandan, W. Meier, Experimental study of unsteady flame structures of an oscillating swirl flame in a gas turbine model combustor, Proceedings of the Combustion Institute, 32 (2009) 2925-2932.

[50] J. Yoon, M.-K. Kim, J. Hwang, J. Lee, Y. Yoon, Effect of fuel–air mixture velocity on combustion instability of a model gas turbine combustor, Applied Thermal Engineering, 54 (2013) 92-101.

[51] S.J. Shanbhogue, S. Husain, T. Lieuwen, Lean blowoff of bluff body stabilized flames: Scaling and dynamics, Progress in Energy and Combustion Science, 35 (2009) 98-120.

[52] W. Roquemore, R. Tankin, H. Chiu, S. Lottes, A study of a bluff-body combustor using laser sheet lighting, Experiments in fluids, 4 (1986) 205-213.

[53] B. Dally, D. Fletcher, A. Masri, Flow and mixing fields of turbulent bluff-body jets and flames, Combustion Theory and Modelling, 2 (1998) 193-219.

[54] I. Esquiva-Dano, H. Nguyen, D. Escudie, Influence of a bluff-body's shape on the stabilization regime of non-premixed flames, Combustion and flame, 127 (2001) 2167-2180.

[55] H. Ma, J. Harn, The jet mixing effect on reaction flow in a bluff-body burner, International journal of heat and mass transfer, 37 (1994) 2957-2967.

[56] H. Tang, D. Yang, T. Zhang, M. Zhu, Characteristics of flame modes for a conical bluff body burner with a central fuel jet, Journal of Engineering for Gas Turbines and Power, 135 (2013) 091507.

[57] K.C. San, Y.Z. Huang, S.C. Yen, Flame Patterns and Combustion Intensity Behind Rifled Bluff-Body Frustums, Journal of Engineering for Gas Turbines and Power, 135 (2013) 121502.

[58] Y.-c. Chen, C.-c. Chang, K.-L. Pan, J.-T. Yang, Flame lift-off and stabilization mechanisms of nonpremixed jet flames on a bluff-body burner, Combustion and flame, 115 (1998) 51-65.

[59] J.-T. Yang, C.-C. Chang, K.-L. Pan, Y.-P. Kang, Y.-P. Lee, Thermal analysis and PLIF imaging of reacting flow behind a disc stabilizer with a central fuel jet, Combustion science and technology, 174 (2002) 71-92.

[60] A. Masri, R. Bilger, Turbulent diffusion flames of hydrocarbon fuels stabilized on a bluff body, in: Symposium (International) on Combustion, Vol. 20, Elsevier, 1985, pp. 319-326.

[61] R. Huang, C. Lin, Characteristic modes and thermal structure of nonpremixed circular-disc stabilized flames, Combustion science and technology, 100 (1994) 123-139.

[62] C.K. Law, Combustion physics, Cambridge university press, 2010.

[63] R. Schefer, M. Namazian, J. Kelly, M. Perrin, Effect of confinement on bluff-body burner recirculation zone characteristics and flame stability, Combustion science and technology, 120 (1996) 185-211.

[64] J.-T. Yang, C.-C. Chang, K.-L. Pan, Flow structures and mixing mechanisms behind a disc stabilizer with a central fuel jet, Combustion science and technology, 174 (2002) 93-124.

[65] R. Schefer, M. Namazian, J. Kelly, Velocity measurements in turbulent bluff-body stabilized flows, AIAA journal, 32 (1994) 1844-1851.

[66] R. Huang, C. Lin, Velocity fields of nonpremixed bluff-body stabilized flames, Journal of energy resources technology, 122 (2000) 88-93.

[67] P. Eriksson, The Zimont TFC model applied to premixed bluff body stabilized combustion using four different RANS turbulence models, in: ASME Turbo Expo 2007: Power for Land, Sea, and Air, American Society of Mechanical Engineers, 2007, pp. 353-361.

[68] S. Chaudhuri, B.M. Cetegen, Blowoff characteristics of bluff-body stabilized conical premixed flames with upstream spatial mixture gradients and velocity oscillations, Combustion and flame, 153 (2008) 616-633.

[69] S. Chaudhuri, B.M. Cetegen, Response dynamics of bluff-body stabilized conical premixed turbulent flames with spatial mixture gradients, Combustion and flame, 156 (2009) 706-720.

[70] S. Chaudhuri, S. Kostka, M.W. Renfro, B.M. Cetegen, Blowoff dynamics of bluff body stabilized turbulent premixed flames, Combustion and flame, 157 (2010) 790-802.

[71] S. Plee, A. Mellor, Characteristic time correlation for lean blowoff of bluff-body-stabilized flames, Combustion and flame, 35 (1979) 61-80.

[72] V. Acharya, B. Emerson, U. Mondragon, D.-H. Shin, C. Brown, V. McDonell, T. Lieuwen, Velocity and flame wrinkling characteristics of a transversely forced, bluff-body stabilized flame, Part II: Flame response modeling and comparison with measurements, Combustion science and technology, 185 (2013) 1077-1097.

[73] B. Emerson, U. Mondragon, V. Acharya, D.-H. Shin, C. Brown, V. McDonell, T. Lieuwen, Velocity and flame wrinkling characteristics of a transversely forced, bluff-body stabilized flame, part I: experiments and data analysis, Combustion science and technology, 185 (2013) 1056-1076.

[74] D. Dovizio, M.M. Salehi, C.B. Devaud, RANS simulation of a turbulent premixed bluff body flame using conditional source-term estimation, Combustion Theory and Modelling, 17 (2013) 935-959.

[75] C.Y. Lee, L.K.B. Li, M.P. Juniper, R.S. Cant, Nonlinear hydrodynamic and thermoacoustic oscillations of a bluff-body stabilised turbulent premixed flame, Combustion Theory and Modelling, 20 (2016) 131-153.

[76] T. Nishimura, T. Kaga, K. Shirotani, J. Kadowaki, Vortex structures and temperature fluctuations in a bluff-body burner, Journal of visualization, 1 (1998) 271-281.

[77] M. Euler, R. Zhou, S. Hochgreb, A. Dreizler, Temperature measurements of the bluff body surface of a Swirl Burner using phosphor thermometry, Combustion and flame, 161 (2014) 2842-2848.

[78] M. Euler, R. Zhou, S. Hochgreb, A. Dreizler, Temperature measurements of the bluff body surface of Cambridge Stratified Swirl Burner using phosphor thermometry, in: European Combustion Meeting, Vol. 11, 2013, pp. 33-33.

[79] M. Russi, I. Cornet, R. Cornog, The influence of flame holder temperature on flame stabilization, in: Symposium (International) on Combustion, Vol. 4, Elsevier, 1953, pp. 743-748.

[80] C.-X. Lin, R.J. Holder, Reacting turbulent flow and thermal field in a channel with inclined bluff body flame holders, Journal of Heat Transfer, 132 (2010) 091203.

[81] P. Guo, S. Zang, B. Ge, Technical brief: Predictions of flow field for circular-disk bluff-body stabilized flame investigated by large eddy simulation and experiments, Journal of Engineering for Gas Turbines and Power, 132 (2010) 054503.

[82] P. Guo, S. Zang, B. Ge, Les and experimental study of flow features in humid-air combustion chamber with non-premixed circular-disc stabilized flames, in: ASME Turbo Expo 2008: Power for Land, Sea, and Air, American Society of Mechanical Engineers, 2008, pp. 709-718.

[83] N.R. Caetano, L.F.F. da Silva, A comparative experimental study of turbulent non premixed flames stabilized by a bluff-body burner, Experimental Thermal and Fluid Science, 63 (2015) 20-33.

[84] P. Kumar, D. Mishra, Effects of bluff-body shape on LPG–H 2 jet diffusion flame, International Journal of Hydrogen Energy, 33 (2008) 2578-2585.

[85] D. Mishra, P. Kumar, Experimental study of bluff-body stabilized LPG–H 2 jet diffusion flame with preheated reactant, Fuel, 89 (2010) 212-218.

[86] R.N. Roy, S. Sreedhara, Modelling of methanol and H 2/CO bluff-body flames using RANS based turbulence models with conditional moment closure model, Applied Thermal Engineering, 93 (2016) 561-570.

[87] K.-L. Pan, C.-C. Li, W.-C. Juan, J.-T. Yang, Low-frequency oscillation of a non-premixed flame on a bluff-body burner, Combustion science and technology, 181 (2009) 1217-1230.

[88] X. Gu, S. Zang, B. Ge, Effect on flow field characteristics in methane–air non-premixed flame with steam addition, Experiments in fluids, 41 (2006) 829-837.

[89] R.-H. Chen, J.F. DRISCOLL, J. Kelly, M. Namazian, R. Schefer, A comparison of bluff-body and swirl-stabilized flames, Combustion science and technology, 71 (1990) 197-217.

[90] A.K. Gupta, D.G. Lilley, N. Syred, Swirl flows, Tunbridge Wells, Kent, England, Abacus Press, 1984, 488 p., (1984).

[91] A. Mestre, A. Benoit, Combustion in swirling flow, in: Symposium (International) on Combustion, Vol. 14, Elsevier, 1973, pp. 719-725.

[92] P.A. Kalt, Y.M. Al-Abdell, A.R. Masri, R.S. Barlow, Swirling turbulent non-premixed flames of methane: flow field and compositional structure, Proceedings of the Combustion Institute, 29 (2002) 1913-1919.

[93] Y.M. Al-Abdeli, A.R. Masri, Stability characteristics and flowfields of turbulent non-premixed swirling flames, Combustion Theory and Modelling, 7 (2003) 731-766.

[94] Y.M. Al-Abdeli, A.R. Masri, Recirculation and flowfield regimes of unconfined non-reacting swirling flows, Experimental Thermal and Fluid Science, 27 (2003) 655-665.

[95] A.R. Masri, P.A. Kalt, R.S. Barlow, The compositional structure of swirl-stabilised turbulent nonpremixed flames, Combustion and flame, 137 (2004) 1-37.

[96] Y.M. Al-Abdeli, A.R. Masri, G.R. Marquez, S.H. Starner, Time-varying behaviour of turbulent swirling nonpremixed flames, Combustion and flame, 146 (2006) 200-214.

[97] Y.M. AL-ABDELI*, A.R. Masri, Turbulent swirling natural gas flames: stability characteristics, unsteady behavior and vortex breakdown, Combustion science and technology, 179 (2007) 207-225.

[98] A. Masri, P. Kalt, Y. Al-Abdeli, R. Barlow, Turbulence–chemistry interactions in non-premixed swirling flames, Combustion Theory and Modelling, 11 (2007) 653-673.

[99] W. Malalasekera, K. Ranga-Dinesh, S.S. Ibrahim, A.R. Masri, LES of recirculation and vortex breakdown in swirling flames, Combustion science and technology, 180 (2008) 809-832.

[100] B. Ge, S.-S. Zang, Experimental study on the interactions for bluff-body and swirl in stabilized flame process, Journal of Thermal Science, 21 (2012) 88-96.

[101] B. Kashir, S. Tabejamaat, N. Jalalatian, A numerical study on combustion characteristics of blended methane-hydrogen bluff-body stabilized swirl diffusion flames, International Journal of Hydrogen Energy, 40 (2015) 6243-6258.

[102] K.R. Dinesh, K.W. Jenkins, A. Savill, M. Kirkpatrick, Influence of Bluff-body and Swirl on Mixing and Intermittency of Jets, Engineering Applications of Computational Fluid Mechanics, 4 (2010) 374-386.

[103] D. LaVision, 8.1 Software, Product Manual, 1003001.

[104] Dantec, Measurement Principles of PIV https://www.dantecdynamics.com/measurement-principles-of-piv, (2015).

[105] A. Kundu, Combustion Characteristics of a Swirl Dry Low Emission Burner Concept for Gas Turbine Application: Experiments and Simulations, (2016).

[106] M. Lauer, T. Sattelmayer, On the utilization of OH chemiluminescence as a measure for local heat release in turbulent flames, (2011).

[107] J.G. Lee, E. Gonzalez, D.A. Santavicca, On the applicability of chemiluminescence to the estimation of unsteady heat-release during unstable combustion in lean premixed combustor, AIAA Paper, 3575 (2005).

[108] A.J. De Rosa, S.J. Peluso, B.D. Quay, D.A. Santavicca, The Effect of Confinement on the Structure and Dynamic Response of Lean-Premixed, Swirl-Stabilized Flames, Journal of Engineering for Gas Turbines and Power, 138 (2016) 061507.

[109] B. Schuermans, V. Bellucci, F. Guethe, F. Meili, P. Flohr, C.O. Paschereit, A detailed analysis of thermoacoustic interaction mechanisms in a turbulent premixed flame, in: ASME Turbo Expo 2004: Power for Land, Sea, and Air, American Society of Mechanical Engineers, 2004, pp. 539-551.

[110] L.M. Smith, D.R. Keefer, S. Sudharsanan, Abel inversion using transform techniques, Journal of Quantitative Spectroscopy and Radiative Transfer, 39 (1988) 367-373.

[111] LIF, Division of Combustion Physics, LTH, Lund University, http://www.forbrf.lth.se/english/research/measurement-methods/laser-induced-fluorescence-lif/, in, 2017.

[112] C. Brackmann, J. Nygren, X. Bai, Z. Li, H. Bladh, B. Axelsson, I. Denbratt, L. Koopmans, P.-E. Bengtsson, M. Aldén, Laser-induced fluorescence of formaldehyde in combustion using third harmonic Nd: YAG laser excitation, Spectrochimica Acta Part A: Molecular and Biomolecular Spectroscopy, 59 (2003) 3347-3356.

[113] Z. Yang, X. Li, Z. Feng, L. Chen, Influence of mixing model constant on local extinction effects and temperature prediction in LES for non-premixed swirling diffusion flames, Applied Thermal Engineering, 103 (2016) 243-251.

[114] S.B. Pope, Turbulent flows, in, IOP Publishing, 2001.

[115] ANSYS FLUENT, 15-Theory Guide, ANSYS, Inc., Canonsburg, PA, (2013).

[116] M.L. Shur, P.R. Spalart, M.K. Strelets, A.K. Travin, A hybrid RANS-LES approach with delayed-DES and wall-modelled LES capabilities, International Journal of Heat and Fluid Flow, 29 (2008) 1638-1649.

[117] X. Liu, A. Elbaz, C. Gong, X. Bai, H. Zheng, W. Roberts, Effect of burner geometry on swirl stabilized methane/air flames: A joint LES/OH-PLIF/PIV study, Fuel, 207 (2017) 533-546.

[118] A. Mardani, S. Tabejamaat, Effect of hydrogen on hydrogen–methane turbulent non-premixed flame under MILD condition, International Journal of Hydrogen Energy, 35 (2010) 11324-11331.

[119] C.D. Pierce, P. Moin, Progress-variable approach for large-eddy simulation of non-premixed turbulent combustion, Journal of Fluid Mechanics, 504 (2004) 73-97.

[120] M. Frenklach, H. Wang, C. Yu, M. Goldenberg, C. Bowman, R. Hanson, D. Davidson, E. Chang, G. Smith, D. Golden, GRI-Mech 1.2, 1995, in, 2015.

[121] N. Peters, Turbulent combustion, Cambridge university press, 2000.

[122] S.B. Pope, PDF methods for turbulent reactive flows, Progress in Energy and Combustion Science, 11 (1985) 119-192.

[123] C. GONG, Numerical Studies of Turbulent Combustion under Diesel Engine Related Conditions, (2016).

[124] D. Haworth, Progress in probability density function methods for turbulent reacting flows, Progress in Energy and Combustion Science, 36 (2010) 168-259.

[125] W. Jones, V. Prasad, Large Eddy Simulation of the Sandia Flame Series (D–F) using the Eulerian stochastic field method, Combustion and flame, 157 (2010) 1621-1636.

[126] M.D. Smooke, V. Giovangigli, Premixed and nonpremixed test problem results, in: Reduced kinetic mechanisms and asymptotic approximations for methane-air flames, Springer, 1991, pp. 29-47.

[127] G.P. Smith, D.M. Golden, M. Frenklach, N.W. Moriarty, B. Eiteneer, M. Goldenberg, C.T. Bowman, R.K. Hanson, S. Song, W.J. Gardiner, GRI 3.0, Gas Research Institute, Chicago, IL, http://www. me. berkeley. edu/gri_mech, (2000).

[128] OpenFOAM, webpage: http://openfoam.com/, (2017).

[129] P. Sayad, A. Schönborn, J. Klingmann, Experimental investigations of the lean blowout limit of different syngas mixtures in an atmospheric, premixed, variable-swirl burner, Energy & Fuels, 27 (2013) 2783-2793.

[130] S. Kheirkhah, Ö.L. Gülder, G. Maurice, F. Halter, I. Gökalp, On periodic behavior of weakly turbulent premixed flame corrugations, Combustion and flame, 168 (2016) 147-165.

[131] Y. Tong, M. Li, M. Thern, J. Klingmann, W. Weng, S. Chen, Z. Li, Experimental Investigation on Effects of Central Air Jet on the Bluff-body Stabilized Premixed Methane-air Flame, Energy Procedia, 107 (2017) 23-32.

Appended publications

Paper I

Proceedings of ASME 2016 Turbo Expo: Turbomachinery Technical Conference and Exposition
GT2016
July 13-17, 2016, Seoul, South Korea

Revised Paper

GT2016-57165

INFLUENCE OF COMBUSTOR GEOMETRY ON SWIRL STABLIZED PREMIXED METHANE-AIR FLAME

Yiheng Tong
Department of Energy Sciences, Lund University
Lund, Sweden

Mao Li
Department of Energy Sciences, Lund University
Lund, Sweden

Jens Klingmann
Department of Energy Sciences, Lund University
Lund, Sweden

ABSTRACT

Flame structures, blowout limits and emissions of swirl-stabilized premixed methane-air flames were studied experimentally in a small atmospheric combustor rig. Combustion sections with rectangular cross section (*30mm* by *40mm*) and circular cross section (inner diameter = *39mm*) were used to investigate effects of combustor geometry on the flame's performance. Flame structures and instabilities were obtained from CH* chemiluminescence captured by a high speed intensified CMOS camera. Maps of flame blowout limits (Φ_{BO}) versus total mass flow rates ($\dot{m} = 70 \sim 130$ standard liter per minute, *SLPM*) were obtained with the combustor inlet flow temperature (T_{in}) kept at $T_{in} = 397 \pm 5K$ and a flow swirl number of $S = 0.6$. Emission data of mole fraction of CO in the exhaust gas versus equivalence ratio was obtained under the conditions of $T_{in} = 293 \pm 5K$ and $S = 0.66$. It is found that the flame became longer and more unstable with decreasing equivalence ratio or increasing total mass flow rates. A strong high-amplitude and low-frequency oscillation was found to be the reason for the flame blowout. A possible reason for flame instability and blowout is presented in the paper. Within the parameters investigated in this study, the equivalence ratio had the strongest impact on flame stabilities and CO emission. Both in the rectangular and circular combustors, when the flame length increased to a critical value (L_{IBO}, which was approximately the same for these two combustors), flame could not be stabilized anymore and blowout occurred. Compared with the rectangular combustor, the circular one had lower blowout limits and was better in stabilizing the flame. Combustor geometry did not significantly affect CO emission in the current study.

INTRODUCTION

In the design process of gas turbine combustors, many requirements have to be fulfilled: combustion stability has to be ensured (particularly in lean premixed combustion cases), emission targets met, etc. Often Computational Fluid Dynamics (CFD) is used in the design process, but in most cases, physical experiments are also required to ensure the design. These experiments may range from conventional measurements such as emission measurements and thermocouples, to more advanced non-intrusive laser based optical measurements, such as Planar Laser Induced Fluorescence (PLIF) or Particle Image Velocimetry (PIV). The latter have the advantage that they provide physical understanding of the burner's behavior at different operating conditions without disturbing the flame structures. Also they provide validation of results from CFD. However, they require adaptation of the experimental setup to measurement techniques. Those laser based diagnostic methods also require optical access and in most cases simplification of the burner/combustor geometry. An often used and particular simplification of geometry is the exclusion of curved walls. The curved combustor walls are found in almost all commercial gas turbines. A circular or annular combustor is simply replaced by combustor with square or rectangular cross section [1-6], which minimizes measuring problems, such as unwanted reflections from lasers, distortion of images, etc.

So, there is currently significant interest in understanding the flame structures and combustion instabilities caused by combustor geometry. It has been observed in experimental research that in a swirl stabilized combustion chamber, flame structures would change with the modification of fuel-air

mixture flow rates, reactant composition, injection temperature or pressure, heat transfer to the burner or the combustion chamber wall and the burner exit geometry. (see e.g., studies in [1, 2, 7, 8]). The change of flame structures would determine combustor performance especially in respects of pollutant emissions, uniformity of the temperature field in the outlet of the combustor, heat load and its spatial distribution to the combustor walls and dynamic instabilities [1, 9-11]. It is thus important to study the effects of combustor geometry and the interaction of flame and combustor wall on flame structures and the corresponding combustor performance.

Rosa et al. [12] investigated the effects of cylindrical single-nozzle swirl-stabilized combustor's diameter on flame structures and its dynamic response. It was concluded that the distribution of heat release rate from the flame and the flow field were altered as the combustor diameter was changed. Fu et al. [13] studied the effect of the geometry of a non-reacting rectangular combustor on the swirling flow of a counter-rotating swirling cup using a two component Laser Doppler Velocimetry (LDV). It was found that the flow structures, including location, size and strength of the outer and inner recirculation zones and the corresponding shear layers are strongly affected by the size of the combustor. Orbay et al. [14] and Wu [15] also found that combustor geometry and the outlet geometrical contraction of the combustor had significant effects on both the non-reacting and reacting flow fields. The production of turbulence near the center line of the combustor could be enhanced by heat release from the combustion. While heat release would not change the fundamental vortex breakdown structures in the flow field [14]. By studying turbulent flames in both highly and less confined swirl-stabilized square combustors, Hauser et al. [16] reported that flame transfer function was altered by changes in the time delays together with the variance of flame shape in different confinement cases. Some other studies about the effects of combustor diameter or lateral confinement on laminar flame could be found in studies [17] and [18].

In a gas turbine, in order to get a stable flame, usually a swirling flow at the burner exit is generated. There are two common methods used to generate swirling flow: tangential injection of fuel/air mixture or swirling guiding vane. In some industrial gas turbine combustors, the cross section area of the combustor is larger than that at the burner exit. In some practical devices, a corner or outer recirculation zone is generated in the corner of the combustor dome and the side walls; while the center or inner recirculation zone is formed due to the vortex breakdown when the flow swirl number is higher than a critical value. Different recirculation zones and the corresponding shear layers in a swirl-stabilized combustor are shown in Fig. 1. The interaction between the inner and outer recirculation zones will dominate the flame shape, flame length, emissions, flame blowout features and even the stability characteristics [14, 19]. Experiments about flame shapes (V shape and M shape), their interactions with combustor walls and the reasons for the alternation between different flame shapes were carried out by Guiberti et al. [1, 2]. Also in a swirl-stabilized combustor, two distinct flame blowout phases were captured: flame blowout due to instability and lean blowout (LBO) [19]. The behavior of different blowout phases were caused by the presence of the inner/outer recirculation zones and the fuel composition.

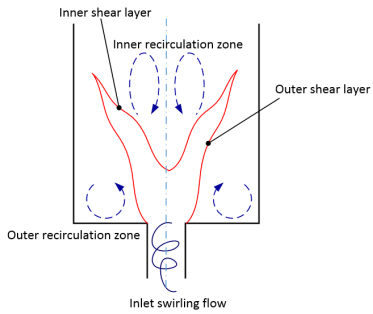

Fig. 1 Schematic of flow structures in a swirl-stabilized combustor (adapted from [1])

Flame behaves corresponding to the interaction of the inner and outer recirculation zones with the combustor walls in different combustor geometries. So the combustor geometry would affect the flow structure and the combustion stability characteristics. But the differences of flame stabilization mechanisms in swirl stabilized rectangular and circular combustors are not clear and need to be further studied. Both experimental and numerical data about the comparison of turbulent flame structures and combustion stability in rectangular and circular combustors is limited. In the present paper, CH* chemiluminescence and emission of CO were captured to investigate the flame behavior in a small atmospheric optical combustor with a rectangular and a circular cross section. Blow out limits for different combustor geometries were studied as well.

EXPERIMENTAL APPROACH AND METHOD

The burner and combustors

The experimental setup used in the present study was a variable-swirl burner and two combustors with circular and rectangular cross-section. The burner and the circular combustor are shown in Fig. 2 and Fig. 3. The combustion chamber with a circular cross section was an optical quartz tube, with inner diameter d_{in} = *39 mm*, outer diameter d_{out} = *42 mm* and length *l=120 mm*. While the rectangular combustor had the cross section dimension of *30 mm* × *40 mm* and the combustor length was *l=120 mm* as well. The cross sectional area for the circular and rectangular combustors were *1194.59 mm*^{2} and *1200 mm*^{2} respectively. The rectangular combustor was enclosed by four optical quartz windows held by a metal frame. The mixing tube, shown in Fig. 3, had an inner diameter of *15 mm* and length of *30 mm*. The swirl mixer was used to generate swirling flow by combining axial and tangential air flows as shown in Fig. 3. The

swirl mixer was located directly upstream of the mixing tube. Methane was premixed with air in the tangential flow before getting into the mixing tube. A small amount of air from the axial air inlet was also mixed into the flow in the case of $S = 0.60$. The tangential flow inlets were four rectangular channels in the tangential direction with width of *3 mm* and height of *10 mm* as shown in Fig. 3.

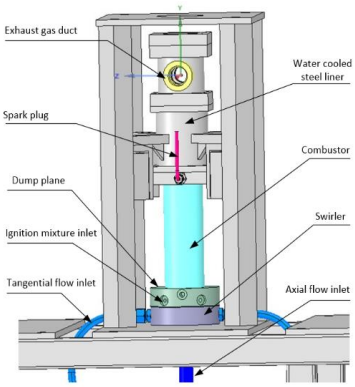

Fig. 2 Schematic of variable-swirl burner with optically accessible circular combustor and exhaust gas duct

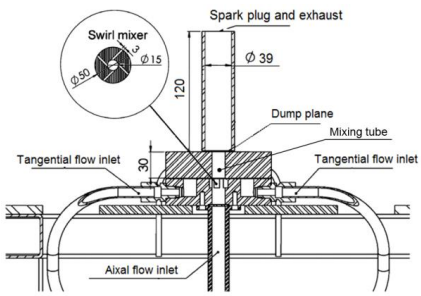

Fig. 3 Cross section of variable-swirl burner and the circular combustor. (The spark plug and exhaust gas duct are not shown)

This burner has the potential to vary the swirl number by changing the proportions of the axial and tangential mass flow rates. In this paper, two swirl number cases ($S=0.6$ and $S=0.66$) were studied. Axial/tangential air flows and the fuel flow were metered individually, using three laminar-flow differential-pressure mass-flow meters (Alicat MCR250). A feedback-controlled air heater (Sylvania Sureheat Jet) was used to heat up the tangential air flow and then mixed with cold axial air flow in the swirl mixer. Air flow temperature (without combustion) at the exit of the burner, captured using a K-type temperature sensor, was treated as the inlet flow temperature (T_{in}) for experimental cases. All test conditions for the rectangular and circular combustors are listed below in Table 1. Here the total mass flow ($\dot{m}$) is defined as the sum of all flows, air and fuel, at $\Phi = 0.7$. All experimental cases were conducted at atmospheric pressure.

Table 1. Test conditions

T_{in} (K)	$\dot{m}(SLPM)$	S
293±5	94	0.66
397±5	70 / 90 / 110 / 130	0.6

Swirl number

As mentioned above, swirl number (S) at the burner exit was varied by changing the ratio of tangential to axial momentum of the flow through the swirl mixer. For a given ratio of tangential to axial momentum of the flow, S can be calculated as [20]:

$$S = \frac{M_t}{RM_a} \tag{1}$$

where $R=7.5$ *mm* is the radius of the exit of the swirl mixer in the present setup, M_t is the axial flux of the tangential momentum, and M_a is the axial flux of the axial momentum. M_t and M_a could be calculated based on Eq (2) and (3) respectively:

$$M_t = 2\pi\int_0^R \rho w u r^2 dr \tag{2}$$

$$M_a = 2\pi\int_0^R \rho u^2 r dr + \int_0^R pr dr \tag{3}$$

where ρ is the density of the incoming flow for the combustor at the exit of the burner, u is the local axial velocity, w is the local tangential velocity, r is the local radius and p is the local static pressure at the burner exit. In some definitions of swirl number, as the one used in this work, the pressure term in Eq (3) is often neglected. Here in the current study, S was calculated based the ratios of axial to tangential momentum of the flow and an empirical relation map obtained using Laser Doppler Anemometry (LDA) measurements 1 *mm* above the dump plane at the same test facility in [21]. A more detailed description of the LDA measurements together with the tangential and axial velocity profiles obtained at different proportions of tangential and axial flows could be found in [21].

Determination of flame blowout limits

To start the series of experiments, the main flame was firstly stabilized by the pilot flame, which was ignited by the spark, as shown in Fig. 2. Then increased the main fuel flow till Φ got high enough to sustain a stable flame and stopped the pilot. After that, slowly increased the fuel flow rate by steps of 0.1 *SLPM* till $\Phi = 0.7$. Flame blowout limits for cases with a specific $\dot{m}$ and S were determined by gradually decreasing Φ from $\Phi = 0.7$ until flame blowout occurred. The decreasing of equivalence ratio was achieved by reducing the fuel mass flow rate by steps of 0.1 *SLPM*. During this procedure, both axial and tangential air mass

flow rates, air flow inlet temperature were kept constant so the flow swirl number was kept approximately constant at the same time. At each step of varying fuel flow rate, the fuel flow was kept constant for at least 2 minutes in order to achieve a thermal equilibrium. In order to avoid systematic errors deriving from the order in which the experiments were carried out, all experiments were carried out in a randomized order among different test conditions (swirl number and total mass flow rates). The flame blowout limits data presented here in this paper corresponds to the average of the values obtained in the repeated experiments.

Image analysis method

A high speed CMOS camera (Vision Research Phantom V 7.1) coupled with an image intensifier (Hamamatsu C4598), a 430 ± 5 *nm* band-pass filter and a phosphate glass lens (UV-Nikkor 105*mm*, *f*/4.5) was used to photograph CH* chemiluminescence around 431*nm* from the flame. A time series of 1450 images were obtained at a recording rate of 2000 frames per second (*fps*). In order to resolve the time-varying flame structures, the exposure time of the camera was set to $4\mu s$ with image spatial resolution ≈ 0.220 *mm*/pixel. CH* chemiluminescence image data provide good estimates of the global distribution of heat release from the flame as well as the unstable feature of flame's center of heat release (*CoHR*) and flame length (*L*) [12]. Since this is a line-of-sight measurement in turbulent flows where the flame sheet is significantly convoluted, interpretation of the flame sheet structure is difficult [22].

To determine the flame length (*L*), CH* chemiluminescence intensity of the pixels within the image is first summed up along the lateral direction. The vertical heat release rate profile illustrates distribution of heat release along the vertical line of the combustors as demonstrated in Fig. 4. The height of flame's center of heat release (H_{CoHR}), which is also shown in Fig. 4, is the vertical location with maximum CH* chemiluminescence intensity [12]. Based on the vertical heat release rate profile, using a selected threshold for the total intensity, the flame length (*L*) could be obtained as shown in Fig. 4. In the integrated intensity profile, the threshold is approximately 8 times of the noise from the background and for all cases below 10% of the maximum integrated light intensity. The unstable feature of the flame, for example the standard deviation of H_{CoHR} and *L*, could be captured based on the unstable change of H_{CoHR} and *L* within the frames as shown in Fig. 5. In Fig. 5, it displays an example of flame with mean flame length *L* of 52.40 *mm* and mean H_{CoHR} of 21.53 *mm*, and the standard deviation for *L* is 0.423 *mm* and for H_{CoHR} is 1.38 *mm*.

A global understanding of flame structures could be obtained from statistical data composed of time averaged and root-mean-square (RMS) images of CH* chemiluminescence [12, 23]. An example of the spastically resolved oscillations of heat release in flame in the circular combustor is shown in Fig. 6. The heat release rate was calculated by correlating the heat release fluctuation at each pixel for the whole recording period. In Fig. 6, the white line simply indicates the combustor wall in the circular combustor or the combustor holder in the rectangular combustor. Inside the white line is the optical window through which chemiluminescence signal could be captured by digital camera. Vertical and lateral distance are the distance from the center of the burner exit. This RMS of CH* chemiluminescence image demonstrates information about global distribution and the strength of heat release fluctuations. The color in the RMS of CH* image is scaled to dimensionless for all cases in order to compare the differences of fluctuation strength between different cases.

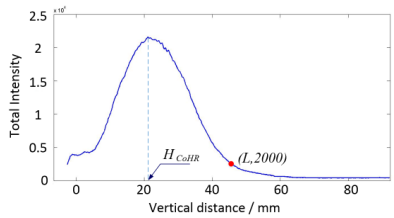

Fig. 4 An example of axial heat release rate profile with height for flame's center of heat release (H_{CoHR}) and flame length (*L*) measurement overlaid

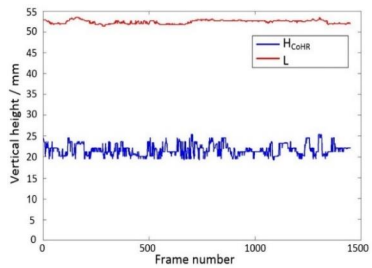

Fig. 5 An example of H_{CoHR} and *L* obtained from the same experimental condition

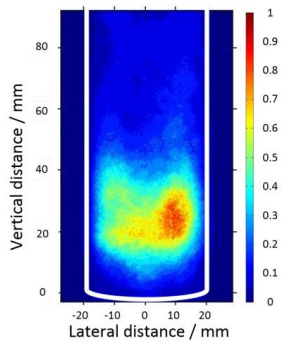

Fig. 6 An example of RMS of CH* chemiluminescence in the circular combustor

Emission measurement

The emission capturing and analysis system consisted of a Rosemount Oxynos 100 paramagnetic O_2 gas analyzer and a Rosemount Binos 100 NDIR (non-dispersive infrared photometers) CO/CO_2 gas analyzer. A combustion exhaust gas sampling probe was placed at the exhaust gas duct which is shown in Fig. 2. A linearly distributed multiple holes on the emission probe can ensure an average sampling of CO, CO_2 and O_2 along the radial/lateral direction. Water vapor in the exhaust gas was removed before entering the analyzers by cooling the exhausts to 4 ℃. The emission gas analyzers were calibrated with standard calibration gas every time before starting series of experiments. The measurements were made in stable combustion where the unburnt hydrocarbons are assumed to be negligible. Previous results showed a good agreement between the calculated equivalence ratios from emission tests and mass flow controllers and the variance from each other was within 3%. Since the mole fractions of O_2 and CO_2 in the exhaust gas were a function of Φ, here in the paper just CO emission is presented and analyzed.

RESULTS AND DISCUSSION

Flame structures and stabilities

In this part, effects of equivalence ratio and total mass flow rate on flame structures and stabilities will be discussed. Effects of equivalence ratio could be observed by the variance of L and H_{CoHR} versus Φ holding $\dot{m} = 70$ SLPM, $T_{in} = 397K$ and $S = 0.6$, as shown in Fig. 7. It could be found from Fig. 7 that both L and H_{CoHR} decrease with the increase of Φ for both the rectangular and circular combustors. When Φ gets higher than 0.64, H_{CoHR} will become approximately constant with the increasing of Φ, while L will decrease further. L is larger in the rectangular combustor than that in the circular case when Φ are the same. Near blowout (for rectangular combustor Φ_{BO} = 0.59 and for circular case Φ_{BO} = 0.54), the two geometries have similar flame length (L), which will be discussed later.

Because the use of a metallic frame in the rectangular case, chemiluminescence signal was blocked in the upstream of 12mm from the dump plane, as shown in Fig. 8. Here, it can be observed that the flame has a heart shape for all cases because of the swirling effects. For both geometries, the size of main heat release zone or flame area will shrink with increasing equivalence ratio. Heat release distributes more uniform at lower equivalence ratios. Also CH* chemiluminescence intensity gets weaker, which is to be expected from the reduced fuel flow at lower equivalence ratios. The smaller reaction zone for the flame with higher equivalence ratio is caused by the higher flame speed. Moreover, it could be observed in cases with higher equivalence ratio (e.g. $\Phi = 0.7$ in the circular combustor in Fig. 8) that flame was attached to the dump plane. The attached flame may be caused by the appearance of inner recirculation zone. That attached premixed flame was stabilized by the balancing of the local flame speed and the flow velocity in the inner recirculation zone. Compared with other cases, the case with higher equivalence ratio has higher adiabatic flame temperature and flame speed, which is easier to cause flame flashback [21] or here in the paper an attached flame.

For cases with the same equivalence ratio, the downstream edge of the flame in the circular combustor is flatter than that in the rectangular combustor. Flame in the rectangular combustor is stretched further near the combustor wall in the downstream region. Moreover, flame in the rectangular combustor seems get separated by the inner recirculation zone. Heat release rate along the radial direction is more uniform in the circular combustor. A possible reason is that the heat release zone in the rectangular combustor probably have an ellipse shape, while in the circular combustor a circular shape. Also the line-of-sight method and the different integration length between different geometries used in the paper could result in the differences in CH* distribution between the upper and lower images in Fig. 8.

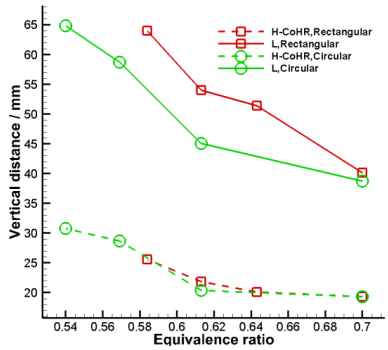

Fig. 7 Effects of Φ on L and H_{CoHR} at $\dot{m} = 70$ SLPM, $T_{in} = 397\pm5$ K and $S = 0.6$.

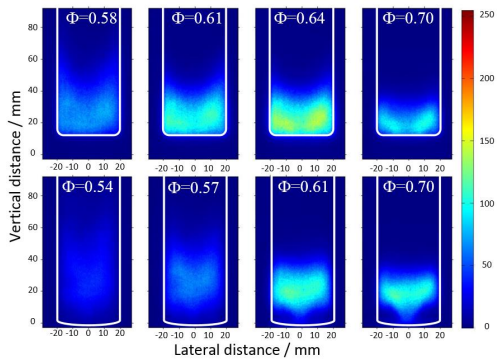

Fig. 8 Effects of Φ on averaged flame structures at $\dot{m} = 70$ SLPM, $T_{in} = 397 \pm 5$ K and $S = 0.6$ (upper images: rectangular combustor; lower images: circular combustor)

Fig. 9 shows the standard deviation of L and H_{CoHR} computed from 1450 images for the two geometries. It can be seen that the standard deviation increases as Φ varies from Φ = 0.7 toward leaner values. The increase in standard deviation is slow at the beginning but when closing towards blowout limits it becomes stronger. Standard deviation of L is similar between the two geometries. But when the equivalence ratio are the same, standard deviation of H_{CoHR} is found slightly higher for the rectangular combustor than the other one.

In the present study, flame blowout in all cases were caused by flame instability, which was also expressed in [19] as one of two distinct blowout phases. Keeping the equivalence ratio constant near blowout limits, the flame showed low-frequency, high-amplitude oscillations and blowout occurred during these oscillation cycles. In this paper, this blowout behavior is defined as flame blowout due to instability (IBO), which is differed from flame lean blowout (LBO) as the other one phase presented in [19]. Flame instability, when occurred at flame blowout process, may be caused by the interaction of unstable heat release with the appearance/disappearance of inner recirculation zone. The appearance of an inner recirculation zone indicates a region with reversal flow. The flame could be stabilized beyond the balance of local flame speed and flow velocity within flow field containing inner recirculation zone. With the alternation of heat release from the unstable combustion and its interaction with flow field, the inner recirculation zone will probably disappear. Then in order to get balanced with local flow speed, the flame in the center of the combustor will get elongated and detached from the dump plane. At the same time, heat release from the flame is varied accompanied with the changing of flow field. During this unstable process, if the tangential flow momentum gets higher, the inner recirculation zone will be formed again which will drag the flame shorter and attached to the dump plane again. The flame instability cycle is formed and fed by the energy from the combustion. When the flow instability is strong or the inner recirculation zone could not be reformed with energy from the unstable combustion process, the flame could not be stabilized anymore and blowout occurs.

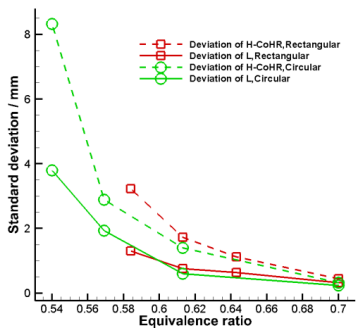

Fig. 9 Effects of Φ on standard deviation of L and H_{CoHR} at $\dot{m}$ = *70 SLPM*, T_{in} = *397 ± 5 K* and S = *0.6*

Effects of Φ on RMS of CH* chemiluminescence images at $\dot{m}$ = *70 SLPM*, T_{in} = *397 ± 5 K* and S = *0.6* are shown in Fig. 10. It can be observed that when Φ is high (e.g. Φ = 0.7), flame is stable with a small RMS of CH* spatial distribution and the RMS intensity is low. With the decrease of Φ, flame becomes unstable with a stronger oscillation near H_{CoHR} for all geometries. It should be noted that the peak RMS of CH* levels are located the same as where peak mean CH* locates near H_{CoHR}. Large fluctuations of CH* reflect the movement of the heat release as it responds to the local flow turbulence and its strong interaction with combustion. When Φ are the same for the rectangular and circular combustors, the RMS of CH* value in the rectangular combustor is higher than that in the other combustor. That indicates a stronger oscillation in the rectangular combustor.

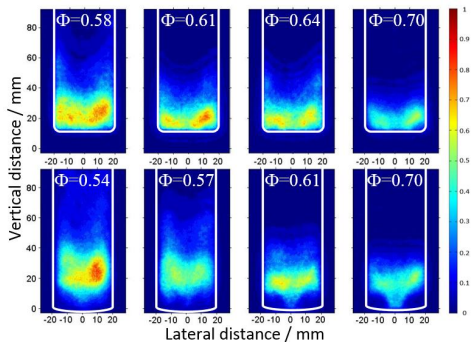

Fig. 10 Effects of Φ on RMS of CH* chemiluminescence at $\dot{m}$ = *70 SLPM*, T_{in} = *397 ± 5 K* and S = *0.6* (upper images: rectangular combustor; lower images: circular combustor)

The influence of total mass flow rate ($\dot{m}$) on L and H_{CoHR} was investigated for $\dot{m}$ ranging from *70 SLPM* to *130 SLPM* by steps of *20 SLPM*, at T_{in} = *397 ± 5 K*, S = *0.6* and Φ = *0.7*. Results of L and H_{CoHR} for different cases are shown in Fig. 11. It could be seen from Fig. 11 that, with the increase of $\dot{m}$, L will get lengthened while H_{CoHR} will keep approximately constant. With the results obtained from the effects of Φ on H_{CoHR}, it could be concluded that Φ is a more dominant parameter than $\dot{m}$ in determination of H_{CoHR}. The rectangular combustor has a larger L compared with that in the circular case. The difference of L in these two combustors increases with the growth of $\dot{m}$. More information about averaged flame structures are shown in Fig. 12.

In all cases shown in Fig. 12, at the exit of the combustors, CH* chemiluminescence intensity gets to almost zero. That means the combustor is long enough for premixed fuel-air mixture at different total mass flow rates to get to chemical equilibrium. It could be observed from Fig. 12 that with the increasing of $\dot{m}$, flame area will get enlarged and flame would be lifted off from the dump plane (which could be observed from the circular combustor cases). Increasing $\dot{m}$ will cause

increasing of the total thermal power in the combustors leading to an increase of flame area. While turbulence intensity of the flow will also get increased due to the increase of flow velocity at the burner exit. Meaning the flame reaction speed will be accelerated and in contrast result in a smaller flame area. Those two effects competed with each other. The increase of thermal power dominates and lead to the increase of flame area. The flame lift off is mainly caused by the increasing of flow velocity. When the burner exit flow velocity is faster than the local flame speed, flame will be detached to the dump plane and lifted off.

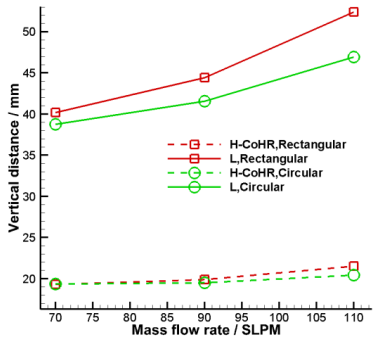

Fig. 11 Effects of $\dot{m}$ on L and H_{CoHR} at $\Phi = 0.7$, $S = 0.6$ and $T_{in} = 397 \pm 5\ K$

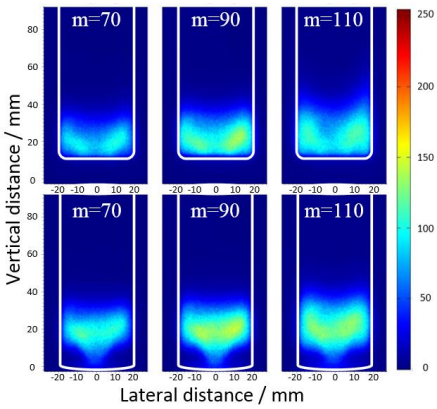

Fig. 12 Averaged flame structures for $\dot{m} = 70, 90, 110 SLPM$ with $\Phi = 0.7$, $S = 0.6$ and $T_{in} = 397 \pm 5\ K$ (upper images: rectangular combustor; lower images: circular combustor)

With the alteration of $\dot{m}$ in these two combustor geometries, H_{CoHR} keeps constant at approximately $20mm$ above the dump plane, which could be found in both Fig. 11 and Fig. 12. H_{CoHR} is the position of the maximum heat release with maximum heat radiation from the flame and it is not strongly affected by the combustor geometry.

Flame becomes unstable with the increase of total mass flow rate, which could be observed in Fig. 13 and Fig. 14. A possible reason for that behavior is the higher turbulence intensity and its stronger interaction with the increased thermal power in cases with higher mass flow rates. Moreover, the standard deviation of L keeps approximately constant for all cases. Flame with a smaller standard deviation of H_{CoHR} in the circular combustor, is more stable than that in the rectangular combustor for all experimental cases in the present study.

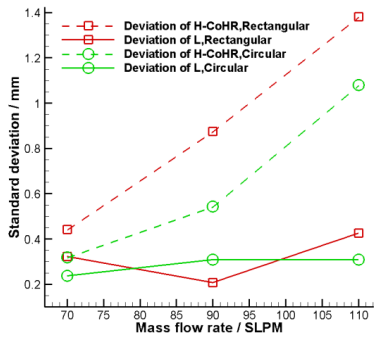

Fig. 13 Effects of $\dot{m}$ on standard deviation of L and H_{CoHR} at $\Phi = 0.7$, $S = 0.6$ and $T_{in} = 397 \pm 5\ K$

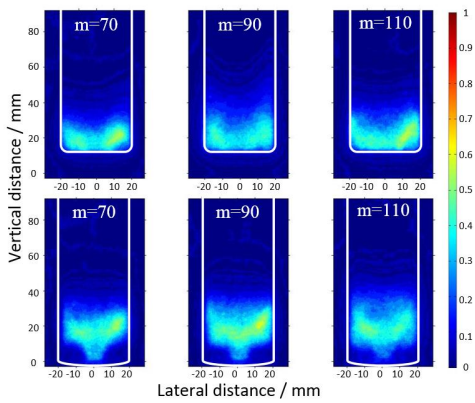

Fig. 14 RMS of CH* chemiluminescence for $\dot{m} = 70, 90, 110 SLPM$ with $\Phi = 0.7$, $S = 0.6$ and $T_{in} = 397 \pm 5\ K$ (upper images: rectangular combustor; lower images: circular combustor)

As shown in Fig. 14, intensity of RMS of CH* does not change significantly with the variance of $\dot{m}$. Compared RMS of CH* chemiluminescence image results from Fig. 10 and Fig. 14,

it could be concluded that flame instability is more depend on Φ while the effects of $\dot{m}$ could be comparable ignored for both rectangular and circular combustors.

Flame blowout limits

Data of flame blowout limits (Φ_{BO}) versus $\dot{m}$ is shown in Fig. 15 and delineates two distinct trends. For $\dot{m}$ < 110 *SLPM*, an increase of $\dot{m}$ will result in a growth of flame blowout limits. This phenomenon matches with the trend of flame lean blowout (LBO) limits presented by Schefer et al. [23] and Griebel et al. [24], although the blowout process presented in the current study differed from LBO. The increased stretch rate at higher mass flow rate conditions was argued as the reason for the trend. A possible further explanation was suggested by Sayad et al. [25] that when $\dot{m}$ and flow velocity are higher, the flame speed should be higher to consume the fuel-air mixture and prevent blowout. But the flame speed was strongly determined by Φ, meaning that higher flow velocity (or $\dot{m}$) should get balanced with higher flame speed (or Φ). So that could be a possible reason for the trend of an increase of Φ_{BO} with $\dot{m}$ when $\dot{m}$ < 110 *SLPM*.

For cases at $\dot{m}$ > 110 *SLPM*, Φ_{BO} will decrease with the further increase of $\dot{m}$. That may be caused by the higher turbulence intensity at higher $\dot{m}$ conditions. Higher turbulence intensity enhances the mixing of products with fresh mixture and the heat transfer process in the combustor which is helpful to stabilize the flame. More experiments about flame blowout limits with much higher total mass flow rate with detailed velocity field measurements should be done to provide further explanation.

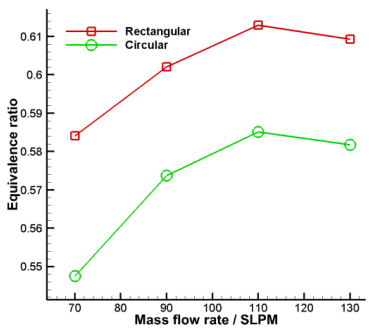

Fig. 15 Effects of $\dot{m}$ on flame blowout limits at $S = 0.6$, $T_{in} = 397 \pm 5$ *K*

It could be observed in Fig. 15 that the circular combustor has a leaner blowout limits indicating a better performance in stabilizing the flame. A possible reason for that is the difference in tangential momentum in these two geometries. At the same vertical distance, there are more tangential momentum lose in the cross section corner in the rectangular combustor than that in the circular combustor. While the local axial momentum is approximately the same in these two geometries indicating a smaller local swirl number in the rectangular combustor. Flame in the rectangular combustor with a smaller local swirl number is more unstable and easier to get blowout.

L and H_{CoHR} at $\Phi = \Phi_{BO}$ (L_{IBO} and $H_{CoHR\text{-}BO}$ respectively for short) are obtained and shown in Fig. 16. They were captured when the equivalence ratio was holding at flame blowout limits and flame preserved a strong and high-amplitude oscillation. The flame could be maintained at least 30 seconds at Φ_{BO}, which is long enough for capturing 1450 frames at the recording rate of 2000 *fps* as mentioned above.

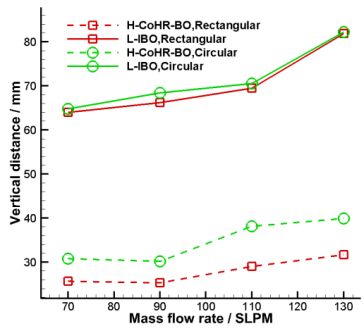

Fig. 16 Effects of $\dot{m}$ on L_{IBO} and $H_{CoHR\text{-}BO}$ at $S = 0.6$, $T_{in} = 397 \pm 5$ *K*

An increase of $\dot{m}$ results in an increase of both L_{IBO} and $H_{CoHR\text{-}BO,}$ which could be observed from Fig. 16. Moreover, when the total mass flow rates are the same for these two geometries (e.g. $\dot{m}$ = 110 *SLPM*), L_{IBO} are approximately the same. Which means the flame blowout is determined by flame length L for both the rectangular and circular combustors.

Based the effects of Φ on flame structures which has been discussed in the paper, flame blowout procedure could be concluded as:

1. At high equivalence ratio (i.e. $\Phi = 0.7$), flame is stable and short in vertical direction with a small heat release zone.
2. With the decreasing of Φ, flame becomes longer and unstable with a high-amplitude and low-frequency oscillation and a larger in size of heat release distribution.
3. Reducing Φ further, both in the rectangular and circular combustors, L gets longer to a critical value ($L_{IBO,}$ which is the same for these two geometries), then flame could not be sustained anymore and after several oscillation cycles flame blowout occurs.

Emission results

Holding $S = 0.66$, $T_{in} = 293 \pm 5$ *K*, $\dot{m}$ = 94 *SLPM*, data about effects of combustor geometry on CO emissions were obtained and illustrated in Fig. 17. What could be expected and

observed in Fig. 17 is that mole fraction of CO decreases to its minimum value at Φ = 0.66~0.7 for these two combustors. The trends of mole fraction of CO emission in the exhaust gas versus Φ could be explained as [19, 26]: A stable flame could be maintained when the equivalence ratio is sufficiently high, then CO oxidation reaction rate would increase with the reducing of Φ due to the decrease of adiabatic flame temperature and result in a lower mole fraction of CO. When Φ reaches a critical value (e.g. Φ = 0.66~0.7 in this paper), CO emission gets low to its minimum. A further decrease of Φ will result in an even lower of flame temperature and the CO oxidation reaction rate. Then the residence time required for CO oxidation reaction became longer than the residence time of the fuel-air flow in the combustor, leading to a sharp increase of mole fraction of CO in the dry exhaust gas.

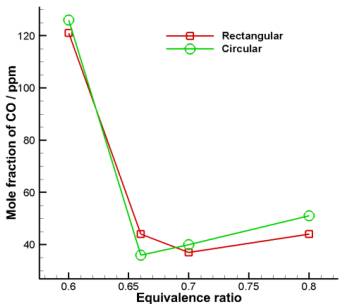

Fig. 17 Effects of equivalence ratio on mole fraction of CO emission at $S = 0.66$, $T_{in} = 293 \pm 5$ K, $\dot{m}$ = 94 SLPM

What should be noted is that when the equivalence ratio is the same, emissions of CO from rectangular and circular combustors are approximately the same with each other, meaning that the combustor geometry would not influence the CO emission from the combustion. CO emission is only determined by Φ for those two combustor geometries in the current study.

CONCLUSIONS

Experimental results about the effects of combustor geometry on flame structures, blowout limits and emissions are presented in the current study. The experiments were conducted using a variable-swirl burner together with both optical rectangular and circular combustors under atmospheric pressure conditions with atmospheric or preheated inlet temperature. In order to capture flame structures, a high speed intensified CMOS camera and the corresponding image analysis methods were adopted. CO emission data was obtained as well.

CH* chemiluminescence based flame images indicate that in overall the downstream edge of the flame front in the circular combustor is flatter than that in the rectangular combustor. The flame gets longer and more unstable with a reduction of Φ or an increase of $\dot{m}$. In the current study, compared with the rectangular combustor, the circular one is better in stabilizing the flame with leaner blowout limits (Φ_{BO}). Flame behavior and blowout procedure in these two combustors could be concluded as:

1. At high equivalence ratio, flame is short in vertical direction and stable with a small heat release zone.
2. With the decreasing of equivalence ratio, flame becomes longer and unstable with a high-amplitude oscillation and a larger heat release area.
3. Decreasing Φ further, both in the rectangular and circular combustors, L gets longer to a critical value (which is approximately the same for these two geometries) and then flame could not be sustained anymore and blowout occurs.

CO emission is not significantly affected by the combustor geometry and mainly determined by Φ. Taking the flame structures and flame stabilization performance into consideration, it is not suggested to simplify a circular combustor in most industrial cases to a rectangular one in laboratory study. More experimental and computational investigation about the flow field and its interaction with flame structures should be done to further explain different flame behaviors caused by combustor geometries presented in the present study.

ACKNOWLEDGMENTS

Authors Yiheng Tong and Mao Li are supported by scholarship from China Scholarship Council (CSC) which is gratefully acknowledged. The authors would like to thank P. Sayad and A. Schönborn for the design of the experimental setup, and Cheng Gong for helpful discussion.

REFERENCES

1. Guiberti, T. F., Durox, D., Scouflaire, P., & Schuller, T. (2015). Impact of heat loss and hydrogen enrichment on the shape of confined swirling flames. Proceedings of the Combustion Institute, 35(2), 1385-1392.
2. Guiberti, T. F., Durox, D., Zimmer, L., & Schuller, T. (2015). Analysis of topology transitions of swirl flames interacting with the combustor side wall. Combustion and Flame.
3. Stöhr, M., Boxx, I., Carter, C. D., & Meier, W. (2012). Experimental study of vortex-flame interaction in a gas turbine model combustor. Combustion and Flame, 159(8), 2636-2649.
4. Meier, W., Boxx, I., Stöhr, M., & Carter, C. D. (2010). Laser-based investigations in gas turbine model combustors. Experiments in fluids, 49(4), 865-882.
5. Weigand, P., Meier, W., Duan, X. R., Stricker, W., & Aigner, M. (2006). Investigations of swirl flames in a gas turbine model combustor: I. Flow field, structures, temperature, and species distributions. Combustion and flame, 144(1), 205-224.
6. Meier, W., Duan, X. R., & Weigand, P. (2006). Investigations of swirl flames in a gas turbine model

combustor: II. Turbulence–chemistry interactions. Combustion and Flame, 144(1), 225-236.
7. Syred, N. (2006). A review of oscillation mechanisms and the role of the precessing vortex core (PVC) in swirl combustion systems. Progress in Energy and Combustion Science, 32(2), 93-161.
8. Stopper, U., Aigner, M., Ax, H., Meier, W., Sadanandan, R., Stöhr, M., & Bonaldo, A. (2010). PIV, 2D-LIF and 1D-Raman measurements of flow field, composition and temperature in premixed gas turbine flames. Experimental Thermal and Fluid Science, 34(3), 396-403.
9. Syred, N., & Beer, J. M. (1973). Effect of combustion upon precessing vortex cores generated by swirl combustors. In International Symposium on Combustion, 14 th, University Park, Pa (p. 1973).
10. Syred, N., Gupta, A. K., & Beer, J. M. (1975, December). Temperature and density gradient changes arising with the precessing vortex core and vortex breakdown in swirl burners. In Symposium (International) on Combustion (Vol. 15, No. 1, pp. 587-597). Elsevier.
11. Li, G., & Gutmark, E. J. (2004). Experimental study of large coherent structures in a swirldump combustor. AIAA paper, 133, 2004.
12. De Rosa, A. J., Peluso, S. J., Quay, B. D., & Santavicca, D. A. (2015, June). The Effect of Confinement on the Structure and Dynamic Response of Lean-Premixed, Swirl-Stabilized Flames. In ASME Turbo Expo 2015: Turbine Technical Conference and Exposition (pp. V04AT04A017-V04AT04A017). American Society of Mechanical Engineers.
13. Fu, Y., Cai, J., Jeng, S. M., & Mongia, H. (2005, January). Confinement effects on the swirling flow of a counter-rotating swirl cup. In ASME Turbo Expo 2005: Power for Land, Sea, and Air (pp. 469-478). American Society of Mechanical Engineers.
14. Orbay, R. C., Nogenmyr, K. J., Klingmann, J., & Bai, X. S. (2013). Swirling turbulent flows in a combustion chamber with and without heat release. Fuel, 104, 133-146.
15. Wu, Y. (2013). Large Eddy Simulation of Turbulent Swirling Flows in Combustor Related Geometries (Doctoral dissertation, Lund University).
16. Hauser, M., Hirsch, C., & Sattelmayer, T. (2011, July). Influence of the confinement on the flame transfer function. In 18th International Congress on Sound and Vibration, Rio de Janeiro, Brazil, July (pp. 10-14).
17. Birbaud, A. L., Durox, D., Ducruix, S., & Candel, S. (2007). Dynamics of confined premixed flames submitted to upstream acoustic modulations. Proceedings of the Combustion Institute, 31(1), 1257-1265.
18. Cuquel, A., Durox, D., & Schuller, T. (2013). Scaling the flame transfer function of confined premixed conical flames. Proceedings of the Combustion Institute, 34(1), 1007-1014.
19. Sayad, P., Schönborn, A., & Klingmann, J. (2013). Experimental Investigations of the Lean Blowout Limit of Different Syngas Mixtures in an Atmospheric, Premixed, Variable-Swirl Burner. Energy & Fuels, 27(5), 2783-2793.
20. Syred, N., & Beer, J. M. (1974). Combustion in swirling flows: a review. Combustion and flame, 23(2), 143-201.
21. P. Sayad, A. Schönborn, M. Li, and J. Klingmann, Visualization of different flashback mechanisms for h2/ch4 mixtures in a variable-swirl burner. Journal of Engineering for Gas Turbines and Power, 2014. 137(3): p. 031507-031507.
22. R. W. Schefer (1997) Flame Sheet Imaging Using CH Chemiluminescence, Combustion Science and Technology, 126:1-6, 255-279, DOI: 10.1080/00102209708935676
23. Schefer, R. W., Wicksall, D. M., & Agrawal, A. K. (2002). Combustion of hydrogen-enriched methane in a lean premixed swirl-stabilized burner. Proceedings of the combustion institute, 29(1), 843-851.
24. Griebel, P., Boschek, E., & Jansohn, P. (2007). Lean blowout limits and NOx emissions of turbulent, lean premixed, hydrogen-enriched methane/air flames at high pressure. Journal of engineering for gas turbines and power, 129(2), 404-410.
25. Sayad, P., Schönborn, A., Clerini, D., & Klingmann, J. (2012, December). Experimental investigation of methane lean blowout limit; effects of dilution, mass flow rate and inlet temperature. In ASME 2012 Gas Turbine India Conference (pp. 815-826). American Society of Mechanical Engineers.
26. Lefebvre, A. H. Gas Turbine Combustion, 2nd ed.; Taylor and Francis Group: Philadelphia, PA, 1999; Chapter 5.

Paper II

Proceeding of the ASME 2017 Power and Energy Conference
PowerEnergy2017
June 25-30, 2017, Charlotte, North Carolina, USA

PowerEnergy2017-3064

AN EXPERIMENTAL STUDY OF EFFECTS OF CONFINEMENT RATIO ON SWIRL STABILIZED FLAME MACROSTRUCTURES

Yiheng Tong, Mao Li, Marcus Thern, Jens Klingmann
Department of Energy Sciences, LTH, Lund University
Lund, Sweden

ABSTRACT

Swirl stabilized premixed flames are common in industrial gas turbines. The flame shape in the combustor is highly related to the combustion stability and the performance of the gas turbine. In the current paper, the effects of confinement on the time averaged flame structures or flame macrostructures are studied experimentally. Experiments are carried out with swirl number S = 0.66 in two cylindrical confinements with diameters of d_1 = 39 mm and d_2 = 64 mm and confinement ratio c_1 = 0.148 and c_2 = 0.0567. All the experiments were carried out in atmospheric. CH* chemiluminescence from the flame was recorded to visualize the flame behavior. An inverse Abel image reconstruction method was employed to better distinguish the flame macrostructures. Different mechanisms forming the time averaged M shape flames are proposed and analyzed. It is found that the confinement wall plays an important role in determining the flame macrostructures. The flow structures including the inner and outer recirculation zones formed in the confinement are revealed to be the main reasons that affects different flame macrostructures. Meanwhile, the alternation of flame shapes determines the flame stability characteristics. A smaller confinement diameter forced the flame front to bend upstream into the outer recirculation zone hence forming a M shape flame. A strong noise caused by the interaction of the flame front in the outer recirculation zone with the combustor wall was observed. Another unsteady behavior of the flame in the bigger combustor, which was caused by the alternation of the flame root position inside and outside the premixing tube, is also presented. The V shape flame in the two combustors radiated weaker chemiluminescence but the main heat release zone was elongated than the M shape flame. Other operating conditions, i.e. total mass flow rate of the air flow and the equivalence ratio also affect the flame macrostructures. The flame blowout limits were also altered under different test conditions. The bigger confinement has better performance in stabilizing the flame by having lower lean blowout limits.

INTRODUCTION

Modern low emission, lean premixed industrial gas turbines commonly rely on swirling flows to stabilize and control the flame over a wide range of operating conditions. The swirl flow induces vortex breakdown and leads to recirculation of the hot burnt products to anchor the flame. The flame structures, which are highly depended on the swirling flow field, determines the flame stability characteristics, the performance of the combustor and also the pollutant emissions [1]-[3].

Flame shapes/topologies/macrostructures have been studied extensively. It was reported that the flame shape is strongly affected by fuel mixture fraction, heat transfer to the combustor wall, combustor geometry, mass flow rate, inlet temperature and other operating conditions [4]-[9]. Guiberti et al. [1] stated that there were mainly two types of flame shape: the M shape and the V shape flame, as shown in. The V shape flame was stabilized mainly in the inner shear layer as shown in Fig.1 (b) with the inner recirculation filled with burnt products. The M shape flame was formed with the reaction zones both in the inner shear layer (ISL) and outer shear layer (OSL). The location of the inner recirculation zone (IRZ) and outer recirculation zone (ORZ) and the corresponding shear layers in the swirling flow with a confinement are also illustrated in Fig.1 .

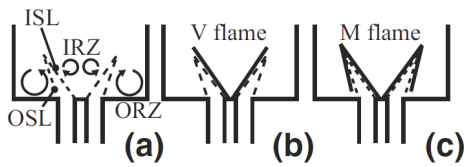

Fig.1 Schematic of a swirl jet flow field in a confinement with (b) a V shape flame (c) a M shape flame [1]

S. J. Shanbhogue et al. [9] defined the time averaged flame shape to be the flame macrostructure in their studies. They observed four flame macrostructures as the equivalence ratio was changed during their experiments. Beyond the typical V shape and M shape flames (here referred to as IRZ and ORZ flames respectively), they also observed the columnar flame that was detached from the center body and a 'bubble' flame. Soufien T. et al. [10] [11] investigated the thermos-acoustic instabilities and their link to the flame macrostructures under different operating conditions within two different confinements. A circular motion in the outer recirculation zone around the confinement centerline was revealed to be the reason for the low frequency flame instability. They also highlighted the flame instability was highly correlated with flame macrostructures. In the recent study of Soufien T. et al. [12], the sudden and intermittent ignition of reactants recirculating in the outer recirculation zone was presented as the reason leading to large fluctuations in the overall heat release and the flame instability. The fluctuations were the main consequences of the transition of flame macrostructures. Flame flashback of the V shape flame tip along the combustor side wall was suggested as the trigger for the sudden transition from the V shape flame to the M shape flame [1][5]. This was supported by the numerical computations indicating that heat losses to the burner walls favored the V-shape [7]. Chterev et al. [4] observed four different flame shapes in their experimental and numerical work. They named different flame shapes using roman numbers, such as flame Ⅰ (the columnar flame), Ⅱ (inner shear layer stabilized bubble flame), Ⅲ (inner shear layer stabilized V shape flame) and Ⅳ (both inner and outer shear layers stabilized M shape flame), in a swirl-stabilized combustor with a center body at the burner exit. Alekseenko et al. [13] studied unconfined premixed propane-air flames at different swirl numbers and observed three flame types: attached flames, quasi-tubular flames and lifted flames. Diagrams of flow Reynolds number versus equivalence ratio and flame blow-off limits for different swirl number cases were obtained as well. Malanoski et al. [14] reported the possible flow and flame structures in a swirl-stabilized combustor with different center body sizes. Based on the behavior of the flow field (whether the vortex breakdown bubble was attached to the center body or not), they separated the flame structures into two groups. They found that the recirculation zones, which were formed downstream of the center body, highly affected the flame macrostructures. However, the effects of the confinement were not considered.

The confinement ratio, which is defined as the cross section area ratio of the burner exit and the confinement, was concluded to have strong effects on both the flame structures and the performance of the combustor [8]. Fu et al. [15] measured the flow structures of a turbulent confined swirling non-reacting flow using a two component LDV system. They concluded that the size and strength of the recirculation zones were larger and stronger respectively with a larger confinement ratio. The inner recirculation zone moved upstream inside to the duct and towards the swirler with the increase of the confinement ratio. While the size of the outer recirculation zone got enlarged with the decreasing of the confinement ratio. Alexander et al [16] investigated the effects of confinement ratio on the flame macrostructures and the dynamic responds of the swirl-stabilized and lean-premixed flame. Changes in the flame macrostructures, i.e. the axial and radial distributions of the heat release rate from the flame, were observed as the confinement ratio was altered. They concluded that the main heat release zone shrunk with a decrease of confinement ratio. The interaction of the flame instability with flame structures was however not fully described. Guiberti, T. F., et al. [17] studied the flame macrostructures in the different confinements and also noted that the flame flashback in the boundary near the combustor wall triggered the flame transition from a V shape to a M shape in the case of strong flame-wall interaction. For a fixed swirl strength and a small confinement ratio, a critical Karlovitz number was shown to well predict the flame transition phenomenon. The flame they investigated was also anchored in a swirling flow with a central bluff-body.

There are also amounts of researches focusing on flame flashback. The flashback occurs when the flame propagates upstream into the premixing zone or along the boundary. Sayad, P., et al [18] summarized four mechanisms leading to flashback in a swirl stabilized flame: flashback in the boundary, flashback due to combustion induced vortex breakdown (CIVB), autoignition in the premixing zone upstream and flame propagation in the high velocity core flow. Sommerer et al. [19] also mentioned the flashback due to CIVB and boundary layer flashback as the two mechanisms in the five possibilities leading to flame flashback. Flame flashback in the boundary layer occurs when the axial velocity gradient at the wall of the upstream flow becomes lower than a critical value. That critical value is determined by the local flow velocity, the normal distance to the wall, the laminar/turbulent flame speed and the quenching distance between the flame front and the wall [18]. It is also possible to predict the boundary layer flashback based on the estimating of a Karlovitz number based on the velocity gradient at the wall and the quenching distance [20]. The CIVB flashback mechanisms has been described in the research of Konle and Sattelmayer [21]. They reported that the occurrence of CIVB flashback is strongly dependent on heat released from the combustion which pushed the inner recirculation zone upstream into the premixing zone with the flame attached to it. Sayad, P. et al. [22] described the CIVB flashback mechanism as: when the reactants were consumed by the flame front, their volume increases and their density decreased in a certain ratio because of the increased temperature. This contributed to the production of azimuthal vorticity which can alter the position of the recirculation zone and thus caused the flame to propagate from the combustor into the premixing zone upstream. Most research focus on the flashback in the flame root, i.e. the leading flame front propagating into the premixing zone in literature [18] [20] [22]. However, flashback could also occur in the flame trailing edge near the combustor wall like what was

observed in the current study and some other literatures, i.e. [1], [5], [7] and [17].

As reviewed above, the flame macrostructures determine the flame dynamics and performance of the combustor. But the flame studied previous were mainly stabilized in the swirling flow with a central rod/bluff-body. Without the central rod, the flow structures and the corresponding flame dynamics would be differently with the previous results. In the current study, flame macrostructures stabilized in the swirling flow without the central rod were investigated. Effects of confinement ratio on flame behavior are highlighted. Two different M shape flames and the corresponding mechanisms are revealed. Flame instabilities under different operating conditions with different flame structures are also presented. Lean blowout limits with different confinement ratios were obtained as well.

EXPERIMENTAL SETUP AND METHODS

Experimental setup

The variable-swirl burner utilized in the current study is shown in Fig.2 The confinement, which is an optical quartz tube, is also schematically shown. Details of the dimensions of burner employed in the current study are illustrated in Fig.3 .

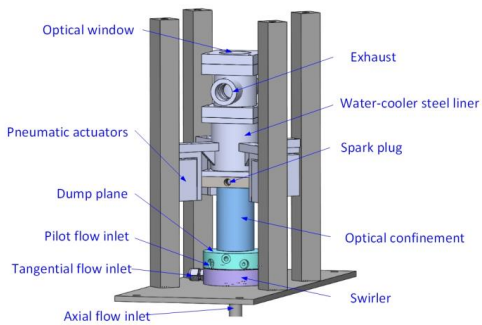

Fig.2 Schematic of the variable swirl burner with confinement

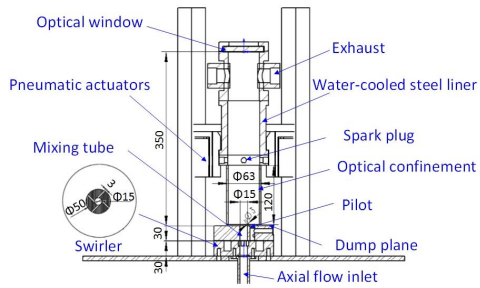

Fig.3 Cross section of the variable-swirl burner and the bigger confinement

The mixing tube (as shown in Fig.3) had an inner diameter of d_{mixing} = 3 mm and length of l_{mixing} = 30 mm. A swirler was located directly upstream of the mixing tube. There are three common ways to generate swirling flows: guiding vane and tangential entry swirler. Compared with a guiding vane swirler, the tangential entry system has better performance in the vorticity contribution to the core from the endwall boundary. The swirler here in the current study utilized the tangential flow entry to generate the swirling flow. The fuel, methane, was premixed with air in the tangential flow 240 mm upstream before getting into the swirler. The swirler had the potential to create flows with different swirl numbers by changing the momentum ratio of the axial and tangential flows. In the current study when S = 0.66, the swirler was only fed by the tangential flow. In other cases, which were not presented in this study, if $S < 0.66$, a small amount of axial flow was also mixed into the swirler. Tangential air flow and the fuel flow were metered individually, using two laminar-flow differential-pressure mass-flow meters (Alicat MCR250). The tangential flow inlets of the swirler were four rectangular channel inlets in the tangential direction with width $w = 3$ mm and height $h = 10$ mm as shown in Fig.3 . The premixing tube led into a stepped expansion, which would hereafter be referred to as the dump plane. On the dump plane, there was a small injection hole for the premixed pilot mixture. The center of the pilot hole was located 4 mm away from the axis of the burner exit and had an inner diameter of d_{pilot} = 3 mm. The pilot flame was only used to sustain the main flame during the ignition process till a stable main flame was obtained. A spark plug, which was utilized to ignite the premixed pilot flame, was mounted at the exit of the confinement. The confinement was held in place by pneumatic pressure provided by four pneumatic actuators. The pneumatic system allowed swift sealing and removal of the confinement during the experiments. The inner diameters of the confinements were d_1 = 39 mm for the smaller confinement and d_2 = 63 mm for the bigger one. Hence the confinement ratios (c) were c_1 = 0.148 and c_2 = 0.0567 respectively. The thickness of the confinement wall was 1.5mm for these two confinements. The lengths of these two confinement were the same at $l_1 = l_2$ = 120 mm.

Swirl number

As mentioned above, swirl number at the burner exit was varied by changing the momentum ratio of the tangential to axial flows through the swirler. For a given momentum ratio of the tangential to axial flows, S could be calculated as [23]:

$$S = \frac{M_t}{RM_a} \quad (1)$$

where R = 1/2 • d_{mixing} = 7.5 mm is the radius at the exit of the mixing tube in the present setup, M_t is the axial flux of the tangential momentum, and M_a is the axial flux of the axial momentum. M_t and M_a could be calculated based on Eq (2) and (3) respectively:

$$M_t = 2\pi\int_0^R \rho w u r^2 dr \quad (2)$$

$$M_a = 2\pi\int_0^R \rho u^2 r dr + \int_0^R p r dr \quad (3)$$

where ρ is the density of the incoming flow for the confinement at the exit of the burner, u is the local axial velocity, w is the local tangential velocity, r is the local radius and p is the local static pressure at the burner exit. In some definitions of swirl number, as the one used in this work, the pressure term in Eq (3) is often neglected. Here in the current study, S was calculated based the momentum ratios of the axial to tangential flows and the empirical relation map reported in the literature [24]. That empirical relation map was obtained by Laser Doppler Anemometry (LDA) measurements 1mm above the dump plane using the same test facility in [24]. A more detailed description of the LDA measurements together with the tangential and axial velocity profiles obtained at different proportions of tangential and axial flows could be found in [24].

Operating procedure

To start the series of experiments, we firstly ignited the pilot flame using the spark as shown in Fig.2 in the swirling flow. Subsequently fed the fuel to the tangential flow until a stable main flame was obtained and shut down the pilot flow. After that, we increased the tangential fuel flow rate by steps of 0.1 standard liter per minute (SLPM) or in terms of $\Delta\Phi < 0.01$ until $\Phi = 0.7$. Flame blowout limits for cases with a specific air mass flow rate were determined by gradually decreasing Φ from $\Phi = 0.7$ until flame blowout occurred. The decreasing of equivalence ratio was achieved by reducing the fuel mass flow rate by steps of 0.1 SLPM or in terms of $\Delta\Phi < 0.01$. During the ignition and test procedures, the tangential air mass flow rates were kept constant so the flow swirl number was stabilized constant at $S = 0.66$ all the time. Between each step of varying the fuel flow rate, the fuel flow was kept constant for at least 2mins in order to achieve a stabilization of the equivalence ratio around the target value and the thermal equilibrium of the burner. In order to avoid systematic errors deriving from the order in which the experiments were carried out, all experiments were carried out in a randomized order among different test conditions (confinement ratios and air mass flow rates). The flame blowout limits data presented in this paper corresponds to the average of the values obtained in the repeated experiments. The flame structures and unstable behaviors were obtained by slowly decreasing the fuel flow rate from $\Phi = 0.7$ till lean blowout, whereas different flame behaviors could be observed during the opposite operating procedure (increasing the fuel flow rates from near lean blowout to $\Phi = 0.7$) and they are not presented in this paper. The air mass flows of the experiments in the current study were altered between $\dot{m} = 90$, 110, 130 and 150 SLPM. All the experiments were operated under atmosphere conditions with both the inlet temperature of the air and fuel at room temperature.

Image analysis methods

A Nikon D70 camera with a 430 ± 10 nm band-pass filter was adopted to capture CH* chemiluminescence from the flame. The camera exposure time was set to $\Delta\tau = 0.77$ *s* and the spatial resolution for the image was $d_p \approx 81.97$ μm/pixel. Three images under the same operating condition were recorded and averaged before doing the further image analysis. This long exposure time (compared to any turbulent fluctuations) and averaging of the raw images has the effect of averaging out the instantaneous winkles of the flame front thus yielding the equivalent of mean-flame structures or named as the flame macrostructures [9]. From the scale image without flame, the center of the burner exit could be obtained. It was set as the origin point (0, 0) to determine the flame structures in the image analysis process. Since CH* chemiluminescence intensity peaks at a light wavelength of 431 nm, only the blue layer in the raw RGB format images was used in the image analysis process while the red and green layers were deleted as noises (the same as in the literature [1]). The raw image obtained in the line-of-sight method was deconvolved using the inverse Abel image reconstruction method developed based on in-house developed Matlab code. Since the confinements were cylindrical, an assumption of axisymmetric was adopted in the image reconstruction analysis procedure. The axisymmetric feather was fulfilled by averaging the left and the right parts of the burner axis on the averaged raw images. The inverse Abel reconstructed image better marked the location of the flame brush in the plane crossing the confinement's centerline and perpendicular to the camera.

RESULTS AND DISCUSSION

Flame structures and dynamics

In the bigger confinement, with the decreasing of the flow equivalence ratio, the averaged flame shape changed from a M shape to a V shape. Moreover, two types of M shape flames, with the vortex breakdown propagated inside or outside the premixing tube, were observed in the bigger confinement. They are shown in Fig.4 and schematically illustrated in Fig.5 . The white line in Fig.4 schematically shows the optical confinement wall. When the equivalence ratio was sufficiently high, i.e. $\Phi = 0.7$, the flame speed was also high leading to flame flashback upstream into the premixing zone. The combustion induced vortex breakdown (CIVB) forced the flame propagating into the premixing tube. When the equivalence ratio decreased to i.e. $\Phi < 0.67$ as shown in Fig.4 , the flame root propagated downstream outside of the premixing tube indicating the flow breakdown was pushed downstream outside of the premixing zone as well. That was caused by the heat released from the flame got reduced with lowering the equivalence ratio. The flow volume increased and the density decreased in a less ratio compared with cases having higher equivalence ratio. Then the azimuthal vorticity got weaker and the recirculation zone was pushed outside the premixing tube.

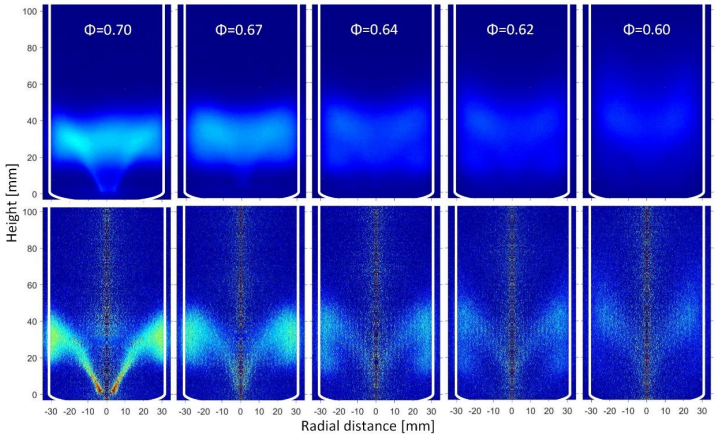

Fig.4 The averaged (upper) and Abel reconstructed (lower) images of flame structures with $\dot{m} = 130$ SLPM in the bigger confinement

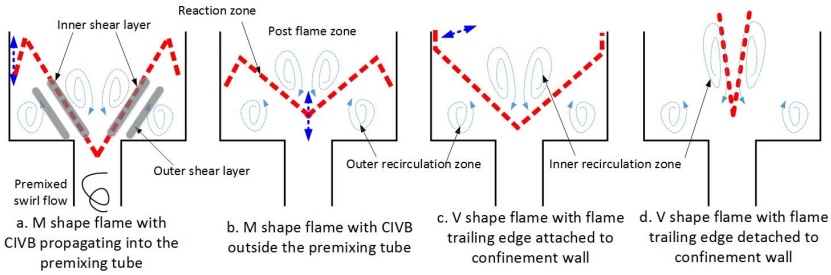

Fig.5 Illustration of different flame shapes and flame dynamics

As shown in Fig.5 those two types of M shape flames, no matter with the vortex breakdown propagated inside or outside the premixing tube, are different with the mechanisms presented in Fig.1 from the literature [5]. In the current study, the outer recirculation zone was filled with fresh fuel-air reactants whereas in Fig.1 the outer recirculation zone was full of combustion products. The flame front did not reach to or get affected by the combustor wall in the literature [5]. However, in the current paper, near the combustor wall the flame flashed back into the outer recirculation zone forming the M shape flame. The flashback mechanism near the combustor wall is believed to be the boundary flashback as mentioned in the literature [15]. In the boundary layer formed by the combustor wall, the flow velocity is lower than the local flame speed then the flame tends to flashback into the outer recirculation zone. The lifted M shape flame, with the vortex breakdown taking place outside the premixing tube, was not observed in the literatures reviewed in the introduction part except in the experiments in literature [1] using a burner without a central rod/bluff-body in the center. The lifted M shape flame in the current study was stabilized by the balance of the local turbulent flame speed and the flow velocity. The reactants were mainly combusted in the inner shear layer as shown in Fig.5 b. Whereas in some other burner geometries with a central rod/bluff-body (as those employed in [1],[4],[5],[11] and [12]), the flow structures were altered with a vortex formed downstream of the central rod/bluff-body to stabilize the flame. Hence the lifted M shape flame is hard to be observed in the burner with a central bluff-body. Moreover, the CIVB in the premixing tube is rarely reported in that type of burner either.

Meanwhile, during the alternation of flame macrostructures from the M shape flame with CIVB to the lifted M shape flame, a low frequency oscillation was also observed. That flame instability was possibly caused by the changing of the flame macrostructures together with the flow structures. The vortex propagated unstably inwards and outwards of the premixing tube leaded to this oscillation, as schematically shown using the blue double-arrows in Fig.5 b. Further decreasing the fuel flow

rate, the oscillation got disappeared with the flame stabilized with a lifted M shape. The height of flame root in the radial center then fluctuated slightly which was generated by flow turbulence. Decreasing the equivalence ratio further, the CH* chemiluminescence from the flame got weaker and the V shape flame appeared as shown in Fig.4 (when $\Phi = 0.6$) and Fig.5 c. The flame trailing edge was then attached to the confinement wall but pointed toward the confinement exit. During that alteration of flame macrostructures, a high amplitude and lower frequency oscillation showed up as well. This oscillation was caused by the unsteady behavior of the flame trailing edge flashing back into the outer recirculation zone or propagating along the wall to the confinement exit as shown in Fig.5 a with the blue double-arrows line. Meanwhile, the flame might even blowout because of this strong oscillation when $\dot{m}$ = 90 SLPM. If the flame could be sustained with this oscillation, further decreasing the fuel flow rate, the flame became stable again with a V shape. The flame trailing edge then got detached from the confinement wall as illustrated in Fig.5 d with the flame became even weaker and was hardly visualized by human eyes. This alternation of flame shapes from the wall-attached to the wall-detached V shape flame was smooth and no strong oscillation appeared. Meanwhile the flame got elongated and sometimes even with the flame tip propagating into the exhaust tube. The same weak flame structure was also observed in the literature [9] with the flame stabilized in the inner recirculation zone before blowing out. Then a further slightly decreasing of fuel flow rate caused the flame blew out peacefully. These two blowout behaviors, the blowouts due to strong oscillation and lean blowout, were also observed and described in the literature [18].

Fig.6 shows the time averaged and inverse Abel reconstructed flame structures within the smaller confinement holding the air flow rate of $\dot{m}$ = 130 SLPM as well. The same as in the bigger confinement, the flame with high equivalence ratio, i.e. Φ = 0.7, shows the M shape macrostructures with CIVB. Similarly, with the reduction of the equivalence ratio, the flame transformed to a V shape. But during that procedure, the lifted M shape flame was not observed within the smaller confinement. Instead, the V shape flame with CIVB showed up as illustrated in Fig.6 During the flame shape transition process, a higher frequency oscillation with a strong noise was observed. A potential candidate for this flame instability is the alternation of the flame trailing edge pointing directions: towards the dump plane or the confinement exit (as schematically shown using the blue double-arrows in Fig.5 a), or the local quenching and reignition of the flame in the outer recirculation zone [12]. The local quenching of the flame in the outer recirculation zone changed the flame macrostructures from a M shape to a V shape hence caused flame dynamics. The local high strain rate at the outer shear layer, the heat released to the dump plane and the combustor wall, the small size of the outer recirculation zone might contribute to the local flame quenching. Another possible reason which might cause this high frequency flame instability is the swirling motion of the flame in the outer recirculation zone around the burner exit as mentioned in [10] and [11]. More detailed LIF experiments or simulation work will be done to get deeper insight into this phenomenon.

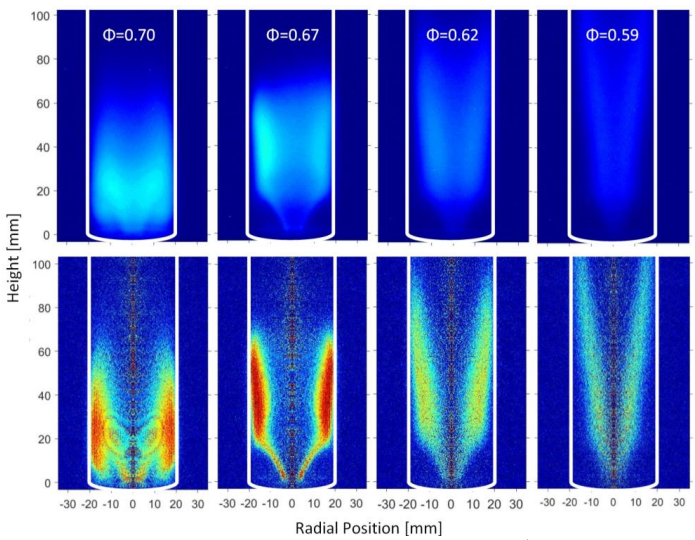

Fig.6 The averaged (upper) and Abel reconstruted (lower) images of flame strcutures with $\dot{m}$ = 130 SLPM in the smaller confinement

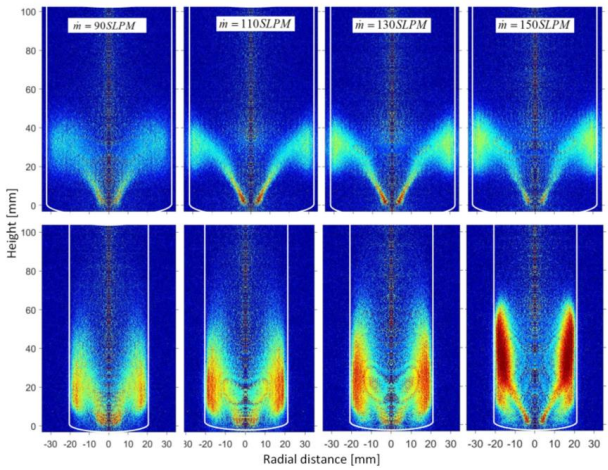

Fig.7 Inver Abel reconstructed flame strucutrues in the bigger (upper) and smaller (blower) confinements holding $\Phi = 0.7$

When $\Phi = 0.67$, the appearance of the V shape flame with CIVB in the smaller confinement rather than the lifted M shape flame in the bigger one, indicates the stronger swirling effect in the smaller confinement and the propagating of CIVB into the premixing tube. As reported in the literature [15], the smaller confinement produced a larger and stronger inner recirculation zone together with a smaller and weaker outer recirculation zone compared with that in the bigger confinement. Moreover, the stronger strain rate in the outer shear layer, which was caused by the higher bulk flow velocity in the confinement with smaller cross section area, should be found in the smaller confinement. The high strain rate caused the local flame quenching in the outer recirculation zone (when $\Phi = 0.67$) resulting at a V shape flame as shown in Fig.6 .

Different from the flame behavior in the bigger confinement, the alteration of flame shapes from a M shape to a V shape did not lead to blowout in the smaller confinement. It was due to the fact that in the smaller confinement the flame root was stabilized in the premixing tube when the flame was changing its macrostructures. However, the flame root in the bigger confinement was unstably lifted and easy to fluctuate axially with the alteration of the flame trailing edge. Similar with that in the bigger confinement, further reduction of the equivalence ratio elongated and weakened the flame. Hence no blowout phenomenon due to oscillation was observed in the smaller confinement. This stable flame behavior was also resulted from the stronger swirling effects and CIVB propagating inside the premixing tube. Finally, the flame got blowout smoothly from a long V shape flame in the inner recirculation zone which was the same as the lean blowout behavior in the bigger confinement.

Fig.7 reveals the inverse Abel reconstructed flame macrostructures in the two confinements holding the equivalence ratio $\Phi = 0.7$ and alternating the air flow rates from $\dot{m}$ = 90 SLPM till $\dot{m}$ =150 SLPM in steps of $\Delta\dot{m}$ =20 SLPM. When $\Phi = 0.7$, a stable flame could be obtained in both confinements with flame root and CIVB propagating into the premixing tube. But the flame macrostructures differed with each other. A stronger chemiluminescence intensity which radiated a higher heat release rate was captured in the smaller confinement due to the local higher heat value per volume. The peak heat release zone in the bigger confinement located in the flame root near the dump plane whereas in the smaller competitor it was found in the flame trailing edge near the confinement wall. The main heat release zone propagated further downstream in the smaller confinement than that in the bigger one. That was resulted from the further downstream propagation of the flame trailing edge near the wall indicating a stronger flame-wall interaction. The axial location of the flame impinging on and propagating along the wall in the bigger confinement was within h_2 = 20 – 40 mm, while in the smaller confinement it was within h_1 = 10 – 60 mm. Holding the flow swirl number constant (here $S = 0.66$), the flame opening angle and the impingement location to the wall did not change significantly with the alternation of the air mass flow rates, especially in the bigger confinement. When $\dot{m}$ = 90 SLPM and $\Phi = 0.7$, flame within the bigger confinement showed much more like a V shape flame whereas in the smaller confinement the flame was stabilized with a M shape. The weaker wall-flame tip interaction in the bigger confinement with low flow velocity was believed to be the reason for this distinction. Fuel in the bigger confinement was almost completely consumed before

getting impinged on the confinement wall, which may also contribute to this flame appearance.

Lean blowout limits

As mentioned above, two blowout phenomenon, including the blowout due to oscillation and lean blowout, were observed during the experiments. But the oscillation flame blowout was only observed within the bigger confinement under the lowest flow rate conditions ($\dot{m}$ = 90 SLPM). So here we only report the blowout limits caused by lean blowout within the two confinements under different operating conditions. Results are shown in Fig.8 .

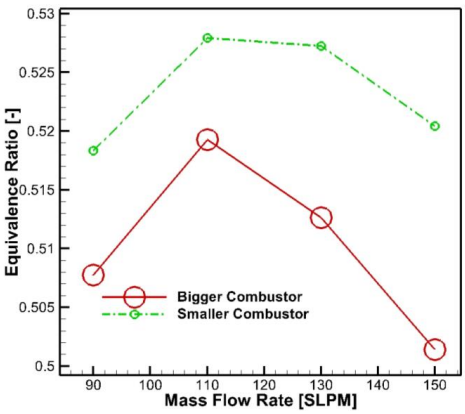

Fig.8 Effects of air mass flow rate on lean blowout limits

It could be observed from Fig.8 that flame within the bigger combustor has lower lean blowout limits indecating a better performance in stabilizing the flame. In the current study, before flame blowing out, both in the bigger and smaller confinements, the flame showed a weak and long V shape macrostrctures. The same as reported in the literature [9], this type of flame was stabilized in the inner recirculation. Under the same operating conditions, the bulk flow speed in the smaller confinement was higher compared with that in the bigger one. At the same time, the strain rate in the inner shear layer within the smaller confinement was stronger which might cause the flame blowout more easily. As reported in the literature [15], a bigger confinement might have two inner recirculation zones downstream outside the burner exit, whereas the smaller combustor had only one recirculation zone closer to or even propagated into the burner exit. In the bigger confinement, the extra recirculation zone formed further downstream of the burner exit may also contribute to the stabilization of the lifted V shape flame before blowing out.

The effect of air flow rate on lean blowout limits shows the same trend in these two confinements. When changing the air mass flow rates from $\dot{m}$ = 90 SLPM to $\dot{m}$ = 110 SLPM, the lean blowout limits increase. Whereas further increasing the air mass flow rate to $\dot{m}$ > 110 SLPM leads to a decrease of the lean blowout limits. The same trend is also observed and reported in our previous investigations with preheated air inlets and flow swirl number $S = 0.60$ in the literature [25]. The alternation of flow structures and the interaction of the flame with the confinement wall may result at this trend. They will be further investigated in our future experimental and numerical studies.

CONCLUSIONS

Effects of confinement ratio on flame macrostructures and instabilities are experimentally studied in the current paper. Two types of M shape flames (the M shape flame with CIVB and the lifted M shape flame) together with two types of V shape flames (the wall-attached and -detached V shape flames) are presented and the mechanisms behind are schematically illustrated. The combustion induced vortex breakdown promotes the flame stabilization while the boundary layer flame flashback near the wall of the confinement forms the M shape flame. Meanwhile, various flame instability patterns and their corresponding mechanisms are also released. The unstable behavior of the flame trailing edge along the wall and the flame root together with the CIVB are believed to be the potential candidates for the flame instability. The flame macrostructures and instability characteristics are highly determined by the confinement ratio and the other operating conditions. The bigger confinement has a better performance in stabilizing the flame by having leaner blowout limits.

ACKNOWLEDGMENTS

Authors Yiheng Tong and Mao Li are supported by scholarship from China Scholarship Council (CSC) which is gratefully acknowledged. The authors would like to thank P. Sayad and A. Schönborn for the design of the experimental setup, and Cheng Gong for helpful discussions.

REFERENCES

[1] Guiberti, Thibault F., et al. "Analysis of topology transitions of swirl flames interacting with the combustor side wall." Combustion and Flame 162.11 (2015): 4342-4357.

[2] Schmitt, Patrick, et al. "Large-eddy simulation and experimental study of heat transfer, nitric oxide emissions and combustion instability in a swirled turbulent high-pressure burner." Journal of Fluid Mechanics 570 (2007): 17-46.

[3] Kim, Kyu Tae, et al. "Characterization of forced flame response of swirl-stabilized turbulent lean-premixed flames in a gas turbine combustor." *Journal of Engineering for Gas Turbines and Power* 132.4 (2010): 041502.

[4] Chterev, I., et al. "Flame and flow topologies in an annular swirling flow." Combustion Science and Technology 186.8 (2014): 1041-1074.

[5] Guiberti, T. F., et al. "Impact of heat loss and hydrogen enrichment on the shape of confined swirling flames." Proceedings of the Combustion Institute35.2 (2015): 1385-1392.

[6] Wicksall, D. M., et al. "The interaction of flame and flow field in a lean premixed swirl-stabilized combustor operated on H 2/CH 4/air." Proceedings of the Combustion Institute 30.2 (2005): 2875-2883.

[7] L. T. W. Chong, T. Komarek, M. Zellhuber, J. Lenz, C. Hirsch, W. Polifke, Proceedings of the European Combustion Meeting, Vienna, Austria, April 14–17, 2009, pp.1–6.

[8] Huang, Ying, and Vigor Yang. "Dynamics and stability of lean-premixed swirl-stabilized combustion." *Progress in Energy and Combustion Science* 35.4 (2009): 293-364.

[9] S. J. Shanbhogue et al., "Flame macrostructures, combustion instability and extinction strain scaling in swirl-stabilized premixed CH4/H2 combustion" Combustion and Flame 163(2016) 494-507.

[10] Taamallah, Soufien, et al. "Thermo-acoustic instabilities in lean premixed swirl-stabilized combustion and their link to acoustically coupled and decoupled flame macrostructures." *Proceedings of the Combustion Institute* 35.3 (2015): 3273-3282.

[11] Taamallah, Soufien, et al. "Correspondence Between "Stable" Flame Macrostructure and Thermo-acoustic Instability in Premixed Swirl-Stabilized Turbulent Combustion." *Journal of Engineering for Gas Turbines and Power*137.7 (2015): 071505.

[12] Taamallah, Soufien, Santosh J. Shanbhogue, and Ahmed F. Ghoniem. "Turbulent flame stabilization modes in premixed swirl combustion: Physical mechanism and Karlovitz number-based criterion." *Combustion and Flame* 166 (2016): 19-33.

[13] Alekseenko, Sergey V., et al. "Flow structure of swirling turbulent propane flames." Flow, turbulence and combustion 87.4 (2011): 569-595.

[14] Malanoski, Michael, et al. "Flame leading edge and flow dynamics in a swirling, lifted flame." Combustion Science and Technology 186.12 (2014): 1816-1843.

[15] Fu, Yongqiang, et al. "Confinement effects on the swirling flow of a counter-rotating swirl cup." *ASME Turbo Expo 2005: Power for Land, Sea, and Air*. American Society of Mechanical Engineers, 2005.

[16] De Rosa, Alexander J., et al. "The Effect of Confinement on the Structure and Dynamic Response of Lean-Premixed, Swirl-Stabilized Flames." *Journal of Engineering for Gas Turbines and Power* 138.6 (2016): 061507.

[17] Guiberti, T. F., et al. "Experimental analysis of V-to M-shape transition of premixed CH4/H2/air swirling flames." *ASME Turbo Expo 2013: Turbine Technical Conference and Exposition*. American Society of Mechanical Engineers, 2013.

[18] Sayad, Parisa, et al. "Visualization of different flashback mechanisms for H2/CH4 mixtures in a variable-swirl burner." *Journal of Engineering for Gas Turbines and Power* 137.3 (2015): 031507.

[19] Sommerer, Yannick, et al. "Large eddy simulation and experimental study of flashback and blow-off in a lean partially premixed swirled burner." *Journal of Turbulence* 5.37 (2004): 1-3.

[20] Syred, Nicholas, et al. "The effect of hydrogen containing fuel blends upon flashback in swirl burners." *Applied Energy* 89.1 (2012): 106-110.

[21] Konle, Marco, and Thomas Sattelmayer. "Interaction of heat release and vortex breakdown during flame flashback driven by combustion induced vortex breakdown." *Experiments in fluids* 47.4-5 (2009): 627-635.

[22] Sayad, Parisa, Alessandro Schönborn, and Jens Klingmann. "Experimental investigation of the stability limits of premixed syngas-air flames at two moderate swirl numbers." *Combustion and Flame* 164 (2016): 270-282.

[23] Syred, N., & Beer, J. M. (1974). Combustion in swirling flows: a review. Combustion and flame, 23(2), 143-201.

[24] P. Sayad, A. Schönborn, M. Li, and J. Klingmann, Visualization of different flashback mechanisms for h2/ch4 mixtures in a variable-swirl burner. Journal of Engineering for Gas Turbines and Power, 2014. 137(3): p. 031507-031507.

[25] Tong, Yiheng, Mao Li, and Jens Klingmann. "Influence of Combustor Geometry on Swirl Stabilized Premixed Methane-Air Flame." *ASME Turbo Expo 2016: Turbomachinery Technical Conference and Exposition*. American Society of Mechanical Engineers, 2016.

Paper III

INTERNATIONAL JOURNAL OF HYDROGEN ENERGY XXX (2017) 1–16

Available online at www.sciencedirect.com

ScienceDirect

journal homepage: www.elsevier.com/locate/he

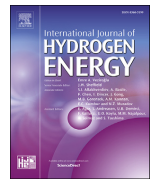

Experimental study on dynamics of a confined low swirl partially premixed methane-hydrogen-air flame

Yiheng Tong [a,*], *Senbin Yu* [a], *Xiao Liu* [b], *Jens Klingmann* [a]

[a] *Department of Energy Sciences, Lund University, Lund, Sweden*
[b] *College of Power and Energy Engineering, Harbin Engineering University, Harbin, China*

ARTICLE INFO

Article history:
Received 21 July 2017
Received in revised form
5 September 2017
Accepted 8 September 2017
Available online xxx

Keywords:
Hydrogen combustion
Swirling flow
Combustion dynamics
Flow fields
Flame structures
Flashback

ABSTRACT

The addition of hydrogen to swirl stabilized methane-air flame in gas turbine has gained more and more attentions in recent years. In the current study, flame structures, flame dynamics and lean blowout limits of partially premixed hydrogen-methane-air flames were investigated. The swirling flow, which was generated from the tangential flow injection, was utilized to stabilize the flame. The flow swirl number was kept low varying from S ≈ 0.28 to S ≈ 0.34 while the thermal power of the burner ranged from 10.8 kW to 13.8 kW. Two different fuel injection strategies were investigated and compared with each other. Long exposure CH^* chemiluminescence from the flame was captured to visualize the time averaged flame shapes. In addition, an intensified high speed camera was adopted to study the flame dynamics. A high speed PIV system was utilized to investigate the interaction of flame dynamics and flow fields oscillations. Based on the experimental results, it can be concluded that: in the current experimental cases, fuel injection strategy plays an important role in determining the flame macro-structures and thus strongly affects the flame dynamics and lean blowout limits. Flame with fuel injected through the axial flow has lower lean blowout limits. The flashback and vortex breakdown were observed when fuel was injected in the tangential flow near lean blowout. High frequency flame oscillations ($f \approx 170$ Hz) were observed when the global equivalence ratio $\Phi_g > 0.72$ while lower frequency oscillations ($f \approx 50$ Hz and $f \approx 20$ Hz) were found near lean blowout limits, $\Phi_g < 0.55$. Combustion dynamic and its interaction with the pressure oscillation, flow fields alternation and mass flow rate oscillation are proposed. The differences on fuel concentration at the burner exit are proposed as the main reason for different flame instabilities and flame structures.

Introduction

Modern premixed gas turbine combustors are usually operated near the lean blowout limits due to the emissions requirements [1]. It is a practical method to reduce thermal NO_x formation due to the lower flame temperature operated in lean conditions [2]. In order to have a better flame stabilization in lean conditions, hydrogen addition to the natural gas-air

* *Corresponding author.*
E-mail address: yiheng.tong@energy.lth.se (Y. Tong).
https://doi.org/10.1016/j.ijhydene.2017.09.066

Please cite this article in press as: Tong Y, et al., Experimental study on dynamics of a confined low swirl partially premixed methane-hydrogen-air flame, International Journal of Hydrogen Energy (2017), https://doi.org/10.1016/j.ijhydene.2017.09.066

Nomenclature

d_c	optical confinement inner diameter [mm]
d_m	mixing tube inner diameter [mm]
d_p	pilot tube inner diameter [mm]
d_{probe}	emission probe inner diameter [mm]
f	oscillation frequency [Hz]
h	axial position [mm]
H_{COHR}	Position of flame's corner of heat release [mm]
h_t	tangential inlet height [mm]
l_c	optical confinement length [mm]
L_F	characteristic flame length [mm]
l_m	mixing tube length [mm]
m_a	axial air mass flow rate [SLPM]
m_{CH4}	methane mass flow rate [SLPM]
m_{H2}	hydrogen mass flow rate [SLPM]
m_t	tangential air mass flow rate [SLPM]
m_{total}	total air mass flow rate [SLPM]
$m_{t\text{-}N2}$	tangential mass flow rate of N_2 [SLPM]
Re	Reynolds number at the burner exit [–]
S	Swirl number [–]
T	oscillation cycle time [s]
U_b	bulk velocity at the burner exit [m/s]
w_t	tangential inlet width [mm]
Δt	time delay between two laser pulses [μs]
Φ_{LBO}	lean blowout equivalence ratio [–]
Φ_g	global equivalence ratio [–]

Abbreviations

COHR	corner of heat release
FFT	Fast Fourier Transform
fps	frames per second
FWHM	full width at half maximum
LBO	lean blowout
LDA	Laser Doppler Anemometry
PIV	Particle Image Velocimetry
PVC	processing vortex core
SLPM	standard litter per minute

premixed flame is a practical strategy. The use of hydrogen addition to extend the lean blowout limits of premixed natural gas-air flames in gas turbine combustors has been investigated by various researchers. Hydrogen addition to the premixed methane-air flame increases the global reaction rate leading to a higher turbulent burning velocity which in turn have the possibility to promote the flame stabilization especially under lean conditions [3–6].

However, with the addition of hydrogen to premixed natural gas-air or premixed methane-air flames, several challenges will show up as well, i.e. flame flashback and even auto-ignition upstream in the premixing tube due to the high combustion chemistry of hydrogen [7] [8]. In addition, the flame oscillation caused by hydrogen addition might cause gas turbines to shut down or even lead to hardware damage. Therefore, the composition of the fuel impacts the turbine life and thus characterizations of the flame behaviors with hydrogen addition are important issues [9]. Tuncer et al. [7] pointed out that under atmospheric conditions the flame speed of a stoichiometric hydrogen-air mixture was about five times faster than that of a premixed methane-air flame. They studied the dynamics of premixed flames with different hydrogen contents and found the 40–47 Hz flame oscillation accompanied with flame flashback when the hydrogen composition was 40–50%. Cheng et al. [8] concluded that the flame shape changing with the enrichment of hydrogen was strongly affected by the increase in turbulent flame speed and the reactants burning in the outer recirculation zone. The increasing of hydrogen concentration in the fuel forced the flame getting closer or even attaching to the burner exit where the local turbulence intensity was high. Strakey et al. [10] found the flame anchoring in the outer recirculation zone prior to lean blowout in the swirl stabilized premixed hydrogen-methane-air flame. Sayad et al. [11] experimentally studied the flashback and lean blowout limits of premixed syngas flames. They found that with the increasing of hydrogen content in the syngas reactants, both the lean blowout limits and flashback equivalence ratio decreased significantly. The change of the flame stabilization limits was caused by the faster reactivity of mixtures with higher hydrogen content, which increased the flame speeds and thus the residence times that was required for the reactions to be completed was shorter.

On the other hand, in order to better stabilize the flame, swirling flows were commonly employed in gas turbine combustors. The typical swirling flow fields with a vortex breakdown inside a confinement is shown in Fig. 1 [12]. As described in Ref. [13], with strong swirling effects, the central vortex breakdown and thus an inner recirculation zone (or central recirculation zone) are formed. While due to the effects from the confinement, an outer recirculation zone (or corner recirculation zone) is generated as well. Between the inner recirculation zone and the main flow is the inner shear layer, while the outer shear layer locates between the main flow and the outer recirculation zone. The flame behaviors are strongly interacted with the swirling flow fields [14]. In addition, there are two common ways to generate swirling flows: the guiding vane and the tangential entry swirler. Compared with a guiding vane swirler, the tangential entry

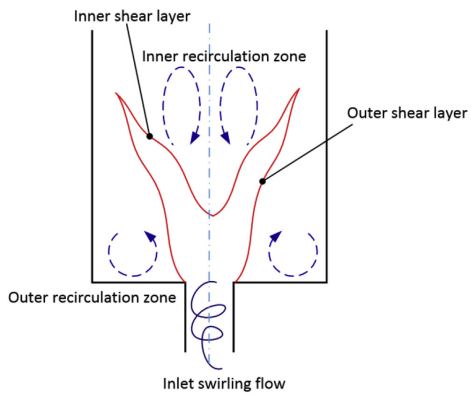

Fig. 1 – Schematic of swirling flow fields with vortex breakdown inside a confinement.

Please cite this article in press as: Tong Y, et al., Experimental study on dynamics of a confined low swirl partially premixed methane-hydrogen-air flame, International Journal of Hydrogen Energy (2017), https://doi.org/10.1016/j.ijhydene.2017.09.066

system has better performance in the vorticity contribution to the core from the endwall boundary [15]. In the guiding vane swirler, the fuel and air were commonly perfectly premixed (with a uniform mixture composition) before or after passing through the guiding vanes [3,7,8,10,16–18]. Researchers have done numerous investigations about fully premixed hydrogen-methane-air flames stabilized by swirling flow. However, in some cases fuels and air might not well premixed before getting into the combustor in practical gas turbine combustors.

Comparing with the research of swirl stabilized premixed hydrogen-methane-air flames, there are less literature concerning with swirl stabilized partially premixed flames. Stöhr et al. [19] studied the flame dynamics caused by fuel-air mixing. They concluded that the precessing vortex core (PVC) in the shear layer played an important role in the fuel-air mixing and thus led to flame dynamics. Meier et al. [20] studied the effects of mixing property on flame oscillations. They observed a thermoacoustic instability at a frequency of approximately 400 Hz and it was caused by the oscillation of temperature and mixture fraction in the combustion chamber. The change of flame shapes and the flame oscillations together with the combustor surface temperature dynamics were studied by Yin et al. [21]. They found that the M-Shape flame dynamic had a good agreement with the bluff-body surface temperature oscillation. K.R. Dinesh [22] mentioned that turbulent syngas swirling flame was not only governed by the inlet flow conditions but also by the fuel mixture which played an important role particularly for high hydrogen content fuels, thereby inducing different diffusivity levels. T.G. Reichel and C.O. Paschereit [23] studied the confined swirl stabilized flame. The swirling strength was varied by the alternation of the tangential and axial flow momentum. In their experiments, the fuel was injected through the axial flow while some additional air dilution was injected near the burner exit wall. Its purpose was to lower the local equivalence ratio near the burner exit wall and thus avoid the boundary layer flashback. They reported that the flame front was pushed downstream with an increase in the equivalence ratio. The increase in the bulk velocity of the flow at the burner exit was proposed as the reason for this phenomenon. W. Meier et al. [24]experimentally studied the partially premixed flames and concluded that the mixture fraction would affect the spatial distribution of CH^* in the flame. The width of the CH^* layers was predominantly determined by the local mixture fraction and by fuel diffusion. W. Meier et al. [25] also concluded that the effects of finite-rate chemistry and unmixedness were more pronounced in the pulsating flame than the 'quiet flame'. Decreasing the equivalence ratio (from $\Phi = 0.85$ to $\Phi = 0.7$) would make the 'quiet flame' to be a self-exited pulsating flame. F. Biagioli et al. [26] reported that the flame anchoring location (inside or outside of the burner) was strongly sensitive to flow and equivalence ratio perturbation in the swirl stabilized partially premixed flames. Y. Sommerer et al. [27] studied the swirl stabilized partially premixed flames with axial fuel injection. They separated the flame structures into different regimes including the flashback flame, the compact flame, the lifted flame till blowoff. They also conclude that the flashback regime is dominated by diffusion flames with lots of unburnt hydrocarbons while compact regimes exhibit premixed flames. A. Sengissen et al. [28] experimentally and numerically investigated the swirl stabilized partially premixed flames with a tangential fuel injection. They summarized that two factors triggering the flame oscillation: vortices oscillation and the fuel/oxidizer mass flow rate oscillation. In summary, researchers have already utilized different fuel injection strategies in their investigations; however, they have not evaluated the effects caused by the alternation of different fuel injection methods.

The swirler in the current study utilized the tangential flow entry to generate the swirling flow. There are two flow streams upstream of the combustor: the axial flow and the tangential flow. Thus, two fuel injection strategies could be applied to practical combustors: adding premixed fuel of hydrogen and methane into the tangential flow or the axial flow. Under conditions with a short premixing tube, the flame was rather a partially premixed flame. The objective in the current study is to investigate the effects of different fuel injection methods on the behavior of low swirl stabilized flames. Partially premixed flame with two fuel injection strategies were studied while holding the flow swirl number at $S \approx 0.31$. Flame structures, flame dynamics and flow fields were captured and analyzed to evaluate the effects of fuel injection strategies.

Experimental setup and methods

The variable-swirl burner

The experimental setup and the approaches are shown in Fig. 2. As shown in Fig. 2 that the filtered and intensified high speed photography together with the high speed particle image velocimetry (PIV) were adopted. They will be introduced further in detail later. Details of the variable-swirl burner which was utilized in the current study is shown in Fig. 3. The partially premixed flame was observed being stabilized in the quartz tube (inner diameter d_c = 64 mm, and length l_c = 120 mm), which acted as the confinement or the combustor. Through the quartz tube, flame structures and instabilities together with the flow fields could be captured. Directly upstream of the confinement, there was a short premixing tube (inner diameter d_m = 15 mm and length l_m = 30 mm) to generate the partially mixed reactants of hydrogen-methane-air. A stepped expansion between the confinement and the premixing tube would hereafter be referred to as the dump plane ($h = 0$ mm). On the dump plane, there was a small torch injection hole for the premixed torch mixture. The torch was located 4 mm away from the mixing tube wall and had an inner diameter of $d_p = 3$ mm. The variable swirler was located directly upstream of the mixing tube with four tangential flow inlets. The dimensions of the tangential flow channel inlets (width $w_t = 3$ mm and height $h_t = 10$ mm) are also shown in Fig. 3. The variable swirl burner has the potential to create flows with different swirl numbers by changing the momentum ratio of the axial to the tangential flows.

A spark plug, which was utilized to ignite the premixed torch flame, was mounted at the exit of the confinement. The confinement was held in place by pneumatic pressure which

Please cite this article in press as: Tong Y, et al., Experimental study on dynamics of a confined low swirl partially premixed methane-hydrogen-air flame, International Journal of Hydrogen Energy (2017), https://doi.org/10.1016/j.ijhydene.2017.09.066

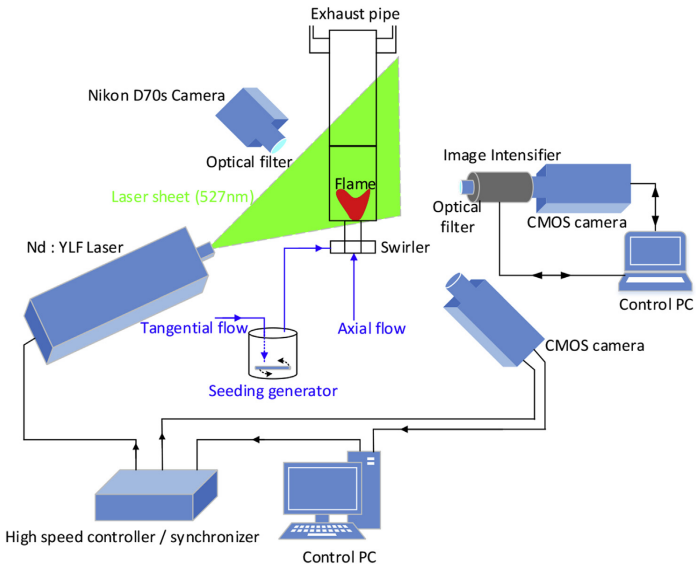

Fig. 2 – Schematic of the experimental setup.

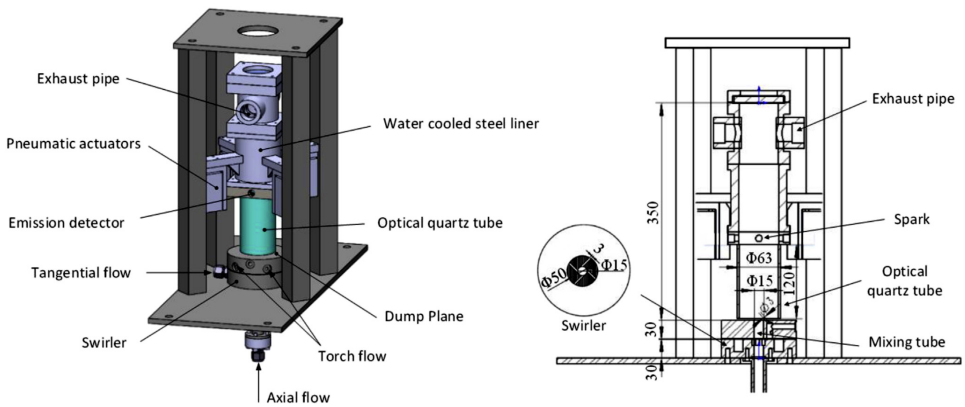

Fig. 3 – Schematic (left) and cross section (right) of the variable swirl burner.

was provided by four pneumatic actuators. The pneumatic system allowed swift sealing and removal of the confinement during the experiments. Hence a closed environment was created for the partially premixed flames.

Photography and image analysis methods

A high spatial resolution Nikon D70s camera together with a 430 ± 10 nm band-pass filter were adopted to capture the CH^* chemiluminescence from the flame. The camera exposure time was set to 0.77s and the resolution of the image was 3008 × 2000 pixel^2. Three images under the same operating condition were recorded and averaged before doing further image analysis. This long exposure time (compared to any turbulent fluctuations) and averaging of the raw images had the effect of averaging out the instantaneous winkles of the flame front thus yielding the equivalent of time averaged flame structures. Since CH^* chemiluminescence intensity peaks at a light wavelength of 431 nm in the blue range, only the blue layer in the raw RGB format images was used in the

Please cite this article in press as: Tong Y, et al., Experimental study on dynamics of a confined low swirl partially premixed methane-hydrogen-air flame, International Journal of Hydrogen Energy (2017), https://doi.org/10.1016/j.ijhydene.2017.09.066

image analysis process (as in the literature [29]). The raw image, which was obtained by the line-of-sight method, was deconvolved using the inverse Abel image reconstruction method based on the in-house developed Matlab code. Since the confinement was cylindrical, an assumption of axisymmetric was adopted in the image reconstruction analysis procedure. As will be shown later, the inverse Abel reconstructed image better marked the location of the time averaged flame brush in the central plane of the confinement.

In addition, to obtain the representative flame length (L_F), CH* chemiluminescence intensity within the time averaged image was first summed up along the lateral direction. Since the CH* intensity has the linearly relationship with the heat release rate [30], the axial heat release rate profile illustrates distribution of heat release along the axial direction inside the confinement as demonstrated in Fig. 4. The position of flame's center of heat release (H_{COHR}), as shown in Fig. 4, is the axial location with maximum CH* chemiluminescence intensity [31]. It should be noted here that H_{COHR} differed with the location with peak CH* chemiluminescence from the flame. As shown in Fig. 4 (b), H_{COHR} represented the peak of the radically integrated heat release. The characteristic flame length, L_F, is the full width at half maximum (FWHM) of heat release distribution profile, as also shown in Fig. 4 (b). This value was calculated by finding the width in the axial profile at an intensity value of half of the peak value [31,32]. The axial position of the flame's center of heat release shown in Fig. 4 is H_{COHR} = 21.9 mm while the representative flame length is L_F = 47.1 mm.

In order to obtain the flame dynamics, as shown in Fig. 2, a high speed CMOS camera (Vision Research Phantom V 7.1) coupled with an image intensifier (Hamamatsu C4598), a 430 ± 5 nm band-pass filter and a phosphate glass lens (UV-Nikkor 105 mm, *f*/4.5) was used to photograph CH* chemiluminescence from the flame. The camera had the spatial resolution of 600 × 800 pixels^2 and depth of 24bit. A time series of 1450 images were obtained at a recording rate of 4000 frames per second (*fps*). In order to resolve the time-varying flame structures, the exposure time of the camera was set to 20μs. An example of the CH* chemiluminescence from the flame is shown in Fig. 5(a) while the white line denotes the quartz tube wall. The oscillation of the flame could be obtained by doing Fast Fourier Transform (FFT) to the time series of the total intensity of the transient images [13]. Digital image process was fulfilled based on in-house developed Matlab code. An example of the flame oscillation with the dominant frequency f = 172 Hz was shown in Fig. 5(b).

High speed PIV system

The flow fields inside the confinement were measured using a high-speed PIV system (Lavision Flowmaster). The schematic of the PIV system is also shown in Fig. 2. A diode-pumped, dual cavity Nd:YLF laser (Litron LDY) was utilized to illuminate the central plane of the confinement with a laser sheet. The thickness of the lase sheet was approximately 1 mm which was generated by an optical sheet lens. The high speed laser had a wavelength of 527 nm and frequency of 2 kHz in the current study. The time delay between two laser pulses was Δt = 50 μs. The laser light scattered off the TiO_2 seed particles in the reacting cases, to visualize the flow fields. The recording rate of the high speed CMOS camera (Vision Research Phantom V 611) was set to 2 kHz with a resolution of 1280 × 800 pixels^2 and a depth of 12 bits. As shown in Fig. 2, the TiO_2 particles were seeded into the tangential air flow using a LaVision solid particle seeder (LaVision Particle blaster 100). A multi-pass cross-correlation algorithm, which was available in the DaVis (v.8.1.4) computer software, was utilized to evaluate the velocity fields inside the confinement. The cross-correlation was performed on interrogation areas of 64 × 64 and subsequently 32 × 32 pixels with a window overlap of 75%.

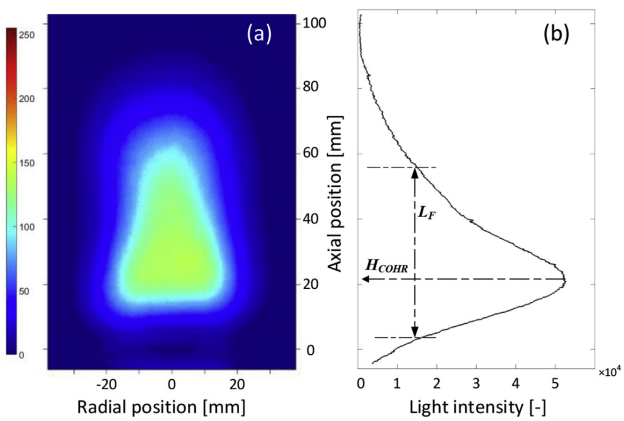

Fig. 4 – (a)Typical time averaged CH* flame structures and (b) height for flame's center of heat release (H_{COHR}) together with flame length (L_F) of full width at half maximum (FWHM) measurement overlaid.

Please cite this article in press as: Tong Y, et al., Experimental study on dynamics of a confined low swirl partially premixed methane-hydrogen-air flame, International Journal of Hydrogen Energy (2017), https://doi.org/10.1016/j.ijhydene.2017.09.066

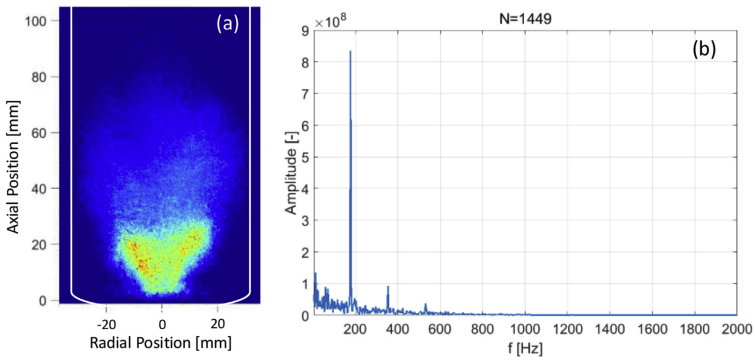

Fig. 5 – (a)Examples of CH* chemiluminescence of the flame from intensified high speed photography and (b) flame oscillation obtained based on the image intensity.

Test conditions

Two different fuel injection strategies (injecting fuel through the tangential direction or the axial direction) were studied in the current paper and they are shown in Table 1. In the case name, A and T stand for the axial and tangential fuel injection strategies, respectively; while the number after S shows the swirl number. For example, case A-S33 stands for case with axial fuel injection strategy while holding the swirl number $S \approx 0.33$. All the experiments were operated under atmospheric conditions. The same as in the literature [33], the experiments conducted at atmospheric pressure could be the basis for the high-pressure experiments in gas turbines. Either in the tangential fuel injection methods or in the axial fuel injection methods, fuel (mixture of methane and hydrogen) was injected and premixed with the air flow at least 200 mm upstream of the swirler. Thus it could be reasonably assumed that fuel and air were perfectly premixed at the tangential or axial flow inlets upstream of the swirler. Then the perfectly mixed fuel-air mixtures would further mix with pure air from the other inlet, forming the partially premixed reactants at the exit of the short premixing tube. Fuel and air mass flow rates were adjusted separately (by Alicat MCR series) in order to achieve the desired test conditions. The total mass flow rate of air ($m_{total} = m_a + m_t = 150$SLPM) and the mass flow rate of hydrogen ($m_{H2} = 3$SLPM) were kept constant. Hence the bulk velocity at the burner exit was $U_b \approx 14.15$ m/s while the Reynolds number based on the bulk velocity was Re ≈ 14000; they were held constant as well. The alternation of global equivalence ratio Φ_g (as defined in Ref. [34]) was fulfilled by changing the mass flow rate of methane, m_{CH4}.

Details about the definition and calculation of swirl number could be found in our previous study [12]. The swirl number was calculated based the momentum ratios of the axial to the tangential flows together with the empirical relation map reported in the literature [35]. The empirical relation map was obtained by Laser Doppler Anemometry (LDA) measurements at 1 mm above the dump plane in Ref. [35] using the same test facility. In order to check the influences caused by the swirling strength, different swirl strengths in cases with $0.284 < S < 0.337$ were experimentally studied.

Mixing property at the burner exit

To obtain the fuel-air mixing profile at the burner exit, the injection strategy of pure nitrogen in the tangential ($m_{t,N2} = 75$SLPM) together with air in the axial flow ($m_a = 75$SLPM) was adopted. Hence the oxygen concentration along the radial direction at the burner exit could be used to denote the fuel-air mixing profiles, as shown in Fig. 6. The data was obtained using a small probe with inner diameter $d_{probe} \approx 1$ mm at

Table 1 – Test conditions.

Case name	Axial flow rate (SLPM)			Tangential flow rate (SLPM)			Swirl Number
	CH_4	H_2	Air	CH_4	H_2	Air	
A-S28	12.6~LBO	3	75	0	0	75	0.284 ± 0.002
T-S33	0	0	75	12.6~LBO	3	75	0.337 ± 0.002
A-S33	10~LBO	3	70	0	0	80	0.332 ± 0.002
T-S28	0	0	80	10~LBO	3	70	0.289 ± 0.002
A-S31	10~LBO	3	72.5	0	0	77.5	0.310 ± 0.002
T-S31	0	0	77.5	10~LBO	3	72.5	0.311 ± 0.002

Please cite this article in press as: Tong Y, et al., Experimental study on dynamics of a confined low swirl partially premixed methane-hydrogen-air flame, International Journal of Hydrogen Energy (2017), https://doi.org/10.1016/j.ijhydene.2017.09.066

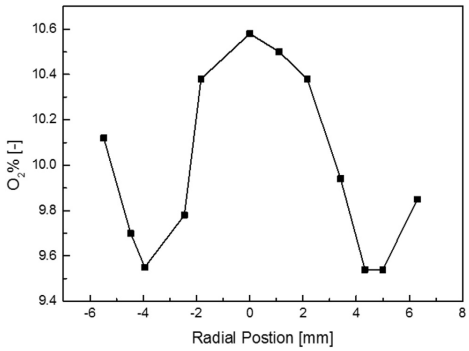

Fig. 6 – Mole fraction of oxygen along the radial direction near the burner exit.

$h \approx 2$ mm downstream of the premixing tube exit without confinement. The oxygen concentration was measured using a Rosemount Oxynos 100 paramagnetic O_2 gas analyzer. It could be seen that the oxygen near the burner axis was higher than that near the burner wall, which indicated a poor mixing of nitrogen and air. When the gas analyzer probe moved near to the mixing tube wall, the oxygen mole fraction became higher due to the dilution of air from the environment. Therefore, it could safely assume that the mixings of fuel and air at the exit of the mixing tube in different fuel injection strategies cases were also poor [19]. For instance, with the fuel injection through the tangential flow, more fuel would be found near the burner wall, or inside the confinement near the confinement wall and the corner recirculation zone. The poor mixing of fuel and air might cause different flame dynamics and flame structures, as will be discussed later.

Results and discussion

Flame structures and dynamics under conditions far from lean blowout

Holding the global equivalence ratio $\Phi_g = 0.85$, the inverse Abel reconstructed time averaged flame structures in cases A-S28 and T-S33 are shown in Fig. 7. In overall, all the flames were observed lifted from the dump plane indicating they were all beyond flame flashback in cases with such a low swirl number, $S \approx 0.31$. It could also be seen that the flame shape altered with each other when changing the fuel injection strategies. With the tangential fuel injection (case T-S33), the time averaged flame structures shown a bell shape, whereas the axial fuel injection (case A-S28) led to a more compact flame. The lifted height from the flame root to the dump plane was larger in case A-S28 than that in the other case. In addition, in cases with the same fuel injection strategy, a slightly change of swirl number did not change the time averaged flame structures significantly. It indicates that the flame structures were more dominated by fuel injection strategies and thus the fuel air mixing at the burner exit. The flame dynamics when holding $\Phi_g = 0.85$ in cases A-S28 and T-S33 are shown and compared with each other in Figs. 8 and 9.

The black arrows in Fig. 8 schematically mark the motion direction of the flame, while T is the cycle time of the oscillation, $T = 1/f$. In the oscillation loop, the flame in case A-S28 started in the downstream region far from the dump plane. Then it propagated upstream while the heat release rate decreased simultaneously. When the flame got to the upstream position near the dump plane, the flame started to propagate back downstream to its original position. Meanwhile, the heat release rate (CH*) became stronger as the flame was pushed farther from the dump plane. It should be mentioned that the flame did not propagate along the radial direction. In addition, the flame was not found in the corner

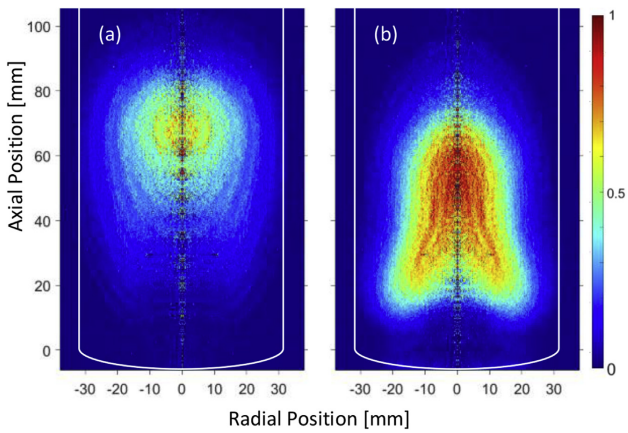

Fig. 7 – Inverse Abel reconstructed time averaged flame structures in (a) case A-S28 and (b) case T-S33 when holding $\Phi_g = 0.85$.

Please cite this article in press as: Tong Y, et al., Experimental study on dynamics of a confined low swirl partially premixed methane-hydrogen-air flame, International Journal of Hydrogen Energy (2017), https://doi.org/10.1016/j.ijhydene.2017.09.066

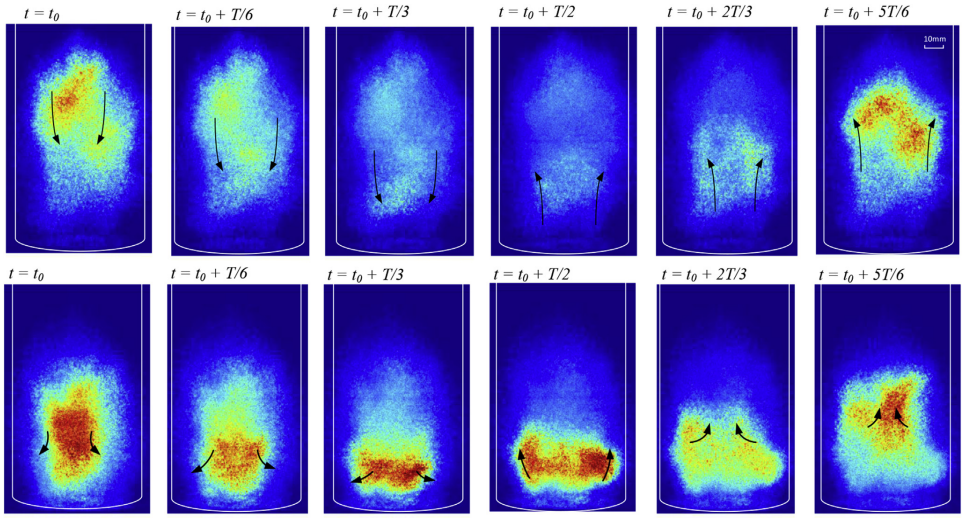

Fig. 8 – Phase locked flame dynamics when holding global $\Phi_g = 0.85$. Upper row: case A-S28; lower row: case T-S33.

recirculation zone. In the case with tangential fuel injection, the flame started at the lifted position downstream of the dump plane in the oscillation loop, which was the same as that in case A-S28. After that, the flame behaved differently with that in case A-S28. The flame started to propagate upstream without becoming weaker. When the flame got close to the dump plane, it propagated along the radial direction towards the corner recirculation zone. After that, because of the corner recirculation vortex, the flame was pushed downstream along the central axis. In the end of the

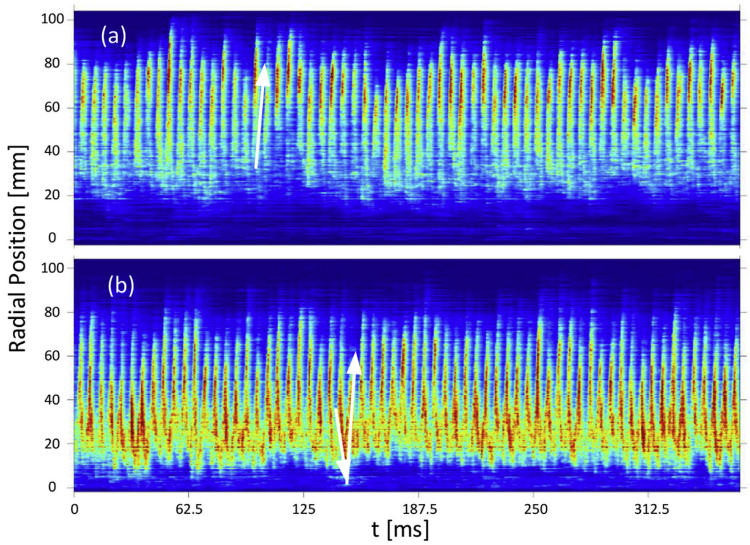

Fig. 9 – Flame segment paths in the center line for (a) case A-S28 and (b) case A-S31 when holding $\Phi_g = 0.85$.

Please cite this article in press as: Tong Y, et al., Experimental study on dynamics of a confined low swirl partially premixed methane-hydrogen-air flame, International Journal of Hydrogen Energy (2017), https://doi.org/10.1016/j.ijhydene.2017.09.066

oscillation loop, the flame located back to the original position downstream of the dump plane. The difference of fuel concentration at the burner exit in these two cases is believed to be the reason for different flame behaviors and thus result at different time averaged flame structures. To be more specifically, in case T-S33, more fuel would be found in the corner recirculation zone; as a consequence, the flame could propagate along the radial direction towards and thus inside the corner recirculation zone. Therefore, the time averaged flame shape in case T-S33 had the bell shape.

In order to better visualize the flame dynamics when holding $\Phi_g = 0.85$, the same as utilized in literature [36–38], paths of CH^* from the flame in the central line of the raw time consequence images are shown in Fig. 9. It stitches the central line of each raw image in the time consequence order. To be more specifically, for example, the first column pixels of the image in Fig. 9(a) was from the central line of the first raw image ($t = 0$) in case A-S28. Additionally, the white lines in Fig. 9 schematically show the flame propagating direction in one oscillation cycle. It could be easily seen that the flames in these two cases were maintained with high frequency oscillations. The flame oscillation frequencies in these two cases were similar with each other at $f \approx 170$ Hz. The same as observed in the time averaged flame structures shown in Fig. 7, the flame lifted higher in case with axial fuel injection strategy; while in the other case, more heat release was found near the dump plane. In agree with that shown in Fig. 8, in case A-S28, the flame got weaker when it is propagating upstream. In the other case, the strong heat releases were found both in the upstream and the downstream flame propagation process.

Flame structures and dynamics near lean blowout

The inverse Abel reconstructed time averaged flame structures near flame blowout ($\Phi_g = 0.62$) in case A-S31, case A-S28, case T-S33 and case T-S31 are shown and compared with each other in Fig. 10. As can be seen from Fig. 10, with fuel in the tangential flow the flame had an heart shape; while in the other case the flame kept the same shape (but elongated) as that in the comparatively higher equivalence ratio conditions (as shown in Fig. 7). The heart shape flame was located near the dump plane. It was unsteadily flashing into and outward from the premixing tube. Strong flame oscillations were observed simultaneously and will be shown later. With a slight change in flow swirl number in cases with the same fuel injection strategies (i.e. case T-S31 and case T-S28), the flame shape did not significantly change. It indicated that different flame behaviors were caused by the local mixing of fuel-air at the burner exit rather than the slight variation of swirl strength.

The flame oscillations near lean blowout ($\Phi_g = 0.62$) in cases A-S28 and T-S33 are shown in Fig. 11. The flame dynamics near lean blowout in case A-S28 was similar to that observed in the comparatively fuel rich condition as described previously in Fig. 8. The strong heat release zone was found in the downstream region while no combustion occurred in the corner recirculation zone. However, in case T-S33 and $\Phi_g = 0.62$, the flame dynamics was different from that under condition of $\Phi_g = 0.85$. The flame flashback into the premixing tube was observed as shown in Fig. 11. When the flame was flashing back towards upstream direction, the flame did not propagate into the corner recirculation zone, as shown in Fig. 8. It kept on propagating further upstream into the premixing tube due to the inner vortex breakdown in the flow fields. After that, the flame got weak near the dump plane with a suddenly sharp increase of the axial velocity from the burner exit (which will be shown later in Fig. 14). Then the flame became weak and distributed homogenously inside the confinement. After that, the flame propagated back to its original position in the oscillation loop.

Holding the global equivalence ratio constant at $\Phi_g = 0.62$, flame segment paths in the central line for cases with different fuel injection strategies and swirl numbers are illustrated in Fig. 12. It could also be easily seen that all the cases have significant oscillations near lean blowout. Flames in cases with the same fuel injection strategy have the similar dominant oscillation frequency. For specifically, flame

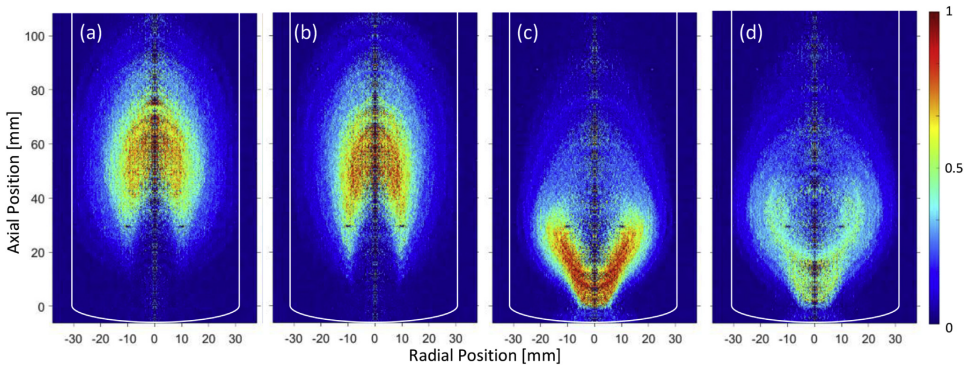

Fig. 10 – Inverse Abel reconstructed flame structures when holding $\Phi_g = 0.62$ near lean blowout. (a) case A-S31; (b) case A-S28; (c) case T-S33; (d)case T-S31.

Please cite this article in press as: Tong Y, et al., Experimental study on dynamics of a confined low swirl partially premixed methane-hydrogen-air flame, International Journal of Hydrogen Energy (2017), https://doi.org/10.1016/j.ijhydene.2017.09.066

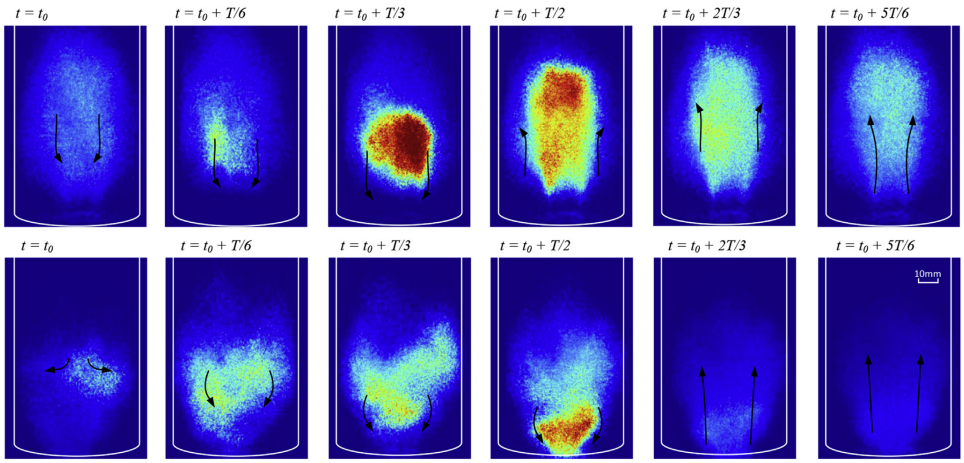

Fig. 11 – Phase locked flame dynamics when holding $\Phi_g = 0.62$ near lean blowout. Upper row: case A-S28; lower row: case T-S33.

oscillation frequencies in cases with axial fuel injection methods ($f \approx 20$) are lower than the other cases ($f \approx 50$). Holding the fuel injection methods unchanged, the small variations of swirl number did not significantly change the flame oscillation frequency. Flames in cases with axial fuel injection methods were lifted, whereas flames in the other cases were found flashback into the upstream region. The direction of the flame propagating in the center line differed with each other when the fuel injection strategy changed. With fuel injected through the tangential flow, the flame started in the downstream region on the central line and then propagated upstream along the central line towards the premixing tube. More heat was released near the dump plane. In the other cases (case A-S28 and case A-S31), the flame started in the downstream region and then propagated upstream as well. However, the flame could not flashback into the premixing tube. When the flame got close to the dump plane, it then propagated downstream with more heat released in the downstream region. The flame motion in these two cases near lean blowout are found different from that in the comparatively rich conditions ($\Phi_g = 0.85$) shown in Fig. 9.

In overall, comparing Fig. 12 (a) and (b) or Fig. 12 (c) and (d) that a slight change in swirl numbers, while holding the fuel injection strategy unchanged, did not change the flame oscillation behaviors near blowout. Hence it could be concluded that the fuel injection strategy, not the change of swirl strength, determined the unstable flame oscillations as well as the lean blowout behavior. The alternation of fuel injection methods would result at different fuel distributions at the burner exit and hence lead to the distinct flame behaviors. They may also affect the flame lean blowout limits as will be discussed later.

The axial velocity segment paths in the central axis for the reacting case T-S33 near lean blowout is shown in Fig. 13. It could be found that the axial velocity also had an obvious oscillation. Additionally, the axial velocity oscillation frequency was the same as the flame dynamics. It indicated the strong interaction of the flame dynamics and the flow fields. High axial velocity were found in the region near the burner exit while strong reversing flow located further downstream. It denoted the formation and location of the vortex breakdown. When the vortex breakdown was pushed upstream till the region near or even inside the premixing tube, a sudden increase of axial velocity was then followed. Meanwhile the recirculation vortex was pushed downstream and finally disappeared. More details about the flow field dynamics and its correlation with flame oscillations are shown in Fig. 14.

Fig. 14 shows the phase locked flow fields in the reacting case T-S31 near lean blowout when holding $\Phi_g = 0.62$. As shown in Figs. 11 and 14, when the flame was homogenously distributed inside the confinement, vortex breakdown could not be generated. Meanwhile, a large corner recirculation zone was observed. After that, with the occurrence of the reaction in the central region, an inner vortex breakdown was generated due to the local high pressure. Because of the reverse flow momentum, the total flow rates and the axial velocity through the burner exit got decreased. Whereas the turbulent flame speed did not decrease significantly which resulted in the imbalance of the local flow velocity with the turbulent flame speed. Therefore, the flame propagated upstream into the premixing zone. At the same time, the central recirculation bubble was enlarged further. The swirling flow downstream of the dump plane expanded more, which led to the formation of a smaller corner recirculation vortex. Then the pressure inside the confinement got to its peak in the oscillation loop. After that, the mass flow rate suddenly increased at the burner exit to maintain the time averaged mass flow rates constant at the set value. Hence the local flow velocity became higher than the turbulent burning velocity of premixed CH4-air. Therefore, the flame suddenly became much weaker and more

Please cite this article in press as: Tong Y, et al., Experimental study on dynamics of a confined low swirl partially premixed methane-hydrogen-air flame, International Journal of Hydrogen Energy (2017), https://doi.org/10.1016/j.ijhydene.2017.09.066

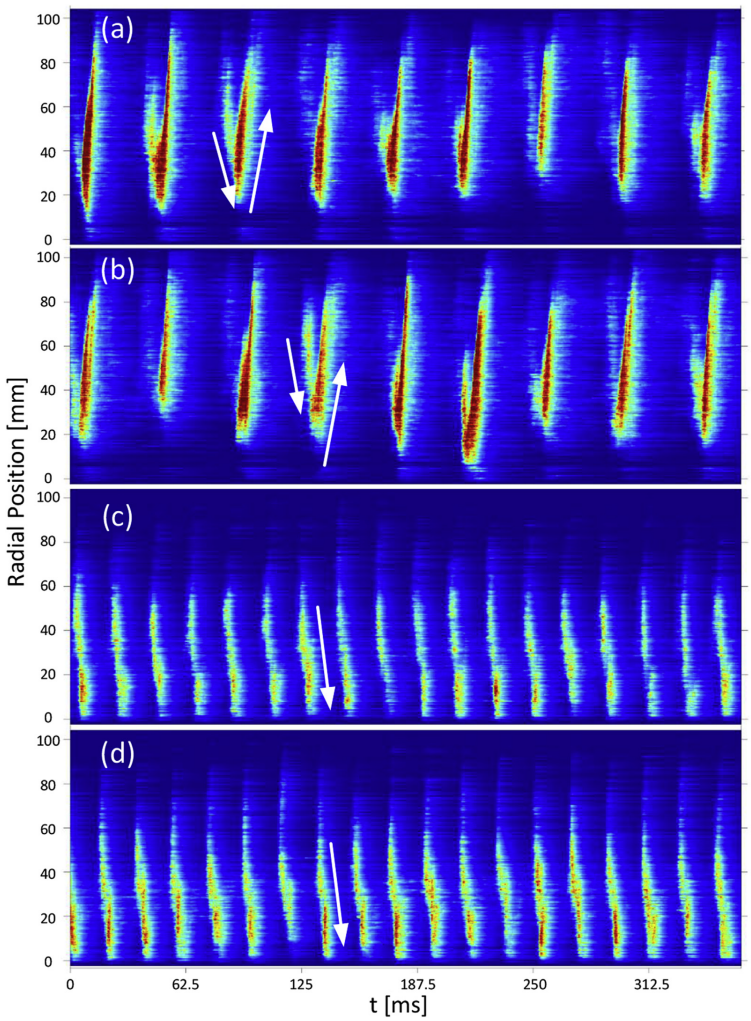

Fig. 12 – Paths of flame segment in the center line for (a) case A-S28, (b) case A-S31, (c) case T-S33 and (d) case T-S31 near lean blowout at $\Phi_g = 0.62$.

homogeneously distributed in the confinement than the 'flashback' flame root. Meanwhile, lots of unburnt reactants were pushed into the confinement which might be combusted under a sufficient temperature and radical conditions. Because of the weak combustion, the local pressure inside the confinement decreased and then the air flow rate dropped as well. Hence the flame oscillation loop was formed. The same as summarized in Ref. [13], the flame oscillation loop and its connections with pressure dynamics are schematically shown in Fig. 15. The flame oscillation is caused by the interaction of oscillations of pressure, mass flow rate together with the change of flow fields.

For case A-S28 and case T-S33, the flame behaves differently under conditions far from or near lean blowout. The differences in turbulent flame speed, fuel distribution and thus the pressure oscillations and flow fields variations might contribute to the differences in flame appearances. To be more specifically, for case T-S33 and $\Phi_g = 0.85$, compared with

Please cite this article in press as: Tong Y, et al., Experimental study on dynamics of a confined low swirl partially premixed methane-hydrogen-air flame, International Journal of Hydrogen Energy (2017), https://doi.org/10.1016/j.ijhydene.2017.09.066

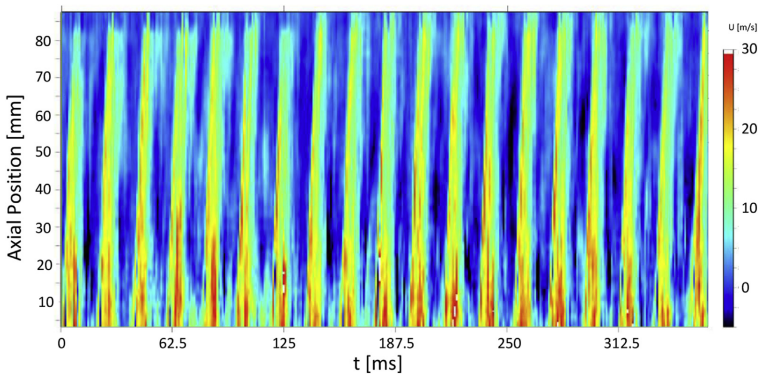

Fig. 13 – Flow field segment paths in the center line for case T-S33 and $\Phi_g = 0.62$.

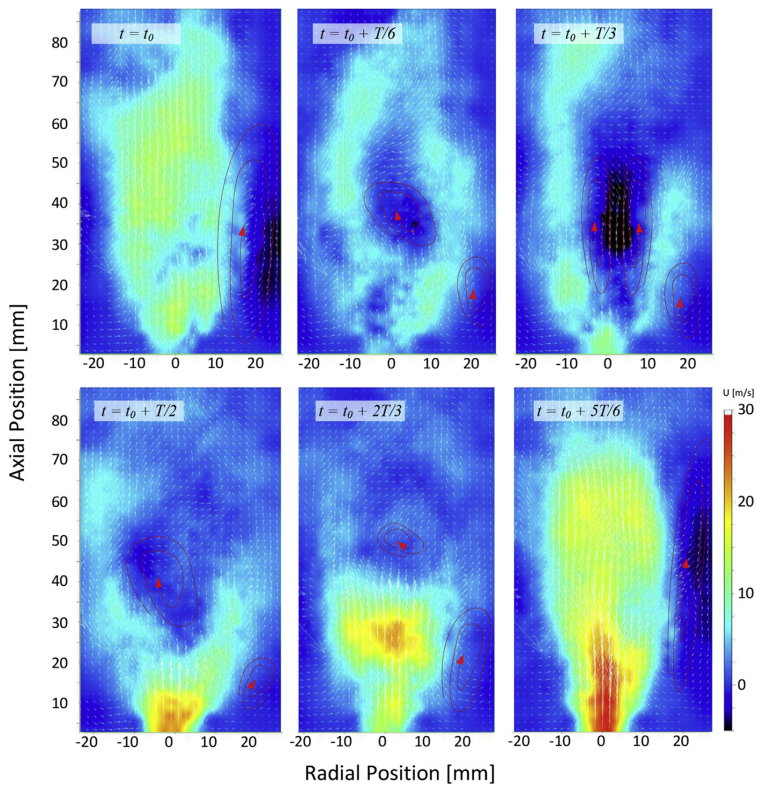

Fig. 14 – Phase locked flow fields in case T-S33 and $\Phi_g = 0.62$.

Please cite this article in press as: Tong Y, et al., Experimental study on dynamics of a confined low swirl partially premixed methane-hydrogen-air flame, International Journal of Hydrogen Energy (2017), https://doi.org/10.1016/j.ijhydene.2017.09.066

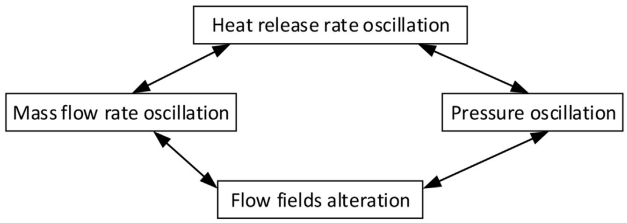

Fig. 15 – Schematic of flame dynamics loop.

the lean conditions $\Phi_g = 0.62$, the flame could propagate into the corner recirculation zone due to the locally fuel richer condition there; while it did not flashback into the premixing tube due to the locally higher flow velocity at the burner exit. The flame oscillation and flow fields dynamics interact with each other, especially under fuel lean conditions near blowout. Pressure dynamics promoted the alternation of flow fields, while the mass flow rate and thus the combustion oscillations were enhanced as a consequence. In the end, the pressure dynamics got strengthened as well, forming the combustion dynamics loop. The low flow swirl number investigated in the paper, $S \approx 0.31$, was near the boundary between the flow conditions with and without reversal flows in the center axis [39]. An increase in the swirl number could cause vortex breakdown in the flow. In the fuel lean conditions, the strong flame dynamics and hence the pressure oscillation caused the change of flow field and thus led to the vortex breakdown. Therefore, with tangential fuel injection strategy in the current paper, the flame flashback could occur in the fuel lean conditions. However, the flame flashback was more commonly observed in fuel rich conditions, such as in literatures [39,40], due to the increase of the flame speed and thus the imbalance with the local flow velocity. Here in the current paper, as reported in Ref. [27], the flame flashback was caused by the flame and flow instabilities near blowout. Further decreasing the global equivalence ratio resulted in a further increase in combustion oscillation and finally led to flame blowout.

Comparing case A-S28 with case T-S33, we found that the oscillation frequency in case T-S33 was higher than the other one. In addition, flame flashback and vortex breakdown were not observed in case A-S28. Different flame behaviors were caused by the differences in the fuel concentrations near the burner exit in these two cases. In case T-S33, more fuel could be found near the wall of the premixing tube. In addition, because of the boundary layer near the premixing tube wall, the local flow velocity might be lower than the turbulent flame speed. It was thus the flame flashing back into the premixing tube could take place in case T-S33. However, in case A-S28, more fuel was distributed near the center of the burner axis, hence the flame could not be expanded into the corner recirculation zone. As a consequence, the flow vortex breakdown could not be generated. Therefore, the flame flashback caused by the combustion induced vortex breakdown (CIVB) could not happen. In addition, under the locally lean condition near the premixing wall, the boundary layer flashback could neither occur. Without the significant change in flow structures in case A-S28 from $\Phi_g = 0.85$ to $\Phi_g = 0.62$, the flame was more compact and more stable than that in case T-S33.

Effects of equivalence ratio on flame behaviors

As described previously, a reduction of the global equivalence ratio would change the flame structures and finally lead to flame blowout. The flame's center of heat release (H_{COHR}) and flame length (L_F) were also determined by Φ_g, as shown in Fig. 16. The location of flame's center of heat release (H_{COHR}) was higher in case A-S28 than that in the other case. For case T-S33, with the alternation of methane flow rates, the flame's center of heat release stayed constant at $H_{COHR} = 20$ mm. However, this did not indicate that the flames in case T-S33 were more stable than that in cases with the other fuel injection strategy. In Fig. 16, it can be seen that the representative flame length changed significantly in case T-S33. When $\Phi_g < 0.68$, the flame length in case T-S33 was shorter than that in the comparatively rich conditions. A notable change in flame shape and strong flame oscillation were captured accompanied with the change of flame length. When $\Phi_g > 0.68$, in case T-S33, the time average flame shape was bell shape; however, when $\Phi_g < 0.68$, flame flashback occurred and the time averaged flame had the heart shape. In all the two cases shown in Fig. 16, the flame length increased more or less when approaching blowout with the reduction of Φ_g. The injection of fuel in the axial flow had the more stable flame length at $L_F = 50$ mm which might contribute to the lower flame blowout limits.

Based on the image analysis methods described previously in the paper, effects of Φ_g and fuel injection strategies on flame dynamic frequencies could be seen from Fig. 17. It could be observed that when the global equivalence ratio was high ($\Phi_g > 0.72$), all the flames had a high frequency oscillation at $f \approx 170$ Hz. It might be the natural frequency of the combustor system with the swirling flow. In addition, with the reduction of Φ_g, stronger flame oscillations showed up with a lower dominant frequency. Near flame blowout, cases with the axial fuel injection methods had the flame oscillation at $f \approx 20$ Hz, whereas the other cases had the dominant flame oscillation frequency higher at $f \approx 50$ Hz. The significant change of the dominant frequency took place when the global equivalence

Please cite this article in press as: Tong Y, et al., Experimental study on dynamics of a confined low swirl partially premixed methane-hydrogen-air flame, International Journal of Hydrogen Energy (2017), https://doi.org/10.1016/j.ijhydene.2017.09.066

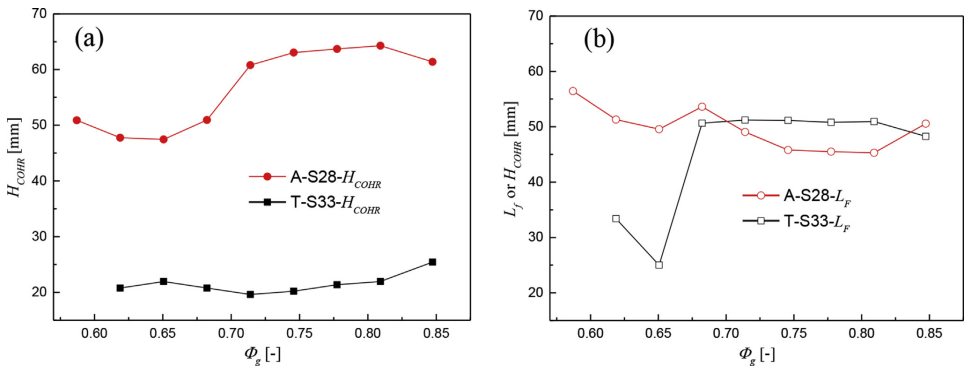

Fig. 16 – (a) H_{COHR} and (b) L_F versus global equivalence ratio (Φ_g).

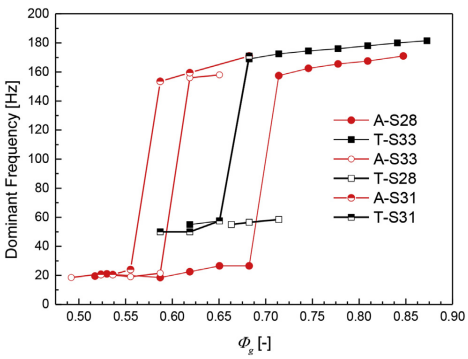

Fig. 17 – Dominant frequency versus the global equivalence ratio (Φ_g).

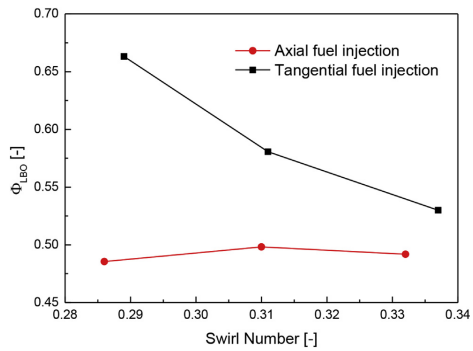

Fig. 18 – LBO limits versus swirl number with different fuel injection methods.

ratio was between $0.55 < \Phi_g < 0.72$. The fuel injection strategy strongly determined the flame oscillation frequency and flame structures near lean blowout. While a slight change of the swirl strength (from S = 0.28 to S = 0.31) did not have significant influences on flame dynamics in the current investigation. The fuel distribution at the burner exit was believed to be the reason behind for this phenomenon.

The fuel injection strategy could also affect the lean blowout limits (Φ_{LBO}), as shown in Fig. 18. The flame lean blowout was obtained by slightly decreasing of the mass flow rate of CH_4 (at steps of 0.2SLPM) while holding the mass flow rate of H_2 constant till flame was visually absent from the confinement. The tangential fuel injection method resulted at a higher Φ_{LBO}, which indicated a worse performance in stabilizing the flame. It was caused by the strong flame oscillation together with the unstable behavior of flame shape alternation near lean blowout. From the time averaged flame shape shown in Fig. 10, it could be observed that the flame with fuel in the tangential direction was less compact than the other fuel injection cases. It would also result in a higher blowout limits. The flame structures were strongly determined by the fuel distributions at the burner exit.

From Fig. 18 it could also be found that, the alteration of swirl number slightly changed the blowout limits in cases with the axial fuel injection method. A stronger influence of swirl number on Φ_{LBO} in case with the tangential fuel injection strategy was observed. More detailed investigations about the flame blowout and its correlation with the change of flame shapes and flame oscillations are needed here.

Conclusions

Flame structures and dynamics were studied with different methane-hydrogen injection strategies. Different fuel injection methods within a low swirl number (S ≈ 0.31) flow were

Please cite this article in press as: Tong Y, et al., Experimental study on dynamics of a confined low swirl partially premixed methane-hydrogen-air flame, International Journal of Hydrogen Energy (2017), https://doi.org/10.1016/j.ijhydene.2017.09.066

investigated and compared with each other. High speed intensified and filtered CH* CMOS camera was used to visualize the flame structures, while high speed PIV system was adopted to capture the dynamics of the flow fields. It is found that the flame shape and flame dynamics were strongly determined by the fuel injection methods. Under conditions with a comparatively higher global equivalence ratio (Φ_g = 0.85), the tangential fuel injection flames had a bell shape, while in the other cases the flame was more compact. Flame with fuel injected in the axial direction had a higher location of flame's center of heat release (H_{COHR}). With tangential fuel injection, the flame changed its shape to heart shape when the global equivalence ratio got lower approaching lean blowout. When the global equivalence was low, the vortex breakdown was observed in cases with the tangential fuel injection strategy. Higher frequency (f = 170 Hz) oscillations were observed in flames with higher global equivalence ratio, while lower frequency oscillations (f = 50 Hz and f = 20 Hz) were found near lean blowout limits. Combustion dynamic and its interaction with the pressure oscillation, flow fields alternation and mass flow rate oscillation were proposed. Axial injection of fuel in the current study was found to be able to better stabilize the flame with leaner blowout limits. The distribution of fuel at the burner exit in the partially premixed flame was proposed as the main reason for different flame instabilities and flame structures. More computational investigations about the flow structures and scalar fields are needed.

Acknowledgements

Authors Yiheng Tong, Senbin Yu and Xiao Liu would like to thank the financial support from the China Scholarship Council (CSC).

REFERENCES

[1] Lawn C. Interaction of the acoustic properties of a combustion chamber with those of premixture supply. J Sound Vib 1999;224:785–808.
[2] Boschek E, Griebel P, Erne D, Jansohn P. Lean blowout limits and NOx emissions of turbulent, lean premixed, high pressure CH4/H2/air flames. In: Eighth international conference on energy for a clean environment-clean air; 2005.
[3] Schefer R. Hydrogen enrichment for improved lean flame stability. Int J Hydrogen Energy 2003;28:1131–41.
[4] Halter F, Chauveau C, Gökalp I. Characterization of the effects of hydrogen addition in premixed methane/air flames. Int J Hydrogen Energy 2007;32:2585–92.
[5] Guo H, Tayebi B, Galizzi C, Escudié D. Burning rates and surface characteristics of hydrogen-enriched turbulent lean premixed methane–air flames. Int J Hydrogen Energy 2010;35:11342–8.
[6] Emadi M, Karkow D, Salameh T, Gohil A, Ratner A. Flame structure changes resulting from hydrogen-enrichment and pressurization for low-swirl premixed methane–air flames. Int J Hydrogen Energy 2012;37:10397–404.
[7] Tuncer O, Acharya S, Uhm JH. Dynamics, NOx and flashback characteristics of confined pre-mixed hydrogen enriched methane flames. In: ASME turbo expo 2007: power for land, sea, and air. American Society of Mechanical Engineers; 2007. p. 857–68.
[8] Cheng R, Littlejohn D, Strakey P, Sidwell T. Laboratory investigations of a low-swirl injector with H 2 and CH 4 at gas turbine conditions. Proc Combust Inst 2009;32:3001–9.
[9] Cowell L, Etheridge C, Smith K. Ten years of DLE industrial gas turbine operating experiences. In: ASME turbo expo 2002: power for land, sea, and air. American Society of Mechanical Engineers; 2002. p. 1123–35.
[10] Strakey P, Sidwell T, Ontko J. Investigation of the effects of hydrogen addition on lean extinction in a swirl stabilized combustor. Proc Combust Inst 2007;31:3173–80.
[11] Sayad P, Schönborn A, Klingmann J. Experimental investigation of the stability limits of premixed syngas-air flames at two moderate swirl numbers. Combust Flame 2016;164:270–82.
[12] Tong Y, Li M, Klingmann J. Influence of combustor geometry on swirl stabilized premixed methane-air flame. In: ASME turbo expo 2016 turbomachinery technical conference and exposition. American Society of Mechanical Engineers; 2016. V04BT04A002–V004BT004A002.
[13] Kim M-K, Yoon J, Park S, Lee M-C, Yoon Y. Effects of unstable flame structure and recirculation zones in a swirl-stabilized dump combustor. Appl Therm Eng 2013;58:125–35.
[14] Guiberti T, Durox D, Scouflaire P, Schuller T. Impact of heat loss and hydrogen enrichment on the shape of confined swirling flames. Proc Combust Inst 2015;35:1385–92.
[15] Wu Y. Large eddy simulation of turbulent swirling flows in combustor related geometries. 2013.
[16] Schefer RW, Wicksall D, Agrawal A. Combustion of hydrogen-enriched methane in a lean premixed swirl-stabilized burner. Proc Combust Inst 2002;29:843–51.
[17] Kim HS, Arghode VK, Linck MB, Gupta AK. Hydrogen addition effects in a confined swirl-stabilized methane-air flame. Int J Hydrogen Energy 2009;34:1054–62.
[18] Kim HS, Arghode VK, Gupta AK. Flame characteristics of hydrogen-enriched methane–air premixed swirling flames. Int J Hydrogen Energy 2009;34:1063–73.
[19] Stöhr M, Arndt CM, Meier W. Transient effects of fuel–air mixing in a partially-premixed turbulent swirl flame. Proc Combust Inst 2015;35:3327–35.
[20] Meier W, Dem C, Arndt C. Mixing and reaction progress in a confined swirl flame undergoing thermo-acoustic oscillations studied with laser Raman scattering. Exp Therm Fluid Sci 2016;73:71–8.
[21] Yin Z, Nau P, Meier W. Responses of combustor surface temperature to flame shape transitions in a turbulent bi-stable swirl flame. Exp Therm Fluid Sci 2017;82:50–7.
[22] Dinesh KR, Luo KH, Kirkpatrick M, Malalasekera W. Burning syngas in a high swirl burner: effects of fuel composition. Int J Hydrogen Energy 2013;38:9028–42.
[23] Reichel TG, Paschereit CO. Interaction mechanisms of fuel momentum with flashback limits in lean-premixed combustion of hydrogen. Int J Hydrogen Energy 2017;42:4518–29.
[24] Meier W, Duan XR, Weigand P. Reaction zone structures and mixing characteristics of partially premixed swirling CH 4/air flames in a gas turbine model combustor. Proc Combust Inst 2005;30:835–42.
[25] Meier W, Weigand P, Duan X, Giezendanner-Thoben R. Detailed characterization of the dynamics of thermoacoustic pulsations in a lean premixed swirl flame. Combust flame 2007;150:2–26.
[26] Biagioli F, Güthe F, Schuermans B. Combustion dynamics linked to flame behaviour in a partially premixed swirled industrial burner. Exp Therm Fluid Sci 2008;32:1344–53.
[27] Sommerer Y, Galley D, Poinsot T, Ducruix S, Lacas F, Veynante D. Large eddy simulation and experimental study

Please cite this article in press as: Tong Y, et al., Experimental study on dynamics of a confined low swirl partially premixed methane-hydrogen-air flame, International Journal of Hydrogen Energy (2017), https://doi.org/10.1016/j.ijhydene.2017.09.066

of flashback and blow-off in a lean partially premixed swirled burner. J Turbul 2004;5:1–3.
[28] Sengissen A, Van Kampen J, Huls R, Stoffels G, Kok J, Poinsot T. LES and experimental studies of cold and reacting flow in a swirled partially premixed burner with and without fuel modulation. Combust flame 2007;150:40–53.
[29] Guiberti TF, Durox D, Zimmer L, Schuller T. Analysis of topology transitions of swirl flames interacting with the combustor side wall. Combust flame 2015;162:4342–57.
[30] Lee JG, Gonzalez E, Santavicca DA. On the applicability of chemiluminescence to the estimation of unsteady heat-release during unstable combustion in lean premixed combustor. AIAA; 2005. Paper, 3575.
[31] De Rosa AJ, Peluso SJ, Quay BD, Santavicca DA. The effect of confinement on the structure and dynamic response of lean-premixed, swirl-stabilized flames. J Eng Gas Turbines Power 2016;138, 061507.
[32] Schuermans B, Bellucci V, Guethe F, Meili F, Flohr P, Paschereit CO. A detailed analysis of thermoacoustic interaction mechanisms in a turbulent premixed flame. In: ASME Turbo Expo 2004: power for Land, Sea, and Air. American Society of Mechanical Engineers; 2004. p. 539–51.
[33] Asgari N, Ahmed SF, Farouk TI, Padak B. NO x formation in post-flame gases from syngas/air combustion at atmospheric pressure. Int J Hydrogen Energy 2017.
[34] Emadi M, Karkow D, Melendez A, Ratner A. Parameter variations and the effects of hydrogen: an experimental investigation in a lean premixed low swirl combustor. Int J Hydrogen Energy 2013;38:5401–9.
[35] Sayad P, Schönborn A, Klingmann J. Experimental investigations of the lean blowout limit of different syngas mixtures in an atmospheric, premixed, variable-swirl burner. Energy Fuels 2013;27:2783–93.
[36] Kheirkhah S, Gülder ÖL, Maurice G, Halter F, Gökalp I. On periodic behavior of weakly turbulent premixed flame corrugations. Combust Flame 2016;168:147–65.
[37] Tang H, Yang D, Zhang T, Zhu M. Characteristics of flame modes for a conical bluff body burner with a central fuel jet. J Eng Gas Turbines Power 2013;135, 091507.
[38] Tong Y, Li M, Thern M, Klingmann J, Weng W, Chen S, et al. Experimental investigation on effects of central air jet on the bluff-body stabilized premixed methane-air flame. Energy Procedia 2017;107:23–32.
[39] Sayad P, Schönborn A, Li M, Klingmann J. Visualization of different flashback mechanisms for H2/CH4 mixtures in a variable-swirl burner. J Eng Gas Turbines Power 2015;137, 031507.
[40] Heeger C, Gordon R, Tummers M, Sattelmayer T, Dreizler A. Experimental analysis of flashback in lean premixed swirling flames: upstream flame propagation. Exp fluids 2010;49:853–63.

Please cite this article in press as: Tong Y, et al., Experimental study on dynamics of a confined low swirl partially premixed methane-hydrogen-air flame, International Journal of Hydrogen Energy (2017), https://doi.org/10.1016/j.ijhydene.2017.09.066

Paper IV

energies

MDPI

Article

Experimental study on bluff-body stabilized premixed flame with a central air/fuel jet

Yiheng Tong [1,] *, Shuang Chen [2], Mao Li [1], Zhongshan Li [3] and Jens Klingmann [1]

[1] Department of Energy Sciences, LTH, Lund University, Lund Sweden;
[2] China Aerodynamics Research and Development Center, Mianyang China;
[3] Division of Combustion Physics, LTH, Lund University, Lund Sweden;
* Correspondence: yiheng.tong@energy.lth.se; Tel.: +46-073-762-9877

Academic Editor: name
Received: date; Accepted: date; Published: date

Abstract: Bluff-body flame holders are commonly employed in many industrial applications. A bluff-body is usually adopted to enhance the downstream mixing of the combustion products and the fresh fuel-air mixtures, thus to improve the flame stability and to control the combustion process. In the present paper, a conical bluff-body flame holder with a central air or fuel jet was studied. Effects of both a central fuel jet and a central air jet on the flame structures, on the blowout limits and on the temperature at the upper surface of the bluff-body were investigated and presented. It was revealed that a central air or fuel jet led to the temperature at the surface of the bluff-body reduced considerably. Thus, it might be used to solving the problem of the bluff-body with high heat loads to it in practical applications. The flame stability characteristics, for example the unstable flame structures and the blowout limits, altered with the injection of a central air or fuel jet. Different blowout behaviors, being with or without the occurrence of flame split and flashing, caused by a central air jet were observed and presented in the paper. In addition, when a small amount of central fuel jet (i.e. $U_f / U_a = 0.045$) was injected into the flow fields, an unsteady circular motion of the flame tip along the outer edge of the bluff-body was observed as well. Whereas, whit an increase in the amount of the central fuel jet, the flame detached from the bluff-body and then became much more unstable. It was found that with a central air or fuel jet injecting into the flow field, the bluff-body stabilized premixed flame became more unstable and easier to blowout.

Keywords: bluff-body; premixed flame; flame structures, flame instabilities, lean blowout

1. Introduction

Premixed flame stabilization has been a subject of significant technological interest for various industrial applications, such as in gas turbines, afterburners, heat recovery steam generators, and industrial furnaces [1]. There are two main flame stabilization schemes employed in premixed combustion systems, including the use of a swirling flow and the use of a bluff-body. A bluff-body is adopted to stabilize the premixed flame due to its simple geometry, the enhanced mixing of reactants and combustion products as well as the ease of combustion control. The recirculation of hot gas downstream of a bluff-body can help to reignite the reactant mixtures and thus to stabilize the flame [2]. The practical importance of a stable flame has given rise to a large number of theoretical and experimental studies about the performance of a bluff-body in stabilizing the flame.

A number of seminal works of bluff-body stabilized premixed flame has been carried out by Zukoski [3,4], Longwell [5,6], Wright [7] and Pan [8]. Researchers concerned mainly with the blowout mechanisms and the lean stabilization limits of the flame for a bluff-body flame holder. Lefebvre et al. [9] studied the effects of inlet air temperature, pressure, velocity, turbulence and bluff-body geometry on the lean blowout performance of bluff-body flame holders. It was recommended by

Lefebvre et al. [9] and Barrere and Mestre [10] that the characteristic dimension of a bluff-body flame holder should not be its geometric width, but rather the maximum aerodynamic width of the wake created downstream of it. Shanbhogue et al. [11] reviewed the dynamics of two-dimensional bluff-body stabilized flames and described the phenomenon of the blowout process in the bluff-body flame holder. They concluded that blowout occurs in multiple steps, associated with local extinction along the flame sheet and large scale wake disruption, followed by blowout whose ultimate 'trigger' is probably associated with wake cooling and shrinking. The first phase of blowout, when the appearance of holes along the flame sheet (where the local strain rate exceeds the extinction strain rate), can be correlated with the local Damköhler number. Chaparro and Baki [12] studied blowout characteristics of bluff-body stabilized conical premixed flames under inlet velocity modulations using three different bluff-body geometries. Flame blowout features in cases with different upstream flow velocities (5, 10 and 15 m/s) and excitation frequencies (from 0 to 400 Hz) were studied. They concluded that the disk-shaped bluff-body provided better flame stability than the rod-shaped flame holder due to the much more significant flow separation and higher degree of wake recirculation for the disk-shaped flame holder. Chaudhuri et al. [13] examined the blowout characteristics of bluff-body stabilized conical premixed flames in a duct with upstream spatial mixture gradients and velocity oscillations. They revealed that the blowout equivalence ratios were higher for the confined flame configuration than the unconfined cases. It was also concluded that: the fuel enrichment near the flame stabilization region reduced the base blowout equivalence ratios significantly. The bluff-body stabilized flame had the features of a centrally piloted flame, with much of the outer flow remaining unburnt at low equivalence ratios. Chaudhuri et al. [14] also summarized and illustrated the hypothesis of blowout mechanism for bluff-body stabilized turbulent premixed flame. A change of flame shape between conical and columnar shapes was observed with the changing of equivalence ratio of the premixed fuel-air mixture. The unstable flame behavior (local extinction and reignition) near blowout was recorded and presented as well. Combustion characteristics of premixed hydrogen/air flame in a micro-combustor with a bluff body was studied experimentally and numerically by Jianlong et al.[15]. Effects of bluff-body geometry on the lean stabilization limits of premixed hydrogen/air flame in a micro-combustor were investigated numerically by Fan et al. [16] and Bagheri et al.[17]. Fan et al. [16] claimed that the difference of flame blowout limits for different bluff-body geometries was caused by the alternation of recirculation zone and flame stretching. The heat lost to the confinement wall was considered to have a negligible effect on the flame blowout limits. Moreover, Fan et al. [18] also concluded that solid materials of the bluff-body with relatively low thermal conductivity and emissivity were beneficial to obtain a large blowout limit.

A bluff-body with a central jet is commonly utilized to stabilize the diffusion flame. Roquemore et al. [19] studied the behavior of reacting and non-reacting flows in an axisymmetric bluff-body burner. They obtained the mixing features of fuel and air downstream of the bluff-body with a central fuel jet. It was concluded that in the cold flow without combustion the flow field downstream of the bluff-body was determined by the velocity ratio of the annular and central jet. Illustration of the time-averaged flow field of a bluff-body with a central jet from [19] is shown in Fig.1. With the increasing of the ratio of central jet and annular flow velocity, the flow field varied from annular jet dominating to neither jet dominating and finally to central jet dominating. Caetano et al. [20] presented three different flame types: (i) a fuel jet dominated flame, (ii) a lifted flame with an intermittent anchoring region and (iii) a fully lifted partially premixed flame in their experimental work. They also observed the similar flow structures as that shown in Figure 1 in both non-reacting and acting flow cases using particle image velocimetry (PIV) measurement. In their examined situations, combustion presented a weak effect on the averaged velocity field. Based on the change of the central jet to annular air velocity ratio together with the corresponding flow structures, Esquiva-Dano et al. [21] summarized six different regimes of non-premixed bluff-body stabilized flames. They also divided the wake structures downstream of the bluff-body into three regimes based on the number of the stagnation points in the flow field. Flow fields with tow stagnation points (the aft and forward stagnation points) corresponded to annular flow dominating flow field, only one stagnation point indicated neither jet dominated the flow structures while zero stagnation point was in the flow field with central jet

dominating. By comparing with the disk shape flame holder, they claimed that the tulip shape flame holder which caused weaker turbulence downstream of the bluff-body promoted flame stabilization. Schefer et al. [22] investigated the effects of confinement on bluff-body stabilized burner recirculation zone and flame stabilities. They found that the recirculation zone characteristics and flame stability were highly depended on the confinement diameter or the blockage ratio. They claimed that the fuel concentration in the recirculation zone played an important role in determining the flame behavior. Tang et al. [23] presented an experimental investigation about bluff-body stabilized non-premixed flame. The effect of both the annular air and central jet Reynolds numbers were studied and conclusions were made as: the central fuel Reynolds number mostly determined whether the extinction phenomenon appeared, while the annular air Reynolds number affected the configuration of the flame under both stable and unstable conditions.

To the author's best knowledge, there are limited number of research concerning with the heat load to the bluff-body. Nishimura et al. [24] utilized a fine wire thermocouple to study the temperature fluctuations of the diffusion flame in a bluff-body burner. The temperature distribution along the axial line of the burner including the surface of the bluff-body temperature was presented. But they focused more on the interaction of the unstable flame and thermal structures. Euler et al. [25,26] measured the surface of the bluff-body temperature of the Cambridge/Sandia Stratified Swirl Burner using laser induced phosphor thermometry. Different premixed and stratification cases with/without swirl were tested. They concluded that the overall operation of the burner was adiabatic since the radiative and convective heat transfer by the bluff-body amounted to less than 0.5% of the thermal input from the combustion. They also mentioned that there were few measurements of the flame holder's temperature distribution, whereas that temperature strongly affected the flame stabilization. In fact, in practical applications in Gas Turbine combustors, the challenge of the bluff-body is the sever heat load and extremely high temperature on the surface of the bluff-body. The heat load to the bluff-body could strongly affect the stability limits of the premixed flame [27]. Moreover, temperature distributions at the surface of the bluff-body are important to the lifetime of a combustion system [28]. Some practical methodologies to reduce the heat load to the surface of the bluff-body are needed.

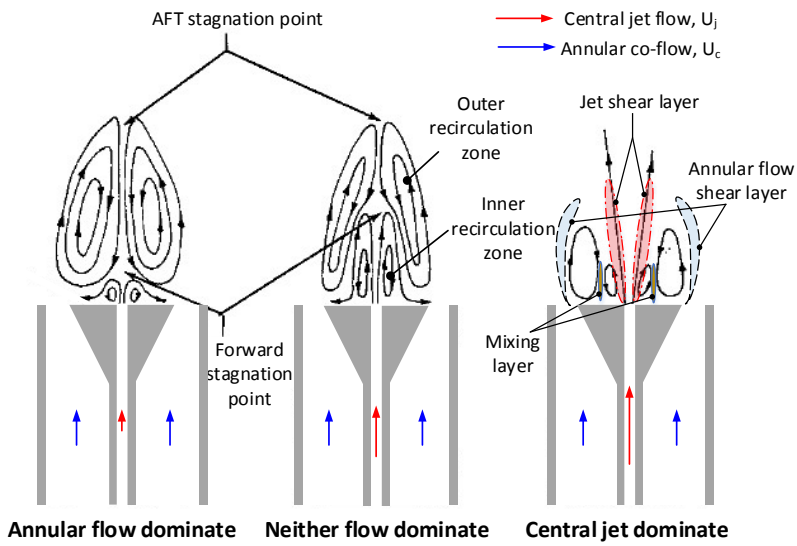

Figure 1. A schematic of the time-averaged flow fields downstream of a bluff-body with a central jet (reproduced from [19])

As summarized above, little effort has been made to investigate the effect of a central jet on the temperature on the surface of the bluff-body and on the premixed flame stabilization. Thus, in the paper, the effects of a central air/fuel jet on the bluff-body stabilized premixed methane-air flame are investigated. Emphasis is made on the temperature on the surface of the bluff-body, on the flame structures, on the flame blowout features and on their interactions.

2. Apparatus and methods

2.1. Experimental setup

As shown schematically in Figure 2, the burner having an annular channel with a 45° conical bluff-body in the center was employed. The inner diameter of the annular channel for the main premixed methane-air flow was d_a = 30mm. The removable stainless steel bluff-body had a top diameter of d_b = 14mm, while the inner diameter for the central jet flow being d_j = 4mm. Premixed methane-air was fed into the annular channel, while pure air flow or pure fuel flow being injected through the central pipe. A ceramic honeycomb was mounted in the annular channel in order to generate a uniform annular flow and to avoid flame flashing back into a further upstream region.

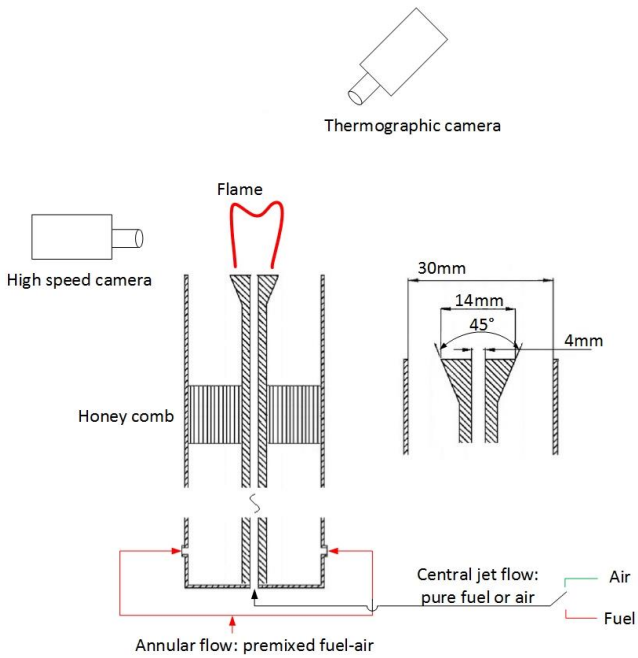

Figure 2. A schematic of the experimental setup and the burner

Three Bronkhorst mass flow controllers were utilized to control the mass flow rates of the central air/fuel jet together with the fuel flow in the annular flow. An Alicat (MCR 150) mass flow controller was employed to control the mass flow rate of the air flow in the annular channel. The mass flow rate that was controlled by Bronkhorst mass flow controllers were calibrated at 300K with an uncertainty of 1%. The bulk velocity of the premixed annular flow (which was calculated on the basis of the exit geometry of the burner) was in the range of 1.85 to 2.77m/s, while the equivalence ratio being set to between $\Phi = 0.64$ to lean blowout limits. When $\Phi = 0.64$, a stable flame could be obtained. The velocity of the central air jet varied between U_a = 0 and 29m/s, while the central fuel velocity ranging from U_f = 0 to 1.33m/s. All experiments were carried out without confinement under the atmospheric conditions.

2.2. High-speed photography

A high-speed photography technique and a thermographic camera were adopted for studying the flame structures and the temperature distribution on the surface of the bluff-body, respectively. A high-speed CMOS camera (Vision Research Phantom V611) having resolution of 800×1280 pixels and depth of 12 bit was utilized to record the broad-band chemiluminescence from the flame. Since the chemiluminescence intensity varied with the equivalence ratio of the annular flow and with the heat release rate from the flame, the frame recording rate altered according to the signal intensity. During the experiments, the recording rate was set between 200fps to 800fps to study the dynamics of the flame. A lower recording rate ensured a longer exposure time for obtaining more chemiluminescence signal from for each frame of the flame. Digital image process was fulfilled based on the DaVis (v.8.1.4) software and the in-house developed Matlab code. Time-averaged and RMS of the flame chemiluminescence were used to evaluate the flame structures and its instabilities.

2.3. Thermography

An infrared thermographic camera (Testo 881-3) was utilized to record the temperature distribution on the surface of the bluff-body. The burner was un-confined ensuring the recording of the temperature on the surface of the bluff-body practical and reliable. The thermographic camera was placed above the burner, as shown in Figure 2. The angle between the burner axis and the thermographic camera's focus plane was approximately 45°. The thermographic camera could record both infrared image (with a spatial resolution of 320×240 pixels) and the real image simultaneously.

Figure 3 shows the typical infrared image of the surface of the bluff-body and its temperature distribution at the symmetric plane along the radial direction. The same as presented in the literature [25], the temperature distribution peaked in the center of the bluff-body. In the present study, however, the high temperature distribution at -2mm < r < 2mm was probably caused by the reflection of infrared light from the curved inner wall of the injection hole. So here in the study, temperature data in the center injection hole was treated as noise and thus deleted in the analysis process. The temperature at the inner edge of the central injection hole is selected and analyzed as the representative temperature T_{edge}. Based on data from [29], the emissivity (ε) of stainless steel type 301 is within the range of 0.54 to 0.63. In the base case without any central jet, setting the emissivity ε = 0.58, the annular flow equivalence ratio Φ = 0.64, U_c = 2.77m/s and U_j = 0m/s, the temperature T_{edge} was approximately 480K, which was referred to as T_0 as the base case in the paper. In order to minimize the error caused by the selecting of the emissivity of the material, the ratio of local temperature to T_0 in different experimental cases was used to evaluate the temperature variances caused by the injection of central jet. The error of the ratio caused by selecting the emissivity from 0.54 to 0.63 was within 2%. Figure 3 also shows the distribution of the ratio of local temperature to the base case temperature (T/T_0) along the radius direction on the surface of the bluff-body.

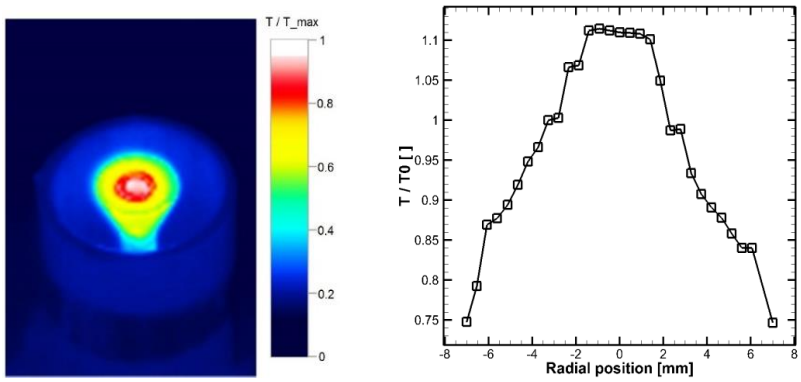

Figure 3. Typical infrared image (left) and temperature distribution along the radius direction (right)

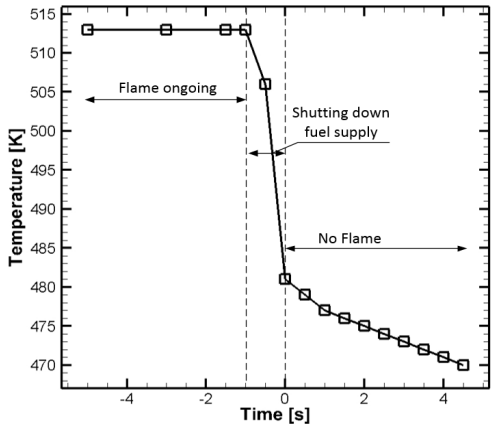

Figure 4. Typical temperature changes of T_{edge} during shutting down the fuel supply

In order to obtain a thermodynamic equilibrium of the bluff body, the flame was maintained stable for at least 5mins, the maximum temperature being showed in the thermographic camera stayed constant for at least 2mins. Then the fuel supply was shut down and the variance of T_{edge} was recorded, as shown in Figure 4. The flame could radiate infrared light which would strongly affect the thermographic results. So the temperature on the surface of the bluff-body was recorded continually since the flame was ongoing until the flame quenched completely, with a recording rate for the thermographic camera at f = 2Hz. A typical temperature variance of T_{edge} during that procedure was shown in Figure 4. When the flame was ongoing, T_{edge} remained stable, indicating a stable flame and a thermodynamic equilibrium condition on the surface of the bluff-body. At the same time, when the flame was ongoing, it could be found that T_{edge} was higher due to the infrared light from the flame. Afterwards, with the shutdown of the fuel supply, the temperature on the surface of the bluff-body dropped considerably. The temperature gradient was sharp initially since a weak flame was remained attaching to the bluff-body. This weak flame was maintained by the fuel that was left in the fuel supply pipe. When the flame vanished completely, the temperature on the surface of the bluff-body decreased slowly, due to the heat convection from the bluff-body to the environment. As shown in Figure 4, the time when the flame quenched completely was set as the time t = 0s. After that, the temperature decreased at a rate of less than 4K/s, which was much lower than that during the fuel shut down procedure. So the representative temperature of the bluff-body T_{edge} was selected at t < 1s after the flame quenched completely. The corresponding error for the temperature selection was within 2%.

3. Results and discussions

3.1. Flame structures

With the injection of a central air/fuel jet, the flame structures change significantly. The time-averaged and the RMS of flame structures under different test conditions are shown in Figure 5 and in Figure 7, when holding the frame recording rates at 500 fps. Effects of a central air jet on the annular premixed methane-air flame structures are shown in Figure 5, when holding U_c = 1.85m/s and Φ = 0.64.

It can be observed from Figure 5 that without the injection of the central air jet, the heat release zone peaks along the axial downstream of the bluff-body. However, with the injection of a central air jet, the main heat release zone got apart from the burner axis. With a small amount of the central air flow (U_a/U_c = 0.79), the flame width (w, as shown in Figure 5) became broader. As that shown in Figure 1, when the annular flow dominated the recirculation zones downstream of the bluff-body,

the small amount of central air jet formed an inner vortex (with an extremely fuel-lean condition) to avoid the flame being attached to the bluff-body. The fresh air inner vortex zone is shown schematically by the white triangle in Figure 5. When the annular flow dominated the flow structures, the flame front was found to be attached to the outer edge of the bluff-body, meanwhile the central air penetrating short downstream of the flame holder. That inner vortex layer formed by the fresh and cold central air jet could also reduce the heat convection from the combusted products to the surface of the bluff-body. As what will be discussed later, it might be the reason for the decrease in the temperature on the surface of the bluff-body.

An increase in the mass flow rate of the central air jet shortened the flame, meanwhile the flame width becoming narrower. The flame was weakened and the size of the heat release zone shrank, with the increase in the velocity of the central air jet. It was caused by the overall reduction in the equivalence ratio in the main flame, with a central air injection. At the same time, with the increase in the mass flow rate of the central air jet, the area of the flame front attached to the surface of the bluff-body became enlarged. The air jet penetrated higher into the main flame zone. The same as shown in Figure 1 and in the literature [19], the flow fields might turn into *neither jet dominating*, then finally to *central jet dominating*. Further research about the flow structures and its effects on the bluff-body stabilized flame behaviors will be presented in our future study.

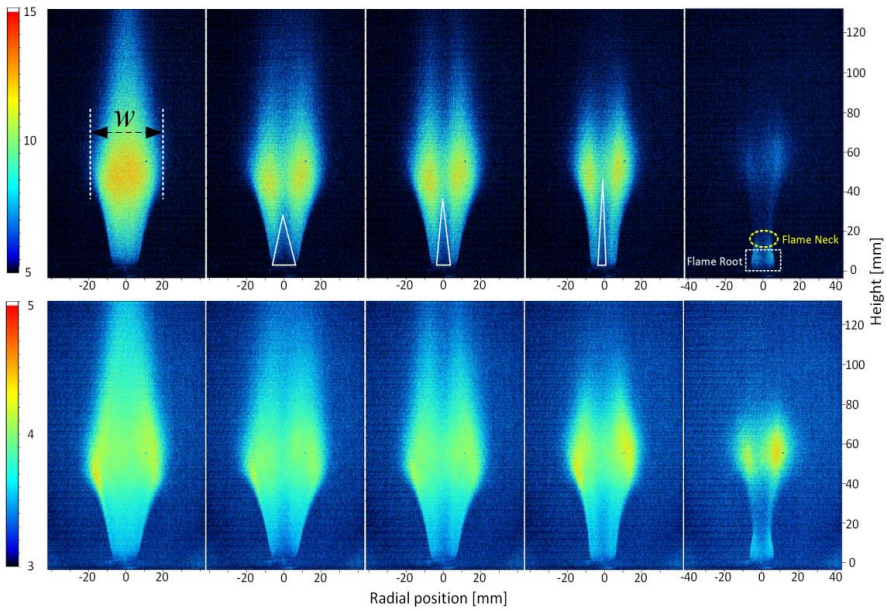

Figure 5. Time-averaged (upper row) and RMS (lower row) images of the flame structures with a central air jet (from left to right: U_a/U_c = 0, 0.79, 3.94, 7.87 and 13.22)

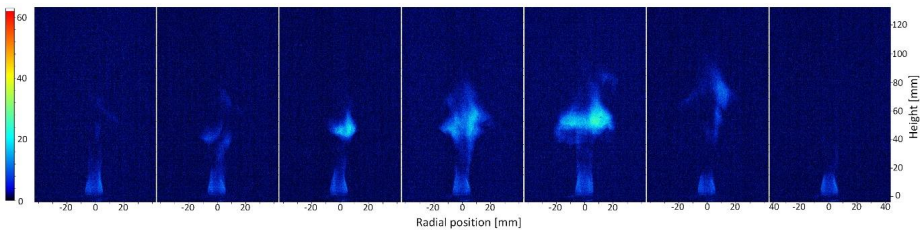

Figure 6. Flame instability near blowout due to a central air jet injection

As shown in Figure 6, the flame neck (where the flame width was narrower than the diameter of the bluff-body) showed up with a large mass flow rate of central air jet (U_a/U_c = 13.22). It was caused by the high strain rate at the jet shear layer. When the mass flow rate of the central air jet increased to a critical value, the flame was then interrupted by the high strain rate at the flame neck. With a further increase in the velocity of the central air jet, the flame in the far downstream region extinct, whereas only the flame root that was attached to the bluff-body being maintained. The unstable flame behavior for case in which U_a/U_c = 13.22 is shown in Figure 6, with the frame recording rate of 200fps. The lower frame recording rate was due to the weak chemiluminescence from the flame. The interval time between two adjacent images shown in Figure 6 is 25ms. As shown in Figure 6, the flame downstream of the flame neck region extinct and later re-ignited by the stable flame root. Thus, the flame was found to be flashing downstream of the flame neck together with a strong noise sound. The high strain rate, strong shear stress and the locally lean condition were believed to be reasons for the flame quenching downstream of the flame neck region. The flame root, which was attached to the bluff-body, supplied the heat and radical sources to re-ignite the fresh fuel-air mixture downstream as originated from the annular flow. The flame root was probably stabilized by the recirculation zone of the bluff-body. The behavior of the flame root was not strongly affected by the downstream flame conditions. To be more specific, the flame root could always be stabilized no matter the flashing flame downstream was ongoing or being quenched. In addition, in the RMS images in Figure 6, it is noted that the heat fluctuation peaked in the annular flow shear layer under conditions with/without a central air injection. In the region near the bluff-body (h < 20mm), the flames in all cases are stable. In the region h = 60mm, the split-flashing flame had the stronger heat fluctuation than any these in other cases.

The injection of a central fuel jet also has strong effects on the flame behavior and on its macro-structures. As shown in Figure 7, with the injection of a central fuel jet, the flame gets detached from the bluff-body. The local fuel-rich condition in the inner vortex caused the flame lifting off from the surface of the bluff-body. The liftoff height increased with the increase in the velocity of the central fuel jet. Since more heat was released with the injection of the central jet fuel, the color scale of the time-averaged flame images in Figure 7 alters with one another. In addition, it was observed that with the increase in the mass flow rate of the central fuel jet, more soot could be formed, which thus changing the color of the lean premixed methane-air flame from bluish to yellowish. The yellowish flame behaved more like a diffusion jet flame, with the annular flow acting as the oxidant. Differed from the effects of a central air jet, the central fuel injection remained the peak heat release zone location in the central axis downstream of the bluff-body. The heat release fluctuation peaked in the flame root region (h < 20mm) under the conditions with a small amount of central fuel injection (U_f/U_c < 0.089). With the increase in the mass flow rate of the central fuel jet, the heat release fluctuation peaked into the jet shear layer.

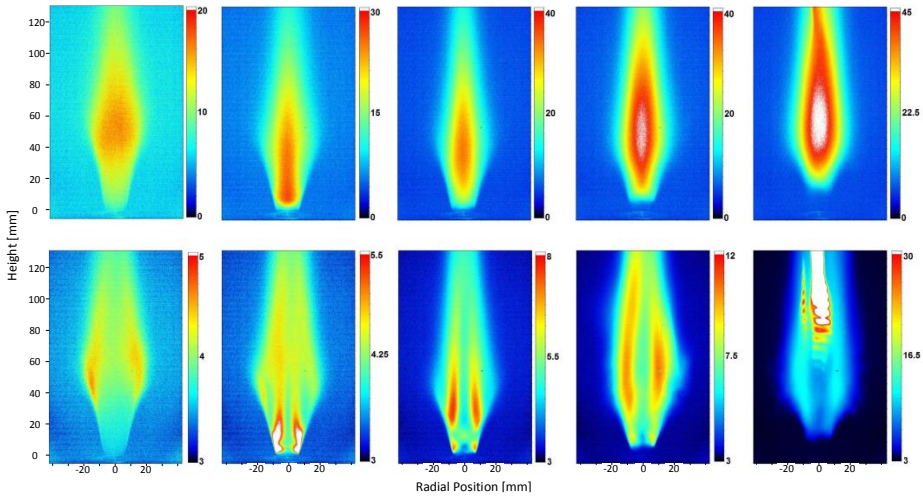

Figure 7. The time-averaged (upper row) and RMS (lower row) images of different flame structures with a central fuel injection (from left to right: U_f/U_c = 0, 0.045, 0.089, 0.22 and 0.36)

With the injection of a central fuel jet, another interesting behavior of the unstable flame was observed, as shown in Figure 8. When small amount of the central fuel jet (U_f/U_c = 0.045) was injected into the flow field, the flame turned to be unstable, with the flame tip attaching to the bluff-body outer edge. The attach point of the flame tip moved circularly along the bluff-body outer edge. This unstable flame behavior was dominated by the central fuel jet, because a change in the equivalence ratio of the annular flow did not significantly alter the flame instability features. The radial position of the unsteady flame tip was shown in Figure 9. A fast Fourier transform (FFT) code in Matlab was used to analysis the oscillations of the flame tip. In Figure 9, one can note that the flame tip alters its position around the axis of the bluff-body at -7mm < r < 7mm, indicating the flame tip was stabilized at the outer edge of the bluff-body. The unstable behavior of the flame tip might be caused by the unstable variance of the local equivalence ratio together with the unstable heat transfer from the flame to the bluff-body. When the flame tip was attached to one point in the outer edge of the bluff-body, more heat was then convected to the bluff-body through that point, thus the local temperature being lowered which might lead to local extinction of the flame. At the same time, the unstable wakes shedding from the bluff-body might also contribute to the instability behavior of the flame tip. The interaction of the wakes with the flame changed the local flow velocity and the local equivalence ratio, which could also result in the flame tip moving along the outer edge of the bluff-body.

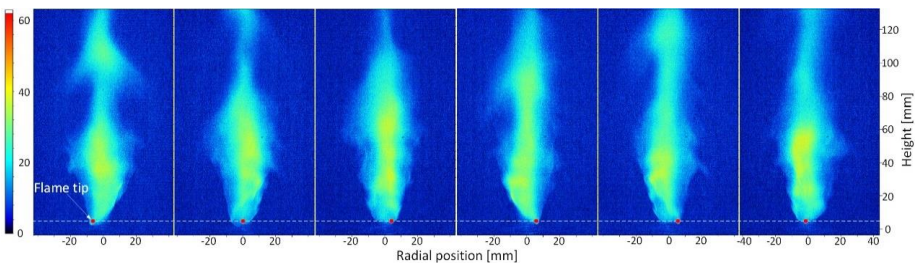

Figure 8. Typical flame instability behavior caused by a central fuel jet injection (the flame tip is moving circularly along the outer edge of the bluff-body)

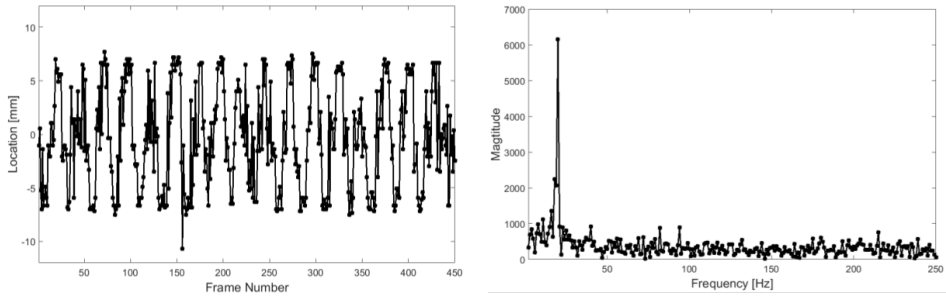

Figure 9. Radial position of flame tip (left) and its FFT results (right)

As shown in Figure 10, the dominate frequency of the oscillation for the flame tip is approximately 20Hz for case with annular mixture equivalence ratio of $\Phi = 0.64$, the bulk velocity of $U_c = 2.77$m/s and $U_f/U_c = 0.045$. An increase in the mass flow rate of the central fuel jet led to a decrease in that dominate frequency. As shown in Figure 7, the increase in the mass flow rate of the central fuel jet also resulted in an increase of the flame liftoff height, which probably being one of the reasons for the variance of the dominate frequency of the oscillation of the flame tip. When the central fuel flow rate exceeded a critical value, the flame overall acted much more like a diffusion jet flame rather than a bluff-body stabilized premixed flame. A deeper insight using PIV, PLIF and numerical simulations concerning the local equivalence ratio, the heat transfer and the corresponding flow structures is needed here.

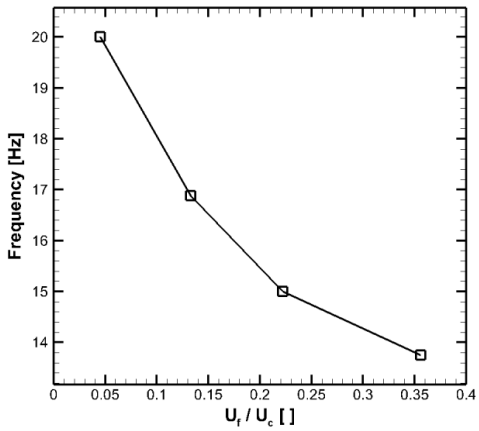

Figure 10. Effects of a central fuel jet on flame tip instability

3.2. Blowout limits

Flame blowout limit is another important feature to evaluate the performance of a flame holder. The blowout limit is the equivalence ratio of the annular flow at which the flame became visualized absence. The flame blowout limit was obtained by reducing the annular fuel flow rate from a stable flame condition (i.e. $\Phi = 0.64$) until the flame being vanished. During the reduction of fuel flow rate (at a step of 0.04 SLPM) the mass flow rates of the annular air and of the central air jet were kept constant. After each step of reducing the annular fuel flow rate, all the flow conditions were kept constant for at least 2mins to achieve a thermal equilibrium before the next fuel-reduction step. The blowout of the annular premixed flame could not be observed with a central fuel injection. This was due to the fact that when the equivalence ratio of the annular flow was reduced to the minimum level,

Φ = 0, (pure air in the annular flow), with a central fuel jet, the flame could also be maintained in terms of a bluff-body stabilized diffusion flame. Hence, in the paper only the effects of the central air injection on the flame blowout limits were studied, as shown in Figure 11.

It could be found in Figure 11 that with a central air jet, the flame blowout limits increase as a whole. The increase in flame blowout limits was caused by the changing of flow structures downstream of the bluff-body. As shown in Figure 1, with a small amount of the central jet, the annular flow dominated the flow structures. Then a fresh air layer was formed, as shown in Figure 5. At the same time, a small area of the flame front was attached to the bluff-body. Thus, the flame was extremely unstable and easy to blowout. Increasing the mass flow rate of the central air jet, the flame blowout limit decreased. It could be explained by the alternation of the flow structures, from *annular flow dominating* to *neither jet dominating* condition, as shown in Figure 1 and Figure 5. The central air jet penetrated more and effects from the central air jet on the near field of the surface of the bluff-body gets weaker. Larger area of the flame front got attached to the surface of the bluff-body, while the flame becoming somewhat more stable. With a further increase in the velocity of the central air jet, the flame blowout limits increased. It is worth noting here that two different blowout phenomenon were observed during the experiments. When $U_a/U_c < 5.5$, the flame blowout occured without the appearance of the split-flashing flame mode. The entire flame vanished suddenly with a small reduction in the mass flow rate of the annular fuel flow. The flame front that was attached to the bluff-body could not be sustained anymore. When $U_a/U_c > 5.5$, however, with a reduction in the equivalence ratio of the annular flow, the split-flashing flame (shown in Figure 6) took place before the occurrence of the flame blowout. A further decrease in the mass flow rate of the annular fuel flow quenched the flashing flame downstream of the blue-body firstly, with only the flame root being stabilized. A little further reduction in the mass flow rate of the annular fuel flow finally quenched the flame root. As discussed above, the occurrence of the flame neck was caused by the penetration of the central air jet. The local flame quenching and re-ignition were supposed to be reasoned by the local high strain rate and the locally fuel-lean condition at the neck region. As shown in Figure 11, a big amount of mass flow of the central air jet ($U_a/U_c > 10$) resulted in higher blowout limits, which might be caused by the enhanced heat convection from the bluff-body to the central jet.

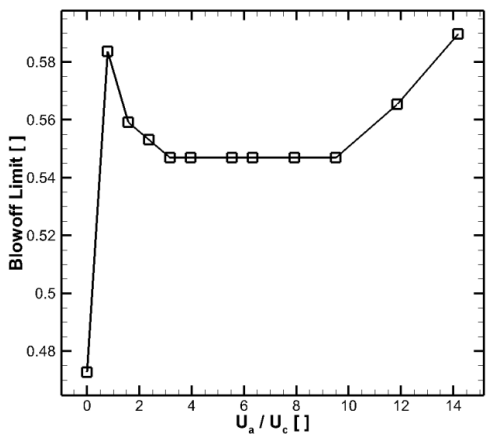

Figure 11. Effects of a central air jet on the flame blowout limits

3.3. Bluff-body upper surface temperature

In this section, results of the temperature on the upper surface of the bluff-body are presented and discussed. Experiments reported here were performed holding the velocity of the premixed annular flow at $U_c = 2.77$m/s and the equivalence ratio at Φ = 0.64. Effects of the central air and fuel

injections were studied on the basis of experiments with U_a/U_c = 0~7.8 and U_f/U_c=0~0.36, respectively. The temperature T_{edge} varied with the injection of a central air/fuel jet, as shown in Figure 12.

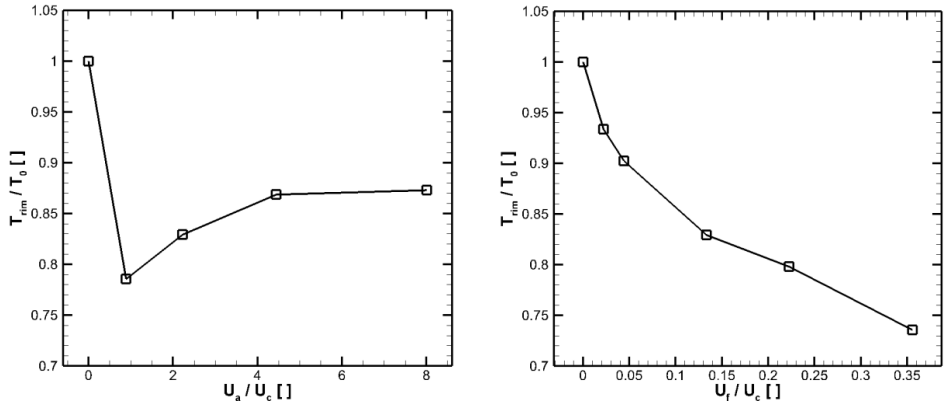

Figure 12. Effects of central air (left) and fuel (right) jet on the temperature of bluff-body surface

With a small amount of a central air injection ($U_a/U_c \approx 1$), the temperature on the surface of the bluff-body dropped to less than 80% of T_0, as shown in Figure 12. For case in which $U_a/U_c \approx 1$, the temperature of the bluff-body was lower than any other cases with a central air jet. That lower temperature was probably produced by the local flow structures near the bluff-body. When $U_a/U_c \approx 1$, the flow fields downstream of the bluff-body were believed to be dominated by the annular flow, as shown in Figure 1. A fresh air layer was then formed above the surface of the bluff-body, preventing the heat convection from the flame to the bluff-body. Afterwards, an increase in the velocity of the central air jet increased the temperature ratio up to approximately 87%. With an increase in the velocity of the central jet flow, the air jet penetrated higher with a weakened heat convection from the bluff-body to the central jet. Thus, as shown in Figure 12 (left), when the flow field was central jet dominating, an increase in the mass flow rate of the central air jet did not significantly change the heat load to the surface of the bluff-body, even when the flame was increasingly weakened by the central air injection.

With the injection of a central fuel jet, the temperature on the surface of the bluff-body decreased significantly, to even less than 75% of T_0. The main reason for that lower temperature was the occurrence of flame lifting off from the bluff-body, with the injection of a central fuel jet. As described previously, with a central fuel jet, the time-averaged flame structure appeared a detached pattern from the bluff-body. At the same time, the transient flame structures showed an increasingly flame instability. The flame liftoff height increased with the increase in the mass flow rate of the central fuel jet, until flame blowout occurred. Thus, the heat load to the surface of the bluff-body was reduced correspondingly at the same time.

Taking the temperature on the surface of the bluff-body into consideration, a central air jet and a central fuel jet are practical methods to reduce the heat load to the bluff-body in bluff-body stabilized premixed flames. However, the disadvantage with a central air injection is that the flame then becomes more unstable and easier to blowout. A central fuel injection, which acts like a pilot, could be used to stabilize the premixed annular flame, with a reduction of the heat load to the surface of the bluff-body.

4. Conclusions

The effects of a central air/fuel jet on the bluff-body stabilized premixed methane-air flames were studied in the paper. The temperature on the surface of the bluff-body and the flame structures were captured on the basis of use of a thermographic camera and a high-speed CMOS camera, respectively. The injection of a central air/fuel jet makes the flame more unstable. A central air jet causes the flame easier to blowout, while two different blowout phenomena (with/without the occurrence of split-

flashing flame mode) being observed. The reduction in the temperature on the surface of the bluff-body with a central fuel injection is found to be caused by the flame lifting off from the bluff-body. The liftoff height increases with the increase in the mass flow rate of the central fuel flow, while the temperature of the bluff-body being decreased correspondingly. The attached point on the outer edge of the bluff-body is unstable under conditions with a central fuel jet. A circular motion of the flame tip along the outer edge of the bluff-body is observed and presented. The dominant frequency of the oscillation of the flame tip decreases with an increase in the velocity of the central fuel jet. Further detailed investigations of the flow structures as well as the interactions of a central jet with the annular flame are required.

Acknowledgements: The work was financially supported by the Swedish Energy Agency, the Swedish Research Council (VR) and the European Research Council (Advanced Grant TUCLA program). Yiheng Tong, Shuang Chen and Mao Li would like to thank the financial support from the China Scholarship Council (CSC).

Author Contributions: Yiheng Tong designed the experiments, conducted the data analysis and wrote the paper; Shuang Chen and Zhongshan Li took part in the burner design; Mao Li took part in the experimental work; Zhongshan Li and Jens Klingmann proofread the paper.

References

1. Chaudhuri, S.; Cetegen, B.M. Blowout characteristics of bluff-body stabilized conical premixed flames with upstream spatial mixture gradients and velocity oscillations. *Combustion and flame* **2008**, *153*, 616-633.
2. Guo, P.; Zang, S.; Ge, B. Technical brief: Predictions of flow field for circular-disk bluff-body stabilized flame investigated by large eddy simulation and experiments. *Journal of Engineering for Gas Turbines and Power* **2010**, *132*, 054503.
3. Zukoski, E.E.; Marble, F.E. The role of wake transition in the process of flame stabilization on bluff bodies. *AGARD Combustion Researches and Reviews* **1955**, 167-180.
4. Zuikoski, E.; Marble, F. Gas dynamic symposium on aerothermochemistry. Northwestern University Press: 1955.
5. Longwell, J. In *Flame stabilization by bluff bodies and turbulent flames in ducts*, Symposium (International) on Combustion, 1953; Elsevier: pp 90-97.
6. Longwell, J.P.; Frost, E.E.; Weiss, M.A. Flame stability in bluff body recirculation zones. *Industrial & Engineering Chemistry* **1953**, *45*, 1629-1633.
7. Wright, F. Bluff-body flame stabilization: Blockage effects. *Combustion and Flame* **1959**, *3*, 319-337.
8. Pan, J.; Vangsness, M.; Ballal, D. In *Aerodynamics of bluff body stabilized confined turbulent premixed flames*, ASME 1991 International Gas Turbine and Aeroengine Congress and Exposition, 1991; American Society of Mechanical Engineers: pp V003T006A019-V003T006A019.
9. Lefebvre, A.H.; Ballal, D.R. *Gas turbine combustion*. CRC Press: 2010.
10. Barrere, M.; Mestre, A. Selected combustion problems. Stabilisation des Flammes par des Obstacles: 1954.
11. Shanbhogue, S.J.; Husain, S.; Lieuwen, T. Lean blowout of bluff body stabilized flames: Scaling and dynamics. *Progress in Energy and Combustion Science* **2009**, *35*, 98-120.
12. Chaparro, A.A.; Cetegen, B.M. Blowout characteristics of bluff-body stabilized conical premixed flames under upstream velocity modulation. *Combustion and flame* **2006**, *144*, 318-335.
13. Chaudhuri, S.; Cetegen, B.M. Blowout characteristics of bluff-body stabilized conical premixed flames in a duct with upstream spatial mixture gradients and velocity oscillations. *Combustion Science and Technology* **2009**, *181*, 555-569.

14. Chaudhuri, S.; Kostka, S.; Renfro, M.W.; Cetegen, B.M. Blowout dynamics of bluff body stabilized turbulent premixed flames. *Combustion and flame* **2010**, *157*, 790-802.
15. Wan, J.; Fan, A.; Maruta, K.; Yao, H.; Liu, W. Experimental and numerical investigation on combustion characteristics of premixed hydrogen/air flame in a micro-combustor with a bluff body. *international journal of hydrogen energy* **2012**, *37*, 19190-19197.
16. Fan, A.; Wan, J.; Liu, Y.; Pi, B.; Yao, H.; Liu, W. Effect of bluff body shape on the blow-off limit of hydrogen/air flame in a planar micro-combustor. *Applied Thermal Engineering* **2014**, *62*, 13-19.
17. Bagheri, G.; Hosseini, S.E.; Wahid, M.A. Effects of bluff body shape on the flame stability in premixed micro-combustion of hydrogen–air mixture. *Applied Thermal Engineering* **2014**, *67*, 266-272.
18. Fan, A.; Wan, J.; Maruta, K.; Yao, H.; Liu, W. Interactions between heat transfer, flow field and flame stabilization in a micro-combustor with a bluff body. *International Journal of Heat and Mass Transfer* **2013**, *66*, 72-79.
19. Roquemore, W.; Tankin, R.; Chiu, H.; Lottes, S. A study of a bluff-body combustor using laser sheet lighting. *Experiments in Fluids* **1986**, *4*, 205-213.
20. Caetano, N.R.; da Silva, L.F.F. A comparative experimental study of turbulent non premixed flames stabilized by a bluff-body burner. *Experimental Thermal and Fluid Science* **2015**, *63*, 20-33.
21. Esquiva-Dano, I.; Nguyen, H.; Escudie, D. Effect of a bluff-body's shape on the stabilization regime of non-premixed flames. *Combustion and Flame* **2001**, *127*, 2167-2180.
22. Schefer, R.; Namazian, M.; Kelly, J.; Perrin, M. Effect of confinement on bluff-body burner recirculation zone characteristics and flame stability. *Combustion Science and Technology* **1996**, *120*, 185-211.
23. Tang, H.; Yang, D.; Zhang, T.; Zhu, M. Characteristics of flame modes for a conical bluff body burner with a central fuel jet. *Journal of Engineering for Gas Turbines and Power* **2013**, *135*, 091507.
24. Nishimura, T.; Kaga, T.; Shirotani, K.; Kadowaki, J. Vortex structures and temperature fluctuations in a bluff-body burner. *Journal of visualization* **1998**, *1*, 271-281.
25. Euler, M.; Zhou, R.; Hochgreb, S.; Dreizler, A. Temperature measurements of the bluff body surface of a swirl burner using phosphor thermometry. *Combustion and Flame* **2014**, *161*, 2842-2848.
26. Euler, M.; Zhou, R.; Hochgreb, S.; Dreizler, A. In *Temperature measurements of the bluff body surface of cambridge stratified swirl burner using phosphor thermometry*, European Combustion Meeting, 2013; pp 33-33.
27. Russi, M.; Cornet, I.; Cornog, R. In *The effect of flame holder temperature on flame stabilization*, Symposium (International) on Combustion, 1953; Elsevier: pp 743-748.
28. Lin, C.-X.; Holder, R.J. Reacting turbulent flow and thermal field in a channel with inclined bluff body flame holders. *Journal of Heat Transfer* **2010**, *132*, 091203.
29. http://www.engineeringtoolbox.com/emissivity-coefficients-d_447.html

Paper V

Experimental and Numerical Study about Effects of Bluff-body's Position on Diffusion Flame Instabilities

Yiheng Tong[1], Xiao Liu[2], Zhongshan Li[3] and Jens Klingmann[1]

1: Department of Energy Sciences, LTH, Lund University, Lund, Sweden

2: College of Power and Energy Engineering, Harbin Engineering University, Harbin, China

3: Division of Combustion Physics, LTH, Lund University, Lund, Sweden

HIGHLIGHTS

1. Effects of bluff-body position on flame patterns and instabilities are studied.
2. A vortex besides the bluff-body outer wall enhances flame stabilization.
3. Combustion enhances central jet penetration, enlarges air driven vortex.

ABSTRACT

Effects of bluff-body position on diffusion flame structures and instability characteristics were investigated experimentally and numerically. The flame regime diagram and stability limits of the methane-air diffusion flame are proposed to evaluate the influences caused by the alternation of the bluff-body position. The disk shape bluff-body was placed 10mm above or at the same height with the annular channel exit. The bulk velocity of the annular air flow varied from $U_a = 0$ to 8m/s; while the jet fuel velocity ranged from $U_j = 0$ to 30m/s. Various flame patterns including the recirculation zone flame, the stable diffusion flame, the split flame and the lifted flame till flame blowoff were observed and recorded by the high speed camera. High speed Particle Image Velocimetry (PIV) were also adopted to give deeper insight into the characteristics of the flow fields and flame patterns. The hybrid RANS/LES model was utilized to simulate the reactants mixing characters, scalar dissipation rates, flow fields and their relation with the flame structures. The size and strength of the recirculation zone downstream of the bluff-body were altered with the changing of bluff-body position. It is found that the flame behaves similarly in the burners with different bluff-body's positions, except for cases with high annular air velocities ($U_a > 6.8$m/s). Placing the disk shape bluff-body 10mm above the annular channel exit could better stabilize the flame. The recirculation vortex formed besides the bluff-body's outer wall played an important role in the flame stabilization. Combustion affected the flow fields significantly by accelerating the central jet and enlarging the outer recirculation zone.

Nomenclature

a	blockage ratio [-]
c	reaction progress variable [-]
d_a	annular channel diameter [mm]
Da	Damköhler number [-]
d_b	bluff-body diameter [mm]
d_j	central jet diameter [mm]
f	mixture fraction [-]
h	axial position [mm]
l	recirculation zone length [mm]
r	radial position [mm]
T	temperature [k]
U_a	annular flow velocity [m s^{-1}]
U_j	central jet velocity [m s^{-1}]
ΔH	distance from the annular channel exit to bluff-body's upper surface [mm]
Δt	Time delay between two laser pulses [μs]
Φ	equivalence ratio [-]

Abbreviations

DES	Detached Eddy Simulation
IDDES	Improved Delayed Detached Eddy Simulation

LES	Large Eddy Simulation
PIV	Particle Image Velocimetry
RANS	Reynolds-Averaged Navier–Stokes
SRS	scale-resolving simulation

INTRODUCTION

Bluff-body stabilized turbulent jet diffusion flame has received renewed attention in recent years due to its practical applications. It is found in a variety of applications, such as gas turbine combustor, afterburner, heat recovery steam generator, and industrial furnace[1]. Bluff-body flame holder is a commonly employed practical methodology to stabilize the flame due to the enhanced mixing characteristics as well as the ease of combustion control. The recirculation of hot gas behind the bluff-body can help to reignite gas mixtures, and thus stabilize the flame[2]. In addition, the longer residence time downstream of the flame holder in some way also enhances the flame stabilization. The bluff-body has also been utilized to increase heat conduction and shorten the flame length in steam boiler and gas turbine[3]. Due to the advantages mentioned above, bluff-body is preferred to stabilize both the premixed and diffusion flames. Moreover, in order to stabilize the diffusion flame, the bluff-body is commonly designed in the axis of the annular channel with a central fuel jet passing through the bluff-body's center.

Herein the introduction part, the iso-thermal and reacting flow structures downstream of the bluff-body with a central jet are first presented. Effects of the combustion on the flow fields are emphasized. After that, studies about flame structures anchored by a bluff-body are reviewed. The burner geometries with different bluff-body's dimensions and positions are summarized as well.

Flow structures

The typical flow fields downstream of the bluff-body with a central jet is shown in Fig.1[4]. Two recirculation zones, namely the inner and outer recirculation zones, could be observed. The outer recirculation zone is driven by the annular flow while the inner recirculation zone is driven by the central jet. These two recirculation zones interact with each other and play an important role in the diffusion flame structures and after all determine the flame stabilization. Dally et al. [5] identified three mixing layers in the recirculation zone: a. an external mixing layer located between the annular air flow and the outer vortex (shown as the annular flow shear layer in Fig.1); b. an intermediate one between the inner and outer vortexes (shown as the mixing shear layer in Fig.1); c. an internal layer between the inter vortex and the central fuel jet (shown as the jet shear layer in Fig.1).

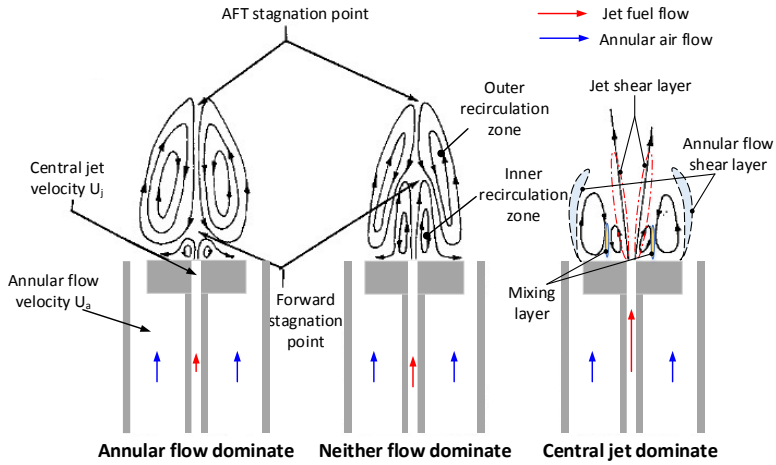

Fig.1 Illustration of the time-averaged flow fields of a bluff-body with a central jet (reproduced from [4])

The flow structures downstream of the bluff-body are strongly dependent on the velocity ratio[4] or the momentum ratio[5] of the central jet to the annular flow. In an axisymmetric bluff-body burner, Roquemore et al.[4] divided the flow topologies into three modes (as shown in Fig.1) based on the fuel to air velocity ratio in the iso-thermal flow. With the increasing of the velocity ratio of the central jet to the annular air flow, the flow structures changed from the annular jet dominating to a transition pattern and finally to the central jet dominating. Esquiva-Dano et al.[6] distinguished three flow patterns base on the number of the stagnation points in the central axis of the flow. When the annular air dominated the flow structures downstream of the bluff-body, two stagnation points could be observed along the centerline. These two stagnation points were related to the central jet penetration and the recirculation zone length respectively. When the central fuel jet dominated the flow structures, there was no more stagnation point located along the centerline. The transition situation was where neither the central fuel jet nor the annular air jet dominated the flow fields. The transition mode was an intermediate state where only one stagnation point could be observed. Schefer et al.[7] also reported that the velocity ratio of the central jet to the annular flow determined the number of stagnation points and the size/strength of the recirculation zones. They were applicable to both reactive and non-reactive cases within different confinements. Whereas, Yang et al.[8] studied the reacting flow structures and distinguished them into four modes. It was also concluded that the flow patterns were highly determined by the interaction between the flow and combustion. Schefer et al.[9] compared the velocity fields downstream of the

bluff-body in the iso-thermal and combusting cases when holding central to annular flow velocity ratio at $U_j / U_a = 0.84$. It was concluded that the velocity in the centerline region was altered between different cases; whereas the velocity distributions in the remainder flows were quantitatively similar with each other. They also reported that combustion would result in an increase of the central jet penetration. However, Huang and Lin[10] reported that the lifted flames did not significantly affect the flow structures near the bluff-body. In the detached flames, combustion in the recirculation bubble leaded to local low pressure and thus enhanced the reinforcement of the development of central jet. The flow patterns and turbulent intensity could affect the combustion via the fuel entrainment, diffusion and mixing capabilities. They classified the flow structures into pre-penetration, penetration and large shear flows according to the central to annular jet velocity ratios. Ma and Harn [11] numerically studied the effects of blockage ratio, cone angle and fuel-air velocity ratio on the flow fields downstream of the bluff-body. It was found that when the blockage ratio was high, a larger recirculation zone would be formed. However, less velocity gradient variation in the major mixing zone would also be observed in case with high blockage ratio. It was predicted that flow in the higher blockage cases had a worse mixing of the central fuel jet with the annular air flows.

Flame patterns

The bluff-body stabilized diffusion flame patterns were of high interest to researchers since they were highly related to the flame stabilization characteristics. Chen et al. [1] proposed a regime diagram of bluff-body stabilized flame patterns which included (a) recirculation zone flame; (b) central jet dominated flame; (c) jet-like flame; (d) partially quenched flame and (e) lifted flame. Tang et al. [2] named the flame structures by stable flame, transitional-state flame, unstable flame and flame blowout. They also observed the split-flashing, split and lift-off flames under different operating conditions. San et al. [3] studied the rifled bluff-body frustums and divided the flame patterns into jet flame, flickering flame, bubble flame, lifted flame and turbulent flame patterns. Yang et al.[12] classified the diffusion flames behind the disc stabilizer into five modes: (1)recirculation zone flame, (2)central jet dominated flame, (3)jet like flame, (4)partially quenched flame and (5)lift-off flame. Masri and Bilger [13] also reported three types of bluff-body stabilized turbulent natural gas and liquefied petrol gas flames: (A) short, recirculation controlled flame; (B) transitional flame; and (C) long, fuel jet dominated flame. Subsequently, Huang and Lin[14] divided the commercial propane diffusion flames into the following seven types: (I) recirculated region, (II) transition, (III) unsteady detached, (IV) laminar ring, (V) developing ring, (VI) split flashing and (VII) lifted flames. Esquiva-Dano et al.[6] investigated the effects of bluff-body shape on

the behavior of non-premixed flames. With the decreasing of the ratio of jet to annular air flow velocity, they classified flames into five different regimes: (1) laminar, (2) transition I, (3) laminar ring, (4) transition II and (5) recirculating flames followed by flame extinction. In the transition I flame regime, bulge, detached and reattached flames were observed. They also reported that the tulip of the bluff-body significantly promotes the flame stabilization. Whereas the disk shape bluff-body, which created a bigger recirculation zone, performed worse in stabilizing the flame. The fuel penetration and fuel-air mixing process were concluded as the dominant parameters determining the flame patterns and stabilization. However, Longwell et al.[15] reported that a larger recirculation zone downstream of the bluff-body could better stabilize the premixed flame. They emphasized that in the larger recirculation zones, reactants could have more residence time and hence promote the flame stabilization. The flow residence time in the recirculation zone was defined as the ratio of the mass entrance rate to the volume of the recirculation zone. It was reviewed by Shanbhogue et al.[16] that the flame patterns were highly associated with the flame dynamics. They reported that flame blowoff occurred as a sequence of events: extinction along the flame sheet, large scale wake disruption and a final blow-off. These flame behaviors were depended on wake cooling and shrinking. In addition, significant differences between the iso-thermal and the reacting flow structures were evidenced. Chen et al.[17] compared the diffusion flame structures stabilized by a bluff-body or a swirling flow. They found the flames had the similar structures and properties when they were operated with the same non-dimensional vortex strength and fuel jet momentum. They observed two types of flame (Type 1: fuel-jet dominated flame and Type 2: recirculating flame) both in the bluff-body and swirl stabilized flames. They also concluded that flame behavior was strongly determined by the flow fields downstream of the bluff-body or the swirler. Herein the current study, according to the literatures [2] and [12], we named the flame patterns as follows: (1) recirculation zone flame, (2) stable diffusion flame, (3) split-flashing flame and (4) lifted flame till flame blowoff.

Burner geometries

The burner geometries could be altered with changing of the bluff-body's shape, position and the blockage ratio (the cross sectional area ratio of the bluff-body to the annular channel) or the confinement ratio (the cross sectional area ratio of the burner to the combustor). Different burner geometries with a bluff-body flame holder are summarized and listed in Table 1. Researchers preferred to place the bluff-body at the same height with the exit of the annular channel, like in literatures [1] [2] [6] [8] [11] [14]. The commonly employed bluff-body shapes are disk or conical shapes. However,

some other designs of bluff-body geometries also obtained investigators' attention, i.e. placing the bluff-body above the annular channel exit in literatures [3] [18] [19] [20] or even below the annular channel exit in the literature [21], or bluff-body with swirling flow in the literature [3]. Schefer et al. [7] investigated the effects of confinement ratio on the recirculation vortexes and the corresponding flame stabilizations. It was concluded that when the confinement ratio was low, the recirculation zones and flame stability were not significantly affected by the confinement. In addition, Yang et al.[12] studied the effects of blockage ratio on flame stabilization and flame patterns. They concluded that when the blockage ratio got increased, the main reaction zone moved to regularly upstream to the inner side of the recirculation zone. It was similar to the phenomenon when increasing the fuel-to-air velocity ratio. Moreover, Esquiva at al.[6] investigated the influence of bluff-body's shape on flame regimes. The tulip shape bluff-body was found to have better performance in stabilizing the flame than the disk shape flame holder. Kumar and Mishra [22, 23] studied the effects of the size of the disk shape bluff-body on liquefied petroleum gas (LPG)–H_2 jet diffusion flame. It was found that with the increasing of the bluff-body's diameter, the flame length got shortened. The recirculation zone downstream of the bluff body performed better mixing of reactants and as a result, reaction zone was likely to propagate toward the bluff body. As a consequence, it leaded to a reduction of the flame length.

However, to the author's best knowledge, rare research is focusing on the effects of the bluff-body position (i.e. at the same height with or above the annular air channel exit) on the recirculation zones and flame structures. Meanwhile, as mentioned above, researchers have already utilized the burners with different bluff-body positions in their research. Whether the bluff-body position could affect the flame patterns is still a topic need to be studied. In the burner design process, more information about the influences of the bluff-body's position on flame behaviors is required. Hence, herein the current paper, we examined the performances of burners with a simple disk shape bluff-body placed at different positions. Two bluff-body positions were investigated: at the same height or 10mm above the annular channel exit. The flow fields downstream of the bluff-body and flame stability limits were investigated as well. Cases with different bluff-body's positions were studied to span the range of interest for practical burners.

APPAARATUS AND METHODS

Experimental setup

The experimental setup and the non-confined bluff-body burner are schematically shown in Fig.2. The burner was an annular channel with a disk shape bluff-body located

in the center. The inner diameter of the annular air flow channel was d_a = 30mm. The removable stainless steel bluff-body had an outer diameter of d_b = 14mm and an inner diameter of d_j = 4mm. The central pipe as well as the bluff-body were removable and adjustable. Commercial air was fed into the annular channel while fuel was injected through the central pipe. Methane was selected as the central fuel jet since it was the main component in natural gas. In addition, the established and detailed chemical reaction mechanisms of methane were available for the numerical simulations. The distance from the bluff-body's upper surface to the exit of the annular air flow channel, ΔH, is also shown in Fig.2. Flow structures and flame patterns of the burner with two bluff-body's positions, including ΔH = 0mm (the bluff-body's upper surface was at the same height with the annular channel exit) and ΔH = 10mm (the bluff-body's upper surface was 10mm outside above the annular channel exit) were investigated. As reviewed in the introduction part, these two bluff-body's positions were commonly used in other researchers' investigations. The blockage ratio for the case with ΔH = 0mm was a_0 = 0.218 and for ΔH = 10mm it was a_{10} = 0.04. A ceramic honeycomb was mounted in the annular channel to form a uniform annular flow upstream of the channel exit.

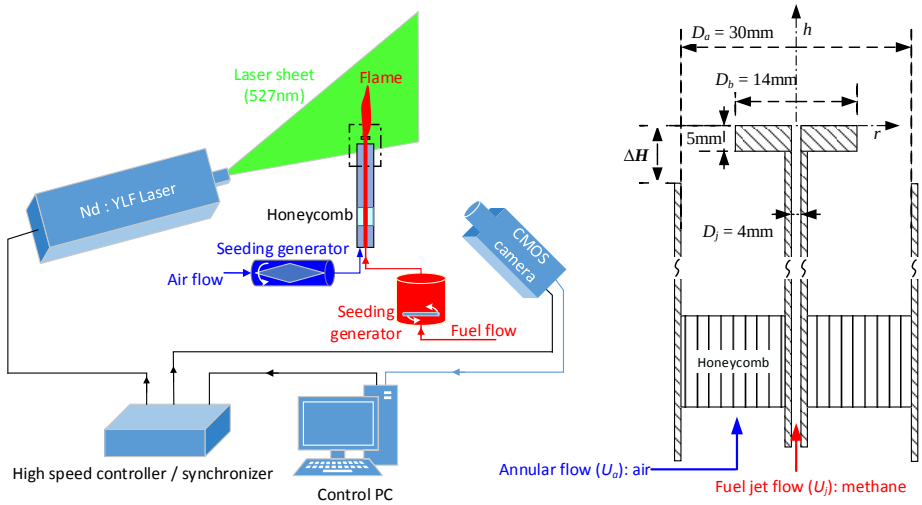

Fig.2 Schematic of the experimental setup (left) and the burner (right)

Particle Image Velocimetry

The flow fields downstream of the bluff-body were measured using a high-speed PIV system (Lavision Flowmaster). The schematic of the PIV system is also shown in Fig.2. A diode-pumped, dual cavity Nd:YLF laser (Litron LDY) was utilized to illuminate

the central plane of the bluff-body with a laser sheet. The thickness of the lase sheet was approximately 1mm which was generated by an optical lens. The high speed laser had a wavelength of 527nm and frequency was set to f = 2kHz in the current study. The time delay between two laser pulses was Δt = 50μs. The laser light scattered off the TiO_2 seed particles which were originated from both the annular and central flows. The recording rate of the high speed CMOS camera (Vision Research Phantom V 611) was set to 2kHz with a resolution of 1280×800 pixels and a depth of 12 bits. As shown in Fig.2, the TiO_2 particles were seeded into both the air flow and the fuel flow using a rotating drum particle seeder (Scitek PS-10) and a LaVision solid particle seeder (LaVision Particle blaster 100) respectively. The seeding particles with the primary diameter of 20nm formed particle clusters of 150–250nm in size. A multi-pass cross-correlation algorithm, which was available in the DaVis (v.8.1.4) computer software, was utilized to evaluate the velocity fields downstream of the bluff-body. The cross-correlation was performed on interrogation areas of 64 × 64 and subsequently 32 × 32 pixels with a window overlap of 50%. The focus area contains the inner and outer recirculation zones and the three main shear layers near the bluff-body.

Test conditions and procedures

The Bronkhorst mass flowmeter was utilized to measure the mass flow rate of the air passing through the annular channel. Meanwhile, the Alicat (MCR 100) mass flow controller was employed to control the mass flow rate of the central fuel jet. The bulk velocity of the annular air flow, U_a, was calculated based on the cross sectional area of the annular channel upstream of the bluff body as shown in Fig.2. It was ranged from U_a = 0 to 8m/s; while the central jet bulk velocity ranged between U_j = 0 to 30m/s. All experiments were carried out without confinement in the atmosphere condition. It thus made the utilization of laser based experiments possible and reliable due to the lack of noises from light/laser reflection from the confinements.

In order to start the series of experiments, a small amount of central fuel jet (i.e. U_j = 3m/s) was fed through the central pipe without the annular air flow. The central fuel jet was then ignited by an ignitor to obtain a stable jet diffusion flame. After that, the fuel flow velocity was accelerated to U_j = 13m/s, meanwhile the annular air flow rate was increased to the target value. As what will be shown in the results and discussions part, when holding U_j = 13m/s, the flame could be stabilized in a wide range of U_a. Afterwards, the central fuel velocity was altered by steps of approximately 0.3m/s to its target value. During each alternation of the central fuel flow velocity, the central fuel and the annular air flow rates were kept constant for at least 1 min. It was thus the mass flow rates of fuel and air were stabilized at a constant value and the bluff-body was under a thermal

equilibrium condition. Holding the mass flow rates of air and fuel at the target values, the transient flame structures were captured utilizing the high speed CMOS camera (Vision Research Phantom V611) at a recording frequency of 1kHz. The broad band emissions radiated from the flame were captured to visualize the flame patterns.

Numerical methods

Large Eddy Simulation (LES) has proven to be a powerful tool for the prediction of transient turbulent reacting flows and flame structures with high resolutions. In addition, the unsteady three dimensional effects and transient detailed flow fields were reported to be predicted better by LES than unsteady RANS (URANS) [24]. However, LES models are only recommended for flows where wall boundary layers (usually with high local Reynolds number) are not relevant and need not be resolved. Hence, the detached eddy simulation (DES) model, which was a hybrid LES-RANS model combining URANS in the wall boundary layer and LES in the separation zones, was adopted in the current study. In addition, the improved delayed detached eddy simulation (IDDES) model, which is based on the shear stress transport (SST) *k-ω* model, has a better performance than DES. It could provide a more flexible and convenient scale-resolving simulation (SRS) model for flows with high Reynolds number [25]. The transport equation for the turbulent kinetic energy (k) and the specific dissipation rate (ω) in the SST-IDDES model are given as follows:

$$\frac{\partial \rho k}{\partial \mathrm{t}} + \nabla \cdot \left(\bar{\rho}\, \widetilde{U}\, \mathrm{k}\right) = \nabla \cdot \left[\left(\mu + \frac{\mu_T}{\sigma_k}\right) \nabla \mathrm{k}\right] + P_k - \rho \beta^* k \omega F_{IDDES}$$

$$\frac{\partial \rho \omega}{\partial \mathrm{t}} + \nabla \cdot \left(\bar{\rho}\, \widetilde{U}\, \omega\right) = \nabla \cdot \left[\left(\mu + \frac{\mu_T}{\sigma_\omega}\right) \nabla \omega\right] + (1 - F_1) 2\rho \frac{\nabla \mathrm{k} \cdot \nabla \omega}{\omega \sigma_{\omega^*}} - \rho \beta^* k \omega F_{IDDES} + \alpha \frac{\omega}{k} P_k - \beta \rho \omega^2$$

$$F_{IDDES} = \frac{l_{RANS}}{l_{IDDES}} = \frac{\sqrt{k} \big/ (\beta^* \omega)}{l_{IDDES}}$$

It is shown above that F_{IDDES} is related to the RANS turbulent length scale and the LES length scales. For more information about the formulations of IDDES model and different length scales, the readers could refer to ANSYS theory guide [25] and paper [26]. In the current study, the IDDES model was utilized to simulate different flame behaviors in the burners with different bluff-body positions.

The transport PDF model [27], EDC model with detailed mechanisms [28] and flamelet based model [29] are commonly used in the simulation of non-premixed combustion. The results based on the models listed above show that different models give fairly good results when comparing with experimental data. In our paper, taking the

computational accuracy and computational CPU time into account, the partially premixed non-adiabatic flamelet combustion model was adopted in the study to get deeper insight into the transient flame patterns. It was suggested by Qureshi et al. [30] that the equilibrium model was only valid when the ratio of diffusion time scale to the chemical time scale is larger than 200. However, the partially premixed steady diffusion flamelet model is suited to predict chemical equilibrium and non-equilibrium due to aerodynamic straining of the flame by the turbulence. The chemistry, however, is assumed to respond rapidly to this strain. So as the strain relaxes to zero, the chemistry tends to equilibrium [25]. The partially premixed combustion model solves a transport equation for the reaction progress variable (*c*, to determine the position of the flame front) as well as the mean mixture fraction (*f*), and the mixture fraction variance (f'). Hence it can simulate non-premixed flame (based on *f*), premixed flame (based on *c*) and partially premixed flame (based on both *f* and *c*). The mixture fraction (*f*) quantifies the extent of mixing between fuel and oxidizer streams in non-premixed combustion. It can be expressed by the atomic mass fraction as:

$$f = \frac{z_i - z_{i,o}}{z_{i,f} - z_{i,o}}$$

where z_i is the elemental mass fraction for species *i*. The subscript *o* stands for the value at the oxidizer flow side and *f* is the value at the fuel side. In the diffusion flamelet model, *f* is assumed to follow the β-function probability density function (PDF) and scalar dissipation fluctuations are ignored. The chemistry of the combustion is then reduced and completely described by the transport equations of *c* and *f* which allows the flamelet calculations to be preprocessed and stored in the look-up tables. Thus the computational costs could be reduced considerably. The transport equations of *f* under the assumption of equal diffusivities is then:

$$\frac{\partial(\rho\bar{f})}{\partial \mathrm{t}} + \nabla \cdot \left(\rho\, \vec{v}\, \bar{f}\right) = \nabla \cdot \left(\frac{\mu_l + \mu_\tau}{\sigma_\tau} \nabla \bar{f}\right) + S_m$$

where μ_l is the laminar viscosity and μ_τ is the turbulent viscosity. S_m is the source term which is determined by the mass transfer from liquid or solid phase into gas phase during the chemical reaction. For diffusion flamelet model adopted in LES region of IDDES model, the mixture fraction variance is modeled as

$$\overline{f'^2} = C_{var} L_s^2 \left|\nabla \bar{f}\right|^2$$

where C_{var} is a constant with C_{var} = 0.5 and L_s is the subgrid length scale. In addition, the progress variable c is a parameter that characterizes the evolution of global chemical status from purely mixing unburnt (c = 0) to fully burnt (c =1). The flame front propagation is modeled by solving a transport equation for the density-weighted mean reaction progress variable, denoted by $\bar{c}$:

$$\frac{\partial(\rho\bar{c})}{\partial \mathrm{t}} + \nabla \cdot (\rho\, \vec{v}\, \bar{\mathrm{c}}) = \nabla \cdot \left(\frac{\mu_\tau \nabla \bar{c}}{Sc_\tau}\right) + \rho S_c$$

Where Sc_τ is the turbulent Schmidt number and S_c is the reaction progress source term. Density weighted mean scalars (such as species fractions and temperature) are calculated from the probability density function (PDF) of f and c. More detailed descriptions for the turbulent models and partially premixed steady flamelet model are available in ANSYS FLUENT Theory Guide [25]. The reduced version of GRI-MECH 1.2 [31] with 19 species and 84 reactions of methane and air was selected with reasonable computation cost. The Peters turbulent flame speed model [32] was selected in the simulation.

The second order upwind scheme was used for the spatial discretization while the bounded second order implicit scheme was selected for the transient formulation. The coupled pressure-velocity coupling algorithm was used to solve the discretized equations. The CFL number employed in the current work was set to 0.7. The incompressible governing equations for mass, momentum and mixture fractions were solved based on a structured 3-D grid and the resolution effects investigated using up to 2.19 million nodes as shown in Fig.3. As can be observed from Fig.3, the computational domain covered 290mm in the streamwise direction with h = 200mm downstream of the bluff-body. The outlet downstream was 160mm in the radial direction. The hybrid grids were refined in the cylindrical domain at $0 < r <$ 15mm and -10mm $< h <$ 50mm, while the boundary refinement was adopted in the bluff-body upper and side walls. Strong shear stresses, the boundary layer flow, fuel-air mixing and most chemical reactions are found in this cylindrical region. Three levels of grid refinement (as shown in Table 2) in case with ΔH = 0mm were adopted and compared with each other in the current study. As shown in Fig.4, the finest grid with 2.19 million nodes could better capture the flow fields near the bluff-body's outer wall region (as shown in Fig.4(a)) as well as the size of the recirculation

zone (as shown in Fig.4(c)). It could be seen from Fig.4(a) that with the further refinement of the grid, the radial velocity near outer wall of the bluff-body matches better and better with the experimental data. However, the radial velocity near the upper surface of the bluff-body (-7mm < r < 7mm) has the best prediction within Grid-2 indicating a further mesh refinement near the upper wall might cause more numerical error. Moreover, as will be shown in the results and discussions part in the current paper, the recirculation bubble besides the outer wall of the bluff-body has strong effect on flame stabilization. Strong fuel-air mixing and scalar dissipation are observed in bluff-body's outer wall region as well. In addition, the simulation results at 20mm downstream of the bluff-body in Grid-3 match fairly well with the experimental data. Hence the finest Grid-3 was chosen in the current paper to carry out the simulation work. The annular channel and the bluff-body were set to adiabatic walls as suggested by Euler et al. [33] based on their experimental investigations. When simulating the iso-thermal flow structures without central jet, the central jet boundary was switched from velocity inlet to adiabatic wall condition.

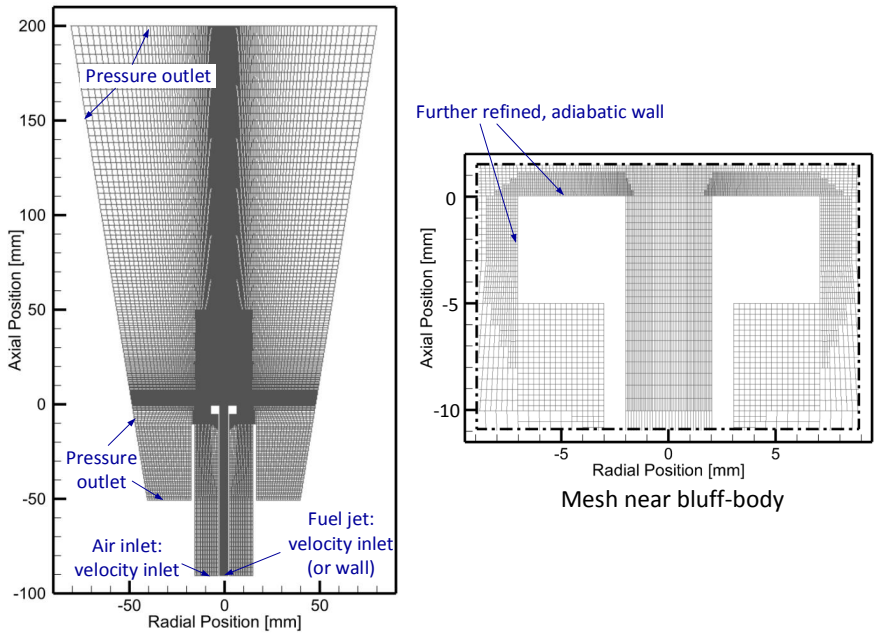

Fig.3 Computational domain and boundary conditions

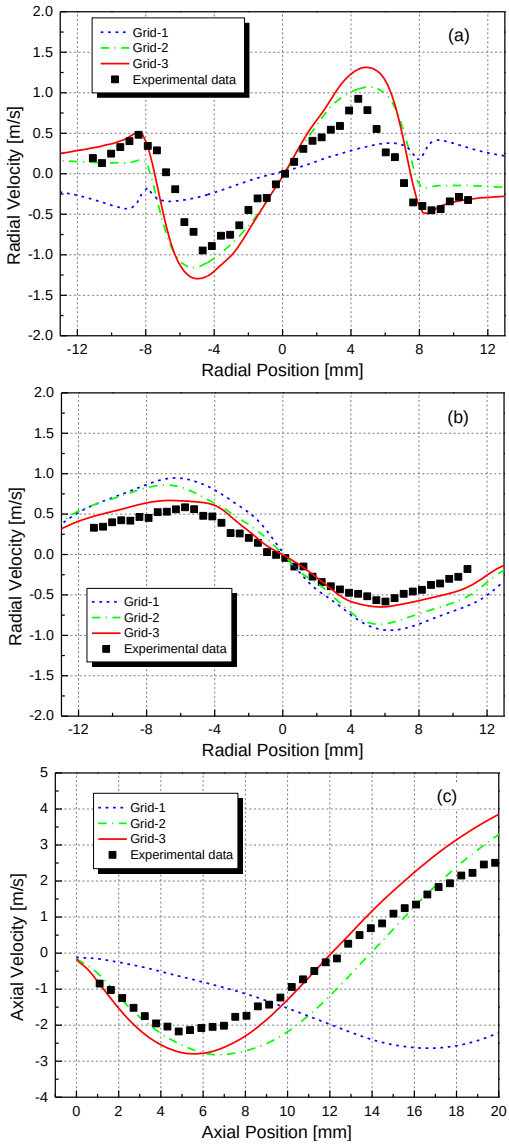

Fig.4 Comparison of experimental data and numerical results from three different levels of mesh refinement: radial velocity along the radial direction at (a) 2mm and (b) 20mm downstream of the bluff-body; (c) axial velocity along the central axis

RESULTS AND DISCUSSIONS

Isothermal flow structures without central jet

When only the annular air flow was considered, the influence of the bluff-body's position is emphasized since the initial flow fields downstream of the bluff-body are undisturbed by the central jet [6]. In the current study, we utilized the definition in the literature [7] to evaluate the length of the recirculation zone. The length (l) of the recirculation zone was defined as the axial distance from the bluff-body's upper surface to the stagnation point which marked the end of the recirculation bubble.

The typical time averaged flow structures (without the central jet) downstream of the bluff-body are shown in Fig.5. The velocity fields in Fig.5 were obtained by averaging 2000 instantaneous vector fields which yielded a time interval of 1s. The color of the vector reveals the value of the axial velocity while the length of the vector shows the value of the velocity magnitude. The axial position in Fig.5 in these two cases shows the local axial distance to the bluff-body upper surface. The left half of Fig.5 shows the velocity fields in case with ΔH = 0mm and the other half illustrates case with ΔH = 10mm. By comparing the two cases, it can be seen that placing the bluff-body 10mm above the annular channel exit enlarges the recirculation vortex.

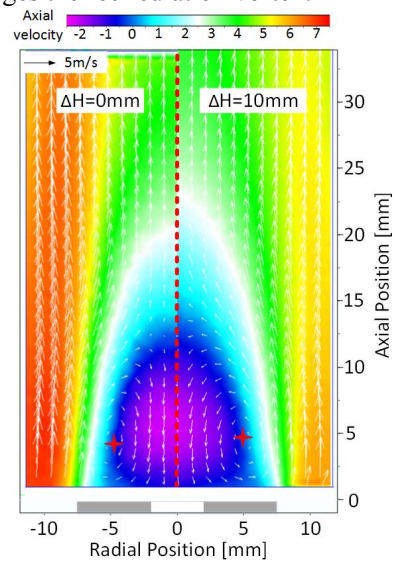

Fig.5 Typical time averaged iso-thermal flow structures downstream of the bluff-body without central jet when holding U_a = 5.84m/s

Simulations were also carried out to simulate the flow fields downstream of the bluff-body with U_a = 5.84m/s in these two burner geometries. All the time averaged numerical results were obtained by averaging 1s time period after the initial transients were convected out of the flow domain over the first 1.5s. Fig.6 reveals the experimental and numerical results of radial velocity distributions at different radial locations. These data were obtained along h = 2mm downstream of the bluff-body in these two cases. It could be observed from Fig.5 that downstream near the bluff-body (-7mm < r < 7mm), due to the formation of the recirculation vortex, the local flow has the monument away from the burner's axis. Whereas near the outer wall of the bluff-body, the axial velocities differ a lot with each other in these two cases. In case with ΔH = 0mm, the annular flow at r > 7.5mm or r < -7.5mm has the momentum towards the burner axis. However, at the same region in case with ΔH = 10mm, the annular flow has the momentum towards the ambient air. Schefer et al. [7] reported that the recirculation zone length and the stagnation point locations were related to the pressure gradients downstream of the bluff-body. In addition, the annular flow curvature constrained by the confinement could also affect the flow fields. In the current study, when the bluff-body was mounted with ΔH = 0mm, the annular channel acted as the confinement. The annular channel's inner wall constrained the air flow to be parallel to the burner axis which would lead to the flow at the region of r > 7.5mm or r < -7.5mm propagating towards the burner axis. However, placing the bluff-body with ΔH = 10mm resulted at a free annular flow expansion to the ambient air, resulting at a flow velocity away from the burner axis. A weaker constrain effect from the annular channel was expected in case with ΔH = 10mm. It is thus the annular air flow was easier to diffuse into the ambient air. Hence the recirculation vortex, which was strongly correlated with the annular air flow streamline curvature near the bluff-body, was larger in the burner with ΔH = 10mm than that in the other case. As will be discussed later, the difference of the recirculation zone size would strongly affect the flame structures and its instabilities. In addition, the recirculation zone length was strongly dependent on the annular flow velocity, U_a, as well. Holding the same annular air flow velocity in these two burner geometries at 2m/s < U_a < 8m/s, larger recirculation zones could always be found in the burner with ΔH = 10mm than that in the other case.

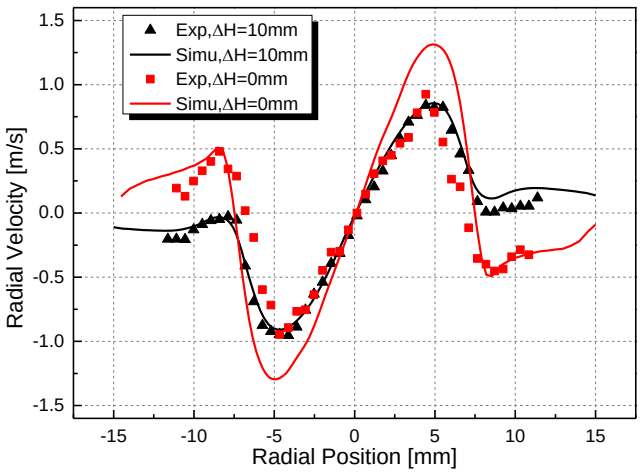

Fig.6 Radial velocity at different radial positions near the bluff-body with ΔH = 10mm and ΔH = 0mm

Flame structures

In this section, flame patterns under different operating conditions are shown firstly. Then the reasons for the different flame structures in the two burner geometries are emphasized. Flame regime maps of the two burners are determined to characterize the influence of bluff-body's position on flame instability. Fig.7 and Fig.8 show the flame regimes and typical transient flame structures in these two burners under different operating conditions.

As shown in Fig.7, when the annular flow velocity was low (i.e. U_a < 2m/s), two flame patterns could be observed in these two burner geometries. While with a moderate U_a, there were three flame patterns under different operating conditions. The flame transition points in these two burner geometries were similar with each other when U_a < 6.8m/s. However, when U_a > 6.8m/s, flame instabilities in these two cases were different. Flame could not be stabilized in the up-left region in Fig.7(a); while in Fig.7(b) it could be stabilized with a recirculation zone flame pattern in the burner with ΔH = 10mm. Two flame extinction phenomenon was observed in the experiments. Flame extinction due to the increasing of central fuel jet velocity when U_j > 10m/s was named as flame blowoff in the current paper. Another flame extinction was caused by the decreasing of fuel flow rate and it was called flame blowout, as shown in the up-left region in Fig.7(a). In overall, the stable diffusion flame region in these two burner geometries shrank with the increasing of annular flow velocity. When $U_a \approx$ 4m/s, flame was easiest to get blowoff in these two cases.

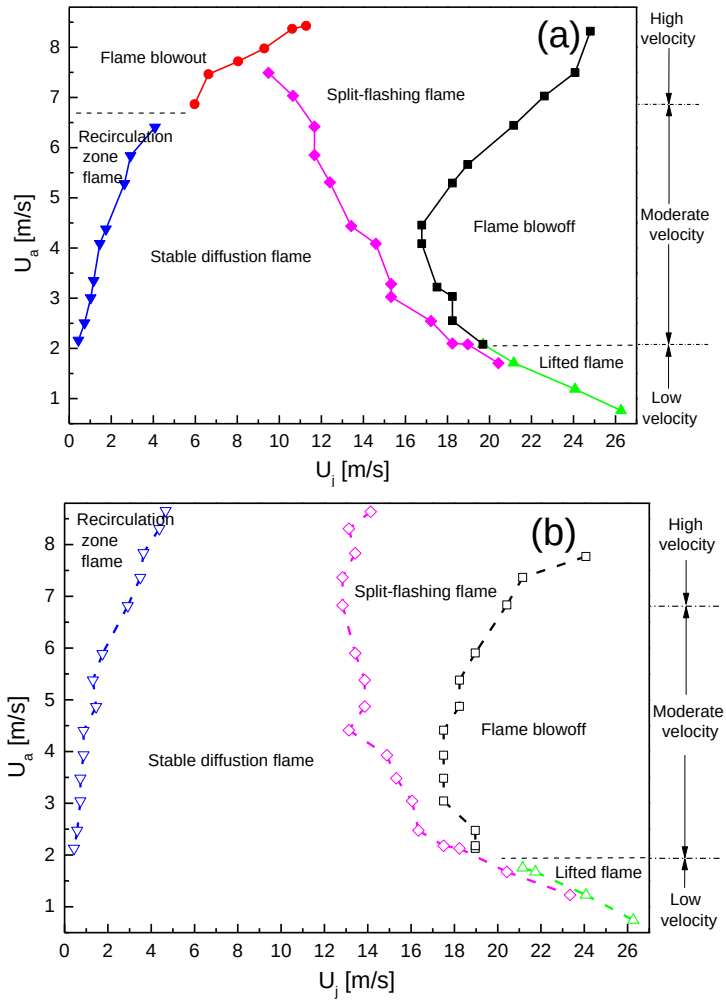

Fig.7 Flame patterns versus different air and fuel velocities in burners with (a) ΔH = -10mm; (b) ΔH = 0mm and (c) ΔH = 10mm

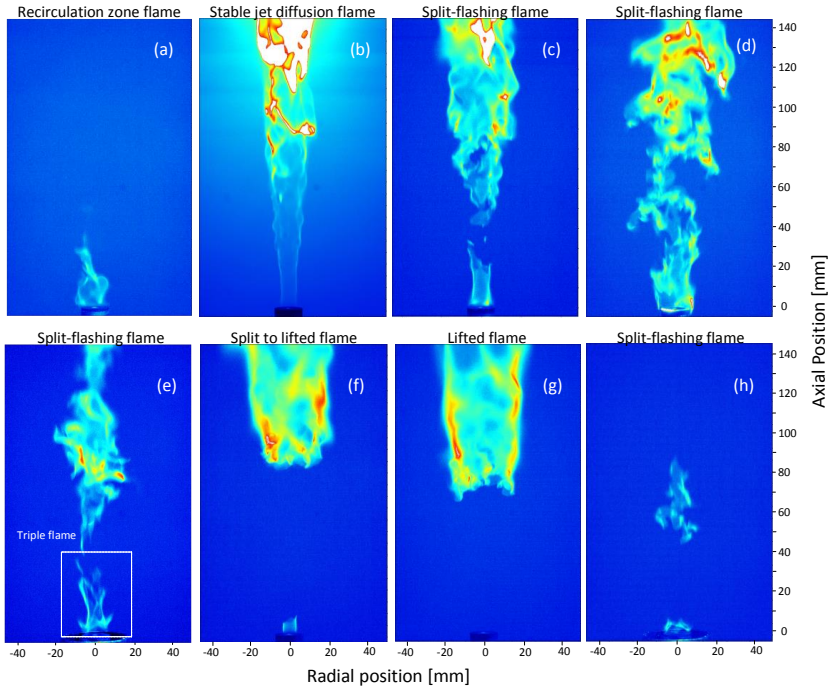

Fig.8 Typical transient flame patterns: (a)recirculation zone flame, (b)stable jet diffusion flame, (c,d,e): split flame, (f) transition from split flame to lifted flame, (g) lifted flame and (h) split-flashing flame

The transient flame structures were shown in Fig.8. More detailed descriptions of different flame structures under different operating conditions will be given later. The different flame behaviors in these two burners are described below according to different annular flow velocity regions: low velocity region (U_a < 2m/s), moderate velocity region (2m/s< U_a < 6.8m/s) and high velocity region (U_a > 6.8m/s). The reasons forming different flame patterns in these two burners are emphasized.

Low annular flow velocity: *When U_a < 2m/s, two patterns could be observed in these two burner geometries: the lifted flame (when U_j is sufficiently high, i.e. U_j > 20m/s) and the stable jet diffusion flame.*

As shown in Fig.8(f), when U_a < 2m/s, with the increasing U_j, the continuous stable diffusion flame got split suddenly while the flame root was kept attached to the bluff-body. A small addition of the central fuel jet enlarged the distance from the flame root to the root of the lifted flame. Moreover, the attached flame under this condition was quite unstable and extinct easily with a small fluctuation of the central jet velocity. Whereas the

lifted part of the flame, as shown in Fig.8(g), was stable and hard to get blowoff. As soon as the flame was lifted from the bluff-body, it was hard to make it reattached to the bluff-body even with a large reduction of U_j. More details about height of the lifted flame root and the hysteresis phenomenon with bluff-body stabilized flame could be found in the literature [34]. In addition, the lifted flame was also hard to blowout with the increasing of central fuel velocity even till U_a = 30m/s. The reactants were partially premixed upstream of the lifted flame by diffusion and convection in the shear layers between the recirculation zones. The lifted flame was stabilized with the balance of the local flow velocity and the flame speed; together with the mixing of the central fuel and the annular air. Hence the lifted flame was a partially premixed flame with a bluish color (which was commonly observed in the premixed CH4-air flame) especially when the fuel flow velocity was low. The flame behaviors in these two burner geometries do not have significant differences with each other.

Moderate annular flow velocity: *When 2m/s < U_a < 6.8m/s, the flame showed three different patterns with the increasing of the central fuel jet velocity: the recirculation zone flame, stable diffusion flame and split-flashing flame then finally till flame blowoff.*

When the central fuel velocity was low (U_a < 3m/s), the flame was stabilized with the recirculation zone flame pattern as shown in Fig.8(a). The recirculation zone flame had a blueish color like that in the premixed CH_4-air flame. It was due to the good mixing of the central fuel jet and the annular air flow prior to combustion. The small amount of central fuel jet did not have sufficient momentum to penetrate the outer recirculation zone. The flow fields under that operating condition were dominated by the annular air flow. Whereas, when the fuel jet penetrated out the outer recirculation zone, the flame structures altered with each other in these two different burner geometries.

In the burner with ΔH = 10mm, when holding U_j at a moderate value, i.e. U_j = 10 m/s, and 2m/s < U_a <6.8m/s, the stable diffusion flame structures altered with the changing of U_a. For specifically, when U_a < 3m/s, the reaction zone near the bluff-body was mainly observed at -4mm < r < 4mm, as can be seen in Fig.8(b), Fig.8(c) and Fig.9(a). The simulation results in Fig.9(a) show that the flow fields downstream of the bluff-body were dominated by the central jet. The central fuel jet could penetrate through the air driven outer recirculation zone. The outer recirculation vortex was small and located close to the bluff-body upper surface. Hence it blocked the convection of the central fuel jet from the central region towards the ambient air. The fuel driven inner recirculation zone core was observed located farther downstream than the outer recirculation zone core. Therefore, the flame near the bluff-body could only be observed along the stoichiometric mixture line (shown by the white line in Fig.9(a)) in the region at -4mm < r < 4mm.

However, increasing the annular flow velocity to i.e. U_a = 5m/s, the reaction zone then was observed in the outer region at -10mm < r < 10mm as shown in Fig.8(d) and Fig.9(b). The outer recirculation bubble then was larger and located further downstream than that in the case with U_a < 3m/s. The inner recirculation bubble core was located at approximately the same height with the outer recirculation bubble. The central fuel propagated in the mixing layer between the inner and outer recirculation zones. The fuel-air mixing layer extended into the pathway between the outer recirculation zone and the bluff-body's upper surface finally into the region at r > 4mm or r < -4mm. Hence, the flame near the bluff-body was found along the stoichiometric mixture line (shown by the white line in Fig.9(b)) downstream of the bluff-body's outer wall. It could also be observed that the flame shown in Fig.8(d) and Fig.9(b) started to propagate upstream into region at h < 0mm where a recirculation bubble was formed besides the bluff-body's outer wall. This recirculation bubble played an important role in flame stabilization and it will be discussed further.

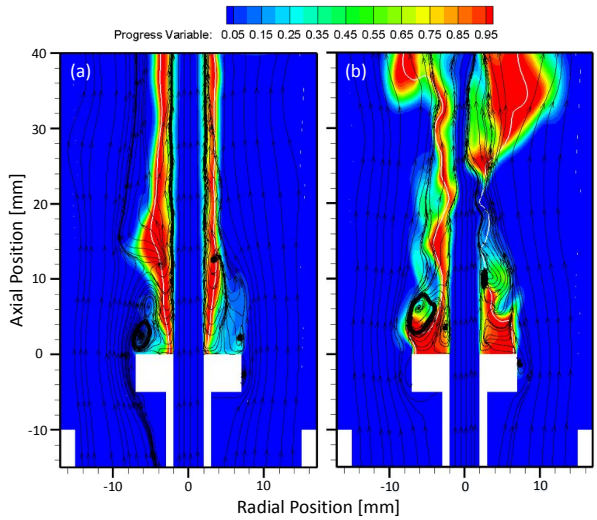

Fig.9 Flame patterns and flow fields near the bluff-body (a) low annular flow velocity (b) moderate annular flow velocity

In the case with ΔH = 0mm, when U_a < 3m/s and U_j was kept at a moderate value, i.e. U_j = 10m/s, the flame was maintained with the same structure as that shown in Fig.8(b). The flow fields were dominated by the central fuel jet. While the inner recirculation bubble core was observed higher than the air driven outer recirculation core, as well. However, when U_a was increased to a higher value (i.e. U_a > 3m/s), the unstable triple flame (as shown in Fig.8(e)) could be observed, instead of the flame shown in

Fig.8(d) in the case with ΔH = 10mm. Moreover, the formation mechanism of the triple flame and flame propagating into the region at h < 0mm in these two burners are compared and shown in Fig.10 respectively. The red lines in Fig.10 denote the position of the flame front while the dashed lines schematically show streamlines of the central fuel and the annular air. The triple flame, or named as the tribsrachial flame [35], consists of three flames: a fuel rich flame on the fuel rich side, a fuel lean flame on the air rich side while in between there is a diffusion flame. The triple flame is usually observed when the diffusion flame is lifted from the burner rim or the bluff-body's upper surface. The annular air diffuses into the inner recirculation zone and mixes with fuel. Then the chemical reaction could take place when the local fuel-air mixture is within the flammability limits. In addition, due to the flammability limits, the premixed flames are not very large or sometimes could not be clearly observed. They consume only a small portion of the fuel. Fuel that is leftover across the rich premixed flame mixes further with the oxygen that survives the lean premixed flame front and they react to form a diffusion flame. Most of the fuel will bypass the fuel rich side of the premixed flame and diffuse directly to the reaction zone of the diffusion flame and reacts with the oxidizer there. Therefore, the length of the diffusion flame branch is much larger than the premixed flame branch [35].

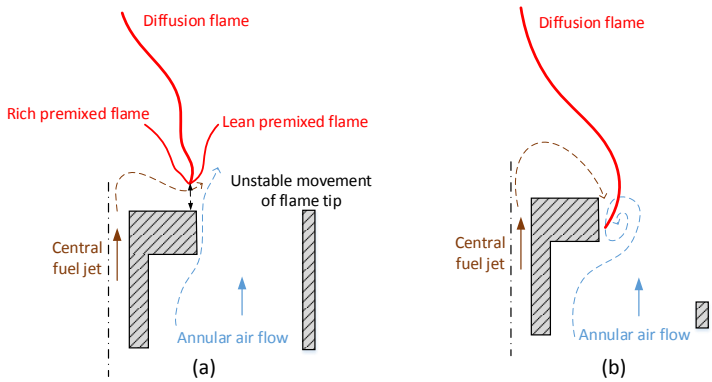

Fig.10 Schematic of (a) unstable triple flame and (b) flame propagating into the region at h < 0mm near the bluff-body

The triple flame was unstable in the experiments due to the unsteady movement of the flame tip near the bluff-body. As schematically shown in Fig.10(a), when the flame tip was lifted far from the bluff-body, a sufficient amount of fuel was convected into the air side through the pathway between the flame tip and bluff-body's upper surface. It would result to the formation of the fuel lean premixed flame branch. Meanwhile it led to an increase of the local temperature and as a consequence the acceleration of flame

speed. With a higher flame speed, the triple flame tip would prone to propagate upstream which probably resulted at the flame tip reattaching to the bluff-body upper surface. It is thus the fuel pathway between the flame tip and the bluff-body's upper wall was narrower. Meanwhile, more heat and radicals were lost to the bluff-body's upper surface since the flame tip was propagating closer to the bluff-body upper surface. So the lean premixed flame branch got quenched with insufficient fuel, heat or/and radicals. At the same time, the local flame speed got decreased consequently. It would lead to the flame tip detaching from the bluff-body's surface until its initial lifted position. By this unstable movement of the flame tip up and down, the unstable loop was formed. However, in the burner with ΔH = 10mm, as shown in Fig.9(b) and Fig.10(b), the triple flame was not observed. Instead, the diffusion flame front propagating into the recirculation bubble besides the bluff-body's outer wall was found. That recirculation bubble created a larger air driven outer recirculation zone downstream of the bluff-body. The local axial flow direction near the bluff-body outer wall differed with each other in these two cases. In case with ΔH = 0mm, the axial flow velocity at h = 0mm and $r \approx$ 7mm was positive towards downstream region. However, in the other case it was reversely towards the upstream region. In the burner with ΔH = 10mm, the central fuel flow convected into the outer wall recirculation bubble, then mixed and reacted with the annular air there. This outer wall recirculation zone flame then propagated downstream forming the main diffusion flame zone. It is thus the triple flame could not be observed in the case with ΔH = 10mm. The flow fields in these two burners highly determined the fuel-air mixing features and the flame structures. The flame stabilized by the outer wall recirculation zone was observed to be more stable than the triple flame.

Moreover, holding the annular flow velocity at a moderate value (2m/s < U_a < 6.8m/s), an increasing of central fuel flow velocity could make the stable diffusion flame to be split in these two burner geometries. Shanbhogue et al. [16] described two phases of bluff-body stabilized premixed flame dynamics near blowoff. The first phase was observed with localized extinction events occurring on the flame front (or names as 'flame hole'). While the second phase was titled with wake/recirculation zone disruption and alteration before blowoff. Here in the current study with a bluff-body anchored non-premixed flame, the flame holes (as shown in Fig.11) were also observed before flame got totally split. The same as reported in literature [16], once a flame hole was initiated, its size might stay constant, grow, or shrink (by 'flame healing'). It was associated with whether the edge flame stays stationary, retreats (a 'failure wave'), or advances (an 'ignition front') into the hole, respectively. The flame hole might propagate with the mean flow with/without a circular movement around the burner axis. In addition, when the

flame hole was formed, the mixing of the fuel and air in the shear layer might be enhanced through the flame holes. Meanwhile, the flame hole also leaded to high efficiency of heat and radical convection from the combustion products to the reactants. With the increasing of the central fuel jet velocity, the diffusion flame was observed to have higher probability of local extinction till it got totally split as shown in Fig.8(c) and (f). The locally high strain rate, high intensity turbulent fluctuations or Da number were explained as the reason for the appearance of flame holes by Shanbhogue et al. [16]. In the diffusion flame stabilization, the locally high scalar dissipation rate together with the local mixing characteristics (with Φ beyond the flammability limits) might also contribute to the local flame extinction. Fig.12(a) reveals the snapshot of local flame extinction in the simulation by showing the temperature distribution and the iso-contours of mixture equivalence ratio $\Phi = 1$. Near the bluff-body, the local flame extinction was observed with local equivalence ratio of $\Phi = 1$, as shown in Fig.12(b). This local flame extinction was caused by the sufficiently high scalar dissipation rate as shown in Fig.12(c). Region with high scalar dissipation rate was found locating in the inner shear layer near the bluff-body. The high scalar dissipation rate at the flame neck region led to the local flame extinction. The same as reported [16], there was a large scale alteration of the wake dynamics after the flame got split. The flame downstream of the split point continued reacting and propagating further downstream with the mean flow until the fuel was consumed completely. The large flame segment, at 100mm $< h <$ 150mm downstream of the bluff-body shown in Fig.12, was developed from the upstream flame blocks with local extinction at flame neck region at $h \approx$ 20mm. The flame upstream of the split position continued propagating downstream till another split point showed up. It is thus the flame dynamic and flame segment were formed. It is worth noting that the locally fuel lean condition might also cause the local flame extinction downstream of the bluff-body. The high product formation rate within the white line shown in Fig.12(c) indicates that the flame starts propagating upstream into the region of $h <$ 0mm. The flame was rooted and stabilized there with locally low scalar dissipation rate and fuel-air mixture was within its flammability limits.

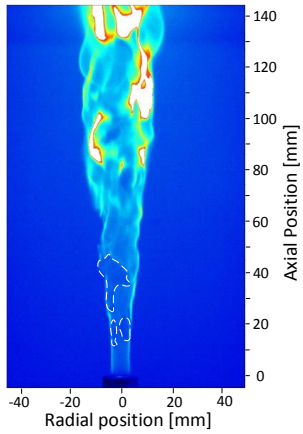

Fig.11 Holes on the flame front before flame got totally split

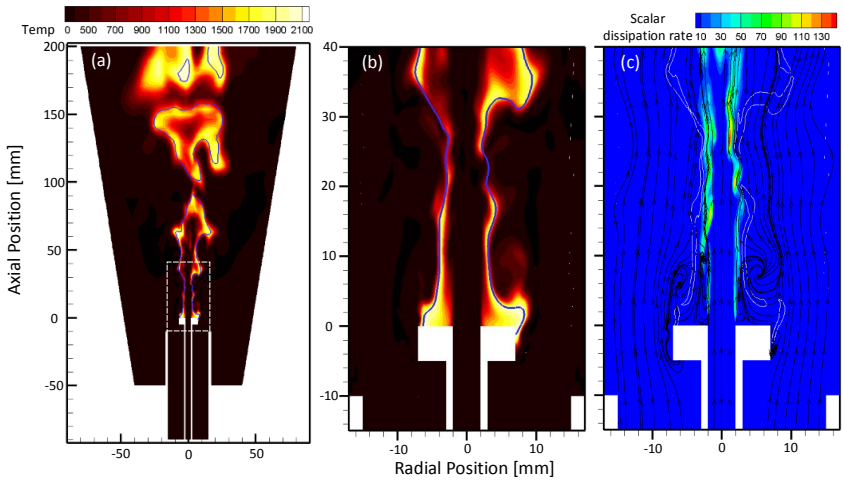

Fig.12 Spatial distribution of temperature and iso-contours of Φ = 1 (a) in a global view and (b) near bluff-body; (c) spatial distribution of scalar dissipation rate and flow fields near the bluff-body; the white line marks the region inside which the product forming rate is higher than 150s^{-}

Different from the unstable flame behavior in cases with U_a < 2m/s, the split flame root with U_a > 2m/s was harder to get quenched. In addition, the flashing unstable flame downstream of the flame neck region was observed as shown in Fig.8(h). As mentioned in the partially extinct split flame, the flame downstream of the neck region was originated from the flame root. If some radicals could survive through the flame neck region (where high scalar dissipation rate could be found), they could ignite the fuel-air mixtures downstream of the neck region. However, most of the radicals were not able to pass

through the neck region. Therefore, the flame downstream of the neck region seems to be flashing. However, the probability density of the flashing flame downstream of the neck region decreased with the increasing of the annular flow velocity. It is since the scalar dissipation rate at the flame neck region increases with the annular flow rate. With the flame approaching totally blowoff, the probability of finding the flashing flame downstream of the flame neck region decreased till none. Then in the end, even the flame root could not be stabilized due to the higher scalar dissipation rate and the annular flow turbulence. The increasing of the air driven outer recirculation zone pushed the inner recirculation zone further closer to the bluff-body's upper wall. It led to more heat and radial loss to the bluff-body upper wall. As a consequence, it may also promote the flame blowoff. Holding the annular flow velocity constant at 2m/s < U_a < 6.8m/s, the flame blowoff could be fulfilled by increasing the fuel flow velocity further till U_j > 20m/s.

High annular flow velocity: *When U_a > 6.8m/s, three flame patterns were observed in the burner with ΔH = 10mm: the recirculation zone flame, stable diffusion flame and split flame till flame blowoff. However, in the other case with ΔH = 0mm, the recirculation zone flame could not be stabilized anymore.*

Placing the bluff-body 10mm above the annular channel exit enhanced the flame stabilization. Fig.13 shows the spatial distribution of the temperature of the flame stabilized with U_a = 7.7m/s, U_j = 7.3m/s and ΔH = 10mm.

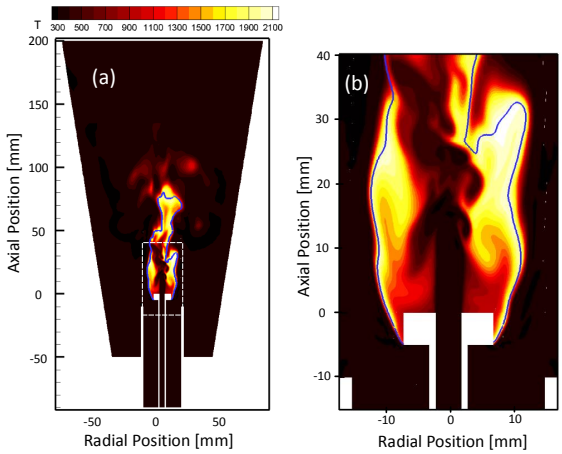

Fig.13 Spatial distribution of temperature and iso-contour of equivalence ratio Φ = 1 with U_a = 7.7m/s, U_j = 7.3m/s and ΔH = 10mm; (a) in the global view and (b) near the bluff-body

The flame shown in Fig.13(a) was shortened compared with the case shown in Fig.12 with lower annular velocity. The flame length was approximately h = 80mm due to the higher turbulence and better fuel-air mixing caused by the annular flow. In addition, the

flame structures obtained from the experiments together with the simulation results under the same operating conditions are shown and compared in Fig.14. It could be seen that the flame tip was propagating further upstream even into the region at h = -5mm. The left part of Fig.15 reveals the experimental data of vectors and streamlines of the reacting flow fields near the bluff-body; while the right part shows the simulation results of flow fields as well as the spatial distribution of the mixture fraction. It is shown that the flow fields near the bluff-body are dominated by the central fuel. A small inner recirculation zone is formed near the bluff-body; while a large outer recirculation zone is observed further downstream. Some other small recirculation bubbles are also observed in the shear layer between the central jet and the annular flow. It is worth noting that a recirculation bubble is found besides the bluff-body's outer wall. The pathway for the central fuel convecting into that recirculation zone is schematically shown by the red dashed lines. The mixing of central fuel het and annular flow could be expressed as: (a) the fuel first mixes with air in the shear layer between the fuel driven inner recirculation zone and the air driven outer recirculation zone; (b) then the fuel rich mixture gets further convected to the recirculation bubble besides the bluff-body; (c) the fuel further mixes with air due to the recirculation of the annular air. The local mixture of reactants might be within the flammability limits or preferably the local equivalence ratio of Φ = 1. Hence flame can be stabilized and originated in that recirculation zone with sufficiently low scalar dissipation rate. As a consequence, flame stabilization was enhanced in the burner with ΔH = 10mm.

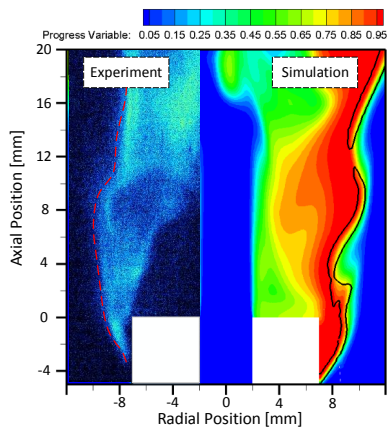

Fig.14 Flame stabilized near the bluff-body with U_a = 7.7m/s, U_j = 7.3m/s and ΔH = 10mm. left: experimental raw image with flame front schematically shown using the dashed red line; right: simulation results with spatial distribution of progress variable and the black line marks the region where the product formation rate is higher than 150s^{-1}

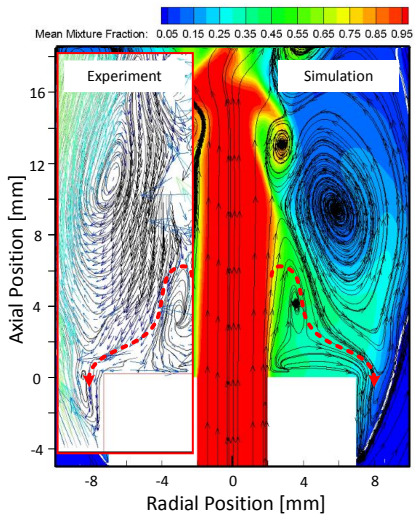

Fig.15 Comparison of simulation results and experimental data of flow structures near the bluff-body (the red dashed line reveals the pathway for the fuel convection)

Comparing the overall flame regimes in the Fig.7 (a) and (b), it could be observed that the burner with ΔH = 10mm has a wider range of the stable flame regime. Hence it could be concluded that mounting the bluff-body 10mm downstream of the annular channel exit could better stabilize the flame.

Effects of combustion on flow fields

Fig.16 compares the time averaged flow fields in both the reacting and isothermal flows in both experiment and simulation. It was reported by Caetano et al. [16] that the combustion presents a weak influence on the averaged flow field. However, other researchers [9] [10] reported that the central jet penetration could be enhanced by the combustion. In the current study, as shown in Fig.16, the combustion significantly changed the flow fields downstream of the bluff-body. The location of the outer recirculation zone core moved farther downstream in the reacting case. In addition, the central jet velocity also got accelerated by combustion. The reason lies in the fact that in the reacting case, fuel density decreases according to the temperature increasing in the recirculation zones. As a consequence, the velocity of the central fuel jet becomes higher. Moreover, the increase of local temperature causes an expansion of local flow volume and thus enlarged the recirculation bubble. In addition, the recirculation bubble besides the bluff-body's outer wall could only be observed in the reacting cases. It is also caused by the flow expansion in the inner and outer recirculation bubbles. Flame thus can

propagate into and be stabilized at the recirculation zone formed besides the bluff-body's outer wall. In the other hand the flow expansion enhances and enlarges this recirculation vortex. The interaction of flow fields and combustion determines different flame structures and flame stability characteristics.

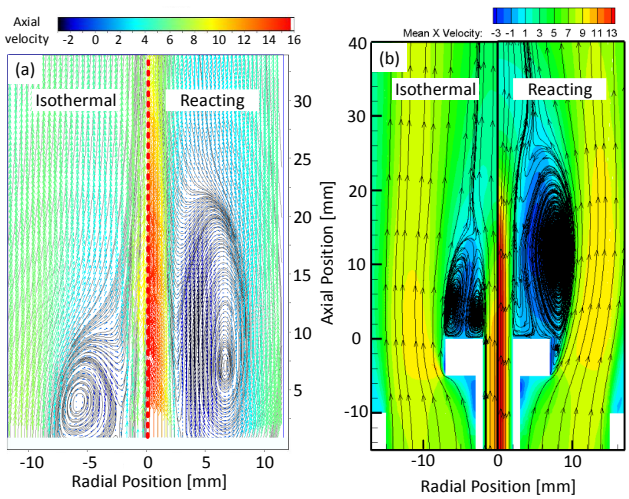

Fig.16 Effects of combustion on flow fields (a) experimental results (b)simulation results

CONCLUSIONS

Experimental and numerical investigations about the effects of bluff-body's position on flame structures and instabilities were carried out in the current study. Different burner geometries, with bluff-body placed 10mm above the annular channel exit or at the same height with the annular channel exit, were studied. It is found that, in the isothermal cases without central jet, the burner geometry with ΔH = 10mm could create at a larger recirculation bubble than that in the other case. Results also bring out that three controlling parameters have to be considered in order to characterize the stabilization regimes: the central fuel and the annular air velocities jointed to the position of the bluff-body. Different flame structures including the recirculation zone flame, stable diffusion flame, split flame and lifted flame were captured and studied. The unstable triple flame and its forming mechanism in the burner with ΔH = 0mm are described as well. The influence of the bluff-body's position is clearly demonstrated, particularly on the recirculation zone flames. Placing the bluff-body downstream of the burner exit promotes recirculation zone flame stabilization. When U_a > 6.8m/s, three flame patterns were observed in the burner with ΔH = 10mm: the recirculation zone flame, stable diffusion

flame and split-flashing flame till flame blowoff. However, in the other case with ΔH = 0mm, the recirculation zone flame could not be stabilized anymore. In overall, the burner with ΔH = 10mm has a larger range of the stable flame regime than the other case indicating the burner with ΔH = 10mm could better stabilize the flame. The small recirculation, which is formed near the bluff-body's side wall, enhances the recirculation zone flame stabilization in cases with ΔH = 10mm. In addition, the effects of combustion on the flow fields near the bluff-body was revealed as: the combustion accelerates the central jet and enlarges the outer recirculation zone. The chemical reaction enhances the formation of the recirculation bubble besides the bluff-body's outer wall in cases with ΔH = 10mm.

ACKNOWLEDGMENTS

The work was financially supported by the Swedish Energy Agency, the Swedish Research Council (VR) and the European Research Council (Advanced Grant TUCLA program). The simulation work was carried out using the computer facilities provided by the Lund University Center for Scientific and Technical Computing (LUNARC). Authors Yiheng Tong and Xiao Liu are supported by scholarship from China Scholarship Council (CSC) which is gratefully acknowledged.

REFERENCES

[1] Y.-c. Chen, C.-c. Chang, K.-L. Pan, J.-T. Yang, Flame lift-off and stabilization mechanisms of nonpremixed jet flames on a bluff-body burner, Combustion and flame, 115 (1998) 51-65.
[2] H. Tang, D. Yang, T. Zhang, M. Zhu, Characteristics of flame modes for a conical bluff body burner with a central fuel jet, Journal of Engineering for Gas Turbines and Power, 135 (2013) 091507.
[3] K.C. San, Y.Z. Huang, S.C. Yen, Flame Patterns and Combustion Intensity Behind Rifled Bluff-Body Frustums, Journal of Engineering for Gas Turbines and Power, 135 (2013) 121502.
[4] W. Roquemore, R. Tankin, H. Chiu, S. Lottes, A study of a bluff-body combustor using laser sheet lighting, Experiments in fluids, 4 (1986) 205-213.
[5] B. Dally, D. Fletcher, A. Masri, Flow and mixing fields of turbulent bluff-body jets and flames, Combustion Theory and Modelling, 2 (1998) 193-219.
[6] I. Esquiva-Dano, H. Nguyen, D. Escudie, Influence of a bluff-body's shape on the stabilization regime of non-premixed flames, Combustion and flame, 127 (2001) 2167-2180.
[7] R. Schefer, M. Namazian, J. Kelly, M. Perrin, Effect of confinement on bluff-body burner recirculation zone characteristics and flame stability, Combustion science and technology, 120 (1996) 185-211.
[8] J.-T. Yang, C.-C. Chang, K.-L. Pan, Flow structures and mixing mechanisms behind a disc stabilizer with a central fuel jet, Combustion science and technology, 174 (2002) 93-124.
[9] R. Schefer, M. Namazian, J. Kelly, Velocity measurements in turbulent bluff-body stabilized flows, AIAA journal, 32 (1994) 1844-1851.
[10] R. Huang, C. Lin, Velocity fields of nonpremixed bluff-body stabilized flames, Journal of energy resources technology, 122 (2000) 88-93.
[11] H. Ma, J. Harn, The jet mixing effect on reaction flow in a bluff-body burner, International journal of heat and mass transfer, 37 (1994) 2957-2967.
[12] J.-T. Yang, C.-C. Chang, K.-L. Pan, Y.-P. Kang, Y.-P. Lee, Thermal analysis and PLIF imaging of reacting flow behind a disc stabilizer with a central fuel jet, Combustion science and technology, 174 (2002) 71-92.

[13] A. Masri, R. Bilger, Turbulent diffusion flames of hydrocarbon fuels stabilized on a bluff body, in: Symposium (International) on Combustion, Vol. 20, Elsevier, 1985, pp. 319-326.
[14] R. Huang, C. Lin, Characteristic modes and thermal structure of nonpremixed circular-disc stabilized flames, Combustion science and technology, 100 (1994) 123-139.
[15] J.P. Longwell, E.E. Frost, M.A. Weiss, Flame stability in bluff body recirculation zones, Industrial & Engineering Chemistry, 45 (1953) 1629-1633.
[16] S.J. Shanbhogue, S. Husain, T. Lieuwen, Lean blowoff of bluff body stabilized flames: Scaling and dynamics, Progress in Energy and Combustion Science, 35 (2009) 98-120.
[17] R.-H. Chen, J.F. DRISCOLL, J. Kelly, M. Namazian, R. Schefer, A comparison of bluff-body and swirl-stabilized flames, Combustion science and technology, 71 (1990) 197-217.
[18] P. Guo, S. Zang, B. Ge, Technical brief: Predictions of flow field for circular-disk bluff-body stabilized flame investigated by large eddy simulation and experiments, Journal of Engineering for Gas Turbines and Power, 132 (2010) 054503.
[19] S. Chaudhuri, B.M. Cetegen, Blowoff characteristics of bluff-body stabilized conical premixed flames with upstream spatial mixture gradients and velocity oscillations, Combustion and flame, 153 (2008) 616-633.
[20] P. Guo, S. Zang, B. Ge, Les and experimental study of flow features in humid-air combustion chamber with non-premixed circular-disc stabilized flames, in: ASME Turbo Expo 2008: Power for Land, Sea, and Air, American Society of Mechanical Engineers, 2008, pp. 709-718.
[21] N.R. Caetano, L.F.F. da Silva, A comparative experimental study of turbulent non premixed flames stabilized by a bluff-body burner, Experimental Thermal and Fluid Science, 63 (2015) 20-33.
[22] P. Kumar, D. Mishra, Effects of bluff-body shape on LPG–H 2 jet diffusion flame, International Journal of Hydrogen Energy, 33 (2008) 2578-2585.
[23] D. Mishra, P. Kumar, Experimental study of bluff-body stabilized LPG–H 2 jet diffusion flame with preheated reactant, Fuel, 89 (2010) 212-218.
[24] Z. Yang, X. Li, Z. Feng, L. Chen, Influence of mixing model constant on local extinction effects and temperature prediction in LES for non-premixed swirling diffusion flames, Applied Thermal Engineering, 103 (2016) 243-251.
[25] A. FLUENT, 15-Theory Guide, ANSYS, Inc., Canonsburg, PA, (2013).
[26] M.L. Shur, P.R. Spalart, M.K. Strelets, A.K. Travin, A hybrid RANS-LES approach with delayed-DES and wall-modelled LES capabilities, International Journal of Heat and Fluid Flow, 29 (2008) 1638-1649.
[27] X. Liu, A. Elbaz, C. Gong, X. Bai, H. Zheng, W. Roberts, Effect of burner geometry on swirl stabilized methane/air flames: A joint LES/OH-PLIF/PIV study, Fuel, 207 (2017) 533-546.
[28] A. Mardani, S. Tabejamaat, Effect of hydrogen on hydrogen–methane turbulent non-premixed flame under MILD condition, International Journal of Hydrogen Energy, 35 (2010) 11324-11331.
[29] C.D. Pierce, P. Moin, Progress-variable approach for large-eddy simulation of non-premixed turbulent combustion, Journal of Fluid Mechanics, 504 (2004) 73-97.
[30] S.R. Qureshi, W.A. Khan, R. Prosser, Large-Eddy Simulation of Bluff-Body Flame Using the Equilibrium Combustion Model, Journal of Thermophysics and Heat Transfer, (2015).
[31] M. Frenklach, H. Wang, C. Yu, M. Goldenberg, C. Bowman, R. Hanson, D. Davidson, E. Chang, G. Smith, D. Golden, GRI-Mech 1.2, 1995, in, 2015.
[32] N. Peters, Turbulent combustion, Cambridge university press, 2000.
[33] M. Euler, R. Zhou, S. Hochgreb, A. Dreizler, Temperature measurements of the bluff body surface of a Swirl Burner using phosphor thermometry, Combustion and flame, 161 (2014) 2842-2848.
[34] T. Nishimura, K. Kunitsugu, K.-i. Morio, The hysteresis phenomenon in flame lift-off on a bluff-body burner under airflow dominant conditions, Combustion and flame, 159 (2012) 1499-1502.
[35] J. Buckmaster, Edge-flames, Progress in Energy and Combustion Science, 28 (2002) 435-475.
[36] X. Gu, S. Zang, B. Ge, Effect on flow field characteristics in methane–air non-premixed flame with steam addition, Experiments in fluids, 41 (2006) 829-837.
[37] K.-L. Pan, C.-C. Li, W.-C. Juan, J.-T. Yang, Low-frequency oscillation of a non-premixed flame on a bluff-body burner, Combustion science and technology, 181 (2009) 1217-1230.
[38] S. Chaudhuri, B.M. Cetegen, Response dynamics of bluff-body stabilized conical premixed turbulent flames with spatial mixture gradients, Combustion and flame, 156 (2009) 706-720.
[39] S. Chaudhuri, S. Kostka, M.W. Renfro, B.M. Cetegen, Blowoff dynamics of bluff body stabilized turbulent premixed flames, Combustion and flame, 157 (2010) 790-802.
[40] R.N. Roy, S. Sreedhara, Modelling of methanol and H 2/CO bluff-body flames using RANS based turbulence models with conditional moment closure model, Applied Thermal Engineering, 93 (2016) 561-570.

Table 1 Bluff-body burners investigated in the literatures and current study

References	d_j(mm)	d_b (mm)	U_j (m/s)	d_a (mm)	U_a (m/s)	ΔH (mm)	Shape	Cone angle
Guo et al. [18, 20, 36]	4	40	2.5-50	60	3.72-12.5	20	Disk / Conical	180 / 60
Yang et al.[1, 8, 12, 37]	3.5	30-45	0-50	55.1	0-20	0	Disk	180
Esquiva-Dano et al.[6]	5	40	0-14	200	3.65	0	Disk / Tulip	180
Huang and Lin[10, 14]	3.4	20	1.25-103	30	3.56-4.52	0	Disk	180
Tang et al.[2]	2.2	27.3		42		0	Conical	45
San et al.[3]	5	30	0-10	30	0-2.5	30	Conical	36.87
Caetano and Silva [21]	7.1	60	4.2-17.9	200	4 / 8	-	-	180
Ma and Harn [11]	8.05	25.2/38.8/43.2	10/14/25	50.25	14/17.9/25	0	Disk / Conical	15/30/45/180
Kumar and Mishra [22, 23]	5	6.5/12.8/18.1	0.816	57	0.016/0.033	0	Disk	180
Chaudhuri and Cetegen [19, 38, 39]	-	10	-	20/40	5-16	90	Disk	180
Roy and Sreedhara [40]	3.6	50	80/134	-	40	0	Disk	180
Current study	4	15	0-30	30	0-8	0 / 10	Disk	180

Table 2 Grid information

Grid name	Mesh size near the bluff-body [μm]		Total grid number
	Upper wall	Outer wall	
Grid-1	250	714.3	1.74 million
Grid-2	62.5	178.6	1.94 million
Grid-3	31.25	89.3	2.18 million

Paper VI

Experimental and Numerical Study on Bluff-body and Swirl Stabilized Diffusion Flames

Yiheng Tong[1,*], Xiao Liu[2], Zhenkan Wang[3] and Jens Klingmann[1]

1: Department of Energy Sciences, LTH, Lund University, Lund Sweden

2: College of Power and Energy Engineering, Harbin Engineering University, Harbin, China

3: Division of Combustion Physics, LTH, Lund University, Lund, Sweden

**: corresponding author: yiheng.tong@energy.lth.se*

Highlights:

1. Combined bluff-body and swirl stabilized diffusion flames are studied.
2. Diffusion flame 'flashback' phenomenon is investigated.
3. Flame stabilized by the larger bluff-body is more compact.
4. A larger bluff-body produces more CO emission.

Abstract:

Bluff-body and swirling flow are commonly utilized to stabilize the diffusion flame in industrial applications, such as gas turbines, ramjets and furnaces. The flame stabilization mechanisms of these two kinds of burners are similar with each other: the interaction between the recirculation zone and the fuel jet. In the current paper, the flow fields of the combinations of swirl and bluff-body stabilized flames were captured using the high speed PIV; while the flame structures were visualized by high speed CH_2O PLIF, the CH* chemiluminescence and broadband chemiluminescence. The global CO emissions from the flames were captured and compared with each other as well. In addition, based on the CFD software OpenFOAM, simulations were adopted to better understand the flame and flow structures. Flames stabilized by different bluff-body sizes (d_b = 14mm and 20mm) or only swirling flow without bluff-body were studied. All reacting experiments were carried out with constant central fuel flow rate (thermal power 2.01kW) and total air flow rates ($m = m_t + m_a$ = 200ln/min). The swirl strength was controlled by the mass flow rate ratio of tangential and axial air. The geometrical swirl number was altered between $S_g = 0$ to $S_g = 4.08$. Simulation results matched well with experimental data. The position of the outer recirculation zone would be affected by the size of the bluff-body and the swirling strength, especially in cases without bluff-body or with a small bluff-body, d_b = 14mm. In addition, the recirculation zone determined the flame structures and the global CO emission levels. With a larger bluff-body, the air driven recirculation zone located more upstream near the burner exit.

Flame prone to be more stable with a larger bluff-body and/or a stronger swirling flow. Flame was observed propagating into the upstream region with higher swirl strength without bluff-body or with the small bluff-body, d_b = 14mm. The mechanism for the diffusion flame 'flashback' was proposed. Flame with a larger swirl number was shorter while its CO emission levels were higher.

Key words: diffusion flame, flow fields, flame structures, PIV, CH_2O PLIF, CO emissions

Nomenclature

c	confinement ratio [-]
d_a	annular channel diameter [mm]
d_b	bluff-body diameter [mm]
d_c	confinement diameter [mm]
d_j	central jet diameter [mm]
d_p	emission probe diameter [mm]
f	focal length [mm]
h	axial position [mm]
h_b	bluff-body height [mm]
H_{COHR}	Position of flame's corner of heat release [mm]
h_q	quartz tube length [mm]
h_t	tangential inlet height [mm]
L_F	representative flame length [mm]
m	total air mass flow rate [ln/min]
m_a	axial air mass flow rate [ln/min]
m_f	fuel mass flow rate [ln/min]
m_t	tangential air mass flow rate [ln/min]
r	radial position [mm]
S	Swirl number [-]
S_g	geometrical Swirl number [-]
U_a	annular flow velocity [m/s]
U_j	central jet velocity [m/s]
w	tangential inlet width [mm]
α	flame open angle [°]
Δt	time delay between two laser pulses [µs]
Φ	equivalence ratio [-]
Φ_g	global equivalence ratio [-]

Abbreviations

CFD	computational fluid dynamics
COHR	corner of heat release
FWHM	full width at half maximum
LES	Large Eddy Simulation
PDF	probability density function
PISO	pressure implicit with splitting of operator
PIV	Particle Image Velocimetry
PLIF	Planar Laser Induced Fluorescence
RANS	Reynolds-Averaged Navier–Stokes

Introduction

Bluff-body and swirling flow are commonly utilized to stabilize the diffusion flame in industrial applications, such as gas turbines, ramjets and furnaces. The recirculation zones, which were created by the swirling flow or the bluff-body, not only enhance the mixing of fuel and air but also bring back the hot products to ignite the reactants. Therefore, the flame is stabilized and in most cases shortened by the recirculation vortex. In addition, the emission levels of CO and NO*x* get altered by the adoption of bluff-body or swirling flow. Easy control of the flame could be achieved by the bluff-body or swirling flow as well.

Researchers usually utilized bluff-body to stabilized the diffusion flame. However, the combination of bluff-body with swirling flow in flame stabilization methods are not commonly seen. Masri et al. [1-7] utilized several modern laser based techniques to test the swirl-stabilized diffusion flame in detail. They obtained complete data set which included flow, mixing, temperature, and composition fields. It was found that, with increasing of swirl number, the stability limits of the flames were broadened but the scatter plots show locally unburnt fluid samples occurring in flames further from global blow-off than non-swirling bluff-body-stabilized flames of similar fuel mixtures. Their experimental data was widely used for the modelers to evaluate their simulations. Chen et al. [8] compared the bluff-body and swirl flow stabilized diffusion flames. They mentioned that there are commonly two types of flames: the strongly recirculating flame and the fuel jet dominated flame, in the bluff-body and swirl flow flame holders. The dimensionless vortex strength and fuel jet momentum were concluded as the fundamental parameters that govern the flame behaviors. A good agreement between the bluff-body flow and the swirl flow with swirl number $S = 0.5$ for both isothermal and reacting cases was reported. Coghe et al. [9] studied the flow fields of the confined diffusion swirl flame using Laser Doppler Velocimetry (LDV). They used the momentum ratio of the fuel jet to the swirl air as one of the main parameters dominating their interaction. The rapid mixing and burning induced by the hot reverse combustion products were concluded as the reason for flame stabilization. Using PIV system, Olivani et al. [10] further investigated the flow fields of the same burner as that studied by Coghe et al. [9]. The fuel concentration was captured by the 2-D laser Mie scattering of seedings in the PIV measurement. In addition, they also investigated the effects of the radial fuel injection on flow and flame structures. It was found that the radial injection of the fuel would result at a near premixed flame whereas the axial fuel injection leaded to a diffusive flame. They emphasized that the swirling motion of the flow governed the flame structures. Santhosh and Basu [11] experimentally studied the blowout and flame structures transitions of unconfined swirling diffusion flame. They observed two flame topology transition modes till blowout based on the alternation of flow swirl number. The primary transition was reported as a transformation from yellow straight jet flame to lifted flame with blue base and finally to swirling seated (burner attached) yellow flame. The secondary transition was from a swirling seated flame to a swirling flame with a conical tail piece and finally to a highly-swirled oxidizer-rich flame near blowout. Loretero and Huang et al. [12] investigated the effects of acoustic

excitation on swirling diffusion flames. They named the flame modes without excitation as: swirling flame, lifted flame and transitional reattached flame. The fuel-air mixing mechanisms and thus the flame modes were found to be altered with the excitation level when holding the flow swirl number constant. They also mentioned that the time averaged flame length decreased with the increasing of flow swirl number. Ge and Zang [13] investigated the interactions of bluff-body and swirl flow in stabilizing the diffusion flame process. Comparisons of bluff-body stabilized flames with and without swirling flow; and swirl stabilized flames with and without bluff-body were made based on the PIV measurement. The same as mentioned in the literature [8], two flame modes: the recirculation zone flame and fuel jet dominated flame were observed in all the cases they tested. Kawahara and Nishimura [14] studied the flame instabilities with swirling adding into a typical bluff-body stabilized diffusion flame. They divided the flame shape into four groups: the inner flame, outer flame, recirculation zone flame and lift flame. The adding of swirl flow was concluded to have strong positive effect in stabilizing the flame. Schmittel et al. [15] studied the swirling diffusion flame with a quarl at the burner exit and observed two types of flame configurations. Focus was on the formation mechanism of NO_x in the flame. Elbaz and Roberts [16] investigated the effects of the quarl geometry on swirling diffusion flame stability, flame structures and emissions. It was found that the straight quarl performed better in stabilizing the flame with a broader range of stable flame. Different recirculation zones near the quarl and the corresponding mixing characteristics were proposed as the reasons for the alternation of flame behaviors. Dinesh [17] et al. numerically studied the mixing feathers of three different basic fluid dynamical problems: a simple turbulent round jet flow, bluff-body stabilized jet and a combination of bluff-body and swirling annular flow stabilized round jet in a co-flow environment. It was found that the scalar mixing in the radial direction was highly enhanced by the bluff-body and swirling motion. However, the results they obtained were only in isothermal cases without reaction. Al-Abdeli et al. [1] studied the unsteady behavior of turbulent diffusion flame stabilized by swirling flow. They mentioned that for a classical swirl burner configuration with a central fuel pipe and a swirling co-flow of air, flame instabilities may be caused by (i) acoustic resonance in the central fuel pipe or the annular air flow, (ii) vortex shedding in the fuel or air supplies, and (iii) the presence of a three dimensional, time-dependent Precessing Vortex Core (PVC). In addition, the pressure field, heater release or confinement wall might also contribute to flame instabilities.

In addition to the experimental investigations of diffusion flame stabilized by swirling flow or bluff-body, there are lots of numerical research as well. Yılmaz [18] employed the commercial CFD Fluent to study the effect of swirl strength on combustion characteristics of natural gas diffusion flame. The 2-D axisymmetric RANS model and eddy dissipation model joint with P-I radiation model were adopted. It was concluded that the flow swirl strength strongly affected the flame characteristics (including the temperature distribution and gas concentrations) and the size and strength of the recirculation zones. Kashir et al. [19] studied the combustion characteristics of blended methane-hydrogen diffusion flame stabilized by the combination of bluff-body and swirling flow. They tested their numerical model with experimental data from Masri et

al. [20] and revealed the typical flow fields downstream of the bluff-body with and without a swirling flow as shown in Fig.1. The inner recirculation zone was driven by the central fuel jet whilst the outer recirculation zone was caused by the bluff-body and driven by the annular air flow. With the increasing of the swirl number of the annular flow, an additional swirling flow driven 'secondary vortex' was formed further downstream of the bluff-body. The flow fields appeared an hourglass shape. However, Malanoski et al. [21] descried the flow fields with different bluff-body sizes in the premixed flames. They claimed that with larger bluff-body or high swirl flows, the secondary recirculation bubble and the wake downstream of the bluff-body merged into a single vortex structure. As shown in Fig.1, Dally et al. [22] identified three shear layers in the recirculation zone downstream of the bluff-body: an outer shear layer between the outer vortex and the air coflow, an intermediate layer (or named as mixing layer) between the outer vortex and the inner vortex, and an inner layer between the inner recirculation zone and the fuel jet. The relative contribution of each layer to the overall mixing varies with the fuel and jet velocity. Moreover, LES approach has a great potential in predicting the details on the flow dynamics in both swirling flow [23-27] and bluff-body [28-32] stabilized flames.

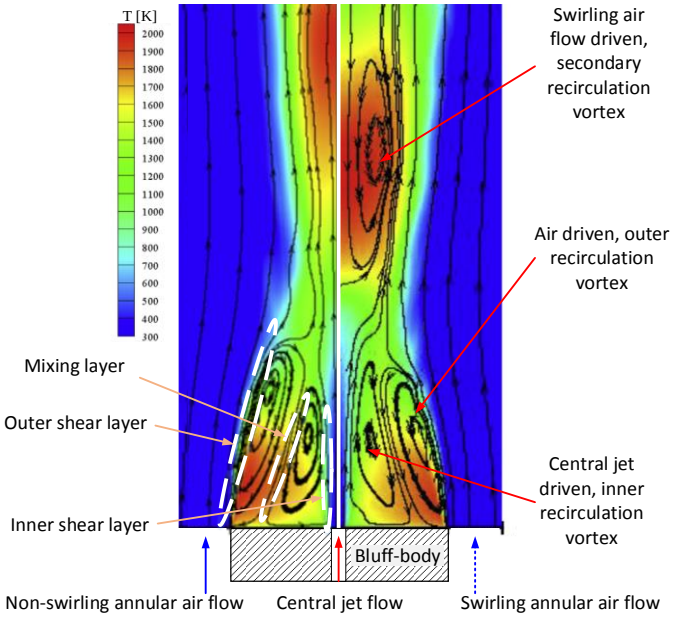

Fig.1 Typical time averaged flow and flame structures downstream of the bluff-body with non-swirling (left) and swirling (right) annular flow (reproduced from [19]).

Here in the current study, we studied the effects of swirling and bluff-body on stabilizing the methane-air diffusion flame. Focuses are on the flame structures and CO emission levels within the bluff-body and swirl stabilized flames. Both experimental study and numerical investigations were carried out to obtain deep insight into the flow fields and scalar structures and their correlations with flame behaviors.

Experimental Setup and Numerical Methods

Experimental Setup: The experimental setup is schematically shown in Fig.2 while the variable swirl burner is shown in Fig.3. The annular flow channel of the burner had a

diameter of d_a = 32mm while the confinement for the setup had a diameter of approximately $d_c \approx 10d_a$. Hence the confinement ratio was $c = (d_a / d_c)^2 \approx 0.01$. Optical windows on the confinement allowed visualization of the flame and the adoption of PIV measurements. As shown in Fig.3, fuel was supplied through the central jet pipe (d_j = 4mm) while the swirling air flow was generated by the swirler and then fed through the annular channel. Methane was selected as the central fuel jet since it is the main component in natural gas. In addition, the established and detailed chemical reaction mechanisms of methane are available for the numerical simulations. The removable bluff-body was mounted at the exit of the fuel pipe. Two sizes of disk shape bluff-bodies (d_b = 14mm and 20mm) were adopted in the experiments. The height of the two bluff-bodies were the same at h_b = 5mm. An optical quartz tube (h_q = 50mm) was placed upstream of the burner exit through which the flame propagating upstream of the bluff-body could be observed. As shown in Fig.3, the swirling flow was generated by eight tangential flow inlets with height of h_t = 10mm and width w_t = 3mm.

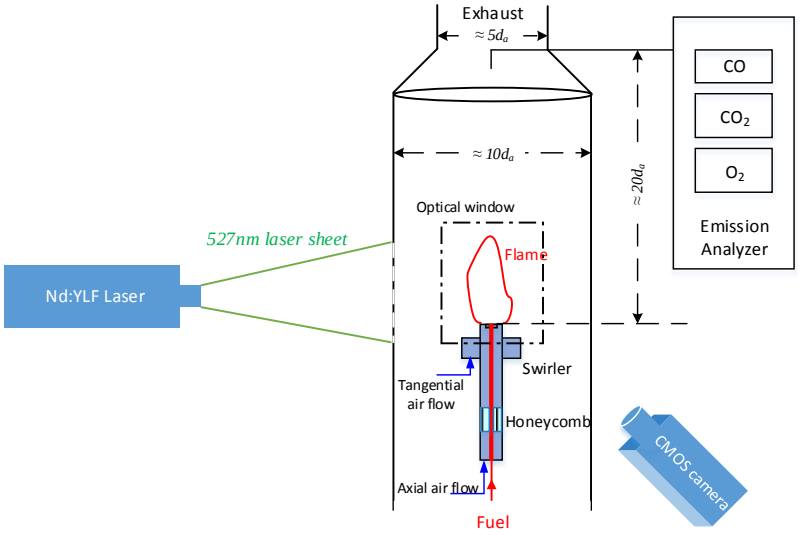

Fig.2 Schematic of experimental setup and the high speed PIV system.

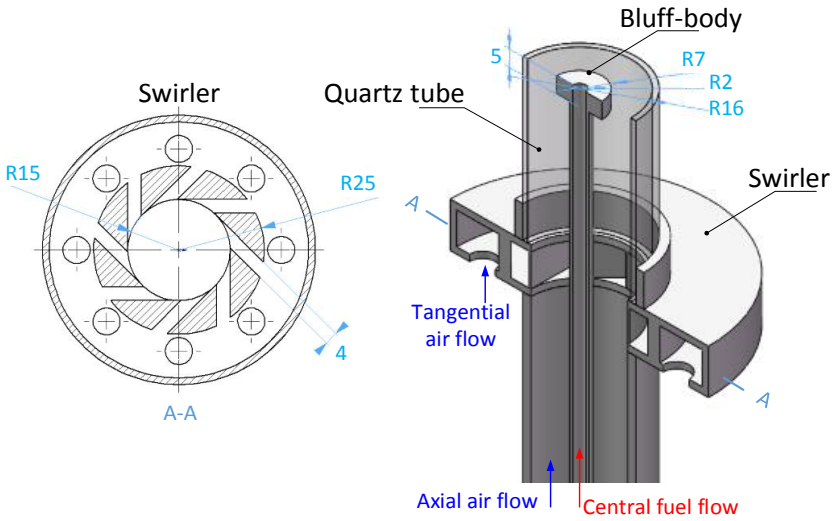

Fig.3 Schematic of the variable swirl burner and the swirler.

Swirl Number and Test Cases: As mentioned above, swirl number at the burner exit was varied by changing the momentum ratio of the tangential to axial flows through the swirler. The same as in the literatures [16] and [33], flow swirl number here is defined using the geometrical swirl number (S_g) which is based on the mass flow rate ratios of the axial air (m_a) and tangential air (m_t). It is defined as

$$S_g = \frac{\pi r_{ch} d_b}{2A_t}\left(\frac{m_t}{m_t + m_a}\right)^2$$

where A_t is the total area of the eight tangential air inlets; d_b is the diameter of the bluff-body (d_b= 4mm, 14mm, 20mm); r_{ch} is the radius of the annular air tube $r_{ch} = d_a - d_t$; as mentioned above, d_a is the diameter of the annular channel (d_a = 32mm). In this work, the geometrical swirl number varied from 0 to 4.08 based on different tangential and axial flow rate ratios and bluff-body sizes. It is worth noting that the total mass flow rate of air, $m = m_t + m_a$ = 200ln/min, and the fuel flow rate, m_f = 3ln/min, were hold constant in all the test cases. Hence the global equivalence ratio was kept constant at Φ_g = 0.14 and the thermal power was hold at 2.01kW. The tests cases investigated in the current study are listed in Table 1.

Table 1. Test Cases.

Case Name	d_b [mm]	m_t [ln/min]	m_a [ln/min]	m_f [ln/min]	m_t/m [-]	S_g [-]
T200-A0-d0	-	200	0	3	1	4.08
T150-A50-d0	-	150	50	3	0.75	2.30
T200-A0-d14	14	200	0	3	1	2.83
T150-A50-d14	14	150	50	3	0.75	1.59
T100-A100-d14	14	100	100	3	0.5	0.71
T50-A150-d14	14	50	150	3	0.25	0.18
T0-A200-d14	14	0	200	3	0	0
T200-A0-d20	20	200	0	3	1	1.88
T150-A50-d20	20	150	50	3	0.75	1.06
T100-A100-d20	20	100	100	3	0.5	0.47
T50-A150-d20	20	50	150	3	0.25	0.11
T0-A200-d20	20	0	200	3	0	0

Photography and image analysis methods: A Nikon D70s camera with a high special resolution (2000×3008 pixels, 24bits, focal length f = 50mm) was used to capture the broadband chemiluminescence of the flame structures with an exposure time of 0.05s. The flame structures were obtained in dark environment to lower the background noises. The same camera together with a band-pass filter (430 ± 10nm) was adopted to capture the CH* chemiluminescence from the sooty diffusion flame. The exposure time was elongated to 1s due to the weak light intensity from the CH* chemiluminescence. In addition, three CH* chemiluminescence images, which were obtained under the same operating condition, were used to get a time averaged flame structures. All the flame photography was obtained without the confinement shown in Fig.2 to have a better visualization of the flame. It was revealed that, when the confinement ratio was lower than 0.25, the confinement had no effect on the flow fields or the flame structures [34].

Therefore, in the current paper with confinement ratio of c = 0.01, the flame structures obtained without confinement was believed to be the same as that within the confinement.

The typical time averaged CH* chemiluminescence from the flame is shown in Fig.4(a). The characteristic flame length (L_F) and the position of flame's center of heat release (H_{COHR}) could be obtained from the CH* chemiluminescence images [35-37]. For specifically, in order to obtain the flame length, CH* chemiluminescence intensity within the image was first summed up along the axial direction. The axial heat release rate profile illustrates distribution of heat release along the axial direction of the confinement as demonstrated in Fig.4(b). The position of flame's center of heat release (H_{COHR}), as shown in Fig.4(b), is the axial location with maximum CH* chemiluminescence intensity. The full width at half maximum (FWHM) of heat release distribution profile as shown in Fig.4 was calculated by finding the width in the axial profile at an intensity value of half of the peak value [35]. The FWHM is representative of the axial distribution of the flame's heat release; it is thus a characteristic flame length, L_F [37]. The position of flame's center of heat release in Fig.4 is H_{COHR} = 24.6mm while the representative flame length is L_F =41.5mm. In addition, to better visualize the flame structures in the central plane of the burner, an inverse Abel image reconstructed method was adopted to the blue layer of the raw images of the CH* chemiluminescence from the flame [36]. The comparison of time averaged CH* chemiluminescence image and its inverse Abel reconstructed flame structures will be shown later.

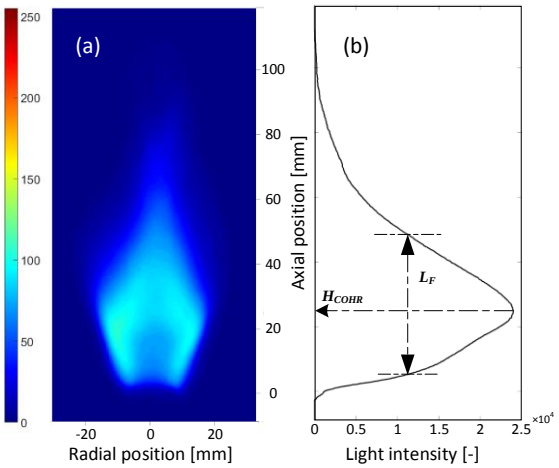

Fig.4 (a)Typical time averaged CH* flame structures and (b) height for flame's center of heat release (H_{COHR}) together with flame length (L_F) of full width at half maximum (FWHM) measurement overlaid.

Particle image velocimetry (PIV)*:* As shown in Fig.2, The flow fields downstream of the bluff-body were measured using a high-speed PIV system (Lavision Flowmaster). A diode-pumped, dual cavity Nd:YLF laser (Litron LDY) was utilized to illuminate the central plane of the bluff-body with a laser sheet thickness of approximately 1mm, using a diverging light sheet generated by an sheet optics. The high speed laser has a wavelength of 527nm and frequency of 2kHz. The time delay between two laser pulses

was set to Δt = 50μs. The laser light scattered off the TiO_2 seed particles and was recorded at a repetition rate of 2kHz with a high speed CMOS camera (Vision Research Phantom V 611). The TiO_2 particles were seeded into the annular air flow using a LaVision solid particle seeder (LaVision Particle blaster 100). It should be noted that no seeding particles were in the central fuel jet flow. Hence the velocity in the central region near the bluff-body was missed. A multi-pass cross-correlation algorithm, which was available in the DaVis (v.8.1.4) computer software, was utilized to evaluate the velocity fields downstream of the bluff-body. The cross-correlation was performed on interrogation areas of 64×64 and subsequently 32×32 pixels with a window overlap of 50%. The focus area contains the inner and outer recirculation zones and the three main shear layers mentioned in the introduction part.

Planar Laser Induced Fluorescence (PLIF): The CH_2O planar laser induced fluorescence (PLIF) was adopted in the experimental investigation. A burst-mode laser (QuasiModo by Spectral Energies, LLC) was used to excite CH_2O molecules at 355nm. More detailed information about the CH_2O PLIF can be found in the literature [38]. A cylindrical lens (f = -40mm) and a spherical lens (f = +500mm) were used to form the laser sheet with 70mm in height and less than 0.5mm in thickness passing through the center of the burner. A high speed COMS camera (Photron Fastcam SA-Z) was placed perpendicular to the laser sheet plane. The exposure time was set as 250 ns in order to reduce the influence of chemiluminescence and Planck radiation from the diffusion flame. A long pass filter (GG385) was used to prevent the scattering light of the laser entering into the camera. A camera lens (f = 50mm, F# =1.2) together with a 12mm extension ring were mounted in front of the camera to create a rectangular field of view by 74 × 65 mm^2.

The pulse width of the laser was set to 10ns. Therefore, the motion of the diffusion flame was ‘‘frozen’’ in each image. The camera and laser were synchronized by a digital delay and pulse generator (DG535) at 22.5kHz. The resolution of the camera was 1024 × 896 pixels. The camera started before the start of the burst-mode laser. Hence, the high speed camera recorded the natural luminosity image of the diffusion flame without the laser as a background image. By subtracting the background image, the noise of chemiluminescence and Planck radiation from the diffusion flame was suppressed. Fig.5(c) shows the results of CH_2O PLIF after the background subtraction. As can be seen from Fig.5, the distribution of CH_2O could be distinguished well from the sooty flame by the background subtraction.

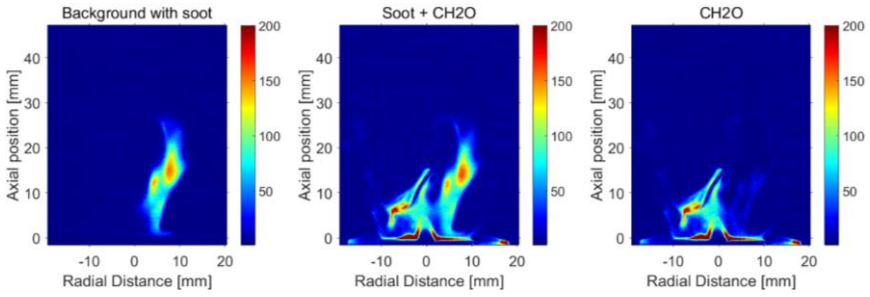

Fig.5 CH_2O PLIF in sooty flame and background subtraction result.

Emission measurement: The emission system consisted of a Rosemount Oxynos 100 paramagnetic O_2 gas analyzer, a Rosemount Binos 100 NDIR (non-dispersive infrared photometer) CO/CO_2 gas analyzer. The measurement ranges for O_2, CO and CO2 were 0–25%, 0–1000ppm and 0–16% respectively. A water-cooled combustion exhaust gas sampling probe was mounted near the combustor exit. The emission probe (with inner diameter d_p = 1mm) was placed at the center of the confinement exit as shown in Fig.2. The global emissions were captured since the distance from the burner exit plane to the emission probe was approximately $20d_a$ which was far longer than the flame length. The confinement ended with a convergent section of $d \approx 5d_a$ in order to have the averaged global emission level. To avoid condensing in the gas analyzer, the sample gas flowed directly into a cooler. With the simple condensation process, the water vapor was removed from the sample gas. The dry emission sample was then analyzed to get the final emission results. In order to minimize measurement errors, the emission gas analyzers were calibrated using standard calibration gases prior to each experiment. The same as in the literatures [39] and [40], all emissions measured were corrected to 15% O_2 by volume for eliminating the dilution effects from the leakage of the confinement. The adjusted emission level (C_{adj}) is calculated as:

$$C_{adj} = C_{meas}\frac{20.9-15}{20.9-O_2\%}$$

where C_{meas} is the measured value of the emission and O_2% is the measured O_2 value.

LES based Eulerian stochastic fields model: As mentioned in the introduction part, LES has proven to be a powerful tool in predicting the transient diffusion flame and flow structures in both bluff-body and swirling flows. By employing the Favre filter, the governing equations for the compressible LES model can be expressed as:

$$\frac{\partial\bar{\rho}}{\partial t}+\frac{\partial\bar{\rho}\tilde{u}_i}{\partial x_i}=0$$

$$\frac{\partial\bar{\rho}\tilde{u}_i}{\partial t}+\frac{\partial\left(\bar{\rho}\tilde{u}_i\tilde{u}_j\right)}{\partial x_j}=-\frac{\partial\bar{\rho}}{\partial x_i}+\frac{\partial}{\partial x_j}\left(\bar{\tau}_{ij}-\bar{\rho}u_i''u_j''\right)$$

The sub-grid stress is closed using the Smagorinsky model.

The composition probability density function (PDF) method [41] was adopted to simulate the turbulent flame structures. As in the literature [41], for the one-point, one-time joint PDF $\tilde{P}_{sgs}(\psi;\mathrm{x},\mathrm{t})$ of the composition vector $\psi=[Y_1,Y_2,\cdots,Y_{Ns},h]$, the modeled transport equation was:

$$\bar{\rho}\frac{\partial\tilde{P}(\psi)}{\partial t}+\bar{\rho}\tilde{u}_j\frac{\partial\tilde{P}(\psi)}{\partial x_j}+\frac{\partial}{\partial\psi_\alpha}\left[\bar{\rho}\dot{\omega}_\alpha(\psi)\tilde{P}(\psi)\right]=-\frac{\partial}{\partial x_i}\left[\left\langle u_i''|\psi\right\rangle\bar{\rho}\tilde{P}(\psi)\right]+\frac{\partial}{\partial\psi_\alpha}\left[\left\langle\frac{\partial J_i^\alpha}{\partial x_i}|\psi\right\rangle\tilde{P}(\psi)\right]$$

where $\langle\cdot|\psi\rangle$ denotes the conditional averaged. Additionally, the sub-grid eddy-viscosity

and interaction-by-exchange-with-mean (IEM) are used to model the sub-grid transport and the micro-mixing terms, respectively.

The Eulerian Stochastic Fields (ESF) method [41-43] is employed to solve the composition PDF equations. The governing equation for the *n*th stochastic field can be expressed as

$$\bar{\rho} d\xi_\alpha^n = -\bar{\rho}\tilde{u}_i \frac{\partial \xi_\alpha^n}{\partial x_i} dt + \bar{\rho} S_\alpha^r(\psi^n) dt + \frac{\partial}{\partial x_i}(\Gamma_t \frac{\partial \xi_\alpha^n}{\partial x_i}) dt - \frac{1}{2}\bar{\rho} C_\phi \omega_T (\xi_\alpha^n - \tilde{\phi}_\alpha) dt + \bar{\rho}\sqrt{2\frac{\Gamma_t}{\bar{\rho}}} \frac{\partial \xi_\alpha^n}{\partial x_i} dW_i^n$$

where, $d\boldsymbol{W}^n$ represents a vector Wiener process that is spatially uniform but different for each field.

The chemical kinetic mechanism of Smooke and Giovangigli [44] is utilized in the present LES. This mechanism is made up of 16 species and 35 reactions. It is known to give similar laminar flame speed as the more comprehensive mechanisms for methane/air combustion, such as GRI3.0 [45], under atmospheric pressure and room temperature conditions. Under the condition of 1atm and 294K and for methane/air one-dimensional counter flow diffusion flame, the critical quenching scalar dissipation rate is about $35s^{-1}$ with the mechanism of Smooke and Giovangigli, while it is $33s^{-1}$ with the GRI3.0 mechanism. The computational cost required with the mechanism of Smooke and Giovangigli [44] is relatively low; thus, it is preferred here since the PDF calculation is time demanding.

Mesh and numerical setup: Fig.6 shows the computational domain and the boundary conditions in the simulation. Fuel (methane) was supplied at a constant jet bulk velocity of U_j = 4.224m/s through the central tube as indicated in Fig.6; while air flow inlet velocity altered according to the bulk velocity of the tangential and axial inlets obtained from the experiments. Downstream the swirler a conical domain was considered in the simulation. A conical domain extending 75 fuel jet diameters (d_j = 4mm) in the downstream direction was adopted in the simulation, with $r = 15d_j$ in radial direction at the swirler exit plane, and $r = 45d_j$ at the outlet plane. The minimum grid scale is 0.2mm inside the quartz tube and the reaction zone. The total grid number was approximate 3 million.

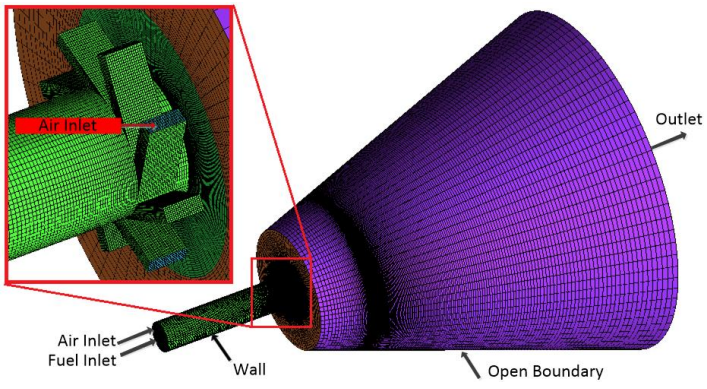

Fig.6 Illustration of computational mesh and boundary conditions.

The open source CFD library, OpenFOAM [48], is adopted for the numerical integration of the governing equations. The second-order filtered linear implicit scheme was used for the spatial discretization and the second-order backward Euler scheme was used for the temporal integration. The pressure implicit with splitting of operator (PISO) algorithm was employed for the pressure-velocity coupling. At the wall boundaries the non-slip boundary condition was applied. A velocity mapping method with a prescribed mass flow rate of the fuel was employed at the fuel inlet. Moreover, at the open boundaries, the pressure condition was applied. It allowed the ambient air to entrain into the domain; meanwhile it also allowed the fluid to flow outside the domain. The experiments were done at 1atm while both the air and the fuel inlet temperature were 294K. They were adopted as the initial boundary conditions in the LES simulation.

Results and Discussions

Effects of bluff-body on flames: Fig.7 shows different flame structures with different cases when holding the fuel flow rates and the ratio of the tangential to the axial air flow rate constant. The dot line in the second row of Fig.7 schematically shows the position of the central fuel pipe, different bluff-bodies and the annular quartz tube. It should be noted that the inverse Abel image reconstruction was only valid downstream of the burner exit where the CH* chemiluminescence was not blocked by the central pipe or the bluff-body. All the time averaged CH* image and the inverse Abel reconstructed images were scaled to better visualize the flame structures.

Flame structures in case T150-A50-d0: From the inverse Abel reconstructed image in Fig.7, the flame expansion was observed downstream near the burner exit. The flame expansion had an open angle α, which was marked by the dash dot line in the third row in Fig.7. At h = 30mm, the flame became compact forming a flame tail till h = 80mm. Between the compact flame tail and the expansion flame region, the flame became less yellowish indicating a region with better fuel-air mixing and thus less soot. The flame tail in the burner without bluff-body was longer than the other cases. Without bluff-body, the flame tip was ‘flashback’ upstream of the fuel pipe exit into the quartz tube. The reason for the flame ‘flashback’ would discussed later with the transient and time averaged flow fields results.

Flame structures in case T150-A50-d14: Downstream of the burner exit, the flame structures in the burner with d_b = 14mm was similar to that in the burner without bluff-body. The same flame expansion near the burner exit and the flame tail downstream could also be observed. However, the flame open angle was smaller than that in case T150-A50-d0. Different with the flame structures in case T150-A50-d0, the flame in case T150-A50-d14 did not propagated further upstream into the quartz tube.

Flame structures in case T150-A50-d20: The flame structures in the case with a larger bluff-body was entirely different from that in the other cases. Although the flame tail still showed up, the flame expansion near the burner exit was not observed. Moreover, the flame was shorter and more compact than other cases. The bluish flame zone was found near the bluff-body other than in the region at h = 50mm in the other two cases.

More details about the reasons for the different flame structures will be discussed later with the flow fields obtained in different cases.

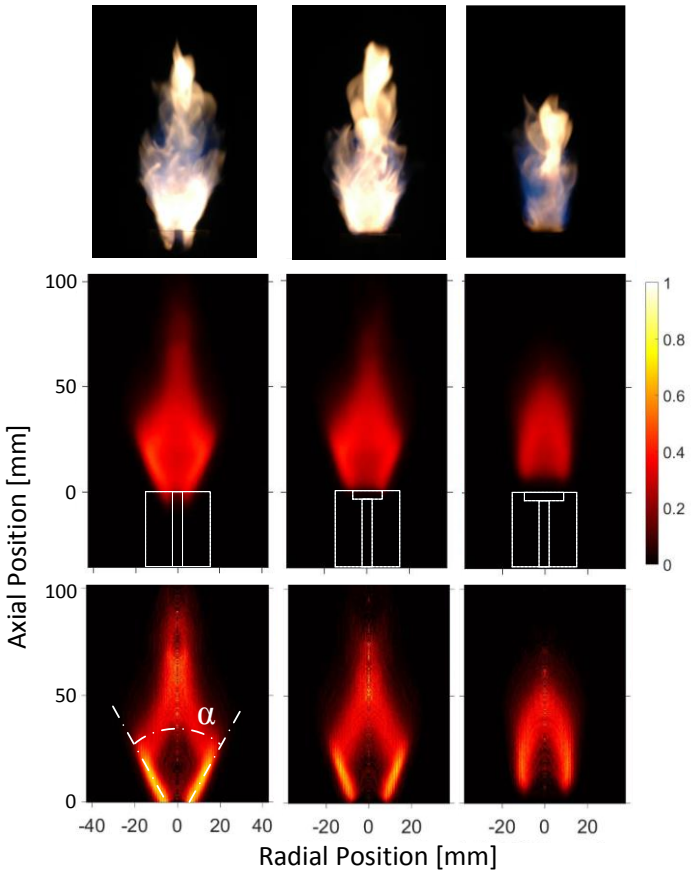

Fig.7 Flame structures within different cases. Left column: T150-A50-d0, center column: T150-A50-d14; right column: T150-A50-d20. Upper row: broadband chemiluminescence; middle row: time averaged CH* chemiluminescence; lower row: inverse Abel reconstructed CH* chemiluminescence.

The typical CH_2O PLIF results for different cases (T150-A50-d0, T150-A50-d14 and T150-A50-d20) are shown and compared with each other in Fig.8. The same as described in Fig.7, flames in cases T150-A50-d14 and T150-A50-d0 were similar with each other by having a wider expansion of CH_2O brush than that in the other case. The spatial distribution of CH_2O in the case T150-A50-d20 was more compact than the other cases. The simulation results show fairly good agreement with the experimental data, especially in capturing the expended CH_2O brush. The flow fields with the iso-contour marking the position with local equivalence ratio at $\Phi = 1$ are also illustrated in the second row in Fig.8. It shows that, in case T150-A50-d0, because of the swirling flow, a recirculation bubble is formed at h = 35mm downstream of the jet exit. The reverse flow motion in the air driven recirculation vortex forced the central fuel jet to propagate upstream and hence pushed the fuel jet expansion to the annular flow. In addition, a small recirculation bubbler was generated besides the central pipe near the jet exit. The recirculation vortex enhanced the fuel-air mixing and brought the fuel into the upstream region $h < 0$ by convection through the mixing layer between the fuel and air driven vortexes. Thus the flame in case T150-A50-d0 could be observed propagating

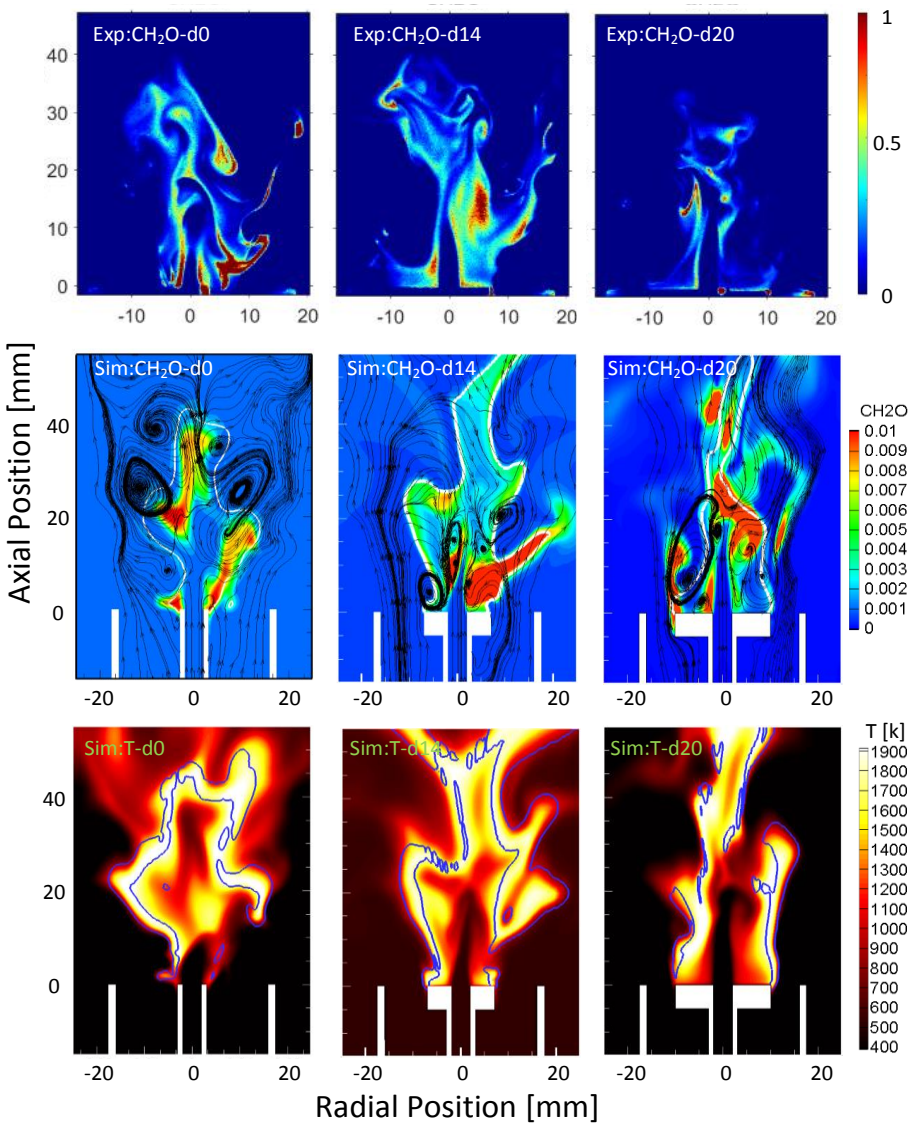

Fig.8 Comparison of experimental results and numerical data for different cases. Upper row: experimental data of CH_2O distribution; middle row: numerical data with CH_2O distribution and flow fields; the white lines denote the iso-contour of stoichiometric mixture; lower row: numerical data with temperature distribution; the blue lines denote the region with high heat release rate.

upstream into the region of $h < 0$ as shown in Fig.7. In addition, some part of the central fuel jet penetrated out the annular air driven recirculation zone. As a consequence, the flame tail could be generated in all the three cases shown in Fig.7. The figures in the third row in Fig.8 illustrate the temperature distribution together with blue lines marking the region with high heat release rates. It could be found that the snapshot of flame shape in the symmetric plane matches fairly well with the time averaged flame structures shown in Fig.7. Moreover, the high heat release rate region was found downstream of the region with high density of CH_2O and stoichiometric mixture. It was due to the fact that CH_2O were always found in the preheat zone while the high heat release and CH* were located in the reaction zone. Comparing the flow fields in the three different cases shown in Fig.8, it could be observed that with the increasing of the

size of bluff-body, the air driven recirculation vortex located more and more close to the jet exit. In the case T150-A50-d20, a large recirculation bubble was found attached to the bluff-body upper surface. The air driven recirculation vortex was believed to be generated due to the bluff-body other than the swirling flow. It was because that even when the flow swirl number was $S_g = 0$, the recirculation bubble could also be generated. It could also be observed that, in all the three cases shown in Fig.8, the strong heat release or the flame front was found in the mixing shear layer which located between the air driven outer recirculation zone and the fuel driven inner recirculation zone. Here the mixture got to stoichiometric condition which promoted the reaction. The flame structures were strongly determined by the flow fields, especially the sizes and locations of the inner and outer recirculation bubbles. With the change of the swirl strength, the flow fields and thus the flame structures would change significantly and they will be discussed later.

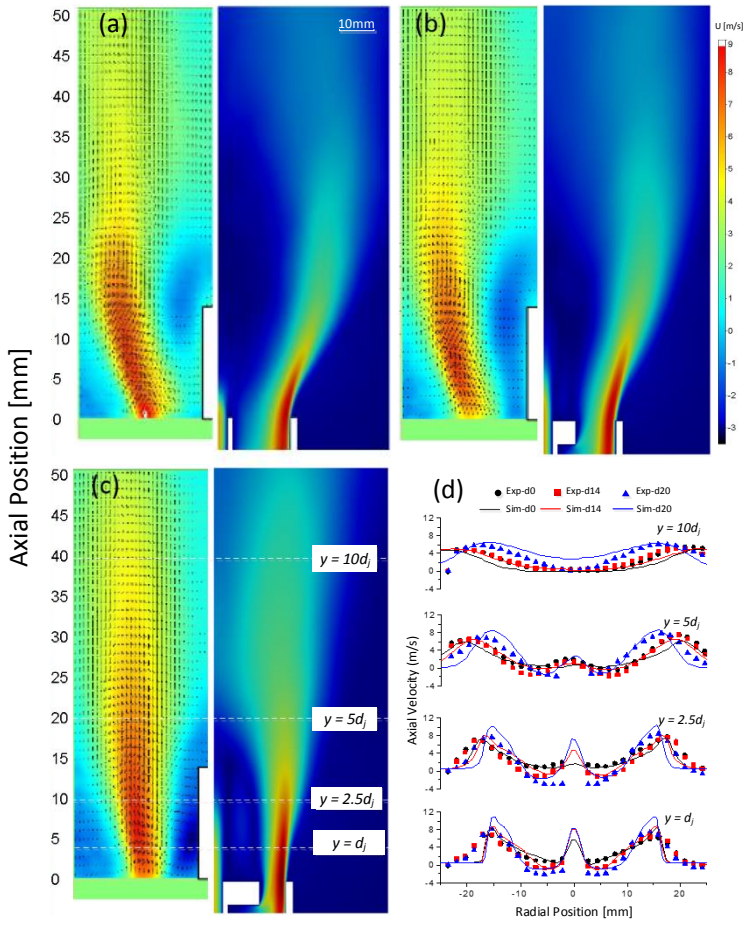

Fig.9 Time averaged flow fields in different cases (a) T150-A50-d0; (b) T150-A50-d0; (c) T150-A50-d0. (a) (b) and (c) Left: experimental data; right: simulation results. (d) axial velocity along radial direction in different axial positions.

In order to get deeper insight into the flame structures in Fig.7, the time averaged flow fields in the reacting cases: T150-A50-d0, T150-A50-d14 and T150-A50-d20 are shown and compared with each other in Fig.9. Since there were no seeding particles in the central fuel jet, the velocity fields in the central region was missed as shown by the

white rectangular region in Fig.9. The color map in Fig.9 stands for the scales of the axial velocity. In agree with the flame structures shown in Fig.7, it could be observed that cases without bluff-body and with the smaller bluff-body (d_b = 14mm) had the similar flow fields with each other under operating conditions of m_t =150ln/min and m_a = 50ln/min. Whereas they were far different from case with a larger bluff-body (d_b = 20mm). In case with the largest bluff-body, the air driven outer recirculation zone was smaller while its core was located more upstream than other cases, which was the same as observed in the snapshot of the flow fields shown in Fig.8. Because of the strongest constrain effects from the annular channel, in the case with the largest bluff-body (d_b = 20mm), the local flow velocity at the annular channel exit was parallel to the burner axis. It thus leaded to the formation of a smaller recirculation zone downstream of the bluff-body. In order to have a more details about the flow fields in these three cases, Fig.9(d) shows the axial velocity distributions along the radial direction at different axial positions.

In could be observed from Fig.9(d) that the time averaged simulation results match fairly well with the experimental data. When $h < 5d_j$, three peaks could be observed along the symmetrical axial velocity distributions. One peak was in the centerline due to the central jet penetration while the other two were on the sides of the centerline symmetrically which were mainly caused by the annular air flow. The location of the axial velocity side peak got farer from the burner axis with the increasing of the axial position (till $h = 10d_j$) which indicated the flow expansion downstream of the burner exit. Both the experimental and numerical results show that, in the case with a larger bluff-body, the value of the side peak in the axial velocity profile was higher than that in the other cases. It was caused by the fact that the axial flow velocity altered with the changing of the cross sectional area of annular channel at the burner exit. With a constant total air flow rate (m = 200ln/min) through the annular channel, the burner with a larger bluff-body could then have a higher bulk axial velocity. In addition, comparing three cases with different bluff-body sizes, it could be found that the location of the side peak axial velocity in case with d_b = 20mm was nearer to the burner axis than that in the other cases. It was consistent with the compactness of the flow structures. When $h < 10d_j$, in the air driven recirculation zone (2mm < r < 10mm or -10mm < r < 2mm), the case with d_b = 20mm had the highest reversing velocity and then the burner with d_b = 14mm. However, when $h = 10d_j$, the case with d_b = 20mm had the higher positive axial velocity in that region than the other cases. It also indicated that case with d_b = 20mm had the smallest air driven recirculation vortex. Comparing these three cases, the central jet velocity was higher in case with d_b = 20mm indicating a stronger shear stress could be found in the inner shear layer between the central jet and the inner recirculation zone. The stronger fuel-air mixing could be found in case with d_b = 20mm which could then lead to a bluish root flame near the bluff-body. However, the size of the air driven recirculation zone in that case was smaller than the other cases which would thus result at a shorter residence time for the fuel-air mixing and thus a higher CO emission levels as will be discussed later.

Effects of swirl on flames: Fig.10 shows the effects of swirl number on flame structures

in case with d_b = 14mm. It could be easily seen that the flame was elongated with the decreasing of swirl number. While the flame open angle became smaller due to the decreasing of the centrifugal effects in the lower swirl strength flows. When the geometrical swirl number was high (S_g = 2.83) for case T200-A0-d14, a flame 'flashback' was observed. The flame was propagating into the region with $h < 0$ upstream of the bluff-body. The flame flashback phenomenon is more commonly observed in the premixed flame studies. Premixing flame flashback occurs when the flame propagates upstream into the premixing section from the combustion chamber. This can be a result of the turbulent flame speed exceeding the flow velocity along some streamlines in the combustor causing the reaction zone to travel upstream [46]. However, the diffusion flame 'flashback' into the quartz tube upstream of the bluff-body in the current study is rarely reported while the mechanism behind needs to be investigated. The more detailed description of the diffusion 'flashback' and the mechanism behind will be discussed later with the simulation results.

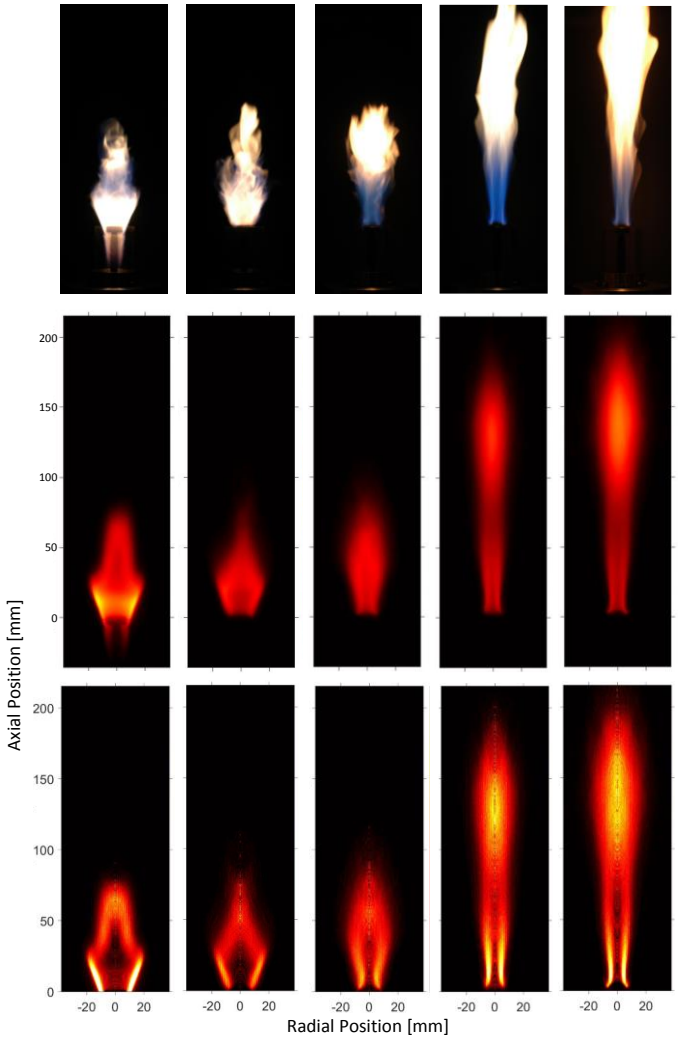

Fig.10 Flame structures with different swirl number. From left to right: T200-A0-d14, T150-A50-d14, T100-A100-d14, T50-A150-d14 and T0-A200-d14; upper row: direct photo, middle row: time averaged CH* chemiluminescence, lower row: inverse Abel reconstructed CH* chemiluminescence.

The interesting phenomenon of the diffusion flame 'flashback' into further upstream region was observed and recorded in the experiments as shown in Fig.11. When holding m_t = 200ln/min and m_a = 0ln/min, the broadband chemiluminescence from the flame (upper row in Fig.11) together with the line-of-sight and time-averaged flame CH* chemiluminescence obtained from the experiments and simulations are shown and compared with each other in Fig.11. The blue line in simulation results in the lower row of Fig.11 denotes the stoichiometric mixture region which can be used to mark the spatial distribution of the fuel. From the broadband flame structures it could be seen that flame in the case T200-A0-d0 had more soot than the other two cases; while flame in the case with d_b = 20mm had a bluish color indicating the best mixing of fuel and air. However, the same as discussed previously, the recirculation zone in the case with the larger bluff-body was smaller than the other two cases. Therefore, it would lead to the higher CO emission levels due to the shorter residence time in the recirculation zone, which will be discussed later. Comparing the flame structures in cases T150-A50-d0 and T150-A50-d14 in Fig.7, it could be seen that the flame with m_t = 200ln/min was propagating further upstream into the quartz tube even till h < -20mm. In cases T200-A0-d0 and T200-A0-d14, the strong reverse flow in the air driven vortex pushed some part of the central fuel jet in the air-fuel mixing layer upstream into the quartz tube. However, in case with d_b = 20mm, the flame could not be pushed upstream into the quartz tube due to the blockage of the large bluff-body. It could also be found that the inner fuel driven vortex was smaller in the case with d_b = 20mm than that in the other cases due to the stronger reverse flow momentum. The central fuel jet could penetrate higher in the case without bluff-body. Comparing the flame structures shown in Fig.7 and Fig.11, for case with d_b = 20mm, a decrease of flame length and the widening of the flame open angle could be observed with the increasing of swirl number. They were caused by the further downstream movement of the air driven recirculation bubbles. The increasing of the swirl number enhanced the outer recirculation zone and thus the reversing flow momentum. It resisted the central jet penetration forming a shorter flame with higher CO emission levels.

Fig.12 shows the effects of bluff-body and swirl strength on flame length (L_F) and H_{COHR} positions. It could be found that flame in case with d_b = 14mm had the largest L_F and the highest H_{COHR}. Flame in case with the larger bluff-body (d_b = 20mm) was more compact than that in other cases by having a shorter L_F and a lower position of H_{COHR}. The same as observed in Fig.10, in case with d_b = 14, with the increasing of the swirl number (or the tangential air mass flow rate), the flame became shorter and more compact. However, in the case with d_b = 20mm, the flame length and its position did not change significantly with the alternation of swirl strength. The reason behind might be the recirculation zone downstream of the larger bluff-body was more dominated by the bluff-body nor the swirling flow. Therefore, the increasing of tangential flow rate did not significantly change the flame structures. It is worth noting that the flame could not be sustained in case without the bluff-body when m_t <120ln/min. The bluff-body enhanced the diffusion flame stabilization especially in case with low swirl number.

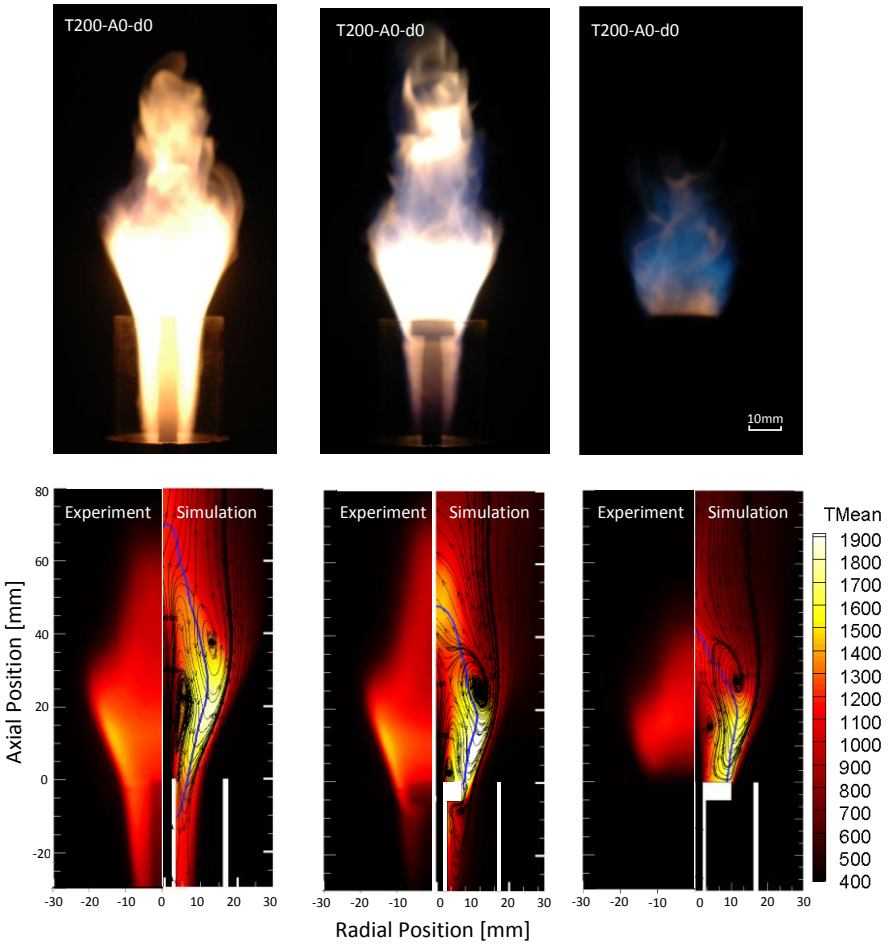

Fig.11 Different flame structures in cases (left column): T200-A0-d0, (middle column) T200-A0-d14 and (right column) T200-A0-d20 when holding tangential air flow rate m_t = 200ln/min. Upper row: broadband chemiluminescence; lower column: comparison of time averaged CH* chemiluminescence and numerical data of temperature distribution and flow structures.

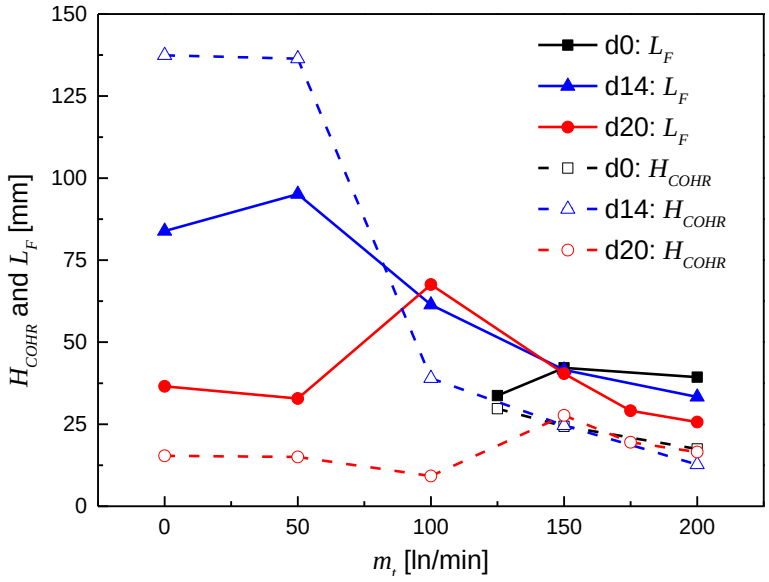

Fig.12 Flame length versus mass flow rate of the tangential air flow.

Emissions: The global CO emission levels are strongly consistent with the combustion efficiency and combustion completion, which generally suggest the mixing between the fuels and air flow and the residence time for the reaction to be completed. Fig.13 shows the global emission of CO for different cases when holding the global equivalence ratio constant. It could be observed that the burner with d_b = 20mm produced the highest levels of CO emissions, while the case without bluff-body had the lowest level of CO emissions. The CO emission is strongly related to the fuel-air mixing and mixture residence time in the recirculation zone. In addition, the CO emission level was found to have strong correlation with the flame length and flame compaction [47]. The longer flame length and a larger recirculation zone implies a longer combustion residence time, allowing a more complete combustion and thus a lower amount of CO emissions. The stronger reverse flow velocity in the recirculation zone downstream of the bluff-body leaded to a better mixing of the fuel and the annular air which then also resulted at a lower CO emission level. Since the central jet velocity and momentum were kept constant, the size of the recirculation zone then determined the penetration of central jet and thus the mixing of fuel and air. Holding the tangential air flow constant, the recirculation zone in case with d_b = 20mm was smaller than any other cases which thus resulted at a highest CO emission levels as shown in Fig.13. The change of CO emission shown in Fig.13 was found to be strongly correlated to the alternation of flame length demonstrated in Fig.12. To be more specifically, for the case with d_b = 20mm, the lowest CO emission at case with m_t = 100ln/min was ascribed to the longest flame length as shown in Fig.12. Additionally, another proof showing that the CO emission was strongly affected by the recirculation zone size was that: for case T200-A0-d14, the recirculation zone in the 'flashback' flame was larger than that in case T150-A50-d14. As a consequence, the CO emission dropped significantly in case T200-A0-d14.

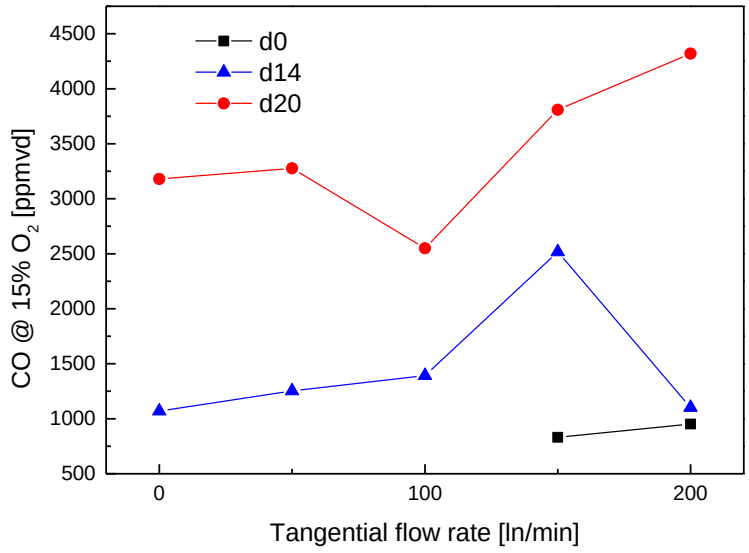

Fig.13 Effects of bluff-body and tangential flow rate on global CO emissions.

Conclusions

Combined swirl and bluff-body stabilized diffusion CH_4-air flames were investigated in the current study. Both experimental and numerical methods were adopted to get deep insight into the flame structures and its emissions. The total air flow rate and fuel flow rate were hold constant at m = 200ln/min and m_f = 3 ln/min respectively. The diffusion flame 'flashback' phenomenon together with its mechanism behind were described in detail. The mixing characteristics of the fuel and air downstream of the bluff-body were released and compared with each other to evaluated the effects of bluff-body size and swirl strength on flame structures and CO emission levels. It is found that when holding the ratio of the tangential and axial flow rates constant, the recirculation zone downstream of the larger bluff-body (d_b = 20mm) was smaller than the other cases, which would lead to a higher CO emission. With a lager bluff-body, the flame was found to be more compact while the flame 'flashback' could not be observed. The air driven recirculation bubble within the case with d_b = 20mm was more dominated by the bluff-body nor the swirling strength. Hence in case with d_b = 20mm, the CO emissions and flame length did not change significantly with the changing of swirling strength. The position of the outer recirculation zone would be affected by the size of the bluff-body. In the cases without bluff-body or d_b = 14mm, the outer recirculation bubble was determined by the swirling strength as well. In the burner without the bluff-body, a larger and stronger air driven recirculation zone was the reason for the diffusion flame 'flashback' upstream into the quartz tube. With the increasing of the swirl strength, in the case with d_b = 14mm, the flame was elongated. In addition, in the case with d_b = 20mm, the CO emission level showed strong relation with the flame length. The utilization of bluff-body significantly enhanced flame stabilization by maintaining flames in cases with m_t < 150 ln/min.

Acknowledgements

Authors Yiheng Tong and Xiao Liu are supported by scholarship from China Scholarship Council (CSC) which is gratefully acknowledged. The simulation work was carried out using the computer facilities provided by the Lund University Center for Scientific and Technical Computing (LUNARC) and Center for Parallel Computers (PDC).

References

[1] Y.M. Al-Abdeli, A.R. Masri, G.R. Marquez, S.H. Starner, Time-varying behaviour of turbulent swirling nonpremixed flames, Combustion and flame, 146 (2006) 200-214.
[2] Y.M. Al-Abdeli, A.R. Masri, Recirculation and flowfield regimes of unconfined non-reacting swirling flows, Experimental Thermal and Fluid Science, 27 (2003) 655-665.
[3] P.A. Kalt, Y.M. Al-Abdell, A.R. Masri, R.S. Barlow, Swirling turbulent non-premixed flames of methane: flow field and compositional structure, Proceedings of the Combustion Institute, 29 (2002) 1913-1919.

[4] A. Masri, P. Kalt, Y. Al-Abdeli, R. Barlow, Turbulence–chemistry interactions in non-premixed swirling flames, Combustion Theory and Modelling, 11 (2007) 653-673.
[5] Y.M. AL-ABDELI∗, A.R. Masri, Turbulent swirling natural gas flames: stability characteristics, unsteady behavior and vortex breakdown, Combustion science and technology, 179 (2007) 207-225.
[6] Y.M. Al-Abdeli, A.R. Masri, Stability characteristics and flowfields of turbulent non-premixed swirling flames, Combustion Theory and Modelling, 7 (2003) 731-766.
[7] W. Malalasekera, K. Ranga-Dinesh, S.S. Ibrahim, A.R. Masri, LES of recirculation and vortex breakdown in swirling flames, Combustion science and technology, 180 (2008) 809-832.
[8] R.-H. Chen, J.F. DRISCOLL, J. Kelly, M. Namazian, R. Schefer, A comparison of bluff-body and swirl-stabilized flames, Combustion science and technology, 71 (1990) 197-217.
[9] A. Coghe, G. Solero, G. Scribano, Recirculation phenomena in a natural gas swirl combustor, Experimental Thermal and Fluid Science, 28 (2004) 709-714.
[10] A. Olivani, G. Solero, F. Cozzi, A. Coghe, Near field flow structure of isothermal swirling flows and reacting non-premixed swirling flames, Experimental Thermal and Fluid Science, 31 (2007) 427-436.
[11] R. Santhosh, S. Basu, Transitions and blowoff of unconfined non-premixed swirling flame, Combustion and flame, 164 (2016) 35-52.
[12] M.E. Loretero, R.F. Huang, Effects of acoustic excitation on a swirling diffusion flame, Journal of Engineering for Gas Turbines and Power, 132 (2010) 121501.
[13] B. Ge, S.-S. Zang, Experimental study on the interactions for bluff-body and swirl in stabilized flame process, Journal of Thermal Science, 21 (2012) 88-96.
[14] H. Kawahara, T. Nishimura, Improvement in flame stability of diffusion flame using a bluff-body swirling jet combustor, HEFAT 2012, (2012).
[15] P. Schmittel, B. Günther, B. Lenze, W. Leuckel, H. Bockhorn, Turbulent swirling flames: Experimental investigation of the flow field and formation of nitrogen oxide, Proceedings of the Combustion Institute, 28 (2000) 303-309.
[16] A.M. Elbaz, W.L. Roberts, Investigation of the effects of quarl and initial conditions on swirling non-premixed methane flames: Flow field, temperature, and species distributions, Fuel, 169 (2016) 120-134.
[17] K.R. Dinesh, K.W. Jenkins, A. Savill, M. Kirkpatrick, Influence of Bluff-body and Swirl on Mixing and Intermittency of Jets, Engineering Applications of Computational Fluid Mechanics, 4 (2010) 374-386.
[18] I. Yılmaz, Effect of swirl number on combustion characteristics in a natural gas diffusion flame, Journal of energy resources technology, 135 (2013) 042204.
[19] B. Kashir, S. Tabejamaat, N. Jalalatian, A numerical study on combustion characteristics of blended methane-hydrogen bluff-body stabilized swirl diffusion flames, International Journal of Hydrogen Energy, 40 (2015) 6243-6258.
[20] A.R. Masri, P.A. Kalt, R.S. Barlow, The compositional structure of swirl-stabilised turbulent nonpremixed flames, Combustion and flame, 137 (2004) 1-37.
[21] M. Malanoski, M. Aguilar, D.-H. Shin, T. Lieuwen, Flame leading edge and flow dynamics in a swirling, lifted flame, Combustion science and technology, 186 (2014)

1816-1843.
[22] B. Dally, A. Masri, R. Barlow, G. Fiechtner, Instantaneous and mean compositional structure of bluff-body stabilized nonpremixed flames, Combustion and flame, 114 (1998) 119-148.
[23] O. Stein, A. Kempf, LES of the Sydney swirl flame series: A study of vortex breakdown in isothermal and reacting flows, Proceedings of the Combustion Institute, 31 (2007) 1755-1763.
[24] H. Pitsch, Large-eddy simulation of turbulent combustion, Annu. Rev. Fluid Mech., 38 (2006) 453-482.
[25] L.Y. Gicquel, G. Staffelbach, T. Poinsot, Large eddy simulations of gaseous flames in gas turbine combustion chambers, Progress in Energy and Combustion Science, 38 (2012) 782-817.
[26] H. El-Asrag, S. Menon, Large eddy simulation of bluff-body stabilized swirling non-premixed flames, Proceedings of the Combustion Institute, 31 (2007) 1747-1754.
[27] A.M.E. X. Liu, C. Gong, X.S. Bai, H.T. Zheng and W.L. Roberts, Effect of burner geometry on swirl stabilized methane/air flames: A joint LES/OH-PLIF/PIV study, Fuel, 207 (2017) 14.
[28] X. Liu, H. Zheng, J. Yang, Y. Li, LES-PDF modeling of blowout analysis in slit bluff-body stabilized flames, International Journal of Spray and Combustion Dynamics, 7 (2015) 131-150.
[29] V. Raman, H. Pitsch, Large-eddy simulation of a bluff-body-stabilized non-premixed flame using a recursive filter-refinement procedure, Combustion and flame, 142 (2005) 329-347.
[30] A. Kempf, R. Lindstedt, J. Janicka, Large-eddy simulation of a bluff-body stabilized nonpremixed flame, Combustion and flame, 144 (2006) 170-189.
[31] P.P. Popov, S.B. Pope, Large eddy simulation/probability density function simulations of bluff body stabilized flames, Combustion and flame, 161 (2014) 3100-3133.
[32] H.-G. Li, P. Khare, H.-G. Sung, V. Yang, A Large-Eddy-Simulation Study of Combustion Dynamics of Bluff-Body Stabilized Flames, Combustion science and technology, 188 (2016) 924-952.
[33] T. Claypole, N. Syred, The effect of swirl burner aerodynamics on NOx formation, in: Symposium (International) on Combustion, Vol. 18, Elsevier, 1981, pp. 81-89.
[34] R. Schefer, M. Namazian, J. Kelly, M. Perrin, Effect of confinement on bluff-body burner recirculation zone characteristics and flame stability, Combustion science and technology, 120 (1996) 185-211.
[35] A.J. De Rosa, S.J. Peluso, B.D. Quay, D.A. Santavicca, The Effect of Confinement on the Structure and Dynamic Response of Lean-Premixed, Swirl-Stabilized Flames, Journal of Engineering for Gas Turbines and Power, 138 (2016) 061507.
[36] Y. Tong, M. Li, J. Klingmann, Influence of Combustor Geometry on Swirl Stabilized Premixed Methane-Air Flame, in: ASME Turbo Expo 2016: Turbomachinery Technical Conference and Exposition, American Society of Mechanical Engineers, 2016, pp. V04BT04A002-V004BT004A002.
[37] B. Schuermans, V. Bellucci, F. Guethe, F. Meili, P. Flohr, C.O. Paschereit, A

detailed analysis of thermoacoustic interaction mechanisms in a turbulent premixed flame, in: ASME Turbo Expo 2004: Power for Land, Sea, and Air, American Society of Mechanical Engineers, 2004, pp. 539-551.
[38] C. Brackmann, J. Nygren, X. Bai, Z. Li, H. Bladh, B. Axelsson, I. Denbratt, L. Koopmans, P.-E. Bengtsson, M. Aldén, Laser-induced fluorescence of formaldehyde in combustion using third harmonic Nd: YAG laser excitation, Spectrochimica Acta Part A: Molecular and Biomolecular Spectroscopy, 59 (2003) 3347-3356.
[39] A. Kundu, J. Klingmann, A.A. Subash, R. Collin, Pilot-Pilot Interaction Effects on a Prototype DLE Gas Turbine Burner Combustion, in: ASME Turbo Expo 2016: Turbomachinery Technical Conference and Exposition, American Society of Mechanical Engineers, 2016, pp. V04BT04A012-V004BT004A012.
[40] M. Li, Y. Tong, M. Thern, J. Klingmann, Investigation of Methane Oxy-Fuel Combustion in a Swirl-Stabilised Gas Turbine Model Combustor, Energies, 10 (2017) 648.
[41] S.B. Pope, PDF methods for turbulent reactive flows, Progress in Energy and Combustion Science, 11 (1985) 119-192.
[42] D. Haworth, Progress in probability density function methods for turbulent reacting flows, Progress in Energy and Combustion Science, 36 (2010) 168-259.
[43] W. Jones, V. Prasad, Large Eddy Simulation of the Sandia Flame Series (D–F) using the Eulerian stochastic field method, Combustion and flame, 157 (2010) 1621-1636.
[44] M.D. Smooke, V. Giovangigli, Premixed and nonpremixed test problem results, in: Reduced kinetic mechanisms and asymptotic approximations for methane-air flames, Springer, 1991, pp. 29-47.
[45] G.P. Smith, D.M. Golden, M. Frenklach, N.W. Moriarty, B. Eiteneer, M. Goldenberg, C.T. Bowman, R.K. Hanson, S. Song, W.J. Gardiner, GRI 3.0, Gas Research Institute, Chicago, IL, http://www. me. berkeley. edu/gri_mech, (2000).
[46] P. Sayad, A. Schönborn, J. Klingmann, Experimental investigation of the stability limits of premixed syngas-air flames at two moderate swirl numbers, Combustion and flame, 164 (2016) 270-282.
[47] Y.-H. Liao, J.C. Hermanson, The CO/NOx emissions of swirled, strongly pulsed jet diffusion flames, Combustion science and technology, 186 (2014) 849-868.
[48] OpenFoam, Openfoam foundation web site:< http://openfoam.com>; 2017